

Rheo-mechanics modelling of 3D concrete printing constructability

by

Pienaar Jacques Kruger



Dissertation presented for the degree of
Doctor of Philosophy in Engineering
in the Faculty of Engineering
at Stellenbosch University

Supervisor: Prof Gideon P.A.G. van Zijl

Co-supervisor: Dr Stephan Zeranka

December 2019

Declaration

By submitting this dissertation electronically, I declare that the entirety of the work contained therein is my own, original work, that I am the sole author thereof (save to the extent explicitly otherwise stated), that reproduction and publication thereof by Stellenbosch University will not infringe any third party rights and that I have not previously in its entirety or in part submitted it for obtaining any qualification.

This dissertation includes 2 original papers published in peer-reviewed journals or books and 2 unpublished publications. The development and writing of the papers (published and unpublished) were the principal responsibility of myself and, for each of the cases where this is not the case, a declaration is included in the dissertation indicating the nature and extent of the contributions of co-authors.

December 2019

Copyright © 2019 Stellenbosch University

All rights reserved

Abstract

Three industrial revolutions have occurred in the last 250 years that resulted in increased productivity for most economic sectors. This generally improved the standard of living for all individuals. Recent research has however found that the productivity of the USA's construction sector regressed at 0.6 % per year over the last 55 years. This indicates that the construction industry has not yet experienced the benefits of industrialisation. The current industrial revolution, commonly referred to as Industry 4.0, presents technology such as 3D printing. Applying this technology in the construction sector yields 3D printing of concrete (3DPC), or digital construction, that holds tremendous potential for enhanced productivity. Early estimates indicate possible construction time savings of 50 % and waste savings of 30 %. Additionally, the realisation of geometrically-complex elements is possible without the need for formwork. Although a promising technology, it remains in the early stages of commercialisation and presents many challenges before mass adoption thereof.

No material characterisation test currently exists that specifically appertains to 3DPC. Fresh state mechanical tests are mostly performed; however, they provide insignificant information on the appropriateness of a material for 3DPC. This process requires a material to be easily transported via pumping, but then also to possess sufficient strength after extrusion to support the weight of subsequent filament layers. The latter is commonly referred to as buildability in 3DPC terminology. Furthermore, limited constructability design guidelines are currently available; consequently, elements are typically printed at randomly chosen speeds and filament layer heights with the hope of a successful outcome i.e. the element does not collapse whilst being printed. The main aim of this research is thus to develop practicable analytical models based on rheological material properties that collectively contribute towards constructability design guidelines for 3DPC.

This research initially presents the design and manufacture of an industrial-grade gantry type 3D concrete printer with a build volume of roughly 1 m³. The development of a high-performance, 3D printable, thixotropic concrete via the Fuller Thompson theory is explained. Progression and mastering of basic 3DPC technology is demonstrated by means of pictures from initial 3D prints conducted at Stellenbosch University to the latest X-project. Thereafter, a bi-linear thixotropy model that specifically appertains to 3DPC is developed. A current thixotropy model that accounts for structuration (A_{thix}) is extended to account for re-flocculation after agitation (R_{thix}), which is a physical process. The material characterisation

is solely conducted by the use of a rheometer. In addition to presenting insight into a material's thixotropy behaviour, the bi-linear static yield shear stress evolution curve depicts the strength gain of a material after it has been extruded from the nozzle. The following chapter presents the development of a filament shape retention model that is based on the bi-linear thixotropy model. The model is simple and practicable, while numerical validation via finite element analysis depicts the conservatism of the model. Thereafter, an analytical buildability model is developed which is also based on the bi-linear thixotropy model. The model only accounts for material failure in the form of plastic yielding. In addition, the model accounts for various filament aspect ratios, which influence the apparent compressive strength of a material. The model is verified by experimental testing, yielding an 8.33 % under prediction of the total number of filament layers before failure.

Finally, the three models are combined to yield a constructability design model for 3DPC. The model predicts the optimum print parameter combination, i.e. filament layer height and print speed, that successfully yields the entire specified print object in the least amount of time. In addition, a statistical design model is presented by incorporating material partial factors to reduce the model's probability of failure to 10 %. In summary, this research contributes a statistically safe and time-optimised constructability design model for the 3DPC industry to facilitate commercialisation of the technology.

Opsomming

Drie industriële rewolusies het plaasgevind in die afgelope 250 jaar wat gelei het tot verhoogde produktiwiteit vir die meeste ekonomiese sektore. Dit het die lewenstandaard vir alle individue oor die algemeen verbeter. Onlangse navorsing het egter bevind dat die produktiwiteit van die VSA se konstruksiesektor die afgelope 55 jaar teen 0,6 % per jaar gedaal het. Dit dui daarop dat die konstruksiebedryf nog nie die voordele van industrialisasie ervaar het nie. Die huidige industriële rewolusie, algemeen bekend as “Industry 4.0”, bied tegnologie soos 3D-drukwerk. Die toepassing van hierdie tegnologie in die konstruksie sektor lewer 3D drukwerk van beton (3DDB), of digitale konstruksie, wat enorme potensiaal inhou vir verhoogde produktiwiteit. Vroeë skattings dui op moontlike konstruksietydbesparings van 50 % en afvalbesparings van 30 %. Daarbenewens is die realisering van geometriese-komplekse elemente moontlik sonder enige bekisting vereistes. Alhoewel ’n belowende tegnologie, bly dit in die vroeë stadiums van kommersialisering en bied dit vele uitdagings voor massa-aanvaarding daarvan.

Daar bestaan tans geen wesenlike materiaal karakteriseringstoets wat spesifiek op 3DDB betrekking het nie. Varstoestand meganiese toetse word meestal uitgevoer, alhoewel dit egter onbeduidende inligting oor die toepaslikheid van ’n materiaal vir 3DDB bied. Hierdie proses vereis dat ’n materiaal maklik vervoer moet kan word deur dit te pomp, maar dan ook voldoende sterkte besit na ekstrusie om die gewig van die daaropvolgende filamentlae te ondersteun. Laasgenoemde word algemeen na verwys as boubaarheid in 3DDB-terminologie. Verder bestaan daar beperkte ontwerpstriglyne vir oprigbaarheid; gevolglik word elemente tipies gedruk met lukraak gekose spoed en filament laaghoogtes met die hoop op ’n suksesvolle uitkoms, d.w.s. die element tuimel nie inmekaar terwyl dit gedruk word nie. Die hoofdoel van hierdie navorsing is dus om uitvoerbare, analitiese modelle te ontwikkel gebaseer op reologiese materiaaleienskappe wat gesamentlik bydra tot oprigbaarheid ontwerpstriglyne vir 3DDB.

Hierdie navorsing bied aanvanklik die ontwerp en vervaardiging van ’n industriële graad “gantry”-tipe 3D beton drukker met ’n bou volume van ongeveer 1 m^3 . Die ontwikkeling van ’n hoëprestasie, 3D-drukbare, thiksotropiese beton met behulp van die Fuller Thompson-teorie word verduidelik. Vordering en bemeestering van basiese 3DDB-tegnologie word getoon deur middel van foto’s van aanvanklike 3D-drukke wat by die Universiteit Stellenbosch uitgevoer is tot die nuutste X-projek. Daarna word ’n bi-lineêre thiksotropie model ontwikkel wat spesifiek op 3DDB betrekking het. ’n Bestaande thiksotropie model wat voorsiening maak vir

strukturering (A_{thix}) word uitgebrei om ook her-flokkulasie na steuring (R_{thix}) in ag te neem, wat 'n fisiese proses is. Die materiaal karakterisering word uitsluitlik uitgevoer deur die gebruik van 'n reometer. Benewens die aanduiding van 'n materiaal se thixotropie gedrag, toon die bi-lineêre statiese swigskuifspanning ewolusie kurwe die sterkte toename van 'n materiaal nadat dit uit 'n spuitstuk geëkstrueer is. Die volgende hoofstuk bied die ontwikkeling van 'n filament vormhoubaarheidsmodel aan wat gebaseer is op die bi-lineêre thixotropie model. Die model is eenvoudig en uitvoerbaar, terwyl numeriese validering via eindige elementontleding die konserwatisme van die model uitbeeld. Daarna word 'n analitiese boubaarheidsmodel ontwikkel wat ook gebaseer is op die bi-lineêre thixotropie model. Die model maak slegs voorsiening vir materiaal faling in die vorm van plastiese swig. Daarbenewens maak die model ook voorsiening vir verskeie filament-aspekverhoudings, wat die oënskynlike druksterkte van 'n materiaal beïnvloed. Die model word geverifieer deur eksperimentele toetsing, wat 'n 8.33 % onder-voorspelling van die totale aantal filamentlae voor faling lewer.

Ten slotte word die drie modelle gekombineer om 'n oprigbaarheidsmodel vir 3DDB te lewer. Die model voorspel die optimale drukparameter kombinasie, d.w.s. filament laaghoogte en drukspoed, wat die hele gespesifiseerde drukobjek in die minste tyd suksesvol sal oplewer. Daarbenewens word 'n statistiese ontwerpmodel voorgelê deur parsieële materiaal-faktore in te sluit om die model se falingswaarskynlikheid tot 10 % te verminder. Ter opsomming, dra hierdie navorsing 'n statisties veilige en tyd-geöptimiseerde oprigbaarheidsmodel tot die 3DDB-industrie by om kommersialisering van dié tegnologie te fasiliteer.

Acknowledgements

I thank the following people for their contribution towards the realisation of this dissertation:

- My supervisor, Professor Gideon van Zijl, for his unwavering support, guidance, mentorship and leadership during this research journey. Except for being an exceptional study leader, Gideon invests in his students by presenting them with remarkable opportunities to grow individually. *Proost, op veel meer reizen!*
- My co-supervisor, Dr. Stephan Zeranka, for his support.
- The 3DPC team, particularly Mr. Seung Cho, Mr. Marchant van den Heever and Mr. Frederick Bester, for joining me on this exciting research journey.
- The laboratory and workshop staff, particularly Mr. Johan van der Merwe “Oom”, for their assistance and guidance with experimental work.
- The 3DPC team at Technische Universiteit Eindhoven (Profs. Salet and Suiker, Drs. Bos and Lucas) for presenting me the opportunity to learn from the best. *Dankjewel!*
- The Wilhelm Frank Trust for their financial support during my postgraduate studies.
- The Concrete Institute and the Department of Trade and Industry for financing this research.
- My family, in particular the Viljoen’s from Draaifontein and the van der Merwe’s from Port Elizabeth, for their continuous interest and support during this research.
- The Bruwer’s from Prospect for their continuous interest and support during this research.
- All my friends for their support and understanding when the going got tough.
- My lady, Suzanne Maude Bruwer “*liefie*”, for her unending love, support, advice and understanding. *Lief vir jou.*
- My Creator for giving me the opportunity, ability and patience to conduct this research. HalleluYah.

“*Doen alles 100%, of eerder glad nie.*” – PJP Kruger

Table of Contents

Declaration	i
Abstract	ii
Opsomming	iv
Acknowledgements	vi
Table of Contents	vii
List of Figures	x
List of Tables	xvi
List of Abbreviations and Acronyms	xviii
List of Symbols	xxi
Chapter 1	1
Introduction	1
1.1 Problem statement.....	4
1.2 Aim and objectives of study.....	5
1.3 Significance, motivation and applicability.....	6
1.4 3D concrete printing literature and terminology	7
1.5 Dissertation structure.....	13
1.6 References	14
Chapter 2	17
Development of a 3D concrete printer	17
2.1 3D concrete printer design	17
2.2 Procurement	23
2.3 Manufacturing of 3D concrete printer.....	24
2.4 Material mix design.....	26
2.5 3D concrete prints	30

2.6	Conclusion.....	34
2.7	References	35
Chapter 3	36
	An ab initio approach for thixotropy characterisation of (nanoparticle-infused) 3D printable concrete.....	36
3.1	Introduction	37
3.2	Thixotropy theory.....	38
3.3	Model development.....	49
3.4	Experimental procedure	52
3.5	Results & discussions.....	60
3.6	Validation of nano-silica influence via 3DPC.....	70
3.7	Conclusions	73
3.8	References	75
Chapter 4	79
	A rheology-based quasi-static shape retention model for digitally fabricated concrete	79
4.1	Introduction	80
4.2	Model development.....	81
4.3	Experimental verification.....	98
4.4	Numerical verification.....	106
4.5	Conclusion.....	113
4.6	References	115
Chapter 5	118
	3D concrete printing: A lower bound analytical model for buildability performance quantification	118
5.1	Introduction	119
5.2	Model development.....	120
5.3	Experimental verification.....	142
5.4	Conclusion.....	152

5.5	References	154
Chapter 6	158
	3D concrete printer parameter optimisation for high rate digital construction avoiding plastic collapse	158
6.1	Introduction	159
6.2	Theoretical framework	160
6.3	Experimental verification.....	166
6.4	Proposed statistical design model	178
6.5	Conclusion.....	183
6.6	References	185
Chapter 7	188
	Conclusions	188
7.1	Research summary and contributions	188
7.2	Main research findings	190
7.3	Recommended future research	192
Addendum A	– Article Declarations	194
Addendum B	– Copyright Permission.....	198

List of Figures

Figure 1.1: Comparison between US construction labour productivity and non-farm labour productivity (Huang, Chapman & Butry, 2009).	2
Figure 1.2: Percentage of South African households that live in formal, informal and traditional dwellings by province in 2017 (Statistics South Africa, 2018).	6
Figure 1.3: Four main 3DPC systems (a) gantry system by TU/e (TU/e, n.d.), (b) robotic system by CyBe Construction (Grunewald, 2015), (c) mobile system by CyBe Construction (Saunders, 2016) and (d) crane system by Apis-Cor (Apis-Cor, 2017c).	8
Figure 1.4: Schematic drawing of the 3DPC execution process.	9
Figure 1.5: Increase in buildability (a) before and (b) after the installation of a real-time feedback system (Wolfs et al., 2017).	12
Figure 2.1: Rendered image of the 3D Inventor model depicting the concrete printer.	18
Figure 2.2: Detail of gantry system to vertical linear rail connection.	20
Figure 2.3: Schematic diagram of the main electrical components.	21
Figure 2.4: Schematic diagram of the pump automation process.	23
Figure 2.5: Manufacturing of the 3D concrete printer indicating the framework (left) and the almost completed mechanical component of the printer (right).	24
Figure 2.6: The completed 3D concrete printer with automation system (left) and the electrical control box (right).	25
Figure 2.7: 3D concrete printer component layout and final assembly.	25
Figure 2.8: Particle size distribution of various different fine aggregates obtained from sieve analyses compared to Fuller’s ideal particle grading.	28
Figure 2.9: Particle size distribution of the reference 3D printable HPC mix compared to Fuller’s ideal grading curve.	29
Figure 2.10: IBS specimen cut from 3DP square hollow section and loaded at third points. 29	
Figure 2.11: (a) Initial print performed in order to calibrate the printer, (b) column printed again with improved material and calibration, (c) column printed again with final 3DPC mix composition and (d) bathtub print with increased geometrical complexity.	31
Figure 2.12: A 250 x 250 x 700 mm square hollow column that twists 45° over its height. ...	32
Figure 2.13: A 250 x 250 x 800 mm square hollow column that twists 90° over a height of 600 mm. The column was printed in less than 25 minutes with a polypropylene fibre reinforced 3D printable concrete.	32

Figure 2.14: Construction of the X-project table (top-left) and bench (top-right) with the undulating surface finish of the bench indicated in the bottom picture.	33
Figure 2.15: Completed prototype of the X-project bench set with 3DPC team members Mr. Marchant van den Heever and Mr. Frederick Bester.	34
Figure 3.1: Describing thixotropy by means of a stress growth rheological characterisation test that depicts the static and dynamic yield stress.	40
Figure 3.2: Forces between atoms and molecules expressed by potential energy as a function of particle centre separation. Re-worked from (Cheng, 1987).	41
Figure 3.3: (a) The electrical double layer and corresponding electrical potential as a function of distance from particle surface, (b) potential energy for electrostatic stabilisation, (c) influence of surface charge or zeta-potential on total potential energy. Re-worked from (Cheng, 1987).	43
Figure 3.4: (a) Tail and loop type macromolecular layers, (b) enthalpic and entropic layer interactions, (c) potential energy for steric stabilisation. Re-worked from (Cheng, 1987).	45
Figure 3.5: Static yield stress evolution as a function of time illustrated by both the re-flocculation and structuration thixotropy mechanisms. Equation numbers presented for their respective relevant sections.....	50
Figure 3.6: SEM image of the SiO ₂ nanoparticles in a flocculated state.....	54
Figure 3.7: Rockcrete TSL rotor stator pump indicating the hopper, hose and large screw...55	
Figure 3.8: Short term re-flocculation graphs depicting static yield shear stress vs. resting time gap of: (a) variation in chemical admixtures; (b) variation in nanoparticle content.....	62
Figure 3.9: Long term structuration graphs depicting static yield shear stress vs. resting time gap of: (a) variation in chemical admixtures; (b) variation in nanoparticle content.....	65
Figure 3.10: Short term dynamic shear stress vs. resting time gap of: (a) variation in chemical admixtures; (b) variation in nanoparticle content.	67
Figure 3.11: Long term dynamic shear stress increase vs. resting time gap of: (a) variation in chemical admixtures; (b) variation in nanoparticle content.....	69
Figure 3.12: 3D printed circular hollow column with: (a) standard concrete mix; (b) 1% nS concrete mix; (c) typical instability that resulted in failure.	71
Figure 3.13: Static yield shear stress evolution of the concrete mixes used for 3D printing of the circular hollow columns.....	72
Figure 4.1: Material stress growth test depicting the static and dynamic yield shear stresses of a thixotropic material.	82

Figure 4.2: Static yield shear stress evolution as a function of resting time illustrated by both the re-flocculation and structuration thixotropy mechanisms (Kruger et al., 2019b).....83

Figure 4.3: a) Cross-section of a 3D printed rectangular filament layer at an arbitrary position along its length indicating an infinitesimal element and b) internal force equilibrium of an infinitesimal element within a filament layer.85

Figure 4.4: a) Shear failure envelope of the Mohr-Coulomb failure criterion indicating the equivalently induced shear stress and b) the Tresca failure criterion indicating the increased equivalently induced shear stress for identical normal stress conditions.88

Figure 4.5: a) Plane strain element with unit thickness of a printed filament layer indicating the relevant coordinate system in terms of principle stresses, b) cross-section of a filament layer with confinement in the bottom and corresponding principle stresses indicated to the right and c) three failure zones within a filament layer.....89

Figure 4.6: Mohr circle for the biaxial stress state that occurs in failure zone 1.90

Figure 4.7: Typical deformation of a filament layer that initiates and propagates from failure zone 2.91

Figure 4.8: Mohr circles that indicate the normal stress state for $\nu = 0$ and $\nu \rightarrow 0.5$ together with accompanying equivalently induced shear stress.92

Figure 4.9: a) Plane strain element of unit thickness that represents the cross-section of a fully constrained filament layer and b) a block that rests on a surface with friction.95

Figure 4.10: Block resting on an inclined surface illustrating the friction and gravitational forces.97

Figure 4.11: Graphical method to determine if confinement occurs for a particular 3DPC setup. Read off the inclination angle that corresponds with the material’s Poisson’s ratio. This angle must be smaller than the angle obtained for when a filament layer starts to slide downwards if the print bed surface is lifted in order for confinement to occur.97

Figure 4.12: Stress growth curve obtained from rheometer testing. Only the first 10 seconds of the total 80-second test duration is shown. 100

Figure 4.13: Custom-built concrete extruder used in this research indicating the control unit, pump motor, platform equipped with rollers, 40x40 mm square nozzle and the concrete feeder location and compressor. 103

Figure 4.14: Extruded filament layer with dimensions 40x40 mm illustrated by a) side view, b) top view and c) perspective view. 105

Figure 4.15: Front view of the filament layer as it is being extruded from the nozzle. Each picture, numbered to indicate chronological order, depicts the cross-section of the filament as it crosses a roller.	106
Figure 4.16: Mechanical properties experimental testing indicating a) Digishear 27-WF2060 direct shear test apparatus and b) FE schematisation of the direct shear box test showing (top) the plane stress representation in the FE modelling approach and (bottom) the isometric view of the shear box.	108
Figure 4.17: FEA of the standard SU 3DPC material with no interparticle friction indicating the a) plastic strains, b) elastic strains, c) vertical stress profile (σ_1) and d) horizontal (confinement) stress profile (σ_2) at the filament height whereby plastic yielding propagates.	111
Figure 4.18: FEA of the standard SU 3DPC material with interparticle friction indicating the a) plastic strains, b) elastic strains, c) vertical stress profile (σ_1) and d) horizontal (confinement) stress profile (σ_2) at the filament height whereby plastic yielding propagates.	112
Figure 5.1: Schematic diagram illustrating a synopsis of the model development process in Section 5.2.	121
Figure 5.2: Material stress growth test depicting the static and dynamic yield shear stresses of a thixotropic material.	122
Figure 5.3: Static yield shear stress evolution as a function of resting time illustrated by both the re-flocculation and structuration thixotropy mechanisms. Equation numbers presented for their respective relevant sections.	123
Figure 5.4: Building rate of an object with uniform geometry, defined as a step function. .	125
Figure 5.5: Cross-section of unit thickness in the longitudinal direction of a printed filament layer.	126
Figure 5.6: A linearised building rate to simplify model development.	127
Figure 5.7: Tresca, Mohr-Coulomb and Rankine behaviour illustrated by means of infinitesimal elements and Mohr circles. Parts of figure reproduced from (Saloustrous et al., 2015).	130
Figure 5.8: Global plane strain element of unit width with its associated principle stress directions.	131
Figure 5.9: Confinement within concrete samples of different aspect ratios together with the respective stress states indicated on infinitesimal elements.	133
Figure 5.10: Strength correction factors for different aspect ratios.	135

Figure 5.11: Shear stress vs time graph depicting different building rates against material strength, as well as the regions where Equations 5.25 and 5.26 are applicable.....	138
Figure 5.12: Material-specific fixed gradient vs building rate gradient.	139
Figure 5.13: Stress redistribution in the critical filament layer that leads to a non-linear building rate and ultimately yields a lower bound model.	141
Figure 5.14: AutoCAD Inventor drawing (left) of the object to be 3D printed including dimensions (mm), which is then exported as .stl file format to Simplify3D (right) that slices the object into multiple layers and processes the data for machine interpretation and execution.	144
Figure 5.15: Rheological protocol for obtaining the required material parameters as input for the model.....	146
Figure 5.16: Stress growth curve obtained from the initial stress growth rheometer test depicting the static and dynamic yield shear stresses.	147
Figure 5.17: Calculation of the re-flocculation (R_{thix}) rate.	148
Figure 5.18: Calculation of the structuration (A_{thix}) rate.....	148
Figure 5.19: Visual representation of the model indicating material strength, building rate of the 3D print and the predicted print failure.....	150
Figure 5.20: Final form of the circular hollow column before failure occurs.	151
Figure 5.21: Failure progression of the column clearly indicates plastic yielding of the bottom layers.	152
Figure 6.1: Bi-linear thixotropy model of the static yield shear stress evolution as a function of material resting time after extrusion (Kruger et al., 2019b).	161
Figure 6.2: Strength correction factors (FAR) for various filament layer aspect ratios (Kruger et al., 2019a).....	163
Figure 6.3: Static yield shear stress evolution curves for each concrete batch tested via the rheometer. The average of these curves are used as material input for the design model.....	170
Figure 6.4: A 630 x 230 x 500 mm rectangular structural wall element with W-type infill printed for experimental verification of the constructability design model.....	172
Figure 6.5: Design envelope depicting the entire feasible design parameter domain and corresponding vertical building rate. Filament layer heights are specified in the legend.....	174
Figure 6.6: Design envelope depicting the feasible design parameter domain and corresponding vertical building rates after implementation of the print speed and filament layer height boundary conditions. Filament layer heights are specified in the legend.	175

Figure 6.7: a) Isometric view of the printed wall element with W-type infill moments before failure and b) front view of the wall element indicating the position of various filament layers.

..... 177

Figure 6.8: Wall failure initiation and propagation indicating a) the development of surface cracks due to plastic yielding in the bottom critical layers, b) flow-onset on the right-hand side of the wall, c) global tumbling of the wall and d) the result of an unsuccessful constructability attempt of a 3DCP structural wall element. 178

Figure 6.9: Influence of the partial factors given in Table 6.7 as applied on the static yield shear stress curve of the material used for the experimental process. 182

List of Tables

Table 2.1: Summary of procurement for the 3D concrete printer.	24
Table 2.2: Concrete mix compositions for initial trial testing.....	26
Table 2.3: Reference 3D printable HPC mix constituent quantities.	28
Table 2.4: Mechanical properties of the reference 3D printable concrete mix with coefficient of variation indicated in brackets. Three specimens were tested for each mechanical property.	30
Table 3.1: Standard HPC mix constituent quantities used for this research, as well as nanoparticle content.	53
Table 3.2: Nano-silica properties as obtained from Nanostructured & Amorphous Materials (Nanostructured & Amorphous Materials, n.d.).	53
Table 3.3: Rheological testing protocol for determination of parameters required to plot static yield shear stress evolution curve.	59
Table 3.4: Initial shear stress values and the re-flocculation rate for each concrete mix.....	63
Table 3.5: Initial and final static shear stress values and the structuration rate for each concrete mix.	65
Table 3.6: Summary of the initial and constant dynamic shear stresses together with a Dr factor.	68
Table 3.7: Summary of the initial dynamic shear stress and the rate of long term dynamic stress increase.	70
Table 3.8: Summary of the main rheological parameters of the two 3D printed concrete mixes.	73
Table 4.1: Standard HPC constituent quantities used for this research.	98
Table 4.2: Rheology test protocol for the determination of the initial static and dynamic yield shear stresses.....	99
Table 4.3: Summarised material parameters as input for the model.....	101
Table 4.4: Maximum stable filament layer heights obtained from Equations 4.15, 4.16 and 4.19, which correspond with failure in zones 1, 2 and 3 respectively.	101
Table 4.5: Summarised material parameters as input for the numerical model. Young's modulus and cohesion adjusted to account for breakdown induced by the pumping process.	109
Table 5.1: Standard HPC constituent quantities used for this research.	142

Table 5.2: Summarised print parameters as input for the model.	145
Table 5.3: Summary of the data points obtained from the rheometer tests.....	147
Table 5.4: Summarised material parameters as input for the model.....	148
Table 5.5: Summary of the results obtained from the model developed in this research.	149
Table 5.6: Summary of the results from the experimental verification.	151
Table 6.1: 3DCP mix constituent quantities.....	167
Table 6.2: Rheology testing protocol followed for each of the 5 concrete batches in order to obtain the required data for the static yield shear stress evolution curves, as depicted in Figure 6.1.	169
Table 6.3: Rheology parameters associated with each of the static yield shear stress evolution curves depicted in Figure 6.3.	171
Table 6.4: Summary of the input parameters for the design model.	173
Table 6.5: Summary of the optimum design parameters obtained from the model that are used for the construction of the wall element.	175
Table 6.6: Results obtained from the FORM analysis for both normal and lognormal distributions assigned to the material parameters of the limit state function.....	180
Table 6.7: Partial factor values for material parameters in the statistical design model.....	181

List of Abbreviations and Acronyms

3D	Three-dimensional
3DCP	Three-dimensional concrete printer/printing
3DP	Three-dimensional print(ed)
3DPC	Three-dimensional printing of concrete
AC	Alternating current
ACI	American Concrete Institute
AI	Artificial intelligence
AM	Additive manufacturing
APS	Average particle size
ASTM	American Society for Testing and Materials
CAD	Computer-aided design
CoV	Coefficient of variation
CPE6M	Six-node triangular elements
CPE8	Eight-node biquadratic plane strain quadrilateral elements
CSR	Constant shear rate
DST	Direct shear test
EN	European Norms
FDM	Fused deposition modelling
FE	Finite element
FEA	Finite element analysis
FORM	First-order reliability method
GDP	Gross domestic product
HPC	High-performance concrete
I/O	Input/output

IBS	Interlayer bond strength
IoT	Internet of things
ITZ	Interfacial transition zone
LL	Lubrication layer
MCU	Microcontroller unit
$M_{x,y,z}$	Moment about x, y, or z axis
NC	Numerical control
NEMA	National Electrical Manufacturers Association
nS	Nano-silica
NSF	Naphthalene Sulfonate Formaldehyde
PCE	Polycarboxylate ether
PhD	Philosophiae doctor
PP	Polypropylene
PSU	Power supply unit
RC	Reinforced concrete
RDP	Reconstruction and Development Program
Ref.	Reference
RUMBA	RepRap Universal Mega Board with Allegro driver
SANS	South African national Standards
SCC	Self-compacting concrete
SD	Secure digital
SEM	Scanning electron microscopy
SLA	Stereolithography apparatus
SP	Superplasticizer
SSA	Specific surface area
Std. Dev	Standard deviation

STL	Standard Tessellation Language
SU	Stellenbosch University
TCI	The Concrete Institute
TU/e	Technische Universiteit Eindhoven
UCS	Unconfined compressive strength
US	United States
USB	Universal Serial bus
UUCT	Unconfined uniaxial compression test
VFD	Variable frequency drive
VMA	Viscosity modifying agent
w/c	Water to cement

List of Symbols

Roman

A_{thix}	Structuration rate
c	Cohesion
D_r	Dynamic shear reduction factor
E	Young's modulus
$F_{\text{AR,expl}}$	Explicit analytical expression of the strength correction factors
F_{AR}	Strength correction factors that account for filament aspect ratios
F_R	Resisting force against plastic yielding
F_{SW}	Self-weight force
g	Gravitational acceleration
G'	Storage modulus
G''	Loss modulus
$G(X)$	Limit state function
h_l	Filament layer height
h_l^*	Chosen filament layer height
$h_{l,\text{max}}$	Maximum specified filament layer height
$h_{l,\text{min}}$	Minimum specified filament layer height
H_{design}^*	Chosen design height of an object
H_{max}	Maximum stable filament layer height
$H_{\text{predicted}}$	Predicted vertical building height of an object
$\dot{H}_{\text{predicted}}$	Predicted vertical building rate
k	Boltzmann constant
K_y	Coefficient of lateral stress
l_p	Constant print path length

m	Particle mass
$m_{\text{Mat.}}$	Material-specific fixed gradient
N_L	Total number of filament layers
$\frac{\text{rev}}{\text{s}}$	Rheometer vane rotational speed
r_i	Radius of rheometer vane
r_o	Radius of rheometer container
R_{thix}	Re-flocculation rate
R^2	Coefficient of determination
t	Time after extrusion/cessation of agitation
t_{print}	Total print duration
t_{rf}	Time period over which re-flocculation occurs
T	Absolute temperature
u_k	Characteristic fractile of the standardised random variable
u_p	P-fractile of the standardised random variable
v	Print speed and/or particle velocity
v^*	Chosen constant print speed
v_{max}	Maximum specified print speed
v_{min}	Minimum specified print speed
V	Potential energy
V_{max}	Potential maximum
V_{min}	Potential minimum
w_1	Filament layer width
$w_{1,c}^*$	Chosen constant filament layer width
w_x	Coefficient of variation of X
y	Distance from bottom of filament layer to position of infinitesimal element

Greek

α	Sensitivity factor
β	Shear failure plane and/or reliability index
γ	Shear strain
$\dot{\gamma}$	Shear rate
$\gamma_{M,1}$	Material partial factor applicable to $\tau_{S,i}$
$\gamma_{M,2}$	Material partial factor applicable to A_{thix}
ε_1	Vertical strain
ε_2	Horizontal strain
ε_3	Longitudinal strain
ζ	Zeta-potential
θ	Inclination angle
μ_s	Static friction coefficient
ν	Poisson's ratio
ρ	Density
σ	Normal stress
σ_1	Vertical normal stress
σ_2	Horizontal normal stress
σ_3	Longitudinal normal stress
σ_{max}	Maximum normal stress
σ_{min}	Minimum normal stress
σ_{SW}	Self-weight induced normal stress
τ	Shear stress
$\tau_{D,i}$	Initial dynamic yield shear stress
τ_{equiv}	Equivalently induced shear stress due to normal stress loading
$\tau_{S,i}$	Initial static yield shear stress

$\tau_s(t)$	Static or apparent yield shear stress at time t after extrusion
φ	Interparticle friction
\emptyset	Diameter
ψ_0	Surface charge/potential

Chapter 1

Introduction

Before the advent of the First Industrial Revolution, which occurred in Britain during the 18th century, manufacturing of goods were mainly performed in homes using hand tools and basic machinery. The iron and textile industries, together with the development of the steam engine, are the most notable advancements that led to the urbanisation and industrialisation of rural societies. Subsequently, an increased volume and variety of manufactured goods were available and most people experienced an improved standard of living.

The Second Industrial Revolution, commonly referred to as the Technological Revolution, largely occurred in America during the 19th century and continued until the start of the First World War. Pre-existing technologies such as iron manufacturing were mostly replaced with steel manufacturing, which is cheaper, stronger and ultimately led to the construction of ships, skyscrapers and larger bridges. Several new industries were discovered of which the most notable include electrical, oil and automobile. It is universally acknowledged that this revolution enabled the onset of globalisation.

The Third Industrial Revolution, also referred to as the Digital Revolution, commenced between 1950 and the late 1970's and marked the transition from analog to digital electronics. Monumental innovations include the digital cellular telephone, computers, industrial robots and the internet. This revolution, which is still advancing at present, enabled the onset of the Information Age that depicts the transition from the traditional industrial production era to one comprising of information and computerisation.

The Fourth Industrial Revolution, also known as Industry 4.0, is rapidly emerging and builds on the Digital Revolution, which is reaching a mature state around the world (Davis, 2016). Industry 4.0 is described as an era where innovative technology comprises of a blend between the physical, digital and biological spheres (Schwab, 2016). Compared to previous industrial revolutions, the fourth is developing at an exponential rather than linear rate, which is expected to disrupt most industries around the world. New Industry 4.0 inventions include artificial intelligence (AI), the Internet of Things (IoT), autonomous vehicles, quantum computing, three-dimensional (3D) printing, nanotechnology and many others. Most of the aforementioned technologies are in the advanced development stage that could drastically change the world as we know it today, ultimately resulting in a highly automated society.

Chapter 1: Introduction

Industrialisation has generally increased the standard of living for most people and Industry 4.0 is anticipated to contribute significantly in that regard.

Although most sectors experienced an increase in productivity over the past century due to multiple industrial revolutions, the construction industry's productivity has remained relatively unchanged at best. According to research by Daneshgari & Moore (2013), the construction industry annually accounts for 4 to 7 % of America's Gross Domestic Product (GDP) and employs 5 to 9 million workers, roughly 3 to 6 % of the total American workforce. While America's manufacturing industry has improved its productivity by 400 % over the last century, the construction industry has regressed at an average of -0.6 % per year, as illustrated in Figure 1.1.

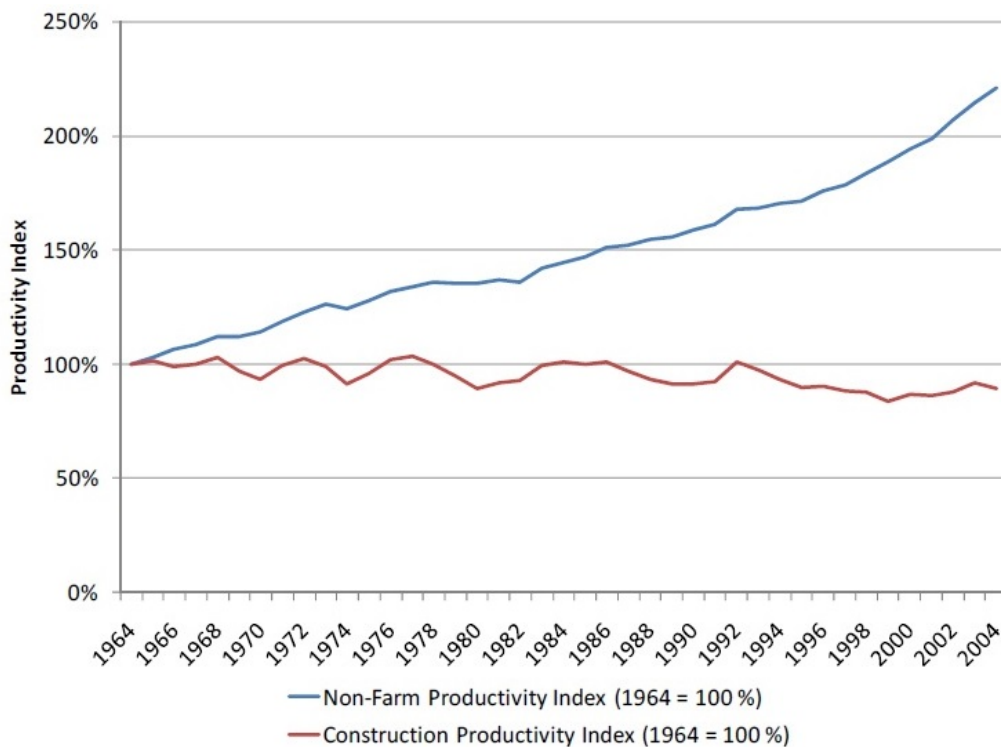


Figure 1.1: Comparison between US construction labour productivity and non-farm labour productivity (Huang, Chapman & Butry, 2009).

Daneshgari & Moore (2013) further indicate that the cost of an automobile in America has decreased from 140 % in 1910 to 33 % in 2012, based on the average national per capita income. In contrast, the cost of an average house has increased from 333 to 619 % of per capita income during the same time period. Evidently, the construction industry of the world's largest economy has not yet experienced the benefits of industrialisation such as increased productivity and reduced costs. However, new automation innovations from Industry 4.0, such as 3D

printing, has the potential to completely redress the construction industry for both developed and developing countries, including South Africa.

The first stereolithography apparatus (SLA), commonly known as a 3D printer, was invented in 1987 by Charles Hull as a means of rapid prototyping (Flynt, 2017). This technology, also referred to as additive manufacturing (AM), essentially is the automation process whereby a three-dimensional solid object is created from a digital file by laying down successive material layers. 3D printing is currently successfully applied in various industries, including the automobile, aviation, biomedical, dental, food, fashion and manufacturing industries. However, this technology can also be applied in the construction industry by upscaling the 3D printer machine to industrial-grade caliber and developing special concrete mixes for the material.

Reinforced concrete (RC) construction is typically divided into three components: concrete, reinforcement and formwork. According to Jha (2012), temporary structures such as formwork comprise 40 to 50 % of total construction costs and constitute towards about 60 to 70 % of total construction time for RC construction. 3D printing, as well as alternative approaches in concrete printing such as Contour Crafting, have the potential to vastly reduce the need for formwork in the construction industry, essentially saving time and money. WinSun, a Chinese-based 3D printing of concrete (3DPC) company, claims their process can decrease construction times by between 50 and 70 % (CNET, 2015). Furthermore, they claim to reduce construction waste by between 30 and 60 %. As a result, less cement would be required for RC construction, which is a major contributor of carbon dioxide (CO₂) emissions. Research by Rubenstein (2012) established that cement production is increasing by 2.5 % annually, and is predicted to rise from 2.55 billion tons in 2006 to 3.7 - 4.4 billion tons by 2050. The cement industry currently accounts for 5 % of the global CO₂ emissions.

3D printing technology is currently at an advanced developmental stage; however, 3D printing of concrete is still in the early stages of implementation and presents many challenges. The biggest concern currently surrounding 3DPC is the lack of steel reinforcement. Obtaining appropriate material behaviour for 3DPC, shape retention capability of extruded filament and buildability performance are the fundamental challenges facing the 3DPC technology. These challenges are mainly the consequences of insufficient concrete rheology, in particular thixotropic behaviour, which is required for superior 3D printing. Despite these challenges, 3DPC possesses remarkable potential to industrialise the construction industry.

1.1 Problem statement

The workability of conventionally cast concrete is typically characterised via the slump test, whilst the hardened concrete strength is determined via the cube or cylinder compressive stress test. These tests are generally sufficient to qualify concrete as appropriate according to the design guidelines specified by the engineer for a specific project. Complex rheological parameters are not required for conventional concrete since formwork constrains concrete to the specified shape; the main challenge is thus for the concrete to enclose dense steel reinforcement and to form a homogeneous section.

However, 3D concrete printing's fundamental advantage of formwork-free construction presents multiple challenges, of which the most cardinal for successful 3DPC is constructability. Constructability refers to the holistic 3DPC construction process in the fresh concrete state, including pumping and extrusion, filament shape retention and buildability (refer to Section 1.4.3 for terminology). Increased emphasis on concrete rheology is thus necessary to characterise the appropriateness of concrete for 3DPC compared to conventional concrete construction. Additionally, the bearing capacity of concrete in its fresh state becomes pivotal in order to maximise vertical building rates. A novel method for characterising concrete material behaviour and strength in the fresh state is desired for 3DPC to enable for accurate constructability quantification. The limited literature that is currently available make use of mechanical tests developed for hardened concrete to characterise 3DPC materials, however, these tests provide little insight into material behaviour in the fresh state. Furthermore, these tests are not always practicable for 3DPC materials that typically have good workability.

In addition to the aforementioned, limited literature exists for quantifying 3DPC constructability via models that predict filament shape retention and buildability. Typically, elements are printed at randomly chosen speeds and nozzle sizes, with the hope of a successful 3DPC outcome. This entails no structural failure in the fresh concrete state due to buckling or material yielding together with adequate surface aesthetics. Current buildability models make use of a material's mechanical properties in the fresh state as input, which as described earlier are not tailored specifically for 3DPC purposes, and prove difficult to implement due to its complexity e.g. finite element numerical models. An exigency is present for a simple and practicable design model that is able to accurately quantify the constructability process for 3DPC. The model should ideally be based on a material characterisation test that is specifically developed for 3DPC application.

1.2 Aim and objectives of study

The main aim of this research is to **develop practicable analytical models based on rheological material properties that collectively contribute towards constructability design for 3DPC**. Five objectives are identified and listed below in methodological order to achieve the aim of this research:

- 1) Design, procure and manufacture a lab-scale 3D concrete printer of roughly 1 m³ build volume. Thereafter, develop a highly thixotropic concrete material suitable for 3D printing. This objective forms the cornerstone of this research as it enables for the practical validation of the models developed in the following objectives.
- 2) Develop a rheological material model that specifically pertains to 3DPC material characterisation. Additionally, emphasis should be placed on classifying the degree of thixotropy of a material as the author postulates that thixotropic materials are superior for 3DPC.
- 3) Develop an analytical filament shape retention model for 3DPC, using the material model developed in (2) as basis. The model should aim to predict the filament layer height at which plastic yielding under self-weight occurs immediately after extrusion. Not only does this ensure for sufficient buildability, but it also assures adequate surface aesthetics of 3D printed elements.
- 4) Develop an analytical buildability model for 3DPC, using the material model developed in (2) as basis. In essence, the model should predict the maximum number of filament layers (or height) achievable at which structural failure occurs. Furthermore, the model should be practicable and easy to apply for industry adoption.
- 5) Develop an analytical model or method that facilitates the constructability design process for 3DPC elements by combining objectives (2), (3) and (4). Ideally, the model should provide the user with the required filament layer cross-sectional dimensions and print speed to ensure for the successful construction of the specified element. Additionally, the model should allow for optimisation. Successful completion of this objective by means of experimental validation verifies that the main aim of this research is achieved.

1.3 Significance, motivation and applicability

A general household survey conducted in 2017 by Statistics South Africa (2018) indicates that 13.6 % of South Africans, or roughly 8 million individuals, live in informal settlements, as illustrated in Figure 1.2. This is a worrisome statistic, especially as the world is progressing into Industry 4.0 while yet millions of people still do not possess the basic need of a safe house. However, the current South African government introduced the Reconstruction and Development Program (RDP) in order to, amongst others, provide housing for the poor. Since 1994, the government has provided more than 4.3 million so-called RDP or state-funded houses, however currently a 2.3 million backlog exists that is growing by 178 000 units per year (Msindo, 2016). Further statistics indicate that 18 % of households living in state-funded houses are unhappy about the condition of their structure (Statistics South Africa, 2016). Evidently, the demand far exceeds the supply.

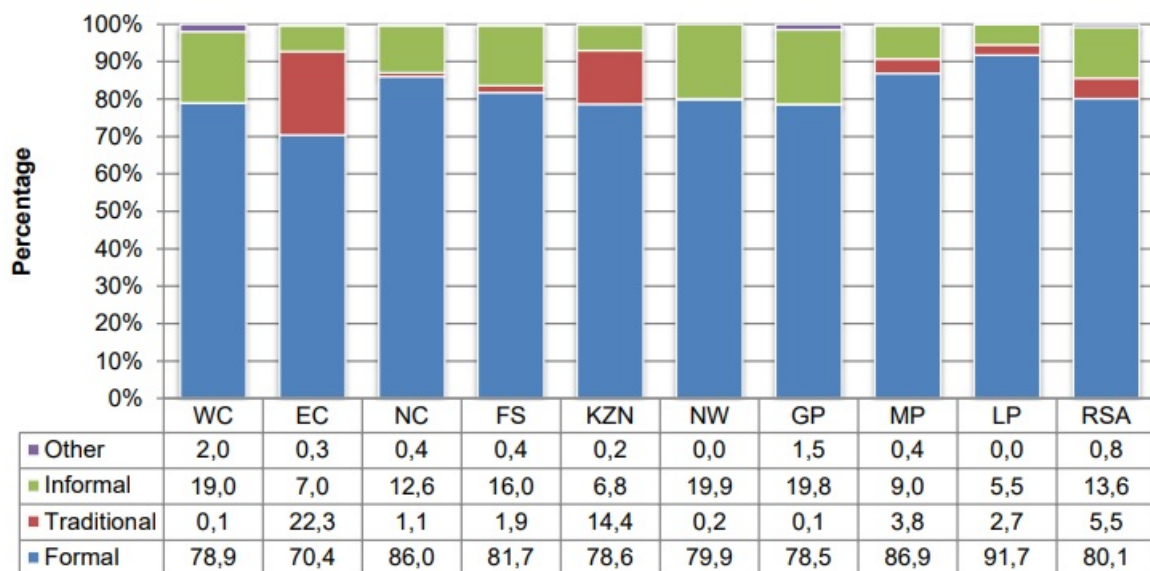


Figure 1.2: Percentage of South African households that live in formal, informal and traditional dwellings by province in 2017 (Statistics South Africa, 2018).

This unfortunate reality is the perfect example to emphasise the potential value that 3DPC can bring to South Africa, namely comparatively inexpensive construction of RDP houses in less time than traditional construction methods whilst maintaining high quality standards. Additionally, less waste is generated via this process and therefore less cement required, ultimately reducing the construction industry's carbon footprint. A further socio-economic benefit is the upskilling of construction workers, yielding better career prospects and redressing the current status quo regarding the construction industry. The simplistic design of a typical RDP house is the perfect large-scale application for the current capabilities of 3DPC. However,

no simple design guides are currently available in terms of printing parameters to be used based on a material's characteristics in order to realise the entire structure without failure during the printing process; hence the motivation for this research.

1.4 3D concrete printing literature and terminology

1.4.1 Classification of 3D concrete printers

There are currently four main categories of 3D concrete printers namely gantry, robotic, crane and mobile systems, as illustrated in Figure 1.3. All four types are successfully implemented at universities and in the construction industry. Gantry systems vary in size, from small-scale laboratory systems at universities to large (40 x 10 x 6 m) industrial-grade scale systems. The disadvantage of such a system is its fixed dimensions, i.e. the build volume is always smaller than the printer's outer dimensions, restricting the concrete printing to a certain volume. An example of a gantry system is the Technical University of Eindhoven's (TU/e) 4-axis 3D concrete printer (9 x 4.5 x 3 m), illustrated in Figure 1.3a (TU/e, n.d.). The fourth axis consists of a revolving nozzle, which is especially convenient for non-circular shaped nozzles. Gantry systems are generally the most affordable, due to their relatively simple mechanics and electronic automation systems compared to the other available 3D concrete printing systems.

CyBe Construction, a 3D concrete printing company based in the Netherlands, developed both a 6-axis robotic and mobile 3D concrete printer as illustrated in Figure 1.3b and 1.3c respectively (CyBe, 2019). The advantage of such 6-axis systems is their increased degrees of freedom, i.e. their ability to print complex geometries with high precision. Mobile systems generally consist of a robotic 3D printer mounted on caterpillar tracks that have the added advantage of having larger, and under certain circumstances unrestricted, build volumes.

Figure 1.3d depicts a crane 3DPC system developed by Apis-Cor. This enables the construction process to occur from within the building that is being 3D printed. The printer can e.g. be disassembled after the successful completion of the first story and then re-assembled on the next story to continue the construction process for multi-story buildings. Alternatively, the printer can be moved horizontally to increase its printing range in the Cartesian plane (Apis-Cor, 2017).

The ideal 3D concrete printing system is primarily selected based on the desired construction scale, geometrical complexity of the envisaged 3D printed objects and cost. Secondly, factors such as the maximum print speed and the practicable variation in nozzle

Chapter 1: Introduction

sizes and shapes must be considered. Lastly, ease of customisability of the printing system is critical for advanced 3DPC applications.

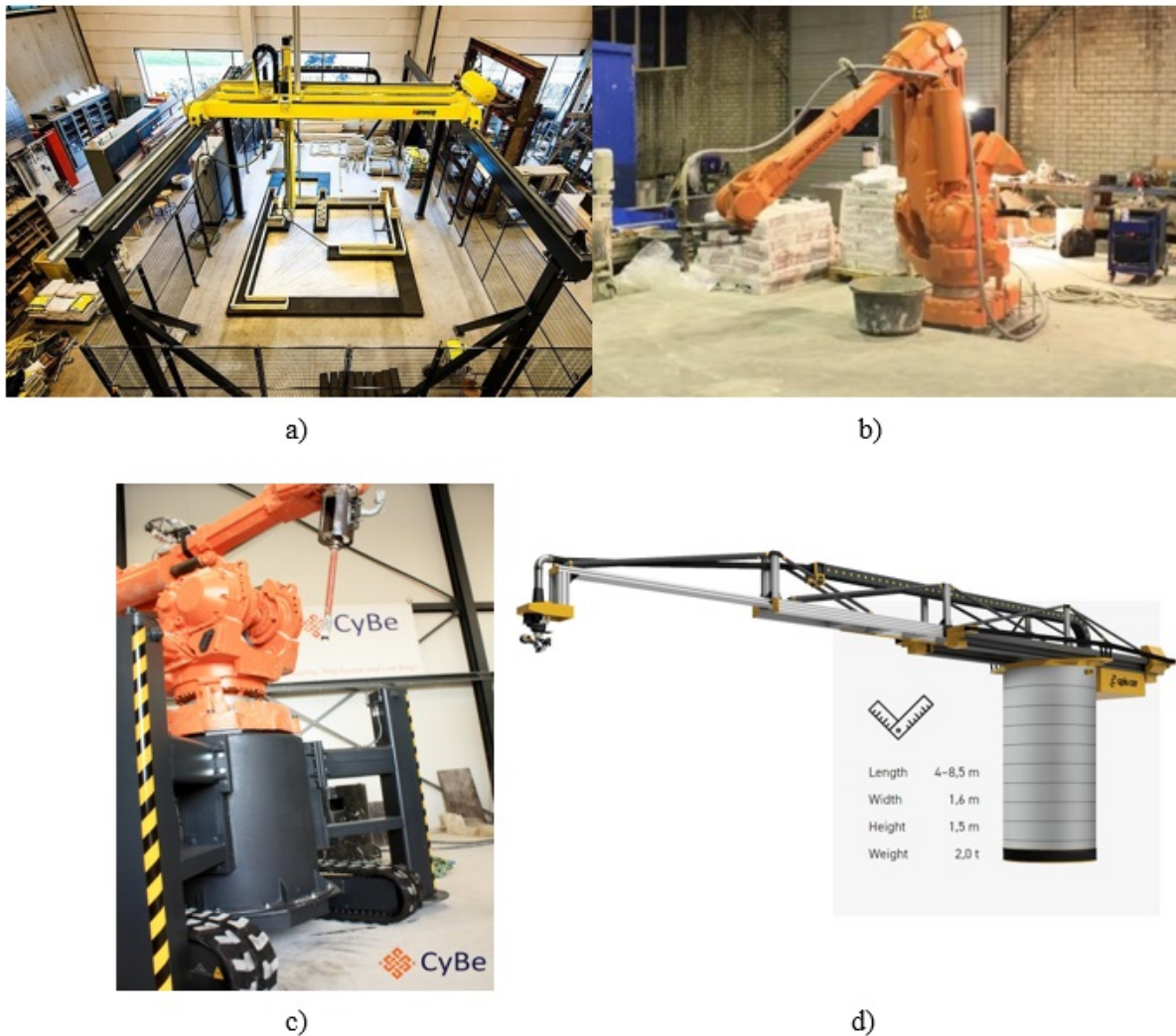


Figure 1.3: Four main 3DPC systems (a) gantry system by TU/e (TU/e, n.d.), (b) robotic system by CyBe Construction (Grunewald, 2015), (c) mobile system by CyBe Construction (Saunders, 2016) and (d) crane system by Apis-Cor (Apis-Cor, 2017c).

1.4.2 3DPC execution process

The fundamental concepts behind 3D concrete printing involves automation and extrusion. The user initially needs an idea of an object to 3D print. This idea must then be transformed into a digital file. Typically, Computer-Aided Design (CAD) software is utilised to realise the idea into a three-dimensional model. Autodesk Inventor, as well as free CAD software such as FreeCAD, Tinkercad and SketchUp can be utilized for this purpose. The 3D digital model must be saved in Standard Tessellation Language (.STL) format as a prerequisite for the next step.

After creating the STL digital file, it must be divided into multiple two-dimensional layers, a process commonly referred to as slicing. This process creates a G-code file that instructs the printer in precise detail how to reproduce the 3D model. G-code, also referred to as G programmable language, is the most widely used numerical control (NC) programming language. Commonly used slicing software include Cura, Slic3r and Simplify3D. The G-code file, typically containing precise Cartesian co-ordinates, extrusion rates, automation speed and specific printer settings, is then sent to the 3D printer's microcontroller via a Universal Serial Bus (USB) connection or a Secure Digital (SD) card.

The user should ensure that the concrete is placed inside the hopper before initiating the print. Thereafter, it is of crucial importance to bleed the pump's hose. Pronterface, a host software with a graphical interface, can be utilised to control the printer by sending a G-code command to it. Thus, it can be employed to extrude material to bleed the system, ensuring no air remains trapped within the hose before commencement of the 3D print.

Once completed, the print can be initiated. The machine's microcontroller unit (MCU) contains firmware, e.g. Marlin, which interprets the G-code file to automate the entire printing process. The 3DPC execution process is summarised in Figure 1.4.

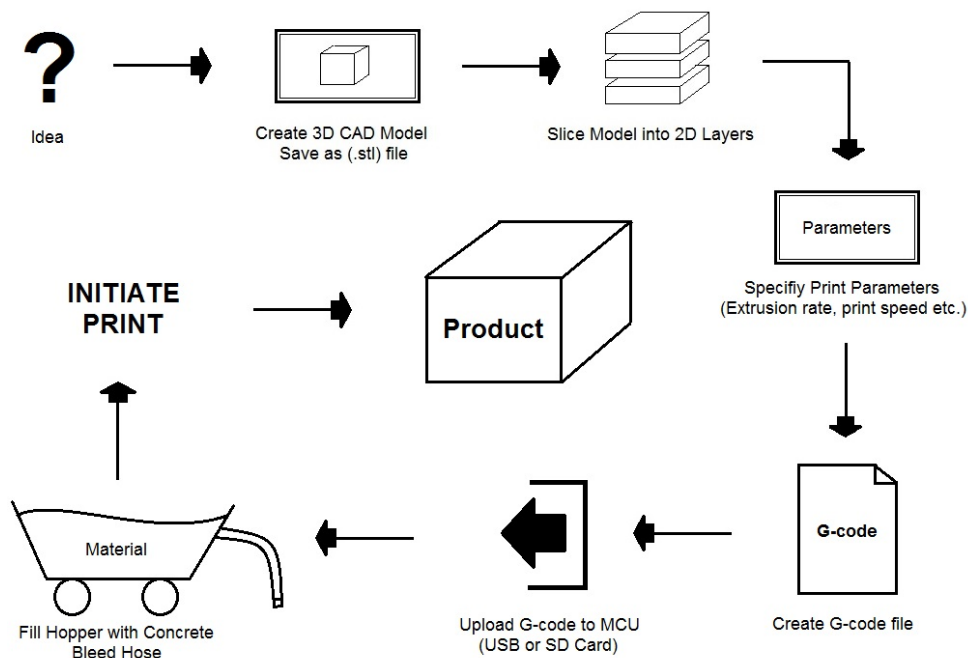


Figure 1.4: Schematic drawing of the 3DPC execution process.

It is important to select the correct speed for both the concrete extrusion as well as the printing (nozzle) speed, in order to obtain the desired filament shape and cross-sectional

dimensions. Selecting the correct speed will enable fast, efficient and accurate construction of elements. The speed is however dependent on several factors such as the material's open time and rheology, printing object size and complexity, and pump capacity. Although there is no correct setting, research conducted by Paul et al. (2017) suggests using an upper limit of 200 mm/s due to issues regarding the quality of the surface textures. Segregation of the concrete constituents due to excessive pressure within the hose may also occur at higher speeds. However, high pressures within the hose may also lead to better compaction of the concrete, which in turn could result in increased material strength. It is therefore crucial to determine the optimum extrusion and print speed combination for each 3DPC material that still yields the desired filament layer size and shape without any form of segregation present.

1.4.3 3DPC terminology

This section provides the terminology relevant to 3DPC, which is necessary to comprehend the research presented in the following chapters. All terminology presented in this section is sourced from Paul et al. (2017), unless otherwise referenced.

Open time

The open time of a 3DPC material is synonymous to the setting time of concrete, which indicates the time required for concrete to change from the plastic state to a solid state. The open time, however, only describes the transition from the dormant stage to the setting stage, i.e. the time required for initial set to occur. This correlates with the time difference between completion of the concrete mixing and the latest time that the concrete can be 3D printed.

Several factors influence the rate of hydration for concrete of which the composition of the mix and environmental factors such as temperature, wind and humidity present the biggest repercussions. It is important to determine the open time of a material before 3D printing with it. Pumpability and extrudability of concrete decreases with time, which could induce significant strain on the pump due to excessive pressures. In a worst-case scenario, the concrete in a pump's hopper achieves initial set while an element is still in the process of being printed, which leads to the inevitable termination of the print.

Green strength

The green strength of concrete is another important concept especially applicable to 3DPC, which is an indication of bearing strength in the plastic concrete state. Due to the additive manufacturing process of 3DPC, whereby concrete is deposited layer by layer, bottom layers typically experience large compressive stresses imparted by the mass of subsequent layers.

3D printable concrete should ideally possess adequate green strength to prevent the development of unaesthetic surface fractures or ultimately structural collapse.

Pumpability, extrudability and shape retention

The pumpability of concrete is generally defined as its capacity to be mobilized and remain stable under pressure, while maintaining its original material properties (Jolin et al., 2009). This is especially applicable to 3DPC as low to no slump concrete is used to obtain sufficient filament shape retention after extrusion. The concrete must be pumped from the hopper to the 3D printer's nozzle via a hose, without any form of segregation occurring, at a pressure that does not impose significant strain on the pump's motor.

Once the pumped concrete exits via the nozzle, it should ideally retain its original intended shape under self-weight in order to achieve a high quality 3D printed element, referred to as filament shape retention. Segregation may occur at the nozzle as nozzle diameters are typically smaller than the hose cross-section, which results in increased pressure. This segregation, which may also include fibre balls, severely affects a material's extrudability.

Although the pumpability and extrudability of a material are related to one another, it is possible to obtain a material that demonstrates excellent pumpability but poor extrudability (e.g. high-volume fibre reinforced concrete), and vice versa. Such materials are not suitable for 3DPC and should be avoided. A material with a good balance between pumpability and extrudability, whilst also possessing sufficient shape retention capabilities, is favoured for 3DPC. Thixotropic materials typically demonstrate these desired material characteristics.

Buildability

Buildability in 3DPC terms refers to a material's ability to resist the weight of successively deposited filament layers during the 3DPC process. This is essential since 3DPC is a formwork-free additive manufacturing process. Typical buildability failure modes include geometrical and physical nonlinearities i.e. thin-walled elastic buckling and plastic material yielding respectively. The buildability performance of a material is typically determined by printing a certain object and counting the total number of filament layers that resulted in structural failure. Thixotropic materials generally demonstrate superior buildability due to their excellent flocculation characteristics. The precision of the 3D printer, especially its ability to follow the exact same printing path for each layer, also affects the buildability of a material.

Buildability can however be improved by increasing the number of filament layers, i.e. to extrude thinner layers. Research conducted by Le et al. (2012) found that the buildability of

their concrete material increased significantly by increasing the number of filaments from one to six. Supportive layers, such as infill connecting two parallel spaced thin-walled layers, as well as the print object's geometry have a significant influence on buildability.

Deposition height, defined as the distance between the previous layer's height and the point of exit on the nozzle, also has a notable influence on the buildability of a material. If this distance is too large, material will not form a good interlayer bond and lead to poor buildability. In contrast, if this distance is too small, the concrete is squeezed out of the nozzle resulting in poor buildability and surface aesthetics. Typically, this distance is a fixed parameter specified by the user. However, settlement of the material and subtle displacements occur as the number of filament layers increases, which increases the distance between the top layer and the nozzle. Therefore, as the number of printed layers increases the buildability decreases due to this offset distance. Wolfs et al. (2017) recently developed a real-time distance feedback system that yielded a notable improvement in buildability, as illustrated in Figure 1.5.

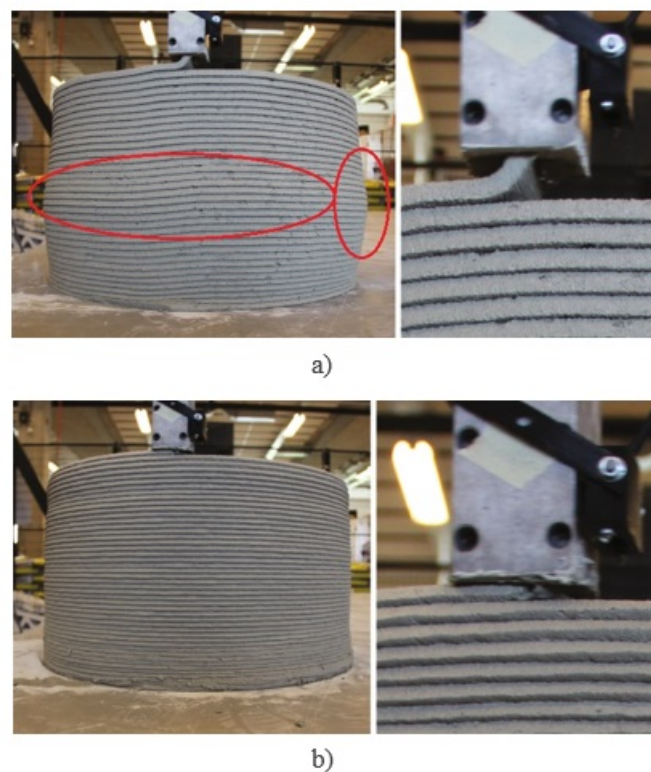


Figure 1.5: Increase in buildability (a) before and (b) after the installation of a real-time feedback system (Wolfs et al., 2017).

1.5 Dissertation structure

This dissertation comprises of written chapters as well as published and/or unpublished journal articles to follow the PhD by publication structure of Stellenbosch University.

Chapter 1 provides the reader with a broad introduction to this research. The research problem statement is explained and followed by the main aim and objectives of the study. A short motivation for the significance of the study is presented. The necessary literature to comprehend the content of the following chapters is provided for the reader's benefit.

Chapter 2 addresses objective (1) by depicting the design, procurement and manufacturing processes of the 3D concrete printer. Details regarding the concrete material design process are provided and the evolution in 3D printing quality depicted by means of figures.

Chapter 3 addresses objective (2) by developing a bi-linear thixotropy model that specifically pertain towards 3DPC. The static yield shear stress curve depicts the material shear strength evolution after extrusion and accounts for shear history i.e. breakdown of interparticle forces by pumping pressures. The model is verified via experimental verification and its significance illustrated by addition of nanoparticles for comparative purposes.

Chapter 4 addresses objective (3) by developing an analytical quasi-static shape retention model. The model's theoretical framework is presented and verified via experimental testing. Additionally, a finite element (FE) model serves as numerical validation of the analytical model.

Chapter 5 addresses objective (4) by developing a lower bound analytical model for buildability performance quantification. The model's theoretical framework is presented and experimentally verified via 3D printing a circular hollow column until structural failure occurs.

Chapter 6 addresses objective (5) by presenting a design method for quantifying constructability of 3DPC elements. The necessary theoretical framework is provided and the method practically applied. A 3DPC structural wall element is 3D printed with the print parameters provided by the design method, which allows for the fastest, yet successful, construction of the element based on the limitations of the printer and concrete rheology.

Chapter 7 presents conclusions and recommendations for future research in 3DPC.

Author contribution declarations for each journal article, as well as legal approval by the publisher for re-use of publications, can be found in the Addendum.

1.6 References

- Apis-Cor. 2017. *Apis-Cor 3D Printer Features*. [Online], Available: apis-cor.com/en/3d-printer [2018, February 15].
- CNET. 2015. *World's first 3D-printed apartment building constructed in China*. [Online], Available: www.cnet.com/news/worlds-first-3d-printed-apartment-building-constructed-in-china/ [2018, December 02].
- CyBe. 2019. *3D Concrete Printers*. [Online], Available: www.cybe.eu/3d-concrete-printers/ [2019, May 17].
- Daneshgari, P. & Moore, H. 2013. *Industrialization of the Construction Industry*. [Online], Available: <http://www.ieci.org/newsroom-and-insights/industrialization-of-the-construction-industry> [2018, February 12].
- Davis, N. 2016. *What is the fourth industrial revolution?* [Online], Available: www.weforum.org/agenda/2016/01/what-is-the-fourth-industrial-revolution/ [2018, February 12].
- Flynt, J. 2017. *A detailed history of 3D printing*. [Online], Available: 3dinsider.com/3d-printing-history/ [2018, February 12].
- Grunewald, S. 2015. *CyBe Construction Releasing 3D Printable Mortar in 2016, Eyes On-Site 3D Concrete Printing Next*. [Online], Available: 3dprint.com/111081/cybe-3d-printable-mortar/ [2018, February 15].
- Huang, A.L., Chapman, R.E. & Butry, D.T. 2009. *Metrics and tools for measuring construction productivity: Technical and empirical considerations*. [Online], Available: www.nist.gov/publications/metrics-and-tools-measuring-construction-productivity-technical-and-empirical.
- Jha, K.N. 2012. *Formwork for Concrete Structures*. New Delhi, India: McGraw-Hill Education. ISBN: 9781259007330
- Jolin, M., Burns, D., Bissonnette, B., Gagnon, F. & Bolduc, L.-S. 2009. Understanding the Pumpability of Concrete. In *Proceedings of the Engineering Conferences International: Shotcrete for Underground Support XI*. [Online], Available: <https://dc.engconfintl.org/shotcrete/17/>.
- Le, T.T., Austin, S.A., Lim, S., Buswell, R.A., Gibb, A.G.F. & Thorpe, T. 2012. Mix design
-

and fresh properties for high-performance printing concrete. *Materials and Structures*. 45(8):1221–1232.

Msindo, E. 2016. *Housing backlog: Protests and the demand for housing in South Africa*. [Online], Available: <https://psam.org.za/wp-content/uploads/2016/11/Housing-backlog.pdf>.

Paul, S.C., van Zijl, G.P.A.G., Tan, M.J. & Gibson, I. 2017. A Review of 3D Concrete Printing Systems and Materials Properties: Current Status and Future Research Prospects. *Rapid Prototyping Journal*. 24(4):784–798.

Rubenstein, M. 2012. *Emissions from the Cement Industry*. [Online], Available: <http://blogs.ei.columbia.edu/2012/05/09/emissions-from-the-cement-industry/> [2018, February 12].

Saunders, S. 2016. *CyBe Construction Unveils New Mobile 3D Concrete Printer, the CyBe RC 3Dp*. [Online], Available: 3dprint.com/158972/cybe-mobile-3d-concrete-printer/ [2018, February 15].

Schwab, K. 2016. *The Fourth Industrial Revolution: what it means, how to respond*. [Online], Available: www.weforum.org/agenda/2016/01/the-fourth-industrial-revolution-what-it-means-and-how-to-respond/ [2018, February 12].

Statistics South Africa. 2016. *Housing from a human settlement perspective: In-depth analysis of the General Household Survey data 2002-2014*. Pretoria, South Africa. [Online], Available: www.statssa.gov.za/publications/Report-03-18-06/Report-03-18-062014.pdf.

Statistics South Africa. 2018. *General Household Survey 2017*. Pretoria, South Africa. [Online], Available: <http://www.statssa.gov.za/publications/P0318/P03182017.pdf>.

TU/e. n.d. *About 3D Concrete Printing*. [Online], Available: www.tue.nl/en/education/tue-graduate-school/graduate-programs/graduate-program-built-environment/phd-program-built-environment/research-groups/structural-design/research/research-areas/concrete-research-areas/3d-concrete-printing/about-3d-concrete-printin [2018a, February 15].

TU/e. n.d. *Photo Gallery*. [Online], Available: www.tue.nl/en/education/tue-graduate-school/graduate-programs/graduate-program-built-environment/phd-program-built-environment/research-groups/structural-design/research/research-areas/concrete-research-areas/3d-concrete-printing/photo-gallery/ [2018b, February 15].

Chapter 1: Introduction

Wolfs, R.J.M., Bos, F.P., van Strien, E.C.F. & Salet, T.A.M. 2017. A real-time height measurement and feedback system for 3D concrete printing. In *Proceedings of the 2017 fib Symposium. High Tech Concrete: Where Technology and Engineering Meet*. 2474–2483.

Chapter 2

Development of a 3D concrete printer

This chapter provides a brief overview of the design procedure that was followed in order to manufacture a 3D concrete printer, which is divided into three categories: mechanical, electrical and pump-and-nozzle system. Detail regarding the cementitious material mix design process that is suitable for 3D printing is presented. The chapter concludes with various 3D concrete prints that were performed at Stellenbosch University.

2.1 3D concrete printer design

2.1.1 Mechanical

As per Objective 1 outlined in Chapter 1, a gantry type 3D concrete printer with roughly 1 cubic meter build volume must be designed and constructed. The printer should be robust and resilient, i.e. industrial-grade to illustrate its capacity to be implemented in practice and not just for academic use. Components and systems available in South Africa should be used as far as possible to demonstrate that such a machine can be manufactured locally.

A computer-aided drafting program, namely Autodesk Inventor Professional (Autodesk, 2019) was used to develop a 3D model of the printer. This enabled the accurate design of mechanical components and systems to ensure each part is correctly aligned. It also allows the user to adjust the design with minimal effort while visually observing these changes in three dimensions. Most importantly, the x, y and z-axis motion systems were simulated to prevent any collisions from occurring, e.g. a stepper motor crashing into a frame member. Two-dimensional manufacturing drawings were effortlessly derived from the 3D model after completion of the mechanical design. A rendered image of the three-dimensional Inventor model is illustrated in Figure 2.1.

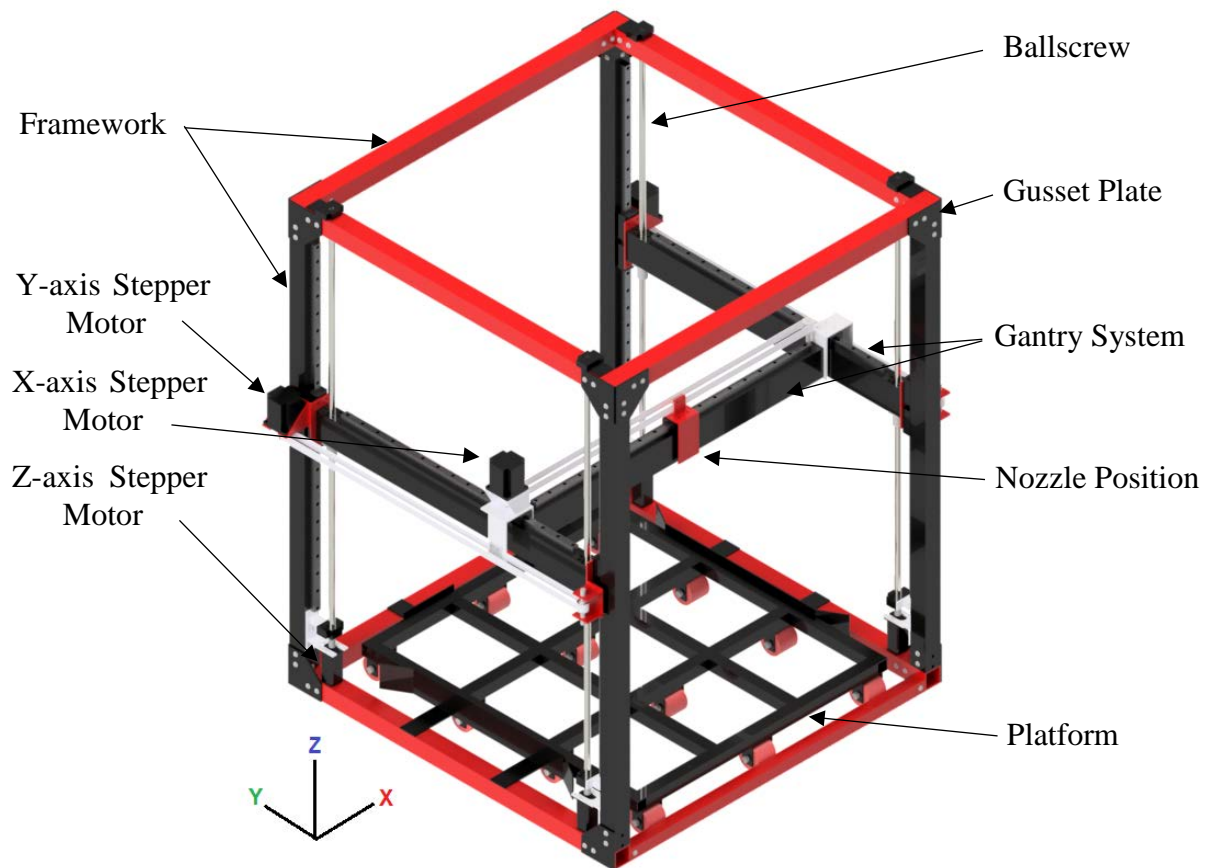


Figure 2.1: Rendered image of the 3D Inventor model depicting the concrete printer.

The printer consists of an outer rectangular framework with dimensions 1.3 x 1.3 m in plan (length x width) and is 1.67 m tall. The framework accommodates the gantry system and provides sufficient rigidity to prevent excessive vibrations and displacements. Grade S355 structural steel with square hollow section profiles (60 x 60 x 3 mm) are selected for the framework and 5 mm thick gusset plates used as connections. The section was carefully selected for appropriate stiffness and robustness under self-weight, but also the inertia of the printer nozzle in various positions during 3D printing operation, as well as fatigue and resonance induced by stepper motors, and acceleration or deceleration of the printer nozzle. Two bolts are used to connect both ends of each member to resemble a partially fixed connection rather than a pinned connection (one bolt) to increase rigidity. The main emphasis is placed on the mass of the steel sections to improve the dynamic behaviour of the structure. Sudden stop movements as well as large accelerations from a standstill position by the moving gantry can result in horizontal vibrations. Furthermore, large stepper motors can also induce vibrations in the system. Thus, the connections were important to provide structural rigidity. The stiffness of the structure is mainly dependent on its external geometry, material properties

such as elastic modulus and section properties such as area moment of inertia. Since the frequencies are expected to be mostly high during operation, an increase in the mass of the structure will yield better dynamic behaviour by yielding lower natural frequencies than the operational frequencies. Steel, and not aluminum which is typically used for 3D printers, is selected as the material for the large 3D printer. Although steel and aluminium present relatively similar density to elastic modulus ratios, thereby yielding an almost identical first natural frequency, steel possesses a remarkably higher elastic stiffness that yields smaller deflections and amplitudes. This ultimately improves the overall dynamic behaviour of the printer during operation.

A structural design is performed to obtain the steel sections required to limit maximum deflection of the gantry system to less than 100 μm under the worst loading condition. This is important as any deflection of the gantry system, especially at the nozzle position, can significantly influence the quality of printed elements. 100 x 50 x 3.5 mm rectangular hollow sections are used for the gantry system. A lighter 40 x 40 x 3 mm section is used for the front-bottom section of the framework and is fixed with one wingnut at each end. This enables the user to remove this section of the framework. The platform, which supports the surface bed on which the elements are printed, consists of 40 x 40 x 3 mm steel tubing and is supported by 12 polyurethane wheels with an ultimate load capacity of 700 kg each. This prevents the platform against excessive displacement due to the printed element's mass (especially for larger and taller elements). Lastly, it enables the platform to be moved outside of the framework so that printed elements can be removed safely and effortlessly from the printer after completion of each print. Guides are provided to hold the platform in the correct position.

Linear guide and rail systems, mounted on the gantry system as well as on the vertical steel sections, allow for accurate and low-friction movement in the x, y and z axes of the printer's Cartesian coordinate system. The appropriate size of both the guide and rail depends on the bending moments acting on it. It was therefore of crucial importance to determine the maximum moments that could occur at each guide (M_x , M_y and M_z) to obtain the most economical yet strong enough linear guide system for the machine.

Movement of the nozzle in the x-y plane is facilitated by a belt and pulley system. Various different sizes are available which includes parameters such as the number of teeth on the pulley and the pitch of the belt. Based on those parameters, factors such as maximum speed, required motor torque, resolution and motor steps per revolution can be determined. A 25 mm wide nylon belt with Kevlar reinforcement is found to be strong enough to safely drive the

maximum possible load. The belt has a pitch of 5 mm and the aluminum pulley has an outer diameter of 36 mm with a total of 20 teeth. This combination was considered to be the optimum motion configuration for the printer.

Ballscrews, a mechanical linear actuator that translates rotational motion into linear motion, are selected to facilitate the movement in the vertical direction i.e. to move the gantry system up or down. Beneficially, ballscrews prevent back drive if there is a loss of power to the motor. It is therefore the preferred method for vertical applications. Much the same as belt and pulley systems, ballscrews also possess a pitch that influences the parameters mentioned earlier. A 20 mm diameter ballscrew with 5 mm pitch is found to be sufficient for the printer. The vertical linear rails prevent buckling of the ballscrews. The gantry system connects to two guides spaced 20 mm apart at each vertical rail, as illustrated in Figure 2.2. This significantly increases the moment capacity of the connection, which resembles a partially fixed connection. A smaller angle of rotation is then obtained at the supports that in turn reduces the horizontal couple force induced on the ballscrews. Consequently, buckling of the ballscrews is prevented.

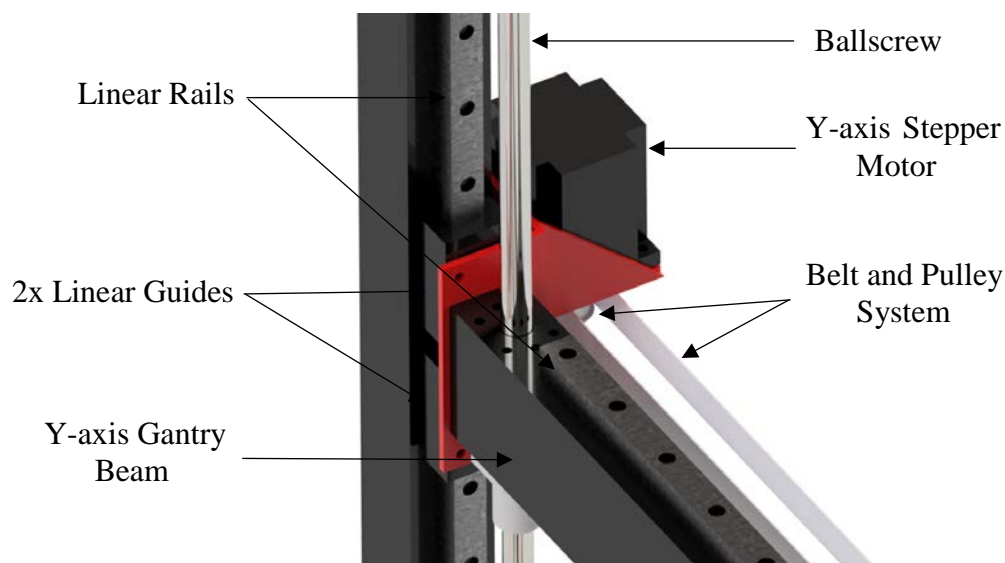


Figure 2.2: Detail of gantry system to vertical linear rail connection.

2.1.2 Electrical

The electrical and automation design is arguably the most important aspect of the 3D concrete printer. Not only should the design be economical and functional, but also flexible to allow for future modifications or additions to the printer.

The core of the printer revolves around a microcontroller unit (MCU). The RepRap Universal Mega Board with Allegro driver, commonly referred to as RUMBA (RepRap, 2019), is selected as the MCU. This board possesses ample processing power together with extensive

input/output (I/O) pins for future expansion. Furthermore, it supports Marlin firmware that is rather easy to configure. A dedicated 12V power supply unit (PSU) is provided for the MCU with sufficient wattage to accommodate other electronic components attached to the MCU such as fans and lighting.

Stepper motors are required to execute the automated process. The MCU interprets the G-code file and communicates with the stepper motors. The size of the stepper motor is mainly based on the torque requirement of each axis. An exceedingly conservative assumption is made that a 100 mm diameter hose filled with concrete is attached to the printer's nozzle. The worst possible load path configuration is then determined and converted to required torque, based on the specifications of the ballscrews and the belt and pulley system. It is determined that 115 mm NEMA 23 motors are required for the z-axis and NEMA 34 motors for the x and y axes. A stepper driver is required to power and control the stepper motors. Thus, a compatible stepper driver should be able to produce enough electrical current to the motor. Furthermore, the microstepping can be set on the stepper driver, which divides one motor step into multiple smaller steps. This increases the accuracy of stepper motors and reduces vibrations. Each motor requires a stepper driver that in turn also requires a PSU. Each motor is provided with a dedicated 48V PSU mainly for safety reasons. The required PSU wattage is determined based on the ampere requirement of each motor. Figure 2.3 presents a schematic diagram that illustrates how the electrical components are connected.

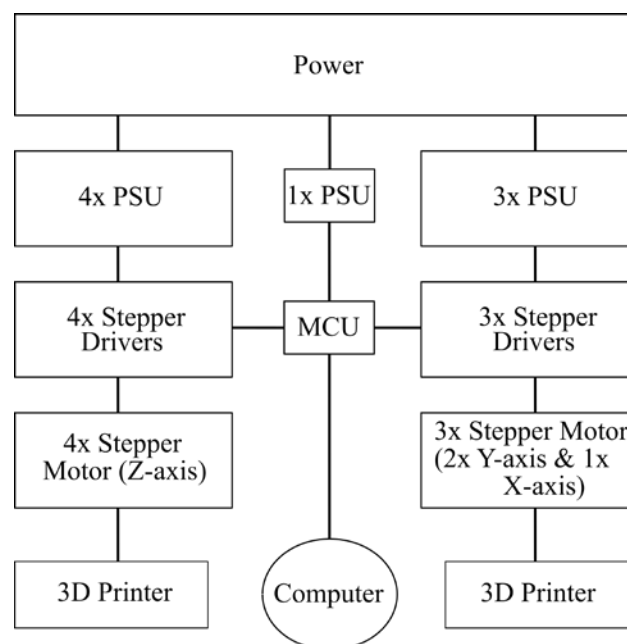


Figure 2.3: Schematic diagram of the main electrical components.

Limit switches are placed at the origin of each axis. These switches consist of an actuator that is mechanically linked to a set of contacts that either opens or closes an electrical circuit when activated. Thus, the zero position of the nozzle ($x = 0$, $y = 0$, $z = 0$) is determined by the location of these switches and then communicated to the software. This is essential for safety and calibration purposes. The limit switches are directly connected to the MCU.

A control box is necessary to house the electrical components. The PSUs, stepper drivers and the MCU are mounted on a back plate within an electrical enclosure. Large fans mounted within the enclosure provide sufficient airflow that prevents the components from overheating. Based on calculations, the control box for the 3D concrete printer requires about 7 kW at full capacity i.e. all motors turning at full speed. The likelihood thereof is very slim as the machine prints in layers, thus the x-y plane motors are active when the z-axis motors are inactive and vice versa. Inactive motors' current are reduced to 50 % of the operating current. Based on 220V AC, the control box consumes a maximum of 32A and therefore two power cables are provided to the box.

2.1.3 Pump and nozzle system

The pump and nozzle system for an industrial-grade 3D concrete printer differs fundamentally from a conventional 3D printer's extrusion process. Firstly, a significantly larger nozzle is required to extrude the concrete. A 25 mm diameter circular nozzle is chosen for the 3DCP. The bracket housing the nozzle is designed to accommodate different nozzle shapes and sizes for future modifications. Furthermore, heating of the nozzle is not required for concrete extrusion as opposed to conventional 3D printers. Hence, only a pump with a hose connected to a nozzle is required for concrete extrusion.

The most notable difference is the extrusion mechanism. Conventional 3D printers use a stepper motor to feed plastic into a heated nozzle. This stepper motor is controlled in the same manner as the other motion control stepper motors. An industrial-grade 3D concrete printer requires a strong pump. Typically, such pumps use 3-phase electric power. The research group already possesses a 3-phase 380V 3kW concrete pump (Rockcrete Equipment, 2019). This pump is a single speed motor and is capable of extruding aggregate sizes of up to 4 mm. However, the pump must be modified to enable for MCU control.

A variable frequency drive (VFD) is required to vary the motor speed that controls the rate of extrusion. A 3.7 kW VFD is found to be suitable for this application. It requires a 10V analog input signal to control the speed. The MCU on the other hand has a 5V digital frequency output,

which typically sends the number of steps to rotate to the stepper motor. This number of steps can be converted into a corresponding frequency. Therefore, a circuit containing a frequency to voltage converter chip is required. The maximum anticipated frequency is correlated to the maximum input voltage (10V) that results in the maximum pump speed. A potentiometer is installed to manually vary the maximum input voltage signal between 0V and 10V as a method for easy calibration of the extrusion rate. This process is illustrated in Figure 2.4. An electrical and electronic engineer, Mr. Johan Muller, was consulted to aid with the design of the pump automation system.

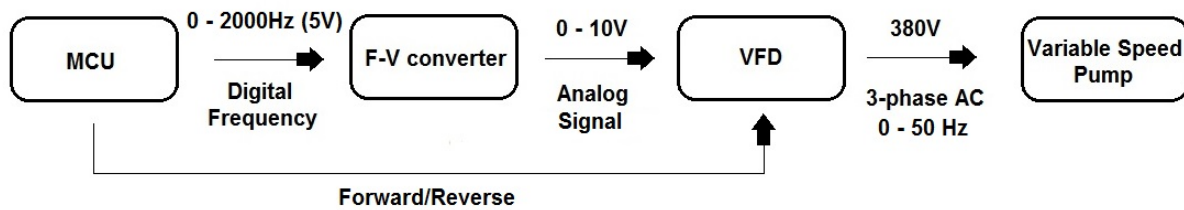


Figure 2.4: Schematic diagram of the pump automation process.

2.2 Procurement

Most of the procurement was conducted after the design of the 3D concrete printer, however some components were ordered at a later stage during the manufacturing process. Roughly 80 % of the procurement process was completed within 2 months i.e. identifying suppliers, placing an order, payment and delivery or collection of items.

Table 2.1 contains a summary of the procurement for the 3D concrete printer. The total cost accumulates to just below R88 000, with the mechanical category contributing 65 % towards the total cost of the printer. All the parts are sourced from a total of 19 different suppliers, each located within South Africa. It is thus evident that a 3D concrete printer can be manufactured in South Africa without directly importing any components required for the printer.

Table 2.1: Summary of procurement for the 3D concrete printer.

Category	Cost	No. of Suppliers
Mechanical	R56 755.09	13
Electrical	R25 272.20	7
Pump System	R5 460.00	2
Total	R87 487.29	19

Note: Pump system excludes concrete pump and electrical excludes computer. Total number of suppliers is less than the sum of each category as some suppliers covered more than one category.

2.3 Manufacturing of 3D concrete printer

The 3D concrete printer was manufactured with the assistance of Mr. Johan van der Merwe, a qualified fitter and turner. The mechanical manufacturing process was completed within 6 months while the electrical manufacturing process was completed in less than a month. Thereafter, the pump and nozzle system was manufactured and fitted to the printer to realise the first test prints in April 2018. The final build volume of the printer after calibration is 990 x 860 x 980 mm (x, y, z). Figures 2.5 and 2.6 illustrate the manufacturing progress of the printer, whilst Figure 2.7 illustrates the completed 3D concrete printer setup at Stellenbosch University.



Figure 2.5: Manufacturing of the 3D concrete printer indicating the framework (left) and the almost completed mechanical component of the printer (right).



Figure 2.6: The completed 3D concrete printer with automation system (left) and the electrical control box (right).

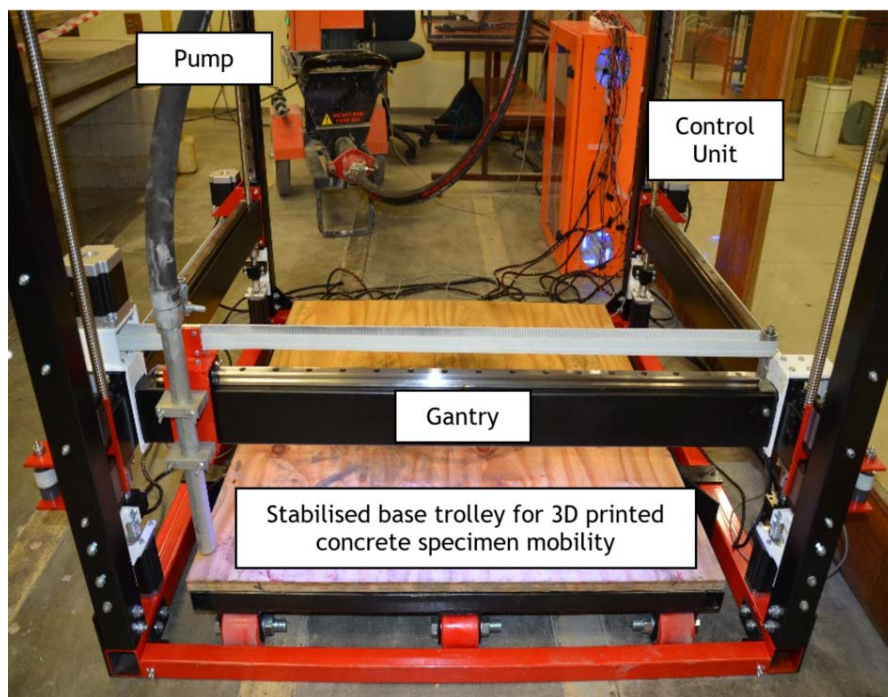


Figure 2.7: 3D concrete printer component layout and final assembly.

2.4 Material mix design

The ideal material for 3DPC is easily pumped and extruded, and provides sufficient green strength after extrusion to allow for adequate filament shape retention and buildability. Furthermore, the hardened concrete strength e.g. compressive, tensile, stiffness and interlayer bond strength (IBS) is of crucial importance to yield safe structures. The material mix design for 3DPC evidently presents many challenges; hence, literature is consulted for published material mix designs that can be used as starting point.

Three concrete mixes from the literature and one locally developed mortar mix are initially selected and tested with the ingredient materials available in South Africa. The respective mix compositions are presented in Table 2.2. In the first stage, the suitability of the mixes for 3DPC are primarily determined via visual inspection of workability. The demonstration of thixotropic behaviour is especially important i.e. the material should possess sufficient stiffness when at rest, but also flow easily when agitated. Thereafter, aspects such as hardened concrete strength and economy are evaluated and the most suitable concrete mix selected.

Table 2.2: Concrete mix compositions for initial trial testing.

Mix No.	Mix Reference	w/c ratio	kg/m ³						
			Cement	Fly Ash	Silica Fume	Sand	Water	SP	Fibre (PP)
1	(Nerella et al., 2016)	0.419	430	170	180	1240	180	10	-
2	(Anell, 2015)	0.346	659	87	83	1140	228	11.6	1.2
3	(Le et al., 2012)	0.401	579	165	83	1241	232	16.5	1.2
4	Mortar	0.752	365	-	-	1646	274	-	-

Note: SP refers to superplasticizer and PP to polypropylene (omitted from study in trial stage).

Mix 3 is found to illustrate the fresh state characteristics most suitable for 3DPC. Additionally, the mix has the highest cube compressive strength of 61.4 MPa, followed by Mix 2 at 55.1 MPa, Mix 1 at 42 MPa and Mix 4 at 18.1 MPa. It has a relatively high cement content, although not the highest of the trial mixes. At this stage, a mix with high paste content is preferred, in order to achieve appropriate rheology for pumping and extrusion in 3DPC (Choi et al., 2013). At later stages, once the printer has been tested and calibrated, mix optimisation for cost, durability and sustainability can be performed. Mix 3 is chosen as the reference mix and further refined for enhanced 3DPC quality.

The first improvement made to the reference mix involves the application of the Fuller Thompson Theory (Fuller & Thompson, 1907). This theory aims to achieve the maximum particle packing density that yields improved pumpability and flexural strength and minimises the probability of particle segregation. The modified Fuller's equation (Li, 2011) is depicted by Equation 2.1 and is widely used for particle gradation design. Recent research applied Fuller's theory to material design for 3DPC and found it to aid significantly with buildability performance (Weng et al., 2018).

$$p_i = \left(\frac{d_i}{D}\right)^{0.45} \quad (2.1)$$

Three locally available natural fine aggregates are evaluated for use in the selected Mix 3. A sample of each sand is graded and compared to Fuller's ideal grading that is scaled to 100 % at 2.36 mm sieve size. From the results indicated in Figure 2.8, it is evident that the coarse sand exhibits the best correlation to Fuller's ideal grading; hence, the coarse sand is acquired and used for the 3DPC material mix.

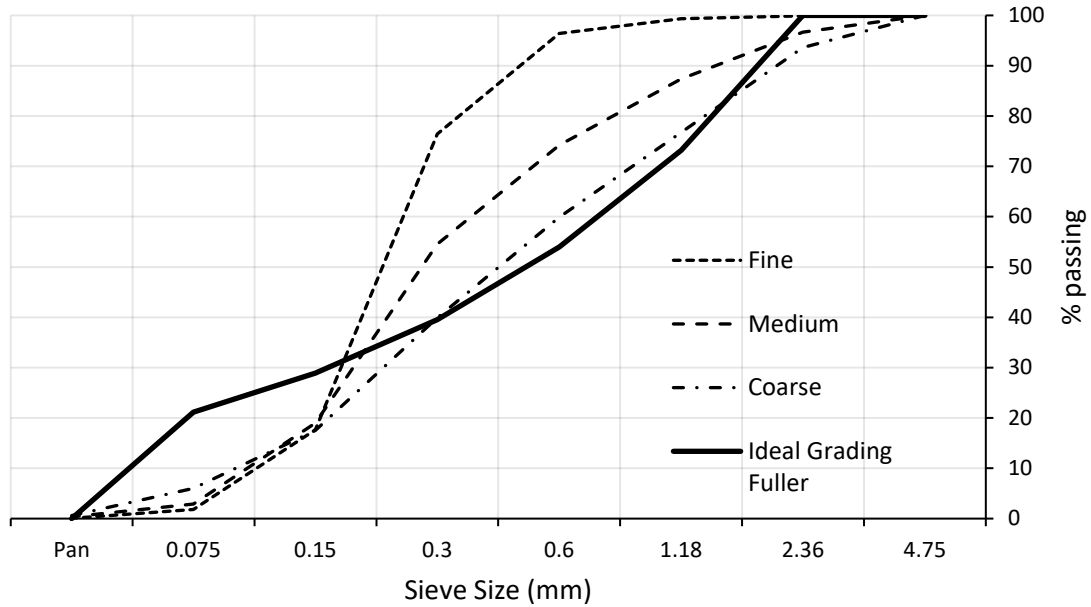


Figure 2.8: Particle size distribution of various different fine aggregates obtained from sieve analyses compared to Fuller's ideal particle grading.

Empirical alterations were made to the sand content, w/c ratio and superplasticizer dosage after several 3D concrete prints with the refined material. The final 3DPC material mix used as the standard high-performance concrete (HPC) printing material at Stellenbosch University is given in Table 2.3, and its quality in terms of buildability and surface aesthetics illustrated in Figure 2.11c. The particle grading analysis of the final mix (binder and sand) is depicted in Figure 2.9 and demonstrates remarkable correlation with Fuller's ideal grading curve.

Table 2.3: Reference 3D printable HPC mix constituent quantities.

Constituent	Description	kg
Cement	PPC SureTech	579
	CEM II/A-L 52.5N	
Fly Ash	Ulula Class S	165
Silica Fume	FerroAtlantica Microfume	83
Fine Aggregate	Malmesbury Coarse	1167
Water	Potable Tap Water	261
Superplasticizer	Chryso Premia 310	12.24

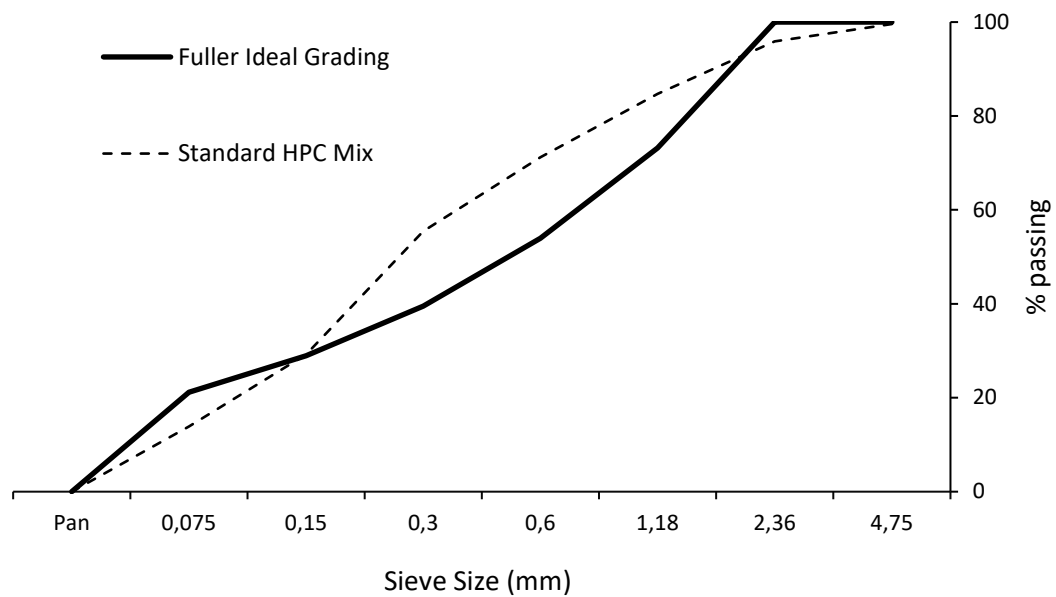


Figure 2.9: Particle size distribution of the reference 3D printable HPC mix compared to Fuller's ideal grading curve.

The hardened mechanical properties of the reference mix is depicted in Table 2.4 with coefficient of variation indicated in brackets as a percentage. The Eurocode is adopted for compressive and flexural strength testing (EN196-1) while the American standard is adopted for the Young's Modulus testing (ASTM C469-02). The interlayer bond strength between filament layers is determined from 40 x 40 x 160 mm specimens cut from a 3D printed square hollow column, loaded in four point bending with filament layers vertically orientated, as illustrated in Figure 2.10. The IBS is classified in terms of the maximum normal stress achievable before delamination of layers occur i.e. failure of the flexural specimen.

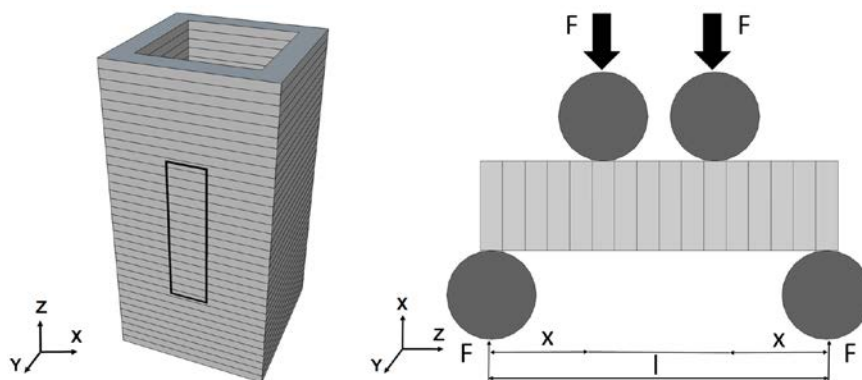


Figure 2.10: IBS specimen cut from 3DP square hollow section and loaded at third points.

Table 2.4: Mechanical properties of the reference 3D printable concrete mix with coefficient of variation indicated in brackets. Three specimens were tested for each mechanical property.

Age (days)	1	7	28	56
Compression Strength (MPa)	7.9 (2.6 %)	55.6 (0.6 %)	70.6 (10.3 %)	80 (15.1 %)
Flexural Strength (MPa)	1.7 (8.1 %)	7.3 (5 %)	8.4 (5.7 %)	8.7 (2 %)
Young's Modulus (GPa)	-	26.6 (2.3 %)	30.7 (2 %)	-
Interlayer Bond Strength (MPa)	-	-	6.8 (2.1 %)	-

2.5 3D concrete prints

Initial 3D concrete printing comprised mainly of calibration prints. Simple shapes such as a circular hollow column were used for this purpose. Additionally, an indication of the material's buildability is obtained by printing the aforementioned shape and counting the total number of layers achieved, as typically found in literature. The first 3D concrete print performed at Stellenbosch University is depicted in Figure 2.11a. It is evident that the printer required significant calibration due to a skewed print. The material also appears too stiff as several filament layer discontinuities were observed during extrusion. After calibration and material alterations, the column was printed again, illustrating a marked improvement in Figure 2.11b. However, the material still proved too stiff for proper extrusion. This result prompted the w/c ratio increase described in the previous section to yield the final 3DPC material composition given in Table 2.3. The column was printed again and a superior surface finish was obtained, as illustrated in Figure 2.11c. As final validation, a bathtub with more complex geometrical curvature was successfully printed and is depicted in Figure 2.11d.

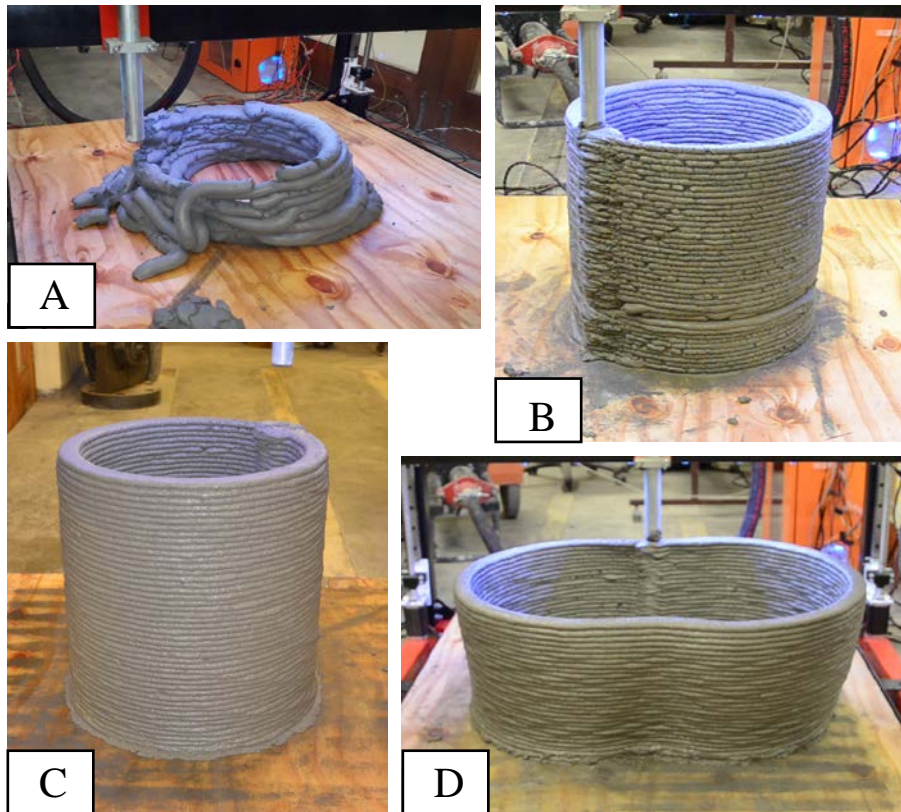


Figure 2.11: (a) Initial print performed in order to calibrate the printer, (b) column printed again with improved material and calibration, (c) column printed again with final 3DPC mix composition and (d) bathtub print with increased geometrical complexity.

Subsequent prints comprised mainly of twisted hollow columns as an alternative to conventionally cast straight concrete columns. Figure 2.12 illustrates a 250 x 250 x 700 mm square hollow column that twists 45° over its height. Slight over extrusion occurred that resulted in an excessive undulating surface finish pattern. Figure 2.13 illustrates a 250 x 250 x 800 mm square hollow column that twists 90° over 600 mm of the column's height. For this column, 6 mm long PP fibres were added to the reference 3DPC mix to aid with plastic shrinkage cracking. Although some irregular layers are present due to air ingress in the pump feeder system, it remains a good example of the potential that 3DPC presents, as the column was printed in under 25 minutes without any formwork requirements. van Zijl et al. (2018) provides more detailed information about the fibre reinforced concrete print.

Chapter 2: 3D Concrete Printer



Figure 2.12: A 250 x 250 x 700 mm square hollow column that twists 45° over its height.

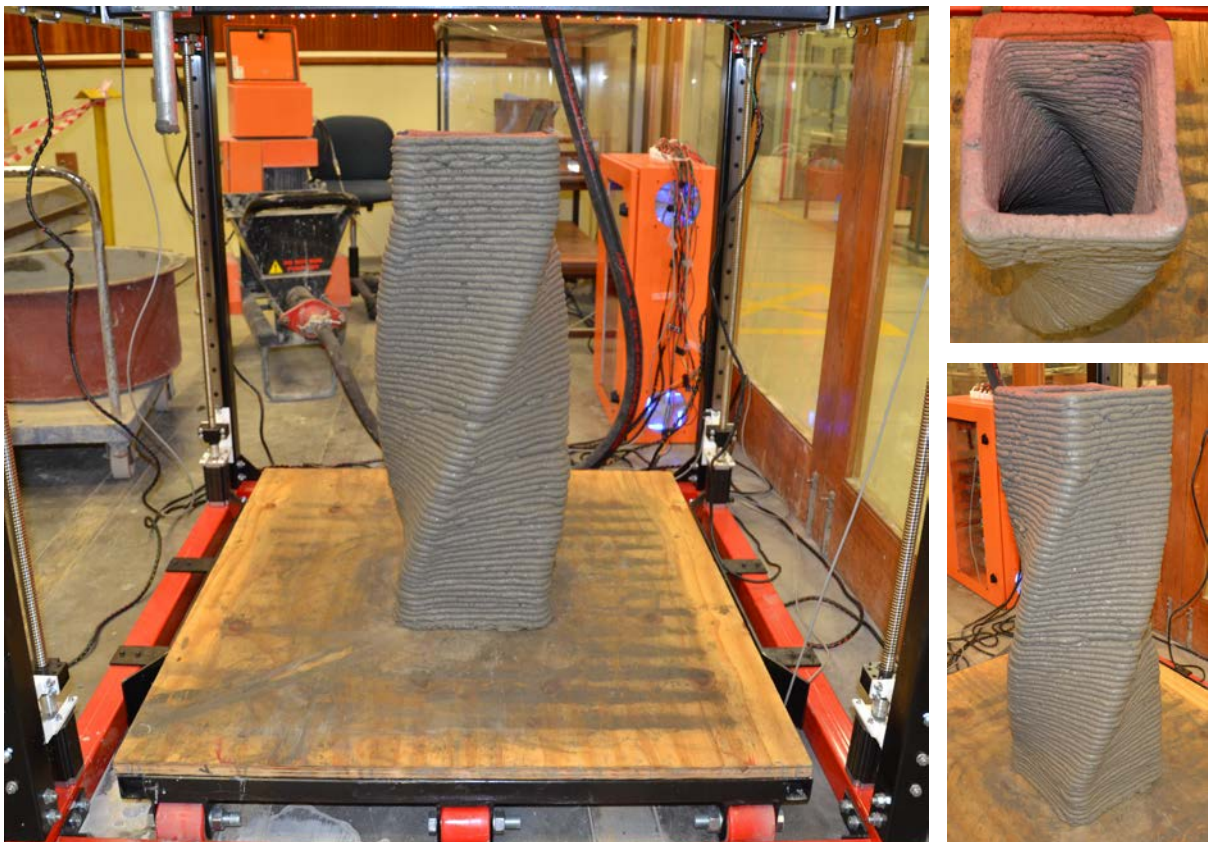


Figure 2.13: A 250 x 250 x 800 mm square hollow column that twists 90° over a height of 600 mm. The column was printed in less than 25 minutes with a polypropylene fibre reinforced 3D printable concrete.

The X-project is the latest endeavour undertaken by the SU 3DPC team in 2019. It consists of an outdoor bench set, i.e. one table and two benches, printed in the shape of an X. In agreement with the University of Stellenbosch, these sets will form part of the campus' outdoor furniture to demonstrate innovation. A fibre reinforced 3D printable concrete is employed for this project to enhance durability, ductility and resilience. A full structural analysis via finite element analysis (FEA) is conducted and all possible loading scenarios considered, including thermo-mechanical behaviour. The bench set will be anchored in the ground by means of a raft slab that constrains all three elements together. A unique surface finish in the form of an undulating “koeksister” pattern is applied to the top of the two benches. Construction costs amount to R1 200/meter bench and R1 500/meter table, which yields a total price of R4 000/meter bench set. A complete set can potentially be constructed in under 4 hours and is strong enough for lifting, handling and instalment one day after construction. No formwork or temporary support is used during the construction process. Construction-phase images are presented in Figure 2.14 and the completed prototype illustrated in Figure 2.15.

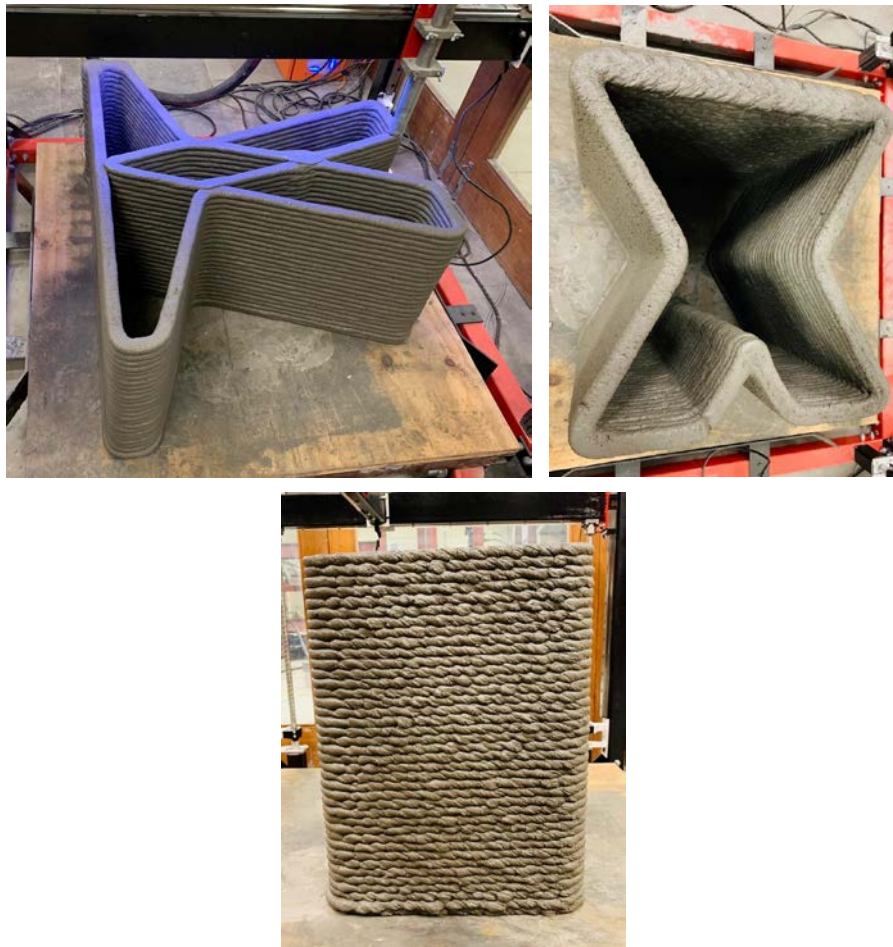


Figure 2.14: Construction of the X-project table (top-left) and bench (top-right) with the undulating surface finish of the bench indicated in the bottom picture.



Figure 2.15: Completed prototype of the X-project bench set with 3DPC team members Mr. Marchant van den Heever and Mr. Frederick Bester.

2.6 Conclusion

This chapter presents the research and development conducted towards achievement of Objective 1 of this dissertation, as defined in Chapter 1. An industrial-grade 3D concrete printer of roughly 1 m³ build volume is designed, procured and manufactured, for conducting the research elaborated in the following chapters. The development process of a 3D printable cementitious material with the Fuller Thompson theory and locally sourced ingredients is then presented and the standard HPC 3D printable material's constituent quantities given. Evolution of 3D concrete printing at SU is manifested by means of pictures of 3D prints from the initial calibration stage through to the X-project bench set, which will be used by the public. However, note that most improvements were made by empirical adjustments of the material, G-code object file and print parameters. Further improvements require theoretical quantification in terms of material suitability for 3DPC, i.e. a thixotropy material model that specifically appertains to 3DPC, as well as constructability models to predict maximum filament layer heights and total vertical building height before collapse. Ideally, these models must be combined in order to specify the required print parameters for successful construction of a 3DPC element. Research towards achieving these objectives is elaborated in the following chapters and allows for theoretical, rather than empirical, quantification of 3DPC constructability to reduce the probability of failure and optimise total construction time.

2.7 References

- Anell, L.H. 2015. Concrete 3d printer. Lund University. [Online], Available: <https://lup.lub.lu.se/student-papers/search/publication/7456059>.
- Autodesk. 2019. *Inventor*. [Online], Available: <https://www.autodesk.com/products/inventor/overview> [2019, May 31].
- Choi, M., Roussel, N., Kim, Y. & Kim, J. 2013. Lubrication layer properties during concrete pumping. *Cement and Concrete Research*. 45:69–78.
- Fuller, W.B. & Thompson, S.E. 1907. The laws of proportioning concrete. *Transactions of the American Society of Civil Engineers*. 57:67–143. [Online], Available: archive.org/details/transactionsofam59amer.
- Le, T.T., Austin, S.A., Lim, S., Buswell, R.A., Law, R., Gibb, A.G.F. & Thorpe, T. 2012. Hardened properties of high-performance printing concrete. *Cement and Concrete Research*. 42(3):558–566.
- Li, Z. 2011. *Advanced concrete technology*. Hoboken, N.J.: Wiley. ISBN: 9780470950067
- Nerella, V.N., Krause, M., Nather, M. & Mechtcherine, V. 2016. Studying printability of fresh concrete for formwork free concrete on-site 3D printing technology (CONPrint3D). In *25th Conference on Rheology of Building Materials*. 236–246.
- RepRap. 2019. *RUMBA*. [Online], Available: <https://reprap.org/wiki/RUMBA> [2019, May 31].
- Rockcrete Equipment. 2019. *Rockcreter TSL Pump*. [Online], Available: <https://www.rockcrete.co.za/rockcrete-products/plaster-pumps/rockcreter-tsl-pump> [2019, May 31].
- van Zijl, G.P.A.G., Kruger, J., Cho, S. & Zeranka, S. 2018. 3D printing polymer fibre concrete. In Cape Town, South Africa. *Proceedings of the International Inorganic-Bonded Fiber Composites Conference*. 5–14.
- Weng, Y., Li, M., Tan, M.J. & Qian, S. 2018. Design 3D printing concrete materials via Fuller Thompson theory. *Construction & Building Materials*. 163:600–610.

Chapter 3

An ab initio approach for thixotropy characterisation of (nanoparticle-infused) 3D printable concrete

Jacques Kruger, Stephan Zeranka, Gideon van Zijl

Division for Structural Engineering and Civil Engineering Informatics, Stellenbosch
University, 7600, South Africa

Reproduced and reformatted from an article published in the *Construction and Building
Materials Journal*. (DOI: 10.1016/j.conbuildmat.2019.07.078)

Abstract

This paper presents a novel rheological thixotropy model that specifically appertains to the characterisation of materials that are suitable for 3D printing of concrete (3DPC). The model accounts for both physical and chemical influences on a material's microstructure, denoted by R_{thix} (re-flocculation) and A_{thix} (structuration) respectively. Rheological analyses are performed on a reference material with varying superplasticizer (SP) and nano-silica (nS) dosages in order to determine their effects on the aforementioned parameters. Specific focus is placed on the re-flocculation thixotropy mechanism. The advantages of adding nanoparticles to concrete for 3DPC is practically validated by printing circular hollow columns until failure occurs. The result is supported by the thixotropy model, which is applied to the materials that are used for the 3DPC tests. It is concluded that, for this study, R_{thix} is a better measure of thixotropy behaviour that is suitable for 3DPC than A_{thix} .

Keywords: 3D concrete printing, nano-silica, rheology, thixotropy, flocculation

3.1 Introduction

3D printing, a technology emanating from Industry 4.0, is being applied in the construction industry as a means of industrialisation. 3D printing of concrete (3DPC) is an extrusion-based process, similar to the fused deposition modelling (FDM) process commonly adapted in the thermoplastic printing industry, however without requiring heat to facilitate extrusion of the material. Extrusion of cementitious materials are mainly achieved by appropriate rheological behaviour and not by thermal effects that result from heating and cooling in the case of plastics. Different types of printers are used for concrete printing to accommodate different build volumes, and include gantry, robotic and crane printers (Paul et al., 2017).

Several research institutions are currently exploring this new technology, seeking solutions to various problems, the largest thereof the lack of steel reinforcement in the construction process (Mechtcherine et al., 2018; Bos et al., 2017). Nevertheless, a recent advancement in this field is the design and manufacturing of the first 3D printed bicycle bridge in the Netherlands (Salet et al., 2018). This was accomplished by 3D printing the bridge in segments off-site, after which they were assembled on site and compressed together via post-tensioned tendons. Remarkable progress is also being made on fibre reinforced concrete resulting in deflection hardening (Nematollahi et al., 2018; van Zijl et al., 2018). Evidently, 3DPC technology is being embraced while still in the early developmental stages, providing good indication for large-scale adoption in the construction industry in the future. However, much research needs to be done on several 3DPC aspects to ensure quality and safety, ultimately resulting in codes of practice.

One such aspect is the rheological characterisation of materials. An alternative to the conventional on-site slump test is required to assess appropriate workability, suitable for the particular 3D printing project requirement. For 3DPC, the rheology of the concrete must be of such nature that it can be pumped without requiring excessive pressure as to avoid segregation, while retaining shape under self-weight and that of subsequent layers after extrusion. A narrow domain in terms of material workability is therefore viable for 3D printing.

Thixotropic materials are characterised by distinct static and dynamic yield stresses. When at rest, such material has semi-stiff, almost dough-like consistency. However, when energy is applied through agitation, the material starts to flow. Therefore, highly thixotropic materials are more suitable for 3DPC. In this research, the effect of superplasticizer dosage on thixotropy is determined. Particular attention is applied to the structuration rate (A_{thix}) as well as a novel

re-flocculation rate (R_{thix}) developed in this research. A novel static yield shear stress evolution curve is then developed that depicts a material's shear strength development after extrusion i.e. the cessation of the applied energy.

Nano-silica (SiO_2) particles are added in 1 % increments by weight of cement in order to perform a sensitivity analysis on the thixotropy of the concrete. Recent research found that nano-silica addition significantly improves the mechanical and durability properties of hardened concrete (Biricik & Sarier, 2014; Said et al., 2018). Although several dispersion methods are available to reach optimum nanoparticle dispersion (Liu et al., 2016), only a superplasticizer is used to this end. This negates other factors that may potentially influence the results. Due to the large surface area to volume ratio, high purity and small diameter of the nano-silica particles, increased thixotropic behaviour is expected (refer to Section 3.2.3 for detailed explanation).

As a practical means of validation, a circular hollow column is 3D printed with the standard 3DPC mix at Stellenbosch University (SU). Thereafter, a column is 3D printed with the standard mix containing nano-silica, which is then compared to the standard mix column in terms of the number of filament layers achieved before failure occurs. A high printing speed relative to the geometry of the column is used to minimize the printing time gap between layers, consequently adding mass to the previous layers at a higher rate. This allows for the practical validation of the theoretical model, specifically the re-flocculation rate (R_{thix}) developed in this research, and the effect of nano-silica addition thereon.

3.2 Thixotropy theory

3.2.1 Rheology & thixotropic behaviour

Subtle deformation and flow of concrete after extrusion can have a significant impact on the quality of 3D printed objects. It is therefore important to study the fresh state properties of concrete before extrusion by means of rheological characterisation. This provides the user with vital information to assess the suitability of the particular concrete before printing commences. Concrete, being a non-Newtonian fluid, comprises of a complex microstructure and can be characterised as a pseudo-plastic, visco-plastic, dilatant or thixotropic fluid, each exhibiting vastly different flow behaviour.

Thixotropic behaviour is of particular importance for 3DPC, since there is a distinct difference between the static and dynamic yield stress of the material, depicted in the stress growth rheology test curve in Figure 3.1. This is due to the shear-thinning property of

thixotropic materials, where a decrease in viscosity is noticed over time due to external energy being applied. This is synonymous to the pumping of concrete, whereby pressure is applied to the concrete to facilitate movement. A material only starts to flow after the static yield stress is exceeded, whereafter the dynamic yield stress is maintained. A lower dynamic yield stress is thus optimal for pumping applications, which not just places less strain on the pump's motor, but also minimizes the probability of water segregating from the mix. Additionally, it facilitates the flow-induced particle migration that leads to the formation of a lubrication layer (also called slippage layer), resulting in less pumping pressure (Roussel, 2011). Furthermore, a higher static yield stress results in a stiffer concrete when at rest, which requires more energy for it to flow and hence demonstrates better buildability for 3DPC purposes. An optimum balance between high static yield stress and low dynamic yield stress is thus ideal for 3DPC applications.

Björn et al. (2012) describe thixotropic fluids as dispersions, which when at rest constructs an intermolecular system of forces that increases the fluid's viscosity, also known as flocculation. In order for the material to flow, a strong external energy is required to break these binding forces, which lowers its viscosity. This is known as the de-flocculation phase. In rheological terms, an applied stress equal to or larger than a material's static yield stress will result in de-flocculation. During this phase, while the structures are broken, the lowest possible viscosity to maintain a constant shear rate is achieved if the material is continuously agitated. This correlates to the dynamic yield stress of a material. The most interesting aspect of thixotropic materials is that they re-flocculate as soon as the external energy is removed and the agitation stops. Therefore, a highly thixotropic material rapidly regains stiffness due to an increase in viscosity after halting of the agitation. In rheological terms, a rapid restoration of shear stress is observed from the dynamic yield stress to the static yield stress. This rapid structural rebuilding of cementitious materials, also referred to as viscosity recovery, is a complex phenomenon that enjoys significant attention in the academia (Qian, 2017; Panda et al., 2018; Panda & Tan, 2019; Panda et al., 2019a).

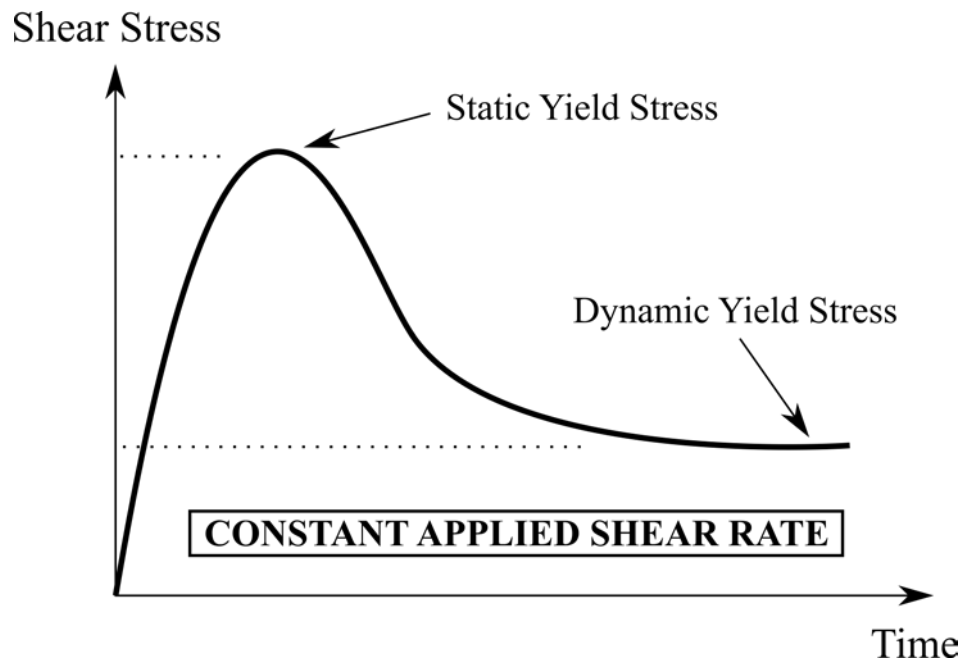


Figure 3.1: Describing thixotropy by means of a stress growth rheological characterisation test that depicts the static and dynamic yield stress.

3.2.2 Interaction between particles suspended in liquids

Time-dependant thixotropic behaviour is ascribed to the existence of microscopic and molecular structure in a material. This structure, functionally described in the previous section, is mainly based on interparticle forces that are derived from interatomic and intermolecular forces on the surface of particles. These forces are typically described in terms of intermolecular potential energy, where positive potential slope gives attraction and negative potential slope repulsion. At small intermolecular distances, strong Born repulsion forces exist. At larger distances, van der Waals' attraction forces exist between particles. These forces are depicted as a function of particle centre separation in Figure 3.2.

Cheng (1987) describes that the van der Waals' forces cause particles to move closer together, however only until repulsion is felt. Equilibrium is thus achieved at the distance where the interparticle force is zero and is depicted by the minimum in the potential function in Figure 3.2. Brownian motion is defined by Barnes (1997) as “*the random thermal agitation of atoms and molecules that results in elements of the microstructure being constantly bombarded, which causes them to move to a favourable position where they can – given the necessary attractive force – attach themselves to other parts of the microstructure*”. This Brownian motion tends to move particles up the potential curve if they are sufficiently small. Consequently, particles are separated and dispersed. Brownian motion becomes increasingly weaker for larger species which then keeps the particles closer to the primary potential

minimum, resulting in coagulation. This implies that particles form large agglomerates that settle out under gravity.

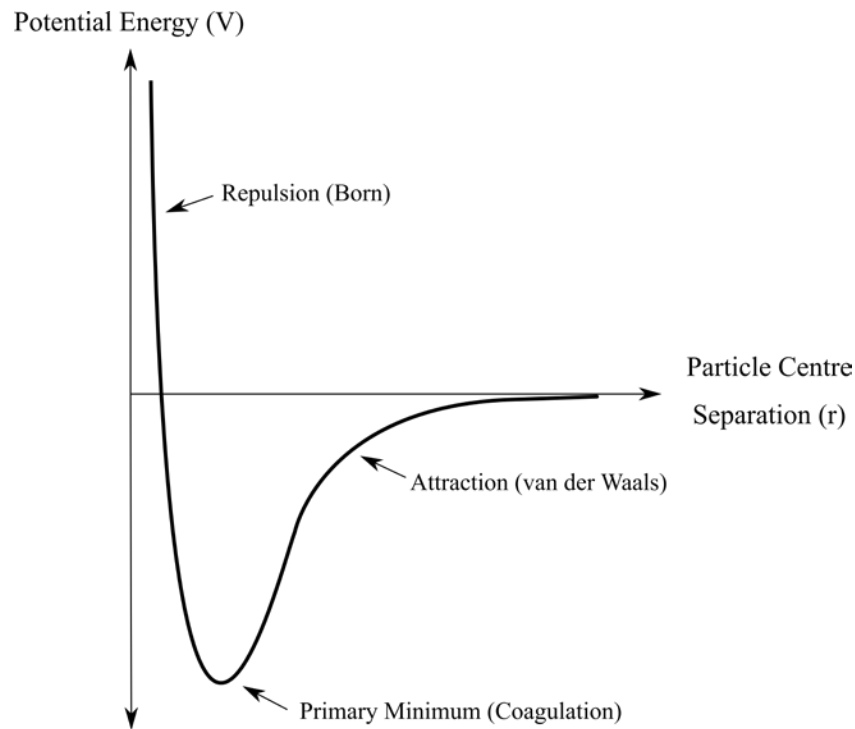


Figure 3.2: Forces between atoms and molecules expressed by potential energy as a function of particle centre separation. Re-worked from (Cheng, 1987).

Coagulation of particles, or the dominating attractive forces, can be prevented through stabilisation as follows (Cheng, 1987; Tadros, 2007):

1. *Electrostatic stabilisation*

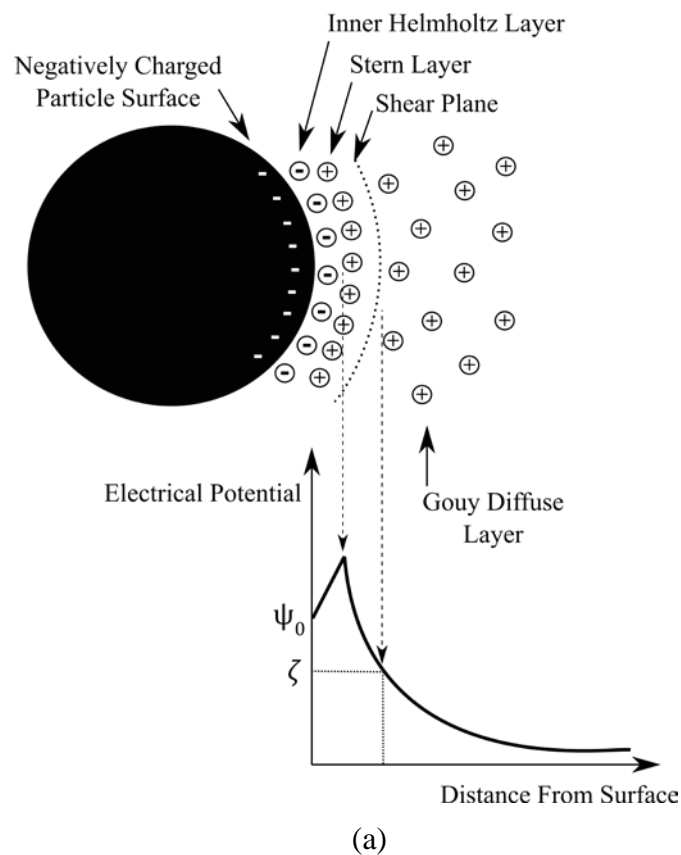
This stabilisation mechanism is based on the electrical double layer around a particle, illustrated in Figure 3.3a. Typically, the surface of a negatively charged particle (ψ_0) suspended in a liquid containing electrolytes may carry adsorbed co-ions, resulting in the formation of the inner Helmholtz layer. Positive counter-ions are then attracted to balance the negative charge, which results in the formation of the strong outer Helmholtz or Stern layer. Counter-ions are increasingly weaker held by the Helmholtz layer as the ion concentration decreases with an increase in distance from the particle, resulting in the Gouy diffuse layer. A shear plane is created between the Stern and Gouy layers due to this differential in potential and is called the zeta-potential (ζ) (Malvern Panalytical, 2013).

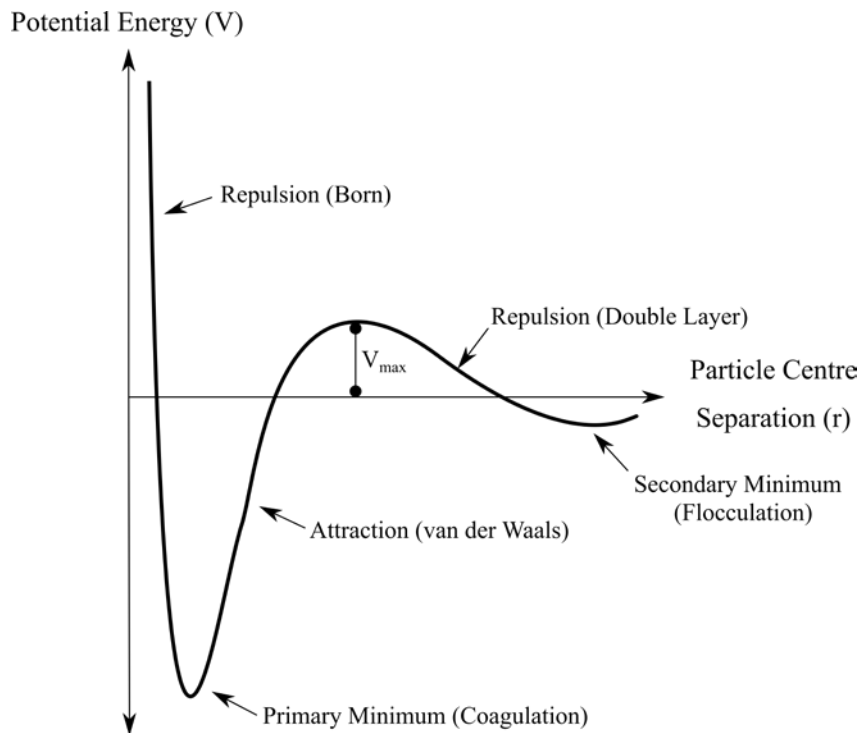
An electrostatic repulsion force is developed when the electrical double layer of two particles interact. Due to this force, the particles move away from the primary minimum,

Chapter 3: Thixotropy Model

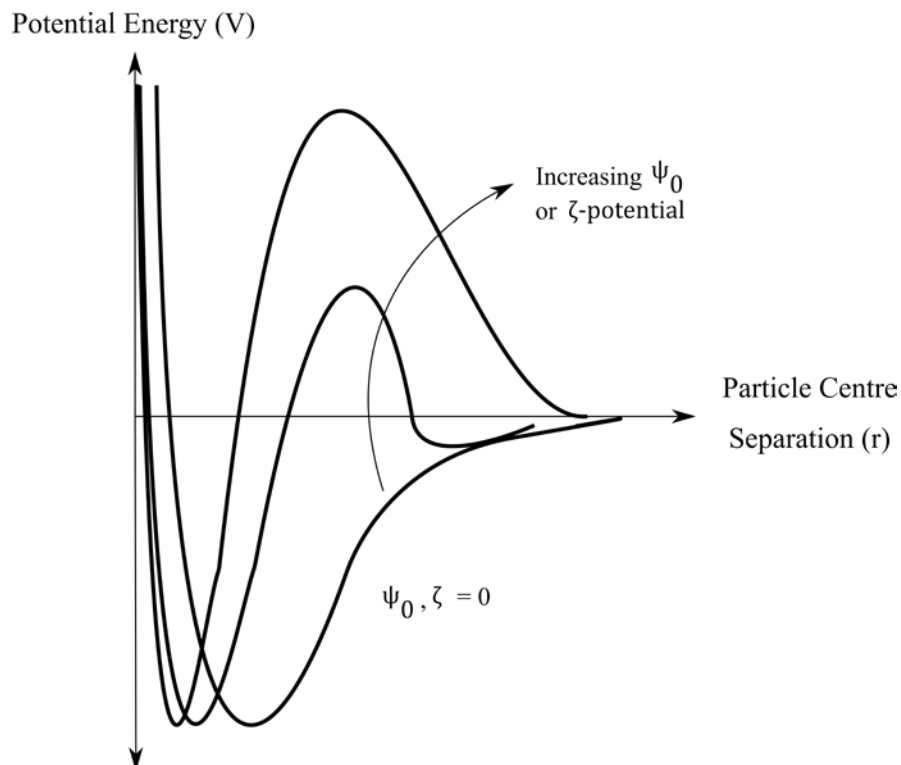
consequently resulting in dispersion. This leads to larger interparticle distances and a potential maximum (V_{\max}) is developed that constitutes a barrier to coagulation, as illustrated in Figure 3.3b. Based on the magnitude of V_{\max} , a secondary minimum is developed at larger interparticle distances that results in flocculation. A shallow secondary minimum yields weak flocs that can easily be de-flocculated, resulting in a lower yield stress. Stronger flocs are formed if the secondary minimum is deep, which is advantageous for 3DPC in terms of buildability.

Figure 3.3c depicts the influence of surface or zeta-potential on the total potential energy. An increase in either of the parameters enhances the potential maximum resulting in a shallower secondary minimum; thus weaker flocs are obtained. Longer shear plane distances yield the same effect. It is evident from Figure 3.3c that an optimum surface or zeta-potential exists for deep secondary minima. If achieved, strong flocs will develop and improve thixotropic behaviour.





(b)



(c)

Figure 3.3: (a) The electrical double layer and corresponding electrical potential as a function of distance from particle surface, (b) potential energy for electrostatic stabilisation, (c) influence of surface charge or zeta-potential on total potential energy. Re-worked from (Cheng, 1987).

2. *Steric stabilisation*

Steric stabilisation involves the adsorption of macromolecules, such as surfactants or polymers without charged groups (non-ionic), onto particle surfaces. Two different anchoring types are possible depending on the functional groups of a molecule's backbone: tails type that is anchored at one end to the particle surface or loop type that can be anchored at multiple positions along its length, as depicted in Figure 3.4a. A combination of both types are also possible on one particle. Two particle layer interaction types are characterised that both result in a repulsive force. The first interaction stems from mixing of the adsorbed macromolecular layers and is referred to as osmotic or enthalpic repulsion. Layers become entwined that increases the osmotic pressure, consequently creating a repulsive force. The second interaction type is referred to as entropic or elastic repulsion, where the volume available for occupation by one particle's adsorbed molecules is restricted or reduced by the presence of another particle's molecules. This volume restriction also produces a repulsive force. Enthalpic and entropic repulsion are visually illustrated in Figure 3.4b.

In contrast to electrostatic stabilisation, steric stabilisation only has one minimum (V_{\min}). The depth of this minimum determines the strength of the flocs that will form. If the minimum is too deep, the flocs will be too strong and consequently can be regarded as semi-coagulated. Molecular weights and structure mainly determine the magnitude of the potential minimum. If the molecular weight is too large, a potential minimum may not be obtained and consequently floc formation is neutralised. The potential energy for steric stabilisation is depicted in Figure 3.4c.

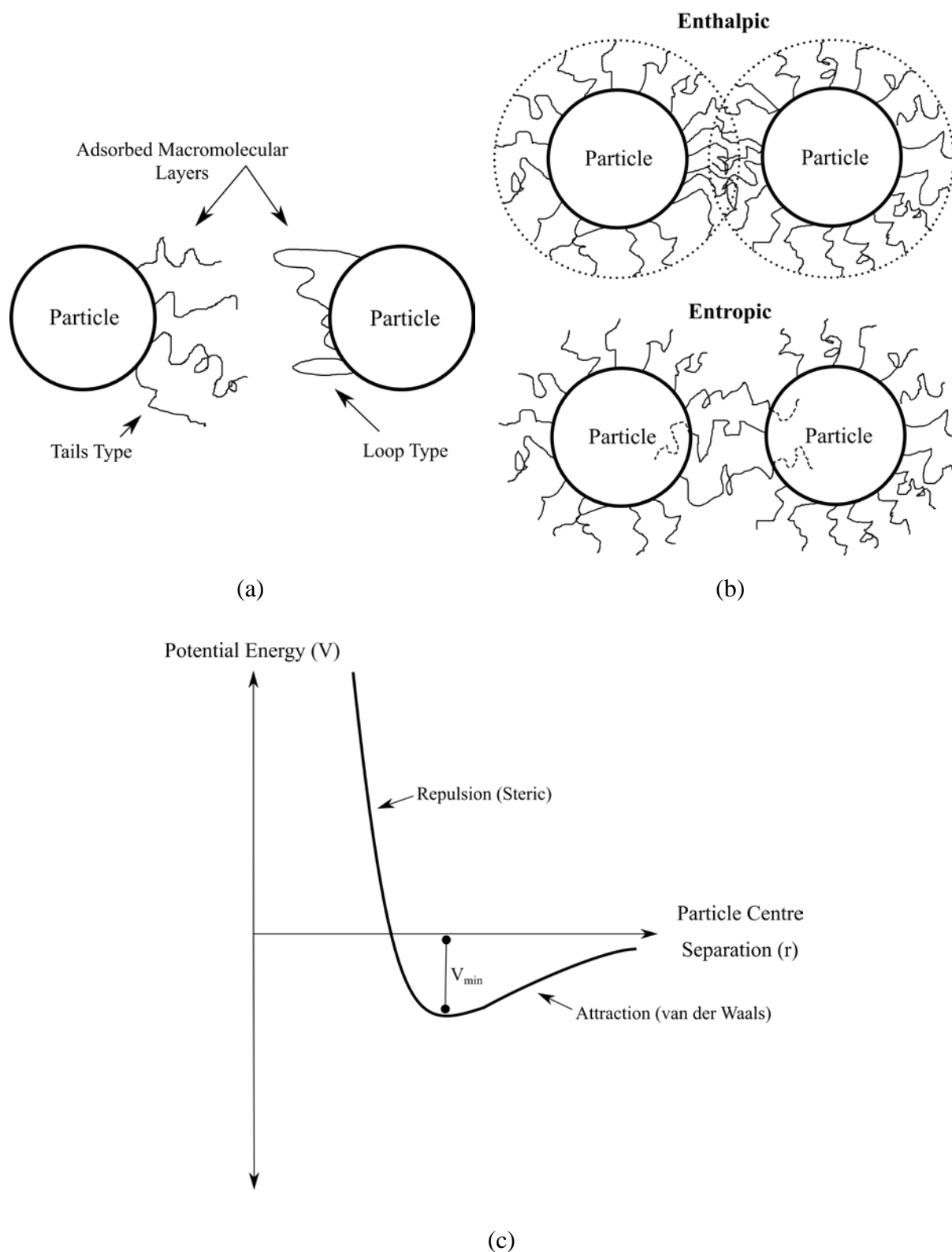


Figure 3.4: (a) Tail and loop type macromolecular layers, (b) enthalpic and entropic layer interactions, (c) potential energy for steric stabilisation. Re-worked from (Cheng, 1987).

3. Polyelectrolyte stabilisation

Polyelectrolyte stabilisation is the dispersing of particles through both electrostatic and steric effects. These macromolecules consist of ionic end-groups that are distributed along its length and side chains. Polycarboxylate Ether (PCE) superplasticizers function on this principle, whereby the negatively charged backbone adsorbs to the particle surface and its non-adsorbing side chains are non-ionic. Consequently, PCE superplasticizers disperse cement particles via both electrostatic and steric effects (Flatt & Schober, 2011). Older generation Naphthalene-based superplasticizers such as Naphthalene Sulfonate Formaldehyde (NSF) are largely based only on electrostatic effects. A study by Uchikawa et al. (1997) found that the contribution of electrostatic repulsion to total repulsive force is very high for NSF and lower for PCE. However, PCE superplasticizers are more effective than NSF superplasticizers mainly due to the combined repulsion effects, subsequently requiring less superplasticizer for full dispersion (Zhang & Kong, 2015). More detailed information on the functionality of these superplasticizers can be found in (Flatt & Schober, 2011; Wiliński et al., 2016).

A PCE superplasticizer is used in this research to disperse the nanoparticles with large surface area to volume ratio that will be added to the concrete. A lower dosage is required compared to NSF superplasticizers, avoiding retardation of hydration that commonly occurs at larger doses. Consequently, a smaller structuration rate is avoided (refer to Section 3.2.4). Evidently, from Figures 3.3b and 3.4c, an optimum superplasticizer dosage exists to yield strong flocs and improve thixotropy. If V_{\min} is too deep, coagulation will occur. However, if V_{\min} is null, no flocs will form as the van der Waals forces are not present (too large interparticle distances). Therefore, a large enough superplasticizer dosage is required to yield pumpable and extrudable concrete but also a highly thixotropic material for buildability and shape retention. If the dosage is too large, self-compacting concrete (SCC) is obtained which will have limited shape retention and thixotropy.

3.2.3 Influence of nanoparticles on thixotropy mechanisms

The use of nanoparticles is receiving significant attention in several disciplines as of late due to their increased effectiveness compared to the properties demonstrated by the bulk material. When particles are smaller than 100 nm their behaviour is influenced by atomic, molecular and ionic interactions to a much larger extent than usual (Panneerselvam & Choi, 2014). As mentioned in the introduction, the addition of nanoparticles to concrete increases its mechanical and durability properties significantly. Furthermore, it has an immense influence

on the rheology of concrete, typically characterised by stiffer and stickier concrete even at low dosages (Senff et al., 2009). Nanoparticles are also found to be useful for thixotropy and concrete printing (Panda et al., 2019b; Panda et al., 2019c). The secondary focus of this research is to determine and characterise the influence that nanoparticles have on thixotropy, specifically their benefits for improved 3DPC buildability. The authors theorise that the following aspects enable nanoparticles to increase thixotropic behaviour:

1. Brownian motion & particle size

Nanoparticles are typically characterised as being smaller than 100 nm. Bergstrom & Pugh (1993) show that when particles are smaller than 100 nm, surface forces such as van der Waals forces, polyelectrolyte forces and Brownian motion dominate gravitational and inertial forces. Stronger flocs can thus be formed at higher re-flocculation rates, due to the absence of gravitational and inertial forces. In rheological terms, a higher static yield shear stress is obtained due to the stronger flocs. Furthermore, after cessation of agitation, or the breakdown of the microstructure, higher re-flocculation rates (R_{thix} , see Section 3.2.4) are obtained due to increased Brownian motion.

This can also be proven mathematically (Billberg, 2006). Kinetic theory states that all particles in suspension have the same average translational energy, regardless of particle size, if no external forces act upon the particles. The magnitude of this average translational energy is equal to $\frac{1}{2} \cdot kT$, which then yields $\frac{1}{2} \cdot mv^2 = \frac{1}{2} \cdot kT$, where (m) is the particle mass, (v) the particle velocity, (k) the Boltzmann constant and (T) the absolute temperature. It is thus evident that, at constant temperature, particle velocity is inversely proportional to particle mass. Thus, from a mass (size) perspective, translational velocity of a smaller particle is higher than that of a bigger one. In other words, smaller particles move significantly faster during Brownian motion that consequently move to favourable positions (flocs) at a higher rate. This results in higher re-flocculation rates when the microstructure rebuilds after removal of applied energy, such as pumping.

2. Specific surface area

The specific surface area (SSA) refers to the surface area to volume ratio of a particle. A larger SSA yields a larger boundary layer and vice versa. A boundary layer is an interface where surface characteristics such as adsorption of materials and polyelectrolyte effects develop. Thus, a larger boundary layer implies stronger physical properties and hence improves particle-particle interaction (Billberg, 2006). A cube with 1 μm side lengths has a boundary

layer volume to total cube volume of 0.6 %, whereas a cube with 10 nm side lengths has a volume ratio of 60 %, assuming a boundary layer thickness of one nanometer. Therefore, nanoparticles are significantly more reactive than larger cement particles, which is theorised to also increase floc strength and formation rate.

3.2.4 Rapid re-flocculation rate (R_{thix}) vs. structuration rate (A_{thix})

The rapid re-flocculation rate (R_{thix}) characterises the reversible particle flocculation process, which is a physical reaction that largely occurs in the first few hundred seconds after removal of applied energy. In rheological terms, it depicts the rebuilding of the shear stress after agitation ceases i.e. the increase in shear stress from the dynamic yield stress to the static yield stress (refer to Figure 3.1). Should a material only comprise of a static yield stress, and no clear dynamic yield stress, then R_{thix} is of no use. R_{thix} is thus only applicable to thixotropic materials where the re-flocculation process is eminent. This process is however of cardinal importance to 3DPC as it aids in shape retention of the material after deposition, whereby the material is sheared after pumping and re-flocculates to its static yield stress. It can thus be seen as a building block for buildability performance in 3DPC. Although some research has been conducted on the characterisation of the re-flocculation process (Kawashima et al., 2013), R_{thix} is newly defined in this research for the characterisation of thixotropic materials required for 3DPC.

It is however important to distinguish the re-flocculation rate (R_{thix}) from the structuration rate (A_{thix}) which is proposed by Roussel (2006) as a thixotropy model. Although both focus on the increase in static yield stress of a thixotropic material over time, it is the time scale which differs, and so too the mechanism that each attempts to characterise rheologically. The structuration rate is determined over a longer time period, typically in the thousands of seconds. In essence, A_{thix} mainly characterises the increase in static yield stress due to chemical reactions, such as the early formation of hydration products (ettringite needles), which decreases the plasticity of fresh concrete. Due to this larger time scale, more factors can potentially influence the structuration rate, such as the hydration process, accelerators, environmental conditions and so forth. The re-flocculation rate is in contrast largely dependent on immediate effects, particularly physical interatomic and intermolecular forces that rebuild the microstructure, and is therefore theoretically a better indicator of thixotropic behaviour.

Nanoparticles are used in this research to increase R_{thix} and the static yield shear stress of a material in order to improve material strength immediately after extrusion for 3DPC and

consequently foster higher vertical printing speeds (refer to Figure 3.13, Section 3.6). Stability-induced failure such as buckling is also possible in 3DPC and is mainly influenced by a material's stiffness (Wolfs et al., 2018). However, this study only focuses on nanoparticles' influence on material strength and thixotropy behaviour. The influence of the nanoparticle addition is characterised by the model developed in the following section that specifically appertains to 3DPC.

3.3 Model development

A thixotropy model that depicts the static yield shear stress evolution of a material was proposed by Roussel (2006). This model is based on the structuration rate, A_{thix} , and follows linear material strength evolution. Perrot et al. (2016) expanded on Roussel's model by proposing an exponential yield stress evolution. This exponential model starts to deviate from the linear model at roughly 40 minutes resting time period for concrete. However, in this research, a bi-linear thixotropy model is proposed that builds on Roussel's model. The authors of this research acknowledge that a cementitious material follows exponential yield stress evolution due to the onset of hydration, but choose to employ a linear structuration rate as the main focus is on the re-flocculation, R_{thix} , process.

This process is described in Section 3.2.2 whereby, if optimum V_{min} exists for steric repulsion or V_{max} for electrostatic repulsion, particles flocculate to form a strong microstructure due to van der Waals attraction forces. However, when a microstructure is broken and then the agitation removed, Brownian motion will result in re-flocculation of the particles that will rebuild the microstructure. This is a physical process whereby the interparticle forces reach equilibrium in a few hundred seconds. Note that this time period is material-dependent and the actual re-flocculation time to restore equilibrium is determined with Equation 3.2. Thus, a distinct difference exists between the re-flocculation rate and the structuration rate, which is largely based on early age hydration products that lead to loss of plasticity.

Research by Winnefeld (2002) & Holzer et al. (2003) found that the storage (G') and loss modulus (G'') over time demonstrate a linear-exponential behaviour. The first short linear phase demonstrates a much larger gradient than the following linear-exponential phase (which is similar to the model Perrot et al. (2016) proposed for structuration). Furthermore, that initial linear phase lasts for a few hundred seconds, which primarily indicates re-flocculation of the microstructure. Thus, the model developed in this section follows on the findings by Winnefeld, but with the characterisation and application focused on 3DPC. This is mainly due

Chapter 3: Thixotropy Model

to pumping of the concrete that breaks the microstructure and consequently, after extrusion, re-flocculates to re-build the microstructure.

The bi-linear thixotropy model is depicted in Figure 3.5 and allows for the determination of a material's static yield shear stress at any time (t) after cessation of agitation or time after deposition for 3DPC. Initially, due to the blade-and-auger mechanism of a pump, a material's microstructure will be broken down and the dynamic shear stress (τ_D) of the material is maintained (refer to Figure 3.1). Based on certain flow parameters, e.g. if a lubrication layer is present, the material can be exposed to either high pressures which could further reduce the dynamic yield shear stress, or lower pressures whereby re-flocculation may slowly occur while still in the pump hose. However, this model assumes re-flocculation occurs when agitation stops which for 3DPC is when the material exits the nozzle and no externally applied forces act on the material. This re-flocculation process occurs over a few hundred seconds, typically until the original microstructure before agitation is restored, which is indicated by the magnitude of the static yield shear stress (refer to Figure 3.1). The rate at which this process occurs is denoted as R_{thix} and indicates the degree of thixotropy of the material. Structuration commences when the static yield shear stress (τ_S) is restored after re-flocculation.

Static Yield Stress

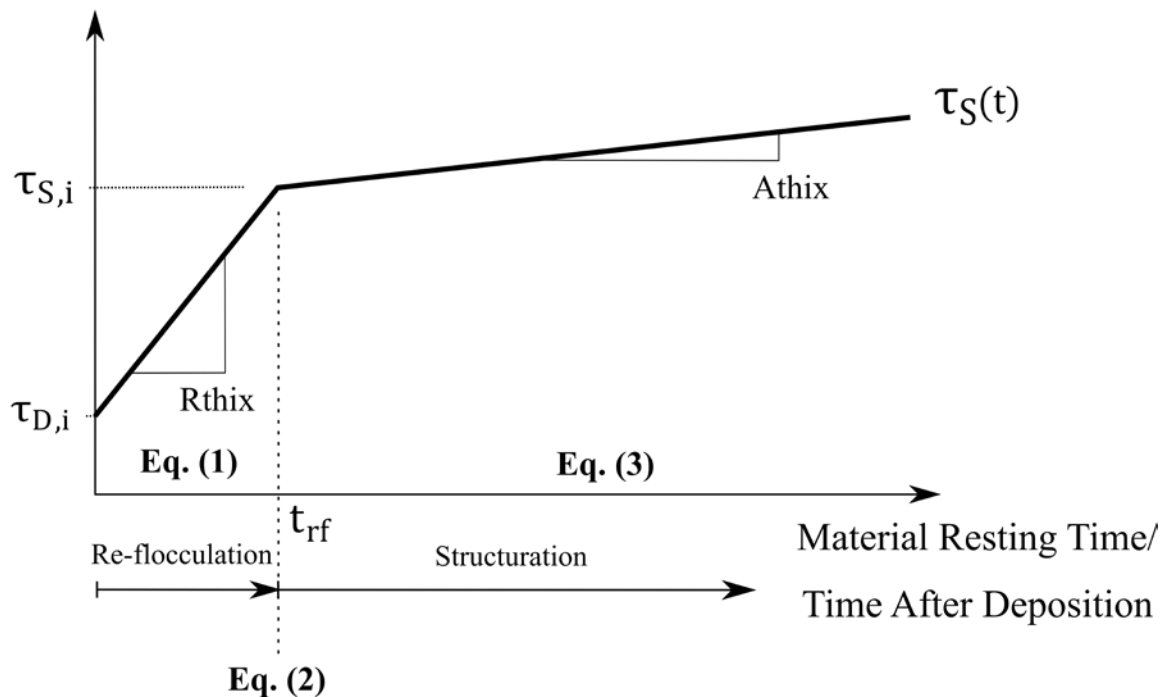


Figure 3.5: Static yield stress evolution as a function of time illustrated by both the re-flocculation and structuration thixotropy mechanisms. Equation numbers presented for their respective relevant sections.

The following linear mathematical model is proposed to depict the static yield shear stress rebuilding characteristic of thixotropic materials after cessation of agitation i.e. the relationship between the dynamic and static yield stress over the short term time scale:

$$\tau_S(t) = \tau_{D,i} + R_{thix} \cdot t \quad (3.1)$$

With the parameters as follows:

$\tau_S(t)$	-	Static or apparent yield stress of the material at time t after agitation (Pa)
$\tau_{D,i}$	-	Initial dynamic yield stress of the material, measured from first rheological test (Pa)
R_{thix}	-	Short term re-flocculation rate (Pa/s)
t	-	Time since cessation of agitation (s), precondition: [$t \leq t_{rf}$]

It is important to note that this model is not only valid for thixotropic materials. In the case of non-thixotropic materials, the value of R_{thix} will approach zero and consequently the static yield stress will equal the dynamic yield stress, which is mostly the case for conventional concrete with large aggregates. This can be described similarly to elastic-perfectly plastic material behaviour whereby one point, the yielding value, depicts the change in slope of the graph. Furthermore, Equation 3.1 is only valid until the initial static shear stress is reached, which can be obtained from the first rheological test. The short term time period over which re-flocculation occurs, and thus where Equation 3.1 is valid, is characterised as follows:

$$t_{rf} = \frac{\tau_{S,i} - \tau_{D,i}}{R_{thix}} \quad (3.2)$$

With the parameters as follows:

t_{rf}	-	Time period over which re-flocculation occurs and dominates shear stress increase (s)
$\tau_{S,i}$	-	Initial static yield stress of the material, measured from first rheological test (Pa)

Chapter 3: Thixotropy Model

In the case where the time input becomes larger than the re-flocculation period ($t > t_{rf}$) for Equation 3.1, the static shear stress model proposed by Roussel becomes applicable for static shear stress determination at time t , as there is a change in the thixotropy mechanism:

$$\tau_S(t) = \tau_{S,i} + A_{thix} \cdot (t - t_{rf}) \quad (3.3)$$

With the parameters as follows:

$\tau_S(t)$	-	Static or apparent yield stress of the material at time t after agitation (Pa)
A_{thix}	-	Structuration rate (Pa/s)
t	-	Time since cessation of agitation (s)

The static yield shear stress of a material can thus be obtained at any time t after cessation of agitation with the Equations proposed in this section. It is initially required to first solve Equation 3.2 to obtain the re-flocculation time period that distinguishes the dominating thixotropic mechanisms from each other. Thereafter, the static yield shear stress of a material can be determined at any time after deposition during 3DPC.

3.4 Experimental procedure

3.4.1 Materials

The standard 3DPC mix at SU, which is a high-performance concrete (HPC) mix with a w/c ratio of 0.45, is used for this research. This mix will act as the reference material and is presented in Table 3.1. The CEM II 52.5N composite cement consists of between 6 and 20 % limestone extender and conforms to SANS 50197-1. Ulula class S fly ash, together with FerroAtlantica silica fume are used as extenders to obtain the required workability properties for 3DPC. The fine aggregate consists of a continuously graded coarse sand that is locally mined with maximum particle size of 4.75 mm. Water used for this mix is common potable tap water. A new generation superplasticizer, Chryso Fluid Premia 310, is utilised which is based on a modified polycarboxylate polymer. Lastly, a small quantity of viscosity modifying agent (VMA), Chryso Quad 20, is added to the mix. Nano-silica (SiO_2) particles, purchased from Nanostructured & Amorphous Materials in the USA (Nanostructured & Amorphous Materials, n.d.), are used for this research with properties depicted in Table 3.2. A scanning electron microscopy (SEM) image of the nanoparticles is presented in Figure 3.6. It is evident that the particles are in a flocculated state and needs appropriate dispersion. Only the superplasticizer

is used for this end in order to negate the influence that other dispersing processes may have on this research.

Table 3.1: Standard HPC mix constituent quantities used for this research, as well as nanoparticle content.

Constituent	kg
Cement	579
Fly Ash	165
Silica Fume	83
Fine aggregate	1167
Water	261
Superplasticizer	1.48% by mass of binder
VMA	0.13% by mass of binder
Nanoparticles	1, 2, 3% by mass of cement

Table 3.2: Nano-silica properties as obtained from Nanostructured & Amorphous Materials (Nanostructured & Amorphous Materials, n.d.).

Purity	99.5%
Average Particle Size (APS)	15-20 nm
Specific Surface Area (SSA)	~ 640 m ² /g
Colour	White
Morphology	Spherical, porous
Bulk density	0.1 g/cm ³
True density	2.2 – 2.6 g/cm ³

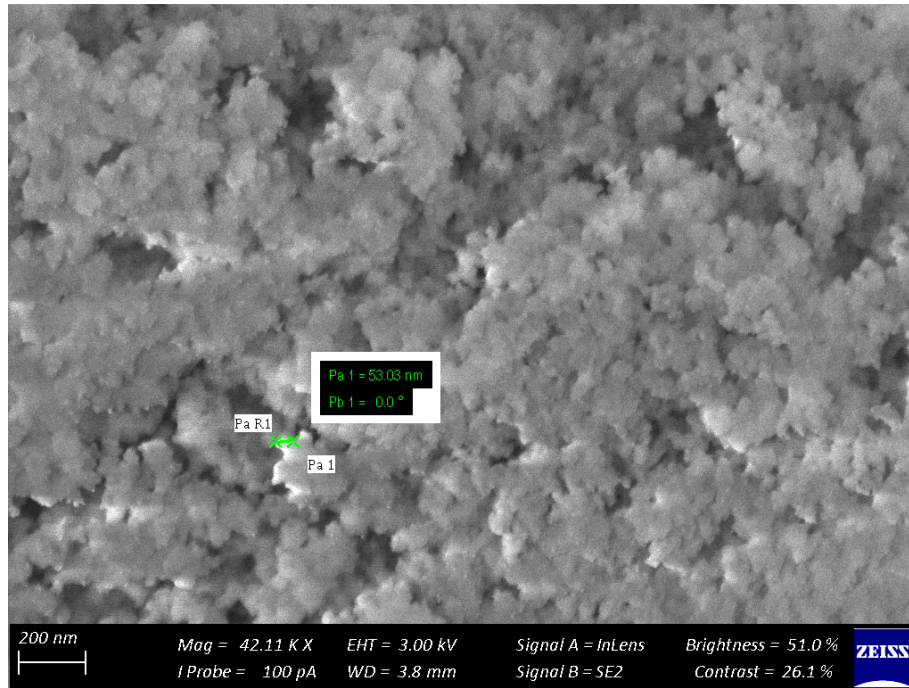


Figure 3.6: SEM image of the SiO₂ nanoparticles in a flocculated state.

3.4.2 Mixing procedure

A fresh 20 litre concrete sample is prepared for every rheological test that needs to be performed. Initially, every constituent is accurately weighed off and temporarily stored in containers. Thereafter, the dry constituents are placed in the 50 litre concrete pan mixer with two blades in the following order: fine aggregate, extenders and cement. This dry batch is then mechanically mixed for at least three minutes until it is visually observed that the constituents form a homogenous dry mixture. Next the water is poured into the pan mixer at a low rate while the mechanical mixing continues. After all of the water is added, the mixture is further mechanically mixed for roughly one minute. Lastly, the superplasticizer is added to the concrete also at a low rate for even distribution of the chemical throughout the concrete mixture. The concrete batch is then further mixed for two minutes. In the case of the nano-silica concrete, the nanoparticles are added after the fine aggregate has been added to the pan mixer. Thereafter, the mixing procedure continues as for the standard concrete mixture without nanoparticles. The concrete is subsequently placed into a specific container for the immediate commencement of the rheological testing and characterisation.

3.4.3 Rheology testing procedure & data processing

A critical component of this research is the rheological characterisation of the materials. No formal guidelines currently exist for such testing and consequently an outcome-orientated approach is followed. The goal is to realise the model depicted in Section 3.3 with an acceptable error, based on sound reasoning. All rheological testing is conducted using the Germann Instruments ICAR rheometer (Germann Instruments, n.d.).

The critical process to imitate with the rheometer is the shearing of the material as it occurs during 3DPC. This includes shearing of the material before and after extrusion. The shearing before extrusion mainly depends on the pump and hose configuration. The Rockcrete TSL pump illustrated in Figure 3.7, which is a rotor stator pump, is used in conjunction with a 3-meter hose for this research. Initially, the concrete is placed into the hopper that is then forced into the rotor stator via a large screw mechanism. The concrete is then pumped by the action of the rotor inside of the stator due to pressure. More pressure can be generated as the concrete travels through the hose depending on factors such as the presence of a lubrication layer and the height or distance that the concrete needs to be pumped. Furthermore, print speed and hence pump speed will influence the shearing of the material tremendously. It is therefore important to correlate the rheometer vane rotational speed with the pump speed, or more sensibly, the shear rate ($\dot{\gamma}$) that each induces due to the geometry. This is, of course, not a simple task and requires much research for accurate prediction.

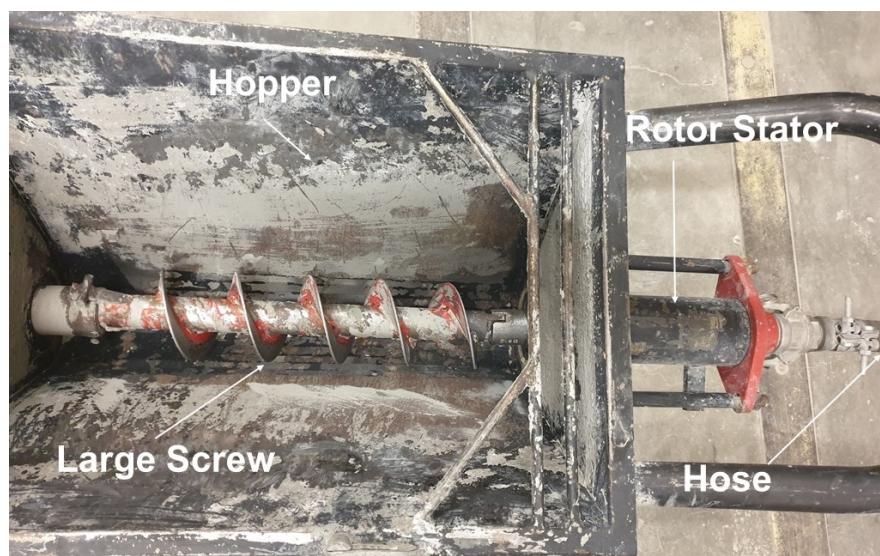


Figure 3.7: Rockcrete TSL rotor stator pump indicating the hopper, hose and large screw.

Chapter 3: Thixotropy Model

Re-flocculation will commence as soon as the material is extruded i.e. exits the nozzle, only if the material's microstructure is broken due to the pumping. If not, structuration will commence. However, the material is also sheared after extrusion due to the additive nature of 3DPC. Layers are deposited on top of each other, yielding a vertical building rate that depends on several print parameters. A shear stress is induced in the bottom critical layer of which the associated rate influences the material's strength. This vertical building rate is synonymous to the loading rate used for hardened concrete mechanical tests. Nerella et al. (2019) suggests using the lowest possible shear rate in the rheometer that yields flow-onset i.e. break-down of the microstructure from static to dynamic yield stress. Low shear rates are appropriate for SCC, but 3D printable materials are typically semi-stiff and require larger shear rates for flow-onset to occur. However, too large shear rates could over estimate a material's strength. Furthermore, large shear strain (γ) values (product of shear rate and shear duration) could result in localised segregation of concrete constituents inside the shearing area of the rheometer. Therefore, the shear rate must be sufficiently large to yield flow-onset, but also small enough to prevent any adverse effects such as localised segregation.

The first step towards rheological characterisation for this research is thus to replicate the pump-induced shearing via a rheometer. In order to achieve this, the vane speed of the rheometer is matched with the screw speed of the pump, at the typical SU laboratory 3D printing speed of 60 mm/s. This equates to roughly 0.2 revolutions per second which, based on the rheometer's geometry, yields a shear rate of 1 s^{-1} . It is acknowledged that the shear rates may not be identical based on just the rotational speeds (especially by excluding the different geometries and rotational actions), however, it is used as an approximation from reasoning. Literature states that pumping of concrete may induce shear rates between 20 and 40 s^{-1} (Roussel, 2006). Significantly smaller shear rates are however anticipated for 3DPC due to the slow printing speeds. Minimal shearing is induced if plug flow occurs due to the formation of a lubrication layer. In contrast, considerable shearing can occur in the absence of a lubrication layer. The formation of a lubrication layer is however highly dependent on the material used. Measuring the degree of aforementioned hose-induced shear is complicated and, due to the lack of such measurements, is included in the shear duration of the rheometer test. Therefore, the shear duration of the rheometer is correlated with the time that it takes for concrete to be pumped from the hopper to the printer nozzle. Based on the aforementioned printing speed and hose length, a duration of roughly 60 seconds is obtained. Thus, a constant shear rate (CSR) of

1 s^{-1} is applied to the concrete sample for 60 seconds to approximately replicate the pump-induced shearing.

This is executed via a stress growth rheological test that determines the static and dynamic yield shear stress, as depicted in Figure 3.1. The material that is extruded from the nozzle has a shear strength equal to the dynamic yield shear stress ($\tau_{D,i}$) indicated in Figure 3.5 due to the shearing action of the pumping process. After deposition of the material the microstructure will begin to rebuild due to the re-flocculation of particles. This process is assumed to continue until the original concrete microstructure before pumping is restored, which is depicted by the static yield shear stress ($\tau_{S,i}$) in Figure 3.5. Note that both these values are obtained from the first rheological stress growth test. The re-flocculation rate (R_{thix}) is determined by conducting multiple stress growth rheological tests in small concrete resting time intervals. The static yield shear stress, which indicates the strength of the concrete microstructure, of each stress growth test is then plotted against the corresponding resting time interval. A linear regression model is fitted to the data and the derivative calculated to yield R_{thix} . With these values known ($\tau_{D,i}$, $\tau_{S,i}$ and R_{thix}), Equations 3.1 and 3.2 can be solved to obtain the first part of the static yield shear stress evolution curve depicted in Figure 3.5. It is important to use the single-batch approach for the determination of R_{thix} as this is a reversible and physical process.

A_{thix} is determined in exactly the same manner as R_{thix} but with larger concrete resting time intervals. Subsequently, Equation 3.3 can be solved and the static yield shear stress evolution curve completed. Ideally, the multi-batch approach must be utilised for the determination of A_{thix} since it mainly is a chemical process. However, only a single-batch approach is used in this research as a limited quantity of nanoparticles is available for experimental testing. One advantage of the single-batch procedure over the multi-batch procedure is that inconsistency with regard to material rheology is avoided, as only one concrete batch is used. However, the single-batch approach may yield inaccurate results for structuration. This is acknowledged and accepted by the authors as the main focus of this research is placed on re-flocculation and its influence on 3DPC. Furthermore, each stress growth test is conducted at a shear rate of 1 s^{-1} for 60 seconds. This is significantly larger than proposed by Nerella et al. (2019) but ensures that flow-onset will always occur. Insufficient amounts of nanoparticles are available to perform a sensitivity analysis that will yield the lowest shear rate for flow-onset to occur at each resting time interval. However, the constant shear rate and duration is deemed adequate for concept demonstration and material comparison. The rheological testing protocol is summarised in Table 3.3. Two different sensitivity analyses

Chapter 3: Thixotropy Model

are performed as part of the experimental program for this research: one that characterises the rheology variation due to superplasticizer dosage and VMA alterations, and another by adding nano-silica in 1 % increments at a constant superplasticizer dosage. The rheological testing protocol in Table 3.3 is followed for each material and the results and discussions presented in the next section.

Table 3.3: Rheological testing protocol for determination of parameters required to plot static yield shear stress evolution curve.

Concrete Age After Mixing (min:s)	Test Number	Resting Time Interval	Shear Rate (s^{-1})	Shear Duration (s)	Action	Result
00:00-01:00	-	-	-	-	Transport concrete to rheometer	-
01:00-02:00	1	0 s (Initial)	1	60	Stress growth test	Obtain initial static and dynamic yield shear stress for shear stress evolution curve (Figure 3.5)
02:10-03:10	2	10 s	1	60	Stress growth test	Obtain static yield stress, plot against time interval, to determine R_{thix}
03:30-04:30	3	20 s	1	60	Stress growth test	Obtain static yield stress, plot against time interval, to determine R_{thix}
05:00-06:00	4	30 s	1	60	Stress growth test	Obtain static yield stress, plot against time interval, to determine R_{thix}
06:40-07:40	5	40 s	1	60	Stress growth test	Obtain static yield stress, plot against time interval, to determine R_{thix}
08:30-09:30	6	50 s	1	60	Stress growth test	Obtain static yield stress, plot against time interval, to determine R_{thix}
10:30-11:30	7	60 s	1	60	Stress growth test	Obtain static yield stress, plot against time interval, to determine R_{thix}
13:00-14:00	8	90 s	1	60	Stress growth test	Obtain static yield stress, plot against time interval, to determine R_{thix}
16:00-17:00	9	120 s	1	60	Stress growth test	Obtain static yield stress, plot against time interval, to determine R_{thix}
37:00-38:00	10	20 min	1	60	Stress growth test	Obtain static yield stress, plot against time interval, to determine A_{thix}
78:00-79:00	11	40 min	1	60	Stress growth test	Obtain static yield stress, plot against time interval, to determine A_{thix}
139:00-140:00	12	60 min	1	60	Stress growth test	Obtain static yield stress, plot against time interval, to determine A_{thix}

3.5 Results & discussions

3.5.1 Phenomenological characterisation

Seven concrete types in total are tested: standard mix (reference), 15 % increase in superplasticizer (SP), 15 % decrease in SP, 0 % VMA, 1 % nano-silica (nS) addition, 2 % nS addition and 3 % nS addition. From a phenomenological point of view the mix with increased SP dosage exhibited significant workability, nearing the workability of self-compacting concrete (SCC), and will definitely achieve the worst buildability in 3DPC terms. In contrast, the mix with decreased SP dosage had the worst workability, stiff and cloddy, and will not be suitable for pumping purposes. Hence, that mix is not suitable for 3DPC. The standard and 0 % VMA mixes demonstrated similar workability properties, however the standard mix seemed slightly more cohesive and sticky. All three of the nS mixes demonstrated workability suitable for 3DPC. However, for each increase in nS content, a significant increase in concrete stiffness is observed. Hence, at 3 % nS addition, excellent buildability can be achieved at the expense of surface finish of the product, as well as increased pumping pressure. 1 % nS addition demonstrated the best fresh properties for 3DPC, based on visual observations. Lastly, it is observed that an increase in nS content increases the rate at which the concrete attains stiffness. Therefore, it is believed that an increase in nS content will lower the setting time of concrete which has already been documented in literature (Senff et al., 2009).

3.5.2 Re-flocculation rate (R_{thix})

The results obtained for the re-flocculation characterisation are shown in Figure 3.8 and summarised in Table 3.4. Linking with the phenomenological characterisation section, the +15 % SP mix has the lowest shear stresses and the -15 % SP the highest, neglecting the nS mixes. Surprisingly, the mix without added VMA presents higher stresses than the standard mix with VMA. The re-flocculation rate of the -15 % SP mix is the lowest at 1.36 Pa/s, whereas the 0 % VMA mix achieved the second largest rate of 7.24 Pa/s.

It is clear from Table 3.4 that an optimum SP dosage exists in order to obtain highly thixotropic behaviour. The -15 % SP mix, which as mentioned is a stiff and unworkable concrete, has little re-flocculation potential. It can be reasoned that too little SP is used that results in a deep V_{min} (refer to Figure 3.4c, Section 3.2.2). Consequently, interparticle force equilibrium occurs at a smaller interparticle distance. Strong van der Waals attraction forces then yield coagulation and not the desired flocculation. The standard mix in contrast has a lower initial shear stress and higher re-flocculation rate. Since more SP is used in the standard mix,

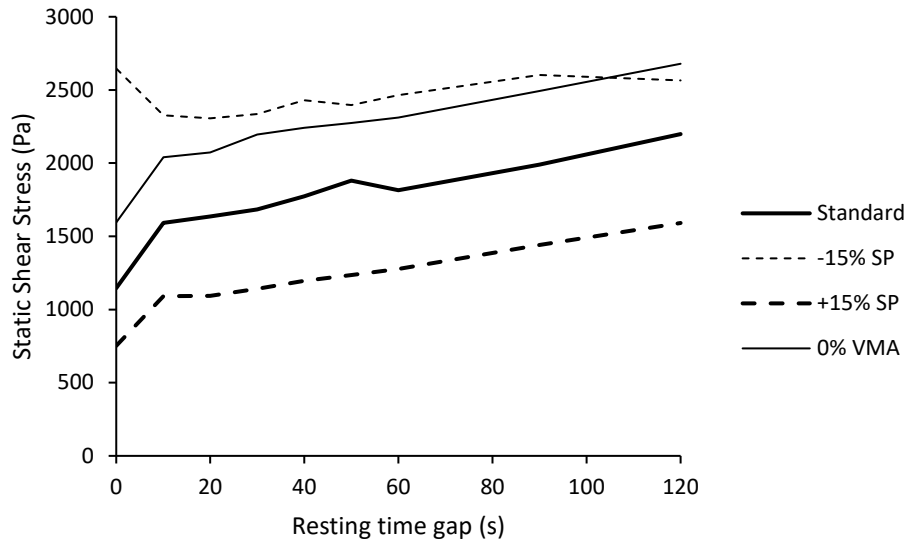
V_{\min} becomes shallower and moves further away from the particle surface. At increased distances, the van der Waals forces become weaker (see Figure 3.2) that results in flocculation rather than coagulation. Consequently, it has a much larger re-flocculation rate of 6.88 Pa/s. In the case of the +15 % SP mix, the initial shear stress and re-flocculation rate of 5.75 Pa/s is lower than that of the standard mix. This indicates that the V_{\min} position is moved too far away from the particle surface. Van der Waals forces deteriorate and flocculation strength decreases, resulting in a weaker microstructure. Consequently, lower shear stresses are obtained as it is easier to break the microstructure. The optimum SP dosage for highly thixotropic behaviour is therefore exceeded with the +15 % SP mix.

As also visually observed, the shear stress of the concrete increases with every percentage increase of nS addition. In the case of the 3 % nS mix, a slightly higher initial shear stress was obtained than the -15 % SP mix, however with slightly better workability. Conversely, an increase in nS dosage resulted in less re-flocculation. This can be ascribed to insufficient superplasticizer to fully disperse the particles, as the total surface area increased dramatically due to the high SSA of the nS ($\sim 640 \text{ m}^2/\text{g}$). Although the -15 % SP and 3 % nS mixes have similar shear stresses (2646 Pa compared to 2803 Pa respectively), the 3 % nS mix has a considerably higher R_{thix} (4.2 Pa/s compared to 1.36 Pa/s respectively). This can be ascribed to the increased Brownian motion induced by the small nanoparticles as described in Section 3.2.3, consequently resulting in faster re-flocculation of the microstructure. With 1 % nS addition, a re-flocculation rate of 8 Pa/s is achieved which equates to a 16.3 % increase over that of the standard mix. At 2 % nS addition, the re-flocculation rate is less than the standard mix. Evidently, 1 % nS addition is the optimum for re-flocculation purposes in this research and confirms that nanoparticles can enhance the re-flocculation mechanism, as theorised in Section 3.2.3. It is this combination of increased shear stress and R_{thix} that holds potential for higher vertical building speeds for 3DPC, as is practically demonstrated in Section 3.6. It should be noted that the optimum nS dosage may vary depending on various constituent properties and that 1 % is not going to yield optimum thixotropic behaviour for every concrete mix.

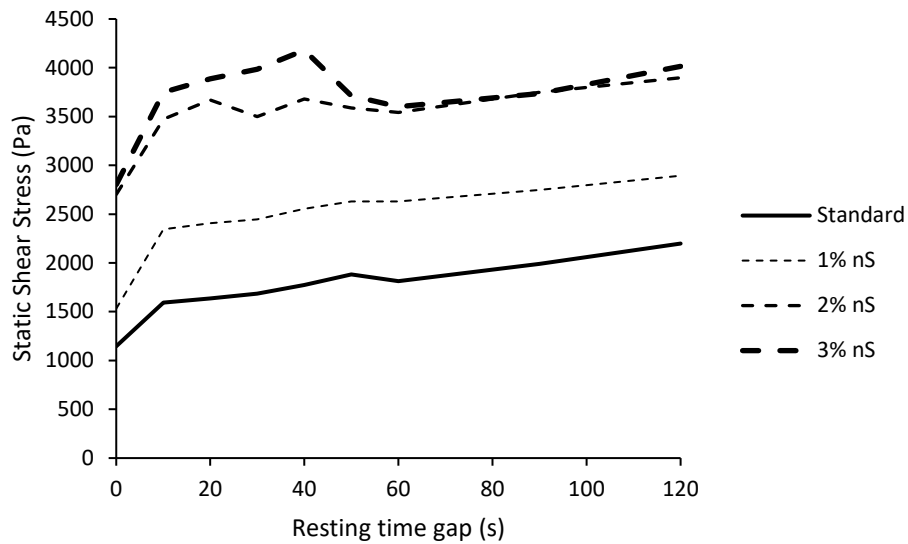
Lastly, it should also be noted that the shear stresses at the 0 second resting time gap in Figure 3.8 (and referred to as initial shear in Table 3.4) is the dynamic yield shear stress of the initial rheological test. It is reasoned that after the initial stress growth test, thus the 0 second resting time gap stress growth test, the material will not have had time to re-flocculate and consequently the static shear stress would be equal to the initial stress growth test's dynamic

Chapter 3: Thixotropy Model

yield shear stress. The ICAR rheometer has a 5-second delay that makes it impossible to test the 0 second resting time gap. Subsequent resting time gap shear stresses are static shear stresses obtained from the respective stress growth tests.



(a)



(b)

Figure 3.8: Short term re-flocculation graphs depicting static yield shear stress vs. resting time gap of: (a) variation in chemical admixtures; (b) variation in nanoparticle content.

Table 3.4: Initial shear stress values and the re-flocculation rate for each concrete mix.

Mix	Initial Shear (Pa)	R_{thix} (Pa/s)
Standard	1146	6.88
-15% SP	2646	1.36
+15% SP	752	5.75
0% VMA	1595	7.24
1% nS	1532	8
2% nS	2702	6.11
3% nS	2803	4.2

3.5.3 Structuration rate (A_{thix})

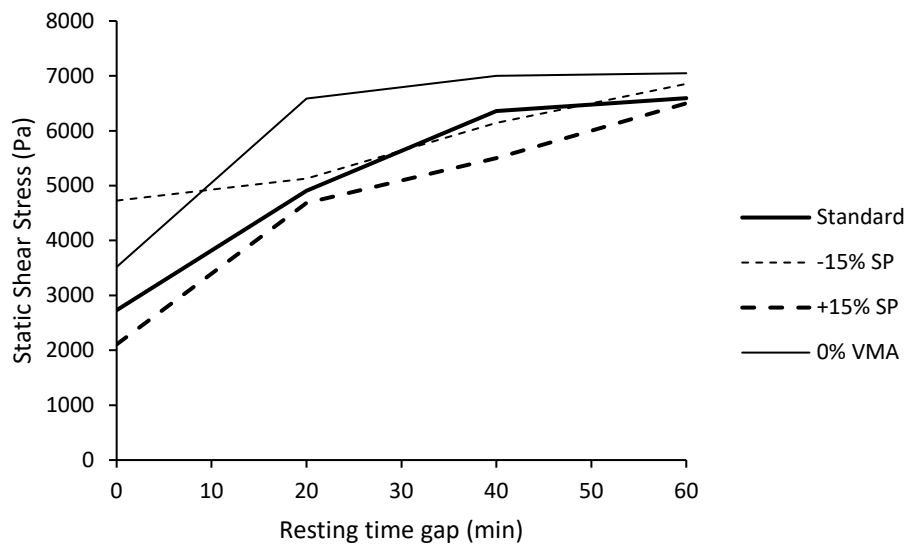
The results obtained for the structuration characterisation are depicted in Figure 3.9 and summarised in Table 3.5. Linking with the phenomenological characterisation section again, the +15 % SP mix has the lowest initial static shear stress and the -15 % SP the highest, neglecting the nS mixes. Surprisingly, the mix without added VMA presents higher stresses than the standard mix with VMA. The structuration rate of the -15 % SP mix is the second lowest at 0.62 Pa/s, whereas the +15 % SP obtained the largest rate of 1.17 Pa/s. It is visually observed that a strong correlation exists between the workability of the mix and the structuration rate. The better the workability of the concrete mix (easier to flow) the higher the structuration rate and vice versa. It is evident that the SP dosage dramatically affects the initial static shear stress of the concrete; however, the difference in the final static shear stress at the 60-minute time interval is considerably less.

The mixes containing nS experienced a vast increase in their initial and final static shear stresses. At just 1 % nS addition, the initial static shear stress increased from 2730 to 3944 Pa. This will have a significant influence on the buildability for 3DPC purposes. At 3 % nS addition, an initial static shear stress of 6483 Pa is obtained, which is too stiff for 3DPC, as mentioned previously. Interestingly, the structuration rate decreases with an increase in nS particle addition. The lowest structuration rate of 0.61 Pa/s is obtained for the 3 % nS mix while the 1 % nS mix presents a rate of 0.91 Pa/s compared to 1.08 Pa/s of the standard mix. Taking into account the considerable, but not excessive, increase in the initial static shear stress of the

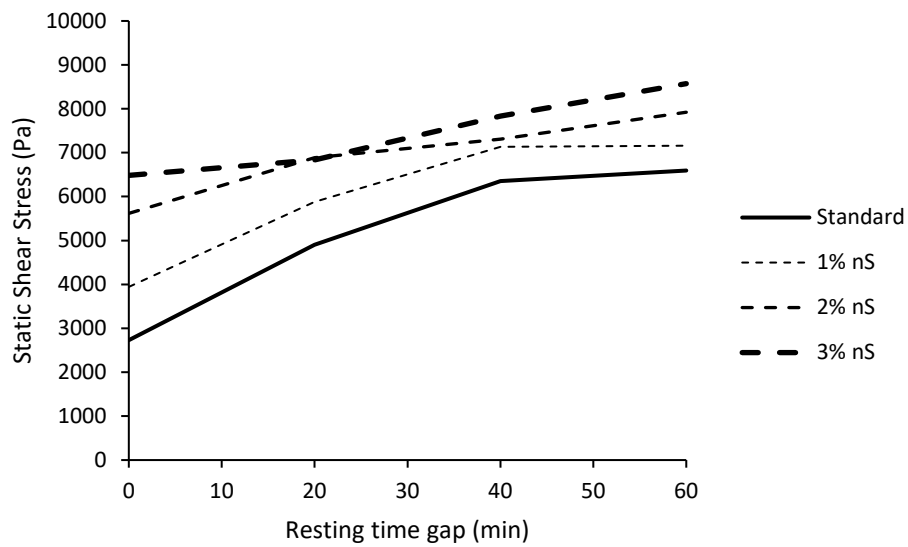
Chapter 3: Thixotropy Model

1 % nS mix, together with a relatively high structuration rate compared to the standard mix, the 1 % nS mix again demonstrates exceptional thixotropy for 3DPC purposes.

It is important to note the significant difference in magnitude between the re-flocculation rate and the structuration rate. Although the structuration rate is much lower, Roussel (2006) proposed that a structuration rate larger than 0.5 Pa/s implies a highly thixotropic material. From that point of view, all the materials in this research can be regarded as highly thixotropic. This is however not the case as it was visually observed that the -15 % SP mix does not demonstrate thixotropic behaviour. Based on A_{thix} , the +15 % SP mix is more thixotropic than the standard mix (1.17 Pa/s to 1.08 Pa/s). R_{thix} suggests otherwise, that the standard mix is more thixotropic than the +15 % SP mix (6.88 Pa/s to 5.75 Pa/s), which also agrees with the visual observations. These results indicate that R_{thix} is a better measure of thixotropic behaviour, i.e. microstructure break-down and re-flocculation potential, than A_{thix} .



(a)



(b)

Figure 3.9: Long term structuration graphs depicting static yield shear stress vs. resting time gap of: (a) variation in chemical admixtures; (b) variation in nanoparticle content.

Table 3.5: Initial and final static shear stress values and the structuration rate for each concrete mix.

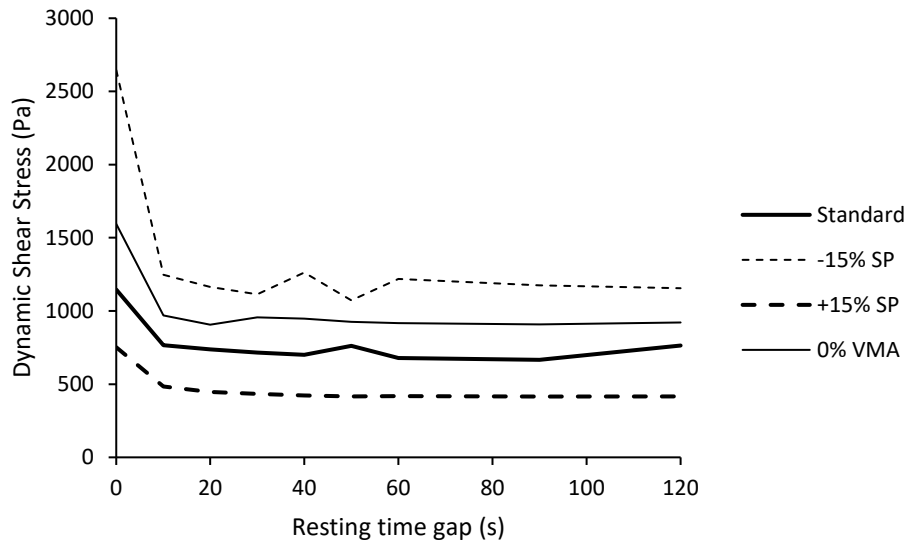
Mix	Initial Static Shear (Pa)	Final Static Shear (Pa)	A_{thix} (Pa/s)
Standard	2730	6594	1.08
-15% SP	4727	6854	0.62
+15% SP	2108	6500	1.17
0% VMA	3518	7048	0.92
1% nS	3944	7159	0.91
2% nS	5618	7922	0.61
3% nS	6483	8573	0.61

3.5.4 Short term dynamic yield stress

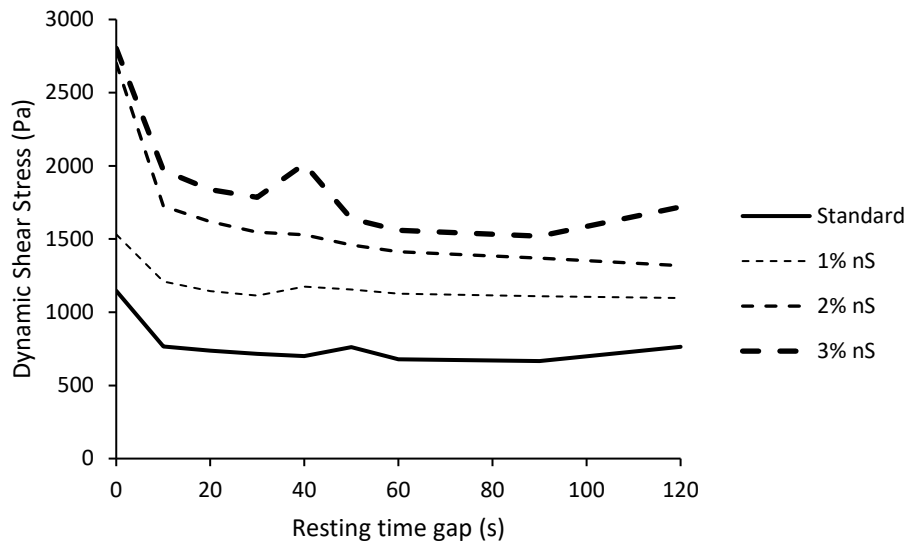
The results obtained for the dynamic yield stress are shown in Figure 3.10 and summarised in Table 3.6. It is firstly observed that the stiffer concrete mixes obtained a significantly higher initial dynamic yield stress (zero time interval) and vice versa. This makes intuitive sense since a stiffer concrete mix would require more pumping pressure. However, in the case of the +15 % SP mix, its dynamic yield stress is too low for 3DPC quality purposes. Although such a small value is ideal for pumping, the concrete does not possess sufficient shape retention after extrusion. Therefore, an optimum dynamic yield stress range exists that is suitable for 3DPC.

The second notable observation is the difference between the initial dynamic shear stress and the rest of the readings. The second time interval (10 seconds) demonstrates a significantly lower dynamic yield stress value than the initial value. At roughly the 30 seconds time interval it seems to reach a state of equilibrium. Thus, a constant yield stress is determined by computing the average dynamic yield shear stress in the range of 30 to 120 seconds. This value is then divided by the initial dynamic shear stress value to obtain a dynamic shear reduction factor (D_r). In general, a lower D_r value correlates with a less thixotropic concrete mix, if compared to R_{thix} values in Table 3.4. As depicted in Table 3.6, the 1 % nS concrete mix achieved the largest D_r value of 0.74 and the stiffest concrete mix the smallest D_r (-15 % SP) 0.44. This behaviour can potentially be ascribed to partial local segregation of the concrete in the vicinity of the vane's path, which results in the formation of an interface. Initially (measurement time 0) the concrete consists of a homogenous microstructure, as it has not yet been sheared. After it has been sheared, the interface separates the less sheared concrete (stronger microstructure) from the highly sheared concrete (weaker microstructure). Subsequent measurements will thus yield lower dynamic yield shear stress values, as the microstructure in the interface region is weak. However, for highly thixotropic materials, the microstructure rebuilds at a faster tempo that consequently yields higher D_r values and vice versa.

No outliers are defined in Figure 3.10 and left out. There is no clear reason for apparently deviating data shear stress value for the 3 % nS response after 40 seconds resting time gap. It can be concluded that the dynamic yield stress of a material is time dependent, and also varies with energy input (e.g. pumping pressure).



(a)



(b)

Figure 3.10: Short term dynamic shear stress vs. resting time gap of: (a) variation in chemical admixtures; (b) variation in nanoparticle content.

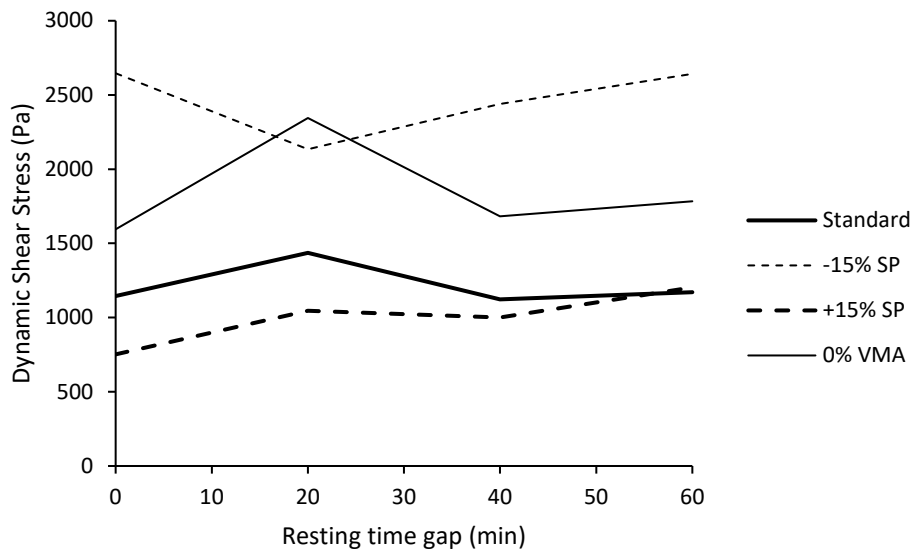
Table 3.6: Summary of the initial and constant dynamic shear stresses together with a D_r factor.

Mix	Initial Dynamic Shear (Pa)	Constant Dynamic Shear (Pa)	D_r
Standard	1146	715	0.62
-15% SP	2646	1166	0.44
+15% SP	752	420	0.56
0% VMA	1595	930	0.58
1% nS	1532	1129	0.74
2% nS	2702	1439	0.53
3% nS	2803	1706	0.61

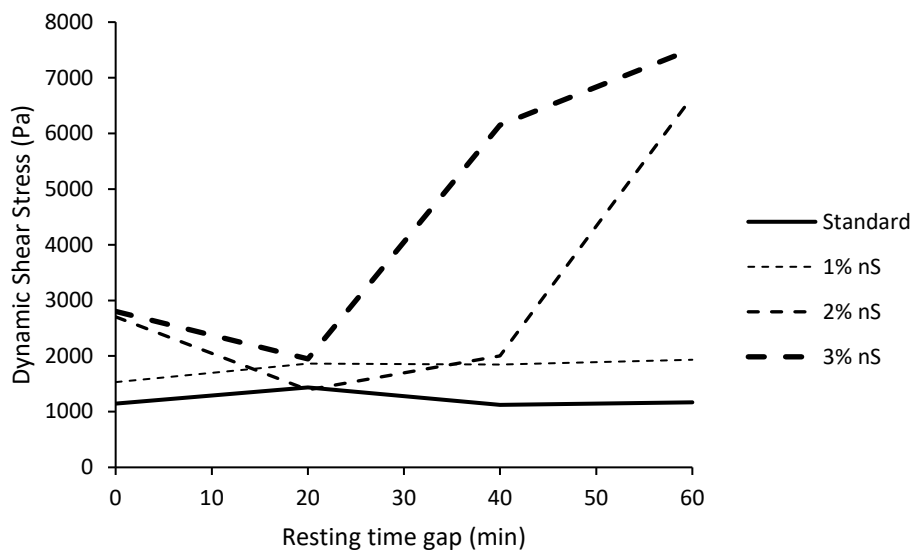
3.5.5 Long term dynamic yield stress

The results obtained for the long term dynamic yield stress are shown in Figure 3.11 and summarised in Table 3.7. A dynamic yield stress increase rate is calculated for each concrete mix. It is found that the -15 % SP mix has the lowest rate at -0.07 Pa/min which can be rounded to 0. In contrast, the +15 % SP mix has a rate of 7.52 Pa/min, though its initial dynamic shear stress is the lowest at 752 Pa. If this rate is too large, pumping difficulties may occur at longer printing times, ultimately influencing the quality of the 3D printed object.

The addition of 1 % nS does not significantly influence the rate. However, with 2 and 3 % nS addition the rate increases to 66 and 79 Pa/min respectively. It was visually observed at the 40-minute time interval that the 3 % nS concrete mix is too stiff and will not be suitable for 3DPC. This can be ascribed to the enhanced chemical reactivity brought by nanoparticle addition that leads to reduced setting time. Since the energy input remains constant and the dynamic yield stress increases over the long term time scale, it is believed the strength of the ettringite needles largely responsible for structuration increases in magnitude. Consequently, stronger and larger flocs form that require larger forces to break down, hence the increase in shear stress for constant flow. This postulation is however open for significant research. It can further be added that at higher nS dosages, the SP quantity to total particle surface area ratio decreases significantly. As a result, less SP concentration is present in the mix and the retarding effect that SP's commonly have on concrete setting time is reduced. Thus, higher dynamic stresses are obtained as the concrete's workability diminishes.



(a)



(b)

Figure 3.11: Long term dynamic shear stress increase vs. resting time gap of: (a) variation in chemical admixtures; (b) variation in nanoparticle content.

Table 3.7: Summary of the initial dynamic shear stress and the rate of long term dynamic stress increase.

Mix	Initial Dynamic Shear (Pa)	Increase (Pa/min)
Standard	1146	0.41
-15% SP	2646	-0.07
+15% SP	752	7.52
0% VMA	1595	3.13
1% nS	1532	6.7
2% nS	2702	65.98
3% nS	2803	78.56

3.6 Validation of nano-silica influence via 3DPC

Two circular hollow columns are 3D printed in this section in order to practically demonstrate and validate the rheological advantages of adding nano-silica to concrete, specifically for 3DPC buildability purposes. Although its favourable effect on the mechanical properties of concrete is well documented, only the fresh state advantages are considered in this research. Based on the results of this research in Section 3.5, especially R_{thix} , A_{thix} and the dynamic shear stress graphs, the 1 % nS concrete mix is chosen together with the standard mix as a point of reference. There is currently no standard benchmark test to assess the buildability of a material. It is however commonly found in literature that a circular hollow column is 3D printed until physical or geometrical nonlinearity occurs that result in failure.

In this test, a circular hollow column with a diameter of 250 mm is printed at a fixed speed of 60 mm/s until failure, in terms of collapse, is observed. A circular shaped nozzle with a diameter of 25 mm is used. Hence, the filament has cross-sectional dimensions of 25 mm wide (minimum) and 10 mm high (layer height). The exact concrete mixing process is followed as for the rheology testing. The result is depicted in Figure 3.12.

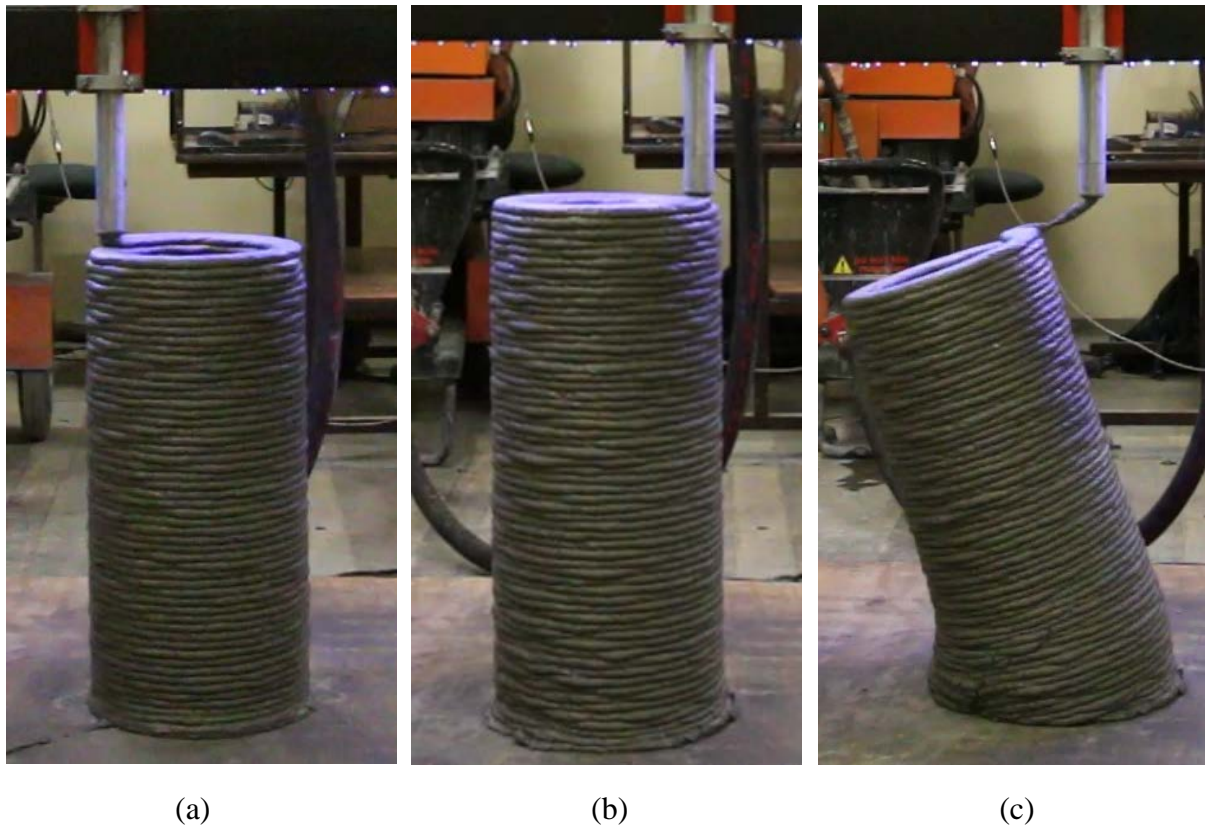


Figure 3.12: 3D printed circular hollow column with: (a) standard concrete mix; (b) 1% nS concrete mix; (c) typical instability that resulted in failure.

A slightly taller column is achieved with the 1 % nS concrete mix than with the standard mix. A total height of 540 mm (54 layers) is achieved with the standard mix within 12 minutes. The 1 % nS mix achieves a height of 590 mm (59 layers) in 13 minutes and 4 seconds. Thus, 5 layers or 50 mm extra height is obtained by adding 1 % of nano-silica to the concrete. The difference does not seem significant. However, calculating the mass of the extra 5 layers, it can be said that 2.11 kg extra mass is added to the column in one minute. From this point of view the difference is significant. Since the bottom filament layer possesses enhanced green strength, higher vertical building rates can be obtained while material failure occurs at the same point in time e.g. 12 minutes as stated earlier. Therefore, higher printing speeds and subsequently reduced construction time is possible with the addition of an optimum nS dosage. The thixotropy mechanism largely responsible for this improvement is the re-flocculation rate after deposition (R_{thix}) due to the short printing duration (see Figure 3.13 for context). The larger initial static yield shear stress of the nS mix also contributed to the result. No troubles were experienced with pumping of the concrete.

Chapter 3: Thixotropy Model

This result correlates with the static yield shear stress evolution model depicted in Figure 3.13 for both concrete mixes. The results obtained in Section 3.5 are applied to Equations 3.1, 3.2 and 3.3 developed in Section 3.3, and summarised in Table 3.8. The failure time of each concrete print is also indicated on the model. The static yield shear stress of the 1 % nS concrete is continually larger than that of the standard mix. Furthermore, it also possesses a higher re-flocculation rate that extends for a longer time period than the standard mix. Evidently, the re-flocculation thixotropy mechanism largely contributes to the static yield shear stress growth from start of print to the failure time, especially for this particular print that has a short printing duration. Thus, the increased re-flocculation rate and duration of the 1 % nS concrete results in a larger initial static yield shear stress that consequently enables better buildability for 3DPC, even though it possesses a lower structuration rate than the standard mix, as its static shear stress is continually the larger of the two mixes.

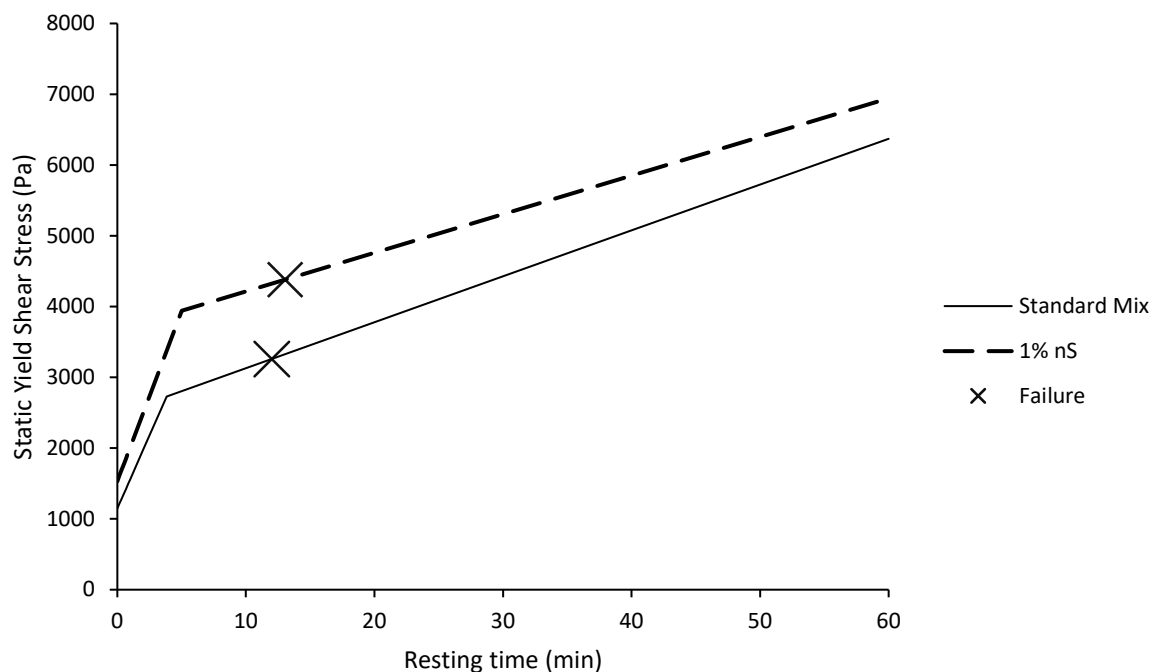


Figure 3.13: Static yield shear stress evolution of the concrete mixes used for 3D printing of the circular hollow columns.

Table 3.8: Summary of the main rheological parameters of the two 3D printed concrete mixes.

Parameter	Ref. mix	1% nS mix	Unit
$\tau_{S,i}$	2730	3944	Pa
$\tau_{D,i}$	1146	1532	Pa
R_{thix}	6.88	8	Pa/s
A_{thix}	1.08	0.91	Pa/s

From this test it is evident that small dosages of nS addition can have a notable effect on the buildability of a material for 3DPC. Proper concrete mix design is however of cardinal importance to obtain good buildability. If too much nS is added, the open time and thixotropic behaviour of the concrete for printing reduces dramatically.

3.7 Conclusions

A new thixotropy model specifically for 3DPC material characterisation is developed in this paper. The model mechanisms are verified via sensitivity analyses performed on varying SP and nS dosages. The theoretical aspects of rheology, in particular thixotropic behaviour and its relevant mechanisms induced mainly by interparticle forces are explained via potential energy. The experimental framework section provides details regarding the concrete mix constituents, mixing process, rheology testing and data processing. From the results, the following can be concluded:

- 1) An optimum dosage of SP exists to obtain highly thixotropic behaviour in the case of HPCs with low w/c ratios. This specific short term time scale thixotropy mechanism, namely re-flocculation, is particularly influenced by SP dosage. This is evident in the re-flocculation rate (R_{thix}) where a higher rate is achieved with optimum SP dosage.
- 2) The addition of nano-silica particles further increases the re-flocculation rate. The highest rate of 8 Pa/s is achieved with 1 % nS addition here. Higher dosages result in significantly lower re-flocculation rates. Hence, over-dosage of nS has a negative influence on thixotropic behaviour.

- 3) An increase in SP dosage results in a decrease in the initial static yield shear stress. In contrast, an increase in nS dosage results in an increase in the initial static yield shear stress, with visibly stiffer concrete.
- 4) More workable and flowable concrete resulted in higher structuration rates (A_{thix}) due to increased SP dosage. The addition of nS particles decreases the structuration rate. The lowest rate of 0.61 Pa/s at 3 % nS dosage is still regarded as highly thixotropic (larger than 0.5 Pa/s). However, it was visually observed that the concrete is not suitable for extrusion due to it being too stiff and unworkable.
- 5) The long term dynamic shear stress increases significantly with an increase in nS dosage. It is visibly notable at 3 % nS addition that the concrete is not suitable for 3D printing at the 40-minute time interval, which is equal to 78 minutes after mixing.
- 6) 1 % nS addition is the optimum dosage to improve thixotropic behaviour of this concrete mix, but may differ for other concrete mix designs.
- 7) The rate of re-building the static yield shear resistance after agitation, is defined in this work as R_{thix} , and shown to be an important buildability parameter for 3D printing. In this study, R_{thix} is a better indicator of appropriate thixotropic behaviour for 3DPC than A_{thix} . For example, the 1 % nS (optimum) mix has a lower A_{thix} value than the standard mix, which implies the 1 % nS mix is less thixotropic. However, the 1 % nS mix has a larger R_{thix} value than the standard mix. The 1 % nS mix performed better in the 3DPC test by achieving 5 layers more than the standard mix, mainly due to the contribution of the increased re-flocculation rate. Additionally, the 1 % nS mix was also visually observed to be the most thixotropic of all mixes.
- 8) The 3D print result together with the static yield shear stress evolution curves of both mixes confirm that optimum nS addition improves a material's buildability for 3DPC.

Acknowledgements

The research is funded by The Concrete Institute (TCI) and the Department of Trade and Industry of South Africa under THRIP Research Grant TP14062772324.

Contribution of authors

This work is part of Jacques Kruger's PhD research, executed under the supervision of Professor Gideon van Zijl and Doctor Stephan Zeranka. Mr Kruger conducted all experimental work, the analysis, interpretation and presentation of data, as well as the writing of the manuscript. Prof. van Zijl and Dr. Zeranka assisted in proofreading of the manuscript and proposed insightful amendments.

3.8 References

- Bergstrom, L. & Pugh, R.J. 1993. *Surface and Colloid Chemistry in Advanced Ceramics Processing*. New York, USA: Routledge.
- Billberg, P. 2006. Form Pressure Generated by Self-Compacting Concrete — Influence of Thixotropy and Structural Behaviour at Rest. Royal Institute of Technology.
- Biricik, H. & Sarier, N. 2014. Comparative study of the characteristics of nano silica-, silica fume- and fly ash-incorporated cement mortars. *Materials Research*. 17(3):570–582.
- Björn, A., de La Monja, P.S., Karlsson, A., Ejlertsson, J. & Svensson, B.H. 2012. *Rheological Characterization, Biogas*. S. Kumar (ed.). InTech.
- Bos, F.P., Ahmed, Z.Y., Jutinov, E.R. & Salet, T.A.M. 2017. Experimental exploration of metal cable as reinforcement in 3D printed concrete. *Materials*. 10(11).
- Cheng, D.C.-H. 1987. Thixotropy. *International Journal of Cosmetic Science*. 9(November 1986):151–191.
- Flatt, R. & Schober, I. 2011. *Superplasticizers and the rheology of concrete*. Woodhead Publishing Limited.
- Germann Instruments. n.d. *ICAR Rheometer*. [Online], Available: <http://germann.org/products-by-application/rheology-of-concrete/icar-rheometer> [2018, July 24].
- Holzer, L., Winnefeld, F., Lothenbach, B. & Zampini, D. 2003. the Early Cement Hydration: a Multi-Method Approach. *11th International Congress on the Chemistry of Cement*. (May):236–248.
-

Chapter 3: Thixotropy Model

- Howard A. Barnes. 1997. Thixotropy - A review. *Journal of Non-Newtonian Fluid Mechanics*. 70(97):1–33.
- Kawashima, S., Chaouche, M., Corr, D.J. & Shah, S.P. 2013. Rate of thixotropic rebuilding of cement pastes modified with highly purified attapulgite clays. *Cement and Concrete Research*. 53:112–118.
- Liu, M., Zhou, Z., Zhang, X., Yang, X. & Cheng, X. 2016. The Effect of Nano-SiO₂ Dispersed Methods on Mechanical Properties of Cement Mortar. In *5th International Conference on Durability of Concrete Structures*. 219–222.
- Malvern Panalytical. 2013. *The Influence of Particle Size, Zeta Potential and Rheology on Suspension Stability*. [Online], Available: <http://www.azom.com/article.aspx?ArticleID=10221>.
- Mechtcherine, V., Grafe, J., Nerella, V.N., Spaniol, E., Hertel, M. & Füssel, U. 2018. 3D-printed steel reinforcement for digital concrete construction – Manufacture, mechanical properties and bond behaviour. *Construction and Building Materials*. 179:125–137.
- Nanostructured & Amorphous Materials. n.d. *About Us*. [Online], Available: www.nanoamor.com/about_us [2018, July 24].
- Nematollahi, B., Vijay, P., Sanjayan, J., Nazari, A., Xia, M., Nerella, V.N. & Mechtcherine, V. 2018. Effect of polypropylene fibre addition on properties of geopolymers made by 3D printing for digital construction. *Materials*. 11(12).
- Nerella, V.N., Beigh, M.A.B., Fataei, S. & Mechtcherine, V. 2019. Strain-based approach for measuring structural build-up of cement pastes in the context of digital construction. *Cement and Concrete Research*. 115(August 2018):530–544.
- Panda, B. & Tan, M.J. 2019. Rheological behavior of high volume fly ash mixtures containing micro silica for digital construction application. *Materials Letters*. 237(December):348–351.
- Panda, B., Unluer, C. & Tan, M.J. 2018. Investigation of the rheology and strength of geopolymer mixtures for extrusion-based 3D printing. *Cement and Concrete Composites*. 94(October):307–314.
- Panda, B., Singh, G.B., Unluer, C. & Tan, M.J. 2019a. Synthesis and characterization of one-part geopolymers for extrusion based 3D concrete printing. *Journal of Cleaner Production*. 220(February):610–619.
-

-
- Panda, B., Ruan, S., Unluer, C. & Tan, M.J. 2019b. Improving the 3D printability of high volume fly ash mixtures via the use of nano attapulgite clay. *Composites Part B*. 165(June 2018):75–83.
- Panda, B., Lim, J.H. & Tan, M.J. 2019c. Mechanical properties and deformation behaviour of early age concrete in the context of digital construction. *Composites Part B*. 165(December 2018):563–571.
- Panneerselvam, S. & Choi, S. 2014. Nanoinformatics: Emerging databases and available tools. *International Journal of Molecular Sciences*. 15(5):7158–7182.
- Paul, S.C., van Zijl, G.P.A.G., Tan, M.J. & Gibson, I. 2017. A Review of 3D Concrete Printing Systems and Materials Properties: Current Status and Future Research Prospects. *Rapid Prototyping Journal*. 24(4):784–798.
- Perrot, A., Rängeard, D. & Pierre, A. 2016. Structural built-up of cement-based materials used for 3D-printing extrusion techniques. *Materials and Structures/Materiaux et Constructions*. 49(4):1213–1220.
- Qian, Y. 2017. Characterization of Structural Rebuilding and Shear Migration in Cementitious Materials in Consideration of Thixotropy.
- Roussel, N. 2006. A thixotropy model for fresh fluid concretes: Theory, validation and applications. *Cement and Concrete Research*. 36(10):1797–1806.
- Roussel, N. 2011. *Understanding the Rheology of Concrete*. N. Roussel (ed.). Woodhead Publishing.
- Said, A., Ayad, A. & Zeidan, M. 2018. Beneficial Use of Nano-Silica in Concrete : A Review. *Trends in Civil Engineering and Material Science*. 1–3.
- Salet, T.A.M., Ahmed, Z.Y., Bos, F.P. & Laagland, H.L.M. 2018. Design of a 3D printed concrete bridge by testing. *Virtual and Physical Prototyping*. 13(3):222–236.
- Senff, L., Labrincha, J.A., Ferreira, V.M., Hotza, D. & Repette, W.L. 2009. Effect of nano-silica on rheology and fresh properties of cement pastes and mortars. *Construction and Building Materials*. 23(7):2487–2491.
- Tadros, T. 2007. General Principles of Colloid Stability and the Role of Surface Forces. *Colloids and Interface Science Series*. 1:1–22.
-

Chapter 3: Thixotropy Model

- Uchikawa, H., Hanehara, S. & Sawaki, D. 1997. The role of steric repulsive force in the dispersion of cement particles in fresh paste prepared with organic admixture. *Cement and Concrete Research*. 27(1):37–50.
- Wiliński, D., Łukowski, P. & Rokicki, G. 2016. Polymeric superplasticizers based on polycarboxylates for ready-mixed concrete: Current state of the art. *Polimery/Polymers*. 61(7–8):474–481.
- Winnefeld, F. 2002. Rheological Behaviour of Portland Cement Pastes during Early Hydration. In San Diego, California, USA *Twenty-Fourth International Conference on Cement Microscopy*. 18–31.
- Wolfs, R.J.M., Bos, F.P. & Salet, T.A.M. 2018. Early age mechanical behaviour of 3D printed concrete: Numerical modelling and experimental testing. *Cement and Concrete Research*. 106(May 2017):103–116.
- Zhang, Y. & Kong, X. 2015. Correlations of the dispersing capability of NSF and PCE types of superplasticizer and their impacts on cement hydration with the adsorption in fresh cement pastes. *Cement and Concrete Research*. 69:1–9.
- van Zijl, G.P.A.G., Kruger, J., Cho, S. & Zeranka, S. 2018. 3D printing polymer fibre concrete. In Cape Town, South Africa: *Proceedings of the International Inorganic-Bonded Fiber Composites Conference*. 5–14.

Chapter 4

A rheology-based quasi-static shape retention model for digitally fabricated concrete

Jacques Kruger, Stephan Zeranka, Gideon van Zijl

Division for Structural Engineering and Civil Engineering Informatics, Stellenbosch
University, 7600, South Africa

Reproduced and reformatted from an article submitted to the *Cement and Concrete
Research Journal*.

Abstract

The shape retention capability of an extruded filament is of cardinal importance for quality 3D printed concrete elements. Not only is it a prerequisite for surface aesthetics, but it also contributes towards buildability. Optimisation of filament layer height allows for construction time and cost saving possibilities. This research develops the theoretical framework for an analytical shape retention model that predicts the maximum stable filament layer height at which no plastic yielding occurs, based only on the rheology of a material. The Mohr-Coulomb failure criterion is employed and the model simplified by conservatively negating the effect of interparticle friction. A model is also developed that determines whether sufficient friction is present to induce confinement within a filament layer. An experimental verification process via filament extrusion confirms the applicability of the model. A 6.7 % difference in stable filament layer height is obtained by comparison with a finite element analysis, proffering as numerical validation for the model.

Keywords: filament shape retention, rheology, analytical modelling, finite element analysis, 3D concrete printing

4.1 Introduction

3D printing of concrete (3DPC), also known as digitally fabricated concrete, is a lineage technology that emanates from additive manufacturing techniques and holds significant value for the construction industry in terms of reduced time, cost and material waste (De Schutter et al., 2018). This novel construction technique nullifies the use of formwork due to its additive nature, which allows for the fabrication of geometrically-optimised elements (Martens et al., 2017; Vantuyghem et al., 2018). Bar formwork cost savings, time savings are facilitated by increasing print speeds or increasing filament layer heights. This effectuates the advantages of automation in the construction industry, namely increasing architectural and structural element fabrication productivity at reduced costs.

However, this technology is only viable if quality assurance is guaranteed at increased productivity rates. Concerning 3DPC, structural integrity must always be achieved in the fresh concrete state, typically by yielding the desired surface finish as a minimum. This is realised by extruding filament layers that do not significantly deform under self-weight (Buswell et al., 2018). Consequently, shape retention of 3D printed filament layers constitutes a pre-requisite in order to achieve good buildability, which is the ability of a material to resist the weight of subsequent deposited filament layers (Paul et al., 2017). Thus, shape retention of individual filament layers should first be assured before utilising buildability models such as those developed by Suiker (2018), Roussel (2018), Wolfs et al. (2018) and Kruger et al. (2019) for 3DPC.

In this research a rheology-based analytical shape retention model is developed that predicts the maximum filament layer height at which no *plastic yielding* at material point level will occur under self-weight, thus preventing *plastic flow*. Importantly, the model does not account for plastic deformations; slight deformations may thus still occur. The model is based on the bi-linear thixotropy model developed by Kruger et al. (2019b) that specifically appertains to 3DPC. The particular effect of the re-flocculation rate (R_{thix}) is illustrated, of which the magnitude influences the shape retention capabilities of a material. The primary model is derived from equilibrium of forces and thereafter refined by incorporating failure mechanisms based on principle stress combinations within a filament cross-section. These stresses are plotted on Mohr's circle to determine the maximum shear stress, which is equated to the material's resistance in terms of its yield shear stress obtained from rheometer stress growth tests. An experimental verification test program is conducted whereby a 3D printable mortar is

extruded at a certain filament layer height and the result compared to that predicted by the aforementioned model. A finite element analysis (FEA) is executed as a means of numerical verification of the analytical model. The aim for the model is to be a simple, practical and accurate means to predict a stable filament layer height that is suitable for 3DPC. Potential applications of the model include: 1) optimising filament layer heights for large-scale digital fabrication that necessitates substantial filament layer cross-section sizes 2) materials with high densities 3) materials that possess low static yield shear stress values i.e. readily flowable under self-weight, such as lightweight foam concrete (Cho et al., 2019) and 4) in conjunction with 3DPC buildability models to ensure holistic structural integrity in the fresh concrete state.

4.2 Model development

4.2.1 Material strength

This model is developed based on a material's shear strength in its plastic state, which can be characterised with a rheometer. Although different classifications of rheological behaviour exist, only thixotropic behaviour is considered for this model. The static and dynamic yield shear stresses are distinguished for a thixotropic material, as illustrated in Figure 4.1. Thixotropic material behaviour is ideal for pumping applications, because of interparticle force breakdown and consequently only the dynamic yield shear stress is required to maintain flow. This results in less strain imparted on the pump as well as a reduced likelihood of segregation. Furthermore, after shearing of the material halts, i.e. after extrusion through the printer's nozzle, the material re-flocculates and rebuilds shear strength up to its static yield shear stress.

The static yield shear stress is the critical shear strength value in this model. It is assumed that material failure will occur if the applied load (self-weight in this case) induces a shear stress that exceeds the material's static yield shear stress. This failure is denoted as *plastic yield*, whereby the material experiences excessive plastic deformation. Plastic yielding within a 3D printed filament layer will result in significant vertical and horizontal deformation and consequently yield a distorted filament shape. This adversely affects an element's aesthetics and, in particular, reduces a material's buildability performance due to eccentricities induced by imperfect layer depositions. The curve illustrated in Figure 4.1 is obtained via a material stress growth test executed using a rheometer at a constant shear rate.

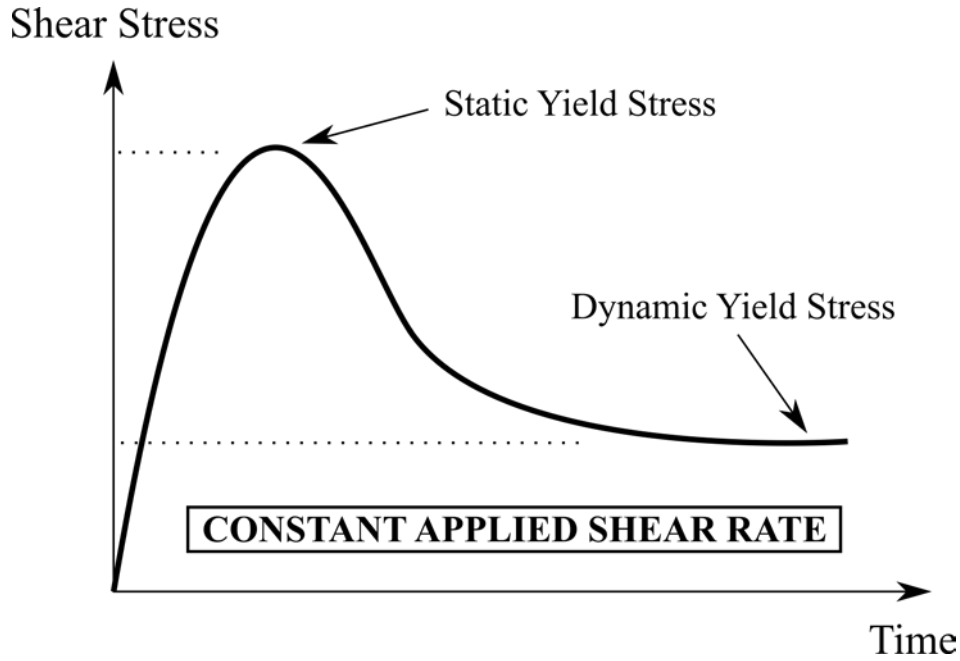


Figure 4.1: Material stress growth test depicting the static and dynamic yield shear stresses of a thixotropic material.

The thixotropy model developed by Kruger et al. (2019b) is employed for this research. A clear distinction is made between the two mechanisms responsible for thixotropic behaviour, namely re-flocculation (R_{thix}) and structuration (A_{thix}) (Roussel, 2006). The model depicts the static yield shear stress evolution of a material after it has been extruded from a nozzle for 3DPC, as schematically illustrated in Figure 4.2. Importantly, it accounts for the shear history of a material induced by the pumping process. The time-dependent material behaviour illustrated in Figure 4.2 is mathematically expressed as follows:

$$\tau_S(t) = \tau_{D,i} + R_{thix} \cdot t \quad (4.1)$$

$$t_{rf} = \frac{\tau_{S,i} - \tau_{D,i}}{R_{thix}} \quad (4.2)$$

$$\tau_S(t) = \tau_{S,i} + A_{thix} \cdot (t - t_{rf}) \quad (4.3)$$

Where $\tau_S(t)$ is the static or apparent yield shear stress of the material at time t after agitation, $\tau_{S,i}$ and $\tau_{D,i}$ the initial static and dynamic yield shear stresses of the material measured from the first rheological test and t_{rf} the time period over which re-flocculation occurs. It is crucially important to account for the shearing of a material induced by the pumping and transport processes during 3DPC. This can be imitated with the use of a rheometer by

corresponding the rheometer's shear rate ($\dot{\gamma}$) to that of the pump during printing (Kruger et al., 2019b; Nerella et al., 2019). The presence of a lubrication layer (LL) during material transport is unaccounted for in this research (Roussel, 2012), however remains very applicable. The formation of a LL is found to be dependent on the concrete mix design and potentially the pipe diameter (Choi et al., 2013). More information on LL formation and coupled rheology is available in the literature (Vosahlik, 2018; Secrieru et al., 2018; Secrieru et al., 2018b).

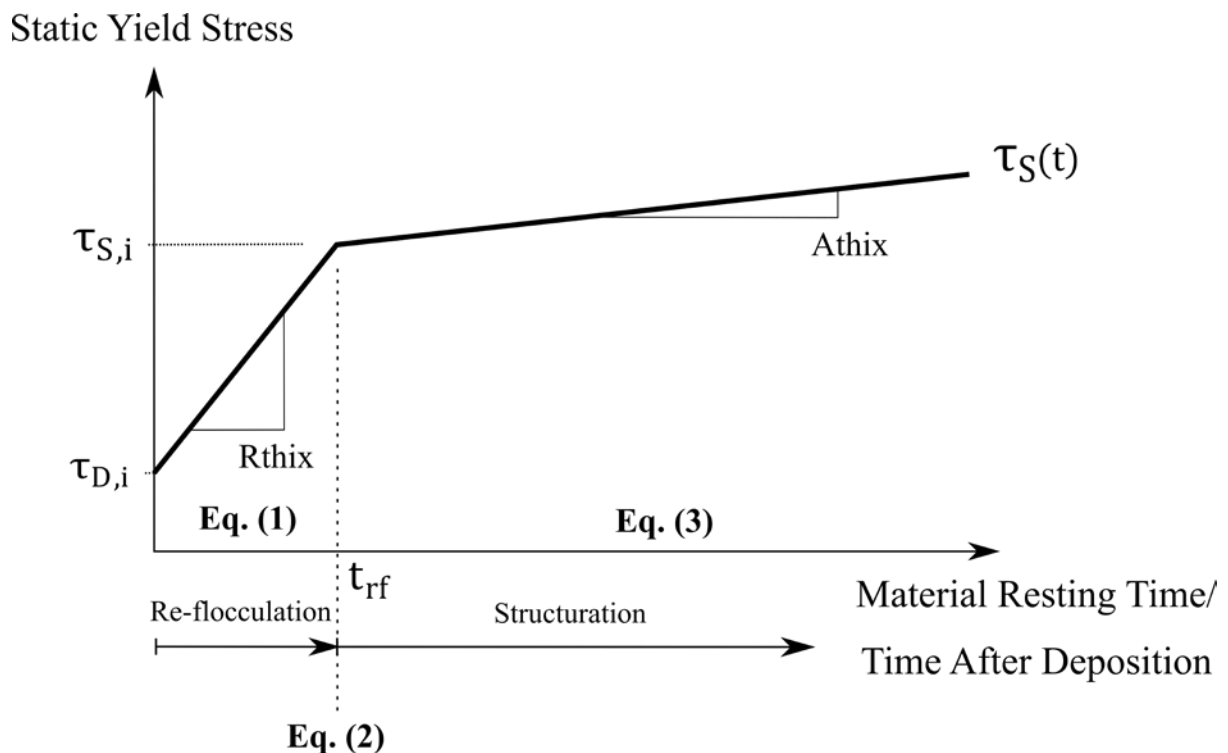


Figure 4.2: Static yield shear stress evolution as a function of resting time illustrated by both the re-flocculation and structuration thixotropy mechanisms (Kruger et al., 2019b).

4.2.2 Equilibrium of forces

This section derives an analytical equation for the shape retention model based on equilibrium of forces. Consider a rectangular cross-section of a 3D printed filament layer with unit length, as presented in Figure 4.3a. The objective is to determine if a material will flow plastically under self-weight, immediately after it is extruded. This is achieved by considering internal force equilibrium on an infinitesimal element within a filament layer at distance y from the print bed. Two forces act on this infinitesimal element, namely the self-weight of the material above the element (F_{SW}) and the resistance provided by the material against plastic flow (F_R), as illustrated in Figure 4.3b. The resisting force must be larger than the self-weight in order to prevent plastic flow. Small plastic deformations are not accounted for in this model and are thus ignored. F_{SW} and F_R are depicted by Equations 4.4 and 4.5 respectively. F_{SW} is determined by multiplying the area above the infinitesimal element with the material's density, whilst F_R is the static yield shear stress of the material obtained from rheometer testing multiplied with the area over which it acts:

$$F_{SW} = w_1 \cdot \rho \cdot g \cdot \left[h_1 - \sum_{i=1}^N \Delta y \right] \quad (4.4)$$

$$F_R = \tau_S(t) \cdot w_1 \quad (4.5)$$

Now, $F_R \geq F_{SW}$:

$$\begin{aligned} \sum F: \quad & \tau_S(t) \cdot w_1 \geq w_1 \cdot \rho \cdot g \cdot \left[h_1 - \sum_{i=1}^N \Delta y \right]; \quad \lim_{\Delta y \rightarrow 0} \sum_{i=1}^N \Delta y \\ & \geq w_1 \cdot \rho \cdot g \cdot \left[h_1 - \int_0^y dy \right] \\ & \quad \vdots \\ & \tau_S(t) \geq \rho \cdot g \cdot [h_1 - y] \end{aligned} \quad (4.6)$$

Where w_1 is the width of the filament layer, h_1 the height of the filament layer, ρ the material density, g the gravitational constant (9.81 m/s^2) and y the distance from the bottom of the filament layer to the position of the infinitesimal element. Equation 4.6 facilitates the internal force equilibrium calculation at any position y within the filament layer's height.

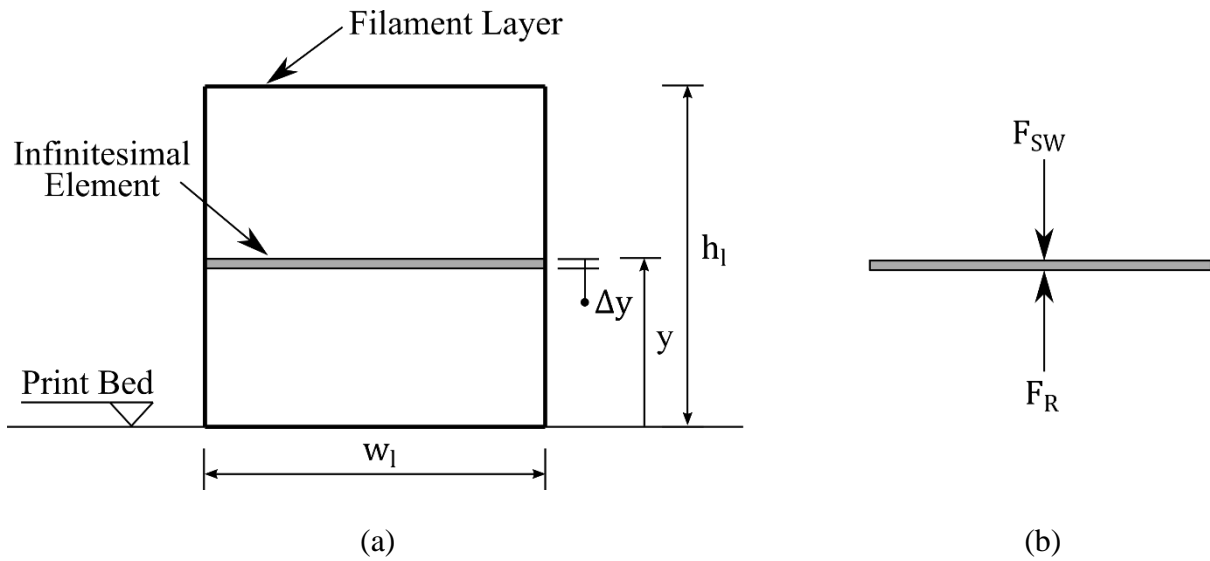


Figure 4.3: a) Cross-section of a 3D printed rectangular filament layer at an arbitrary position along its length indicating an infinitesimal element and b) internal force equilibrium of an infinitesimal element within a filament layer.

A cementitious material develops strength over time due to the hydration process. Early age hydration products such as ettringite needles reduce the plasticity of cement mixtures in the fresh state, thus increasing its yield stress. The resistance provided by the material against plastic flow is therefore time-dependent, as depicted in Equations 4.5 and 4.6. Another crucial factor that influences a material's yield stress is its shear history, especially for thixotropic materials that exhibit significant interparticle forces. Agitation that breaks a thixotropic material's microstructure results in less resistance provided by the material when the agitation halts, as the particles have to re-flocculate to rebuild the original microstructure. Therefore, the shear history of a material, in terms of the shearing magnitude and duration as well as the time since cessation of the shearing, becomes pivotal in obtaining accurate time-dependent strengths. In the case of 3DPC, a filament layer must ideally retain its shape as soon as it exits from the nozzle. Equation 4.1 depicts a material's shear strength evolution immediately after cessation of shearing, i.e. after extrusion for 3DPC. In the case of no shearing and thus negligible microstructural breakdown, $\tau_{D,i}$ can be replaced with $\tau_{S,i}$ and R_{thix} with A_{thix} . Equation 4.6 is thus expanded as follows:

$$\begin{aligned}
 \text{Shearing:} \quad & \tau_{D,i} + R_{\text{thix}} \cdot t \geq \rho \cdot g \cdot [h_1 - y] \\
 & t \geq \frac{\rho \cdot g \cdot [h_1 - y] - \tau_{D,i}}{R_{\text{thix}}} \quad (4.7)
 \end{aligned}$$

$$\begin{aligned}
 \text{No shearing:} \quad & \tau_{S,i} + A_{\text{thix}} \cdot t \geq \rho \cdot g \cdot [h_1 - y] \\
 & t \geq \frac{\rho \cdot g \cdot [h_1 - y] - \tau_{S,i}}{A_{\text{thix}}} \quad (4.8)
 \end{aligned}$$

Equations 4.7 and 4.8 depict the time that a filament layer will experience plastic deformations, based on material and geometrical properties, before it reaches equilibrium. No deformation will occur in the case where the right-hand side of Equations 4.7 and 4.8 yield negative values. These equations can however be simplified by assuming quasi-static conditions; typical A_{thix} values range between 0 and 1 Pa/s (Roussel, 2006; Kruger et al., 2019b) and R_{thix} values between 0 and 10 Pa/s (Kruger et al., 2019b). It is thus conservative to exclude A_{thix} in Equation 4.8, which yields a quasi-static solution. In contrast, an R_{thix} value of 10 Pa/s can reduce the plastic deformation time by one order of magnitude. However, a more pragmatic approach for 3DPC is to determine the maximum stable filament layer height that is attainable based on a material's characteristics. This is achieved by equating the time t in Equations 4.7 and 4.8 to zero, effectively nullifying the influence of R_{thix} and A_{thix} . Quasi-static solutions are again obtained and subsequently inertial effects are negligible. Furthermore, the position of the infinitesimal element is assumed to be at the bottom of the filament layer ($y = 0$). The two variables t and y are eliminated to deduce a simple quasi-static solution that is ultimately conservative:

$$H_{\text{max}} = \frac{\tau_{D,i}}{\rho \cdot g} \quad (4.9)$$

Where H_{max} is the maximum stable filament layer height. $\tau_{D,i}$ can be replaced with $\tau_{S,i}$ in the case where no shearing of the material is assumed. Equation 4.9 presents the primitive analytical equation for this model. Equations 4.7 and 4.8 can be applied in more complex situations, for instance where a certain filament layer height must be achieved that exceeds a material's capacity and the corresponding plastic deformation time obtained. However, note that up until now the self-weight induced normal stress is equated to a material's resistance in

terms of shear stress, which is incompatible. The following section addresses this incompatibility and defines the material failure theory.

4.2.3 Failure theory & analytical expression of model

Concrete in its fresh plastic state illustrates similar behaviour to soils. Both possess significantly less capacity in tension than in compression. Furthermore, failure in compression is due to relative movement of particles i.e. shear failure, and not by crushing of the constituents. The pressure-dependent shear stress is described by the Mohr-Coulomb failure criterion, which accounts for both interparticle friction (φ) as well as cohesion (c). This criterion essentially depicts the shear envelope of a material as a function of normal stress, which is illustrated in Figure 4.4a and analytically expressed as follows:

$$\tau = c + \sigma \cdot \tan(\varphi) \quad (4.10)$$

The Mohr-Coulomb failure criterion has been successfully employed in buildability modelling for 3DPC purposes (Suiker, 2018; Wolfs et al., 2018). This research adapts this failure criterion by conservatively assuming no interparticle friction ($\varphi = 0$), consequently demanding less material tests (in this case the direct shear test) for material characterisation. The equivalently induced shear stress from a normally applied stress is therefore only depicted by cohesion, denoted as the y-axis intercept on the failure envelope. This simplifies into the maximum shear stress theory, also known as the Tresca failure criterion, and relates the normal stress to the shear stress as follows (refer to Figure 4.4b in unison):

$$\tau = c = \frac{\sigma_{\max} - \sigma_{\min}}{2} \quad (4.11)$$

Where σ_{\max} and σ_{\min} are the maximum and minimum normal stresses at a material point level, typically depicted by Mohr's circle. These stresses develop due to applied loading on a filament layer, or in this research the self-weight of a layer. An equivalently induced shear stress can be derived with Equation 4.11 and then compared to the critical shear stress value, depicted by the model illustrated in Figure 4.2, or more specific to this research the initial dynamic yield shear stress ($\tau_{D,i}$) value obtained from rheometer testing relevant to Equation 4.9. Note that the normal stress due to self-weight is equal to $\rho \cdot g \cdot h_1$. The conservative equivalent shear stress obtained by Tresca compared to the actual equivalent shear stress obtained by the Mohr-Coulomb criterion is illustrated in Figure 4.4.

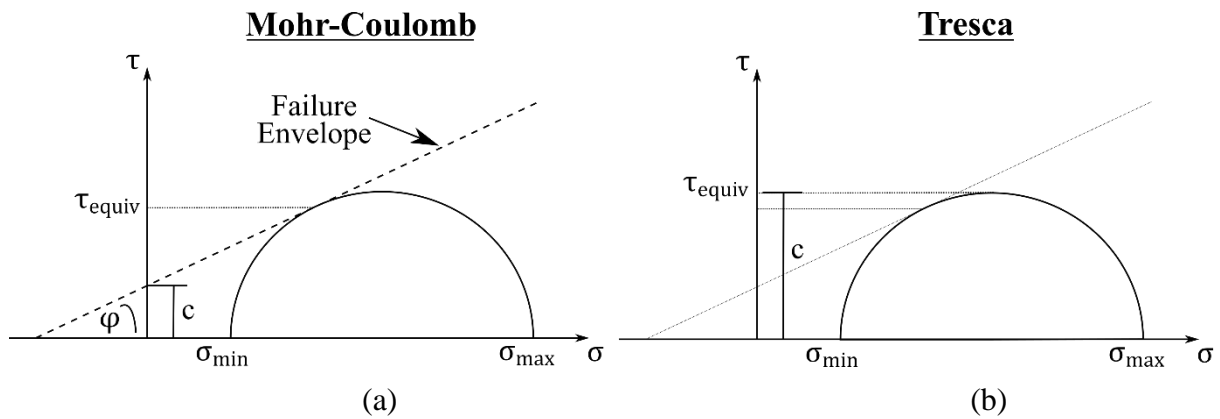


Figure 4.4: a) Shear failure envelope of the Mohr-Coulomb failure criterion indicating the equivalently induced shear stress and b) the Tresca failure criterion indicating the increased equivalently induced shear stress for identical normal stress conditions.

Now, consider a plane strain element with unit thickness as indicated in Figure 4.5a together with the relevant coordinate system. Note that plane strain conditions imply that $\epsilon_3 = 0$ and consequently $\sigma_3 \neq 0$, which is in accord as the element is bilaterally supported by filament and its accompanied inertia in the longitudinal direction. Most deformation would thus occur transversely and not longitudinally; hence, longitudinal strain can be assumed to be zero. Furthermore, this research assumes that sufficient friction is present between the print bed and filament layer so that no slip will occur. In the case where insignificant friction is present, the filament deformation can be approximated by determining the Young's Modulus of the material and employing Hooke's law. More information regarding friction is presented in Section 4.2.4.

A benefit of sufficient friction is the emergence of confinement within a filament layer, as indicated in Figure 4.5b. Confinement refers to the condition whereby a multiaxial state of stress develops in a material that subsequently yields a lower equivalent shear stress as compared to the uniaxial stress state (Kruger et al., 2019). Therefore, in the case of plastic concrete that predominantly fails in shear, the yield compressive strength is increased. The principle stress distribution induced by self-weight of a confined filament layer is indicated in Figure 4.5b. The vertical stress, which will always be the largest stress, is depicted by Equation 4.12 and varies linearly over the height of the filament layer. The horizontally induced stress due to confinement is always in compression and assumed to vary linearly. A small horizontal tensile stress may develop in the top of a filament layer, which is ignored due

to the insubstantial magnitude of the vertical stress at the same position. The longitudinal stress is a function of both the horizontal and vertical stresses and can be determined with Equation 4.13:

$$\sigma_1(y) = \sigma_{SW} = \rho \cdot g \cdot [h_1 - y] \quad (4.12)$$

$$\sigma_3 = \nu \cdot [\sigma_1(y) + \sigma_2] \quad (4.13)$$

Where ν is the Poisson's ratio of the material. The aforementioned stress combinations yield three different failure zones within the cross-section of a filament layer, as depicted in Figure 4.5c. Each zone presents its own normal stress state and equivalent shear stress that will now be discussed individually.

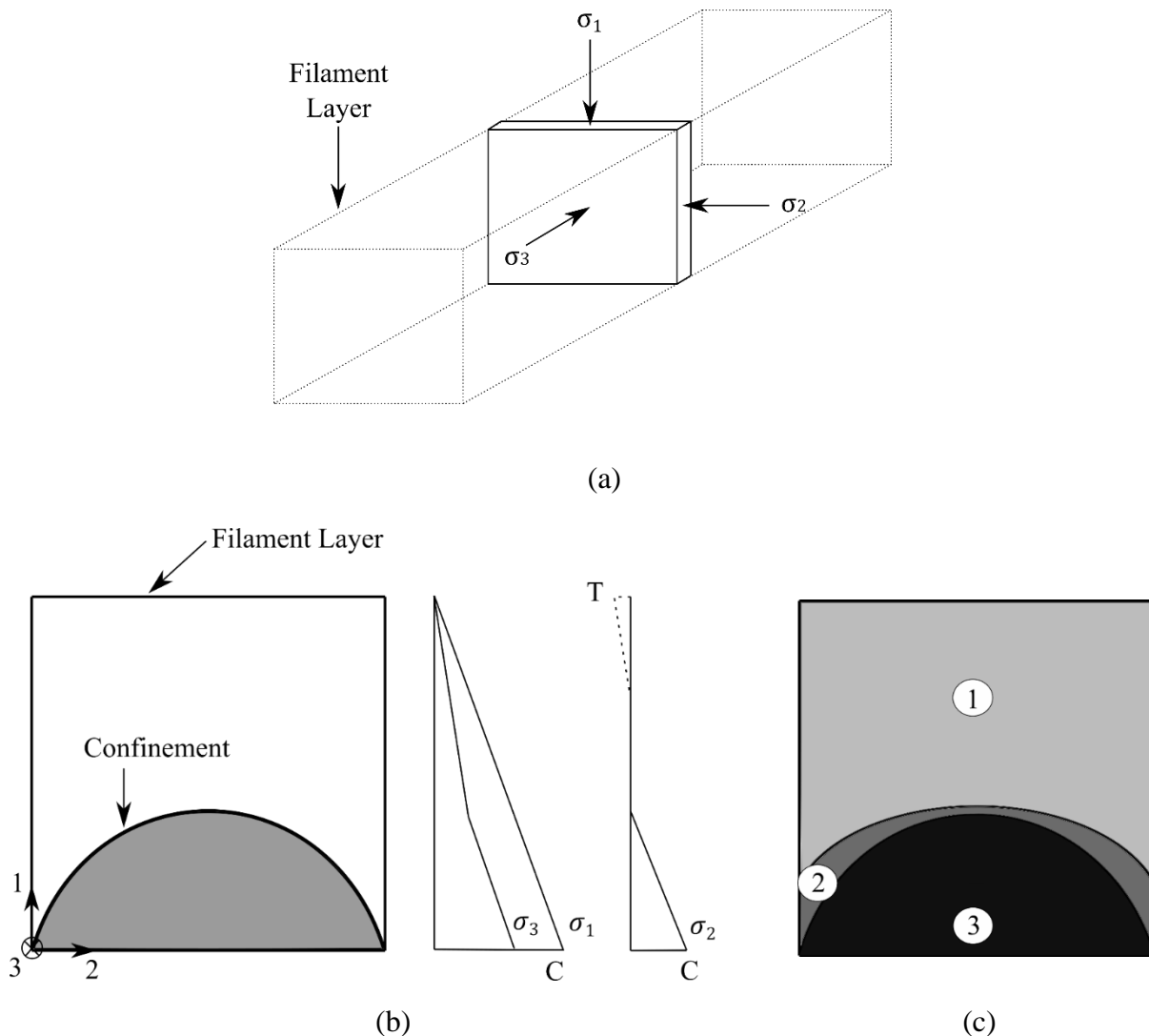


Figure 4.5: a) Plane strain element with unit thickness of a printed filament layer indicating the relevant coordinate system in terms of principle stresses, b) cross-section of a filament layer with confinement in the bottom and corresponding principle stresses indicated to the right and c) three failure zones within a filament layer.

Failure zone 1

Zone 1 is depicted in Figure 4.5c and comprises of a vertical stress induced by self-weight that yields a biaxial state of stress. No lateral confinement is present in this region, but there is confinement in the extrusion direction. From Figure 4.5b it is observed that the transverse stress is the smallest in magnitude, assuming that the tensile stress at the top of the filament layer is insignificant and therefore ignored. A longitudinal stress is present and varies between σ_1 and σ_2 , depending on the material's Poisson's ratio. These stresses are graphically presented in Figure 4.6 by means of Mohr's circle that illustrates the maximum and minimum stresses respectively.

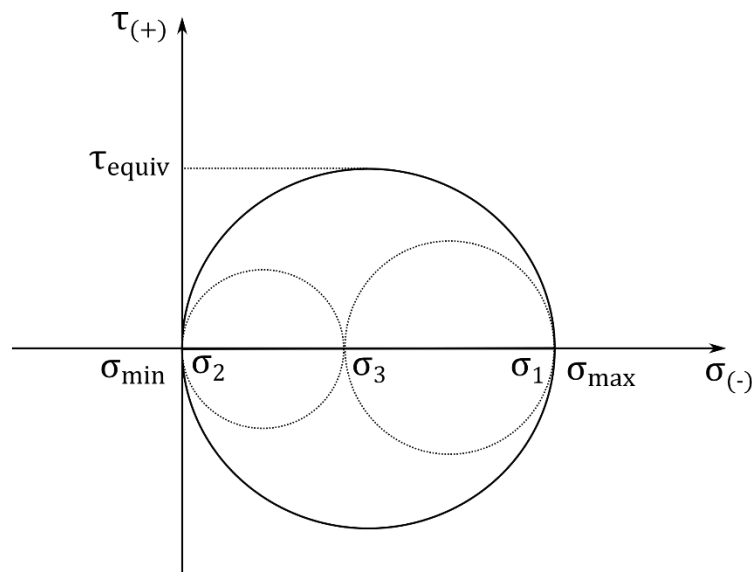


Figure 4.6: Mohr circle for the biaxial stress state that occurs in failure zone 1.

The equivalently induced shear stress is obtained by following the Tresca yield criterion i.e. assuming no interparticle friction, which forms the lower bound of the Mohr-Coulomb failure criterion:

$$\begin{aligned}
 \tau_{\text{equiv}} &= \frac{\sigma_{\text{max}} - \sigma_{\text{min}}}{2} \\
 &= \frac{\sigma_1 - \sigma_2}{2} \\
 &= \frac{\sigma_1}{2} \\
 &\equiv \frac{\sigma_{\text{SW}}}{2}
 \end{aligned} \tag{4.14}$$

It is required that $\tau_{\text{equiv}} < \tau_{D,i}$ in order to prevent plastic yielding of the material (refer to Equation 4.9) after extrusion. This yields Equation 4.15 that presents the analytical expression for failure in zone 1:

$$H_{\text{max}} = \frac{2 \cdot \tau_{D,i}}{\rho \cdot g} \quad (4.15)$$

Failure zone 2

Zone 2 is depicted in Figure 4.5c and represents the figurative macroscopic interfacial transition zone (ITZ) between the laterally unconfined and confined areas within a filament layer. The confined area experiences a compressive stress due to the suppression of lateral deformation by friction. This area therefore remains largely stationary, but the unconfined area experiences vertical and horizontal deformations. The largest deformations occur in the regions where the vertical stresses are the most significant, namely just above the confined area on both horizontal extremes of a filament layer. A tensile stress develops in those regions due to the unconfined area shearing away and outwards from the confined area in the absence of any lateral restraints on the edges of a filament layer above the print bed surface. Figure 4.7 visually illustrates this process.

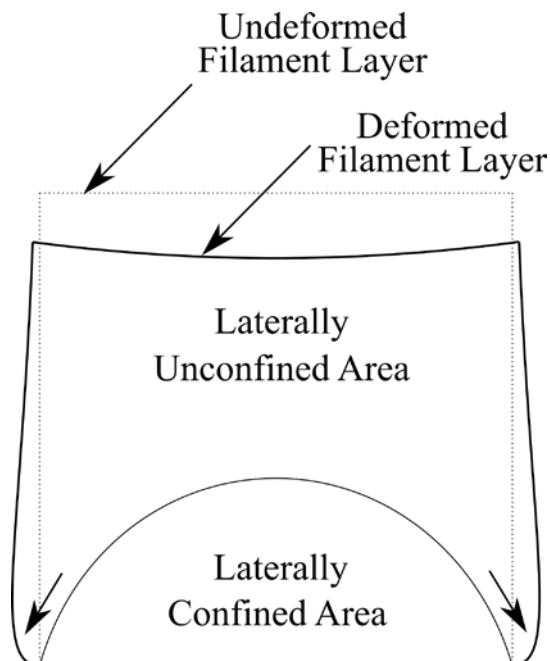


Figure 4.7: Typical deformation of a filament layer that initiates and propagates from failure zone 2.

Chapter 4: Shape Retention Model

Failure zone 2 is critically assessed by performing a sensitivity analysis with the Poisson's ratio. In the improbable case where a material has a Poisson's ratio of $\nu = 0$, no lateral deformation occurs in the ITZ. Equation 4.14 therefore presents the equivalently induced shear stress as no transverse tensile stress develops and consequently the smallest normal stress is zero. However, it is deduced from sound reasoning that the transverse stress in the ITZ's unconfined area will always be tensile in nature, as this area can only displace outwards from the confined area within the filament layer. Therefore, in the case where a material is incompressible ($\nu = 0.5$), a tensile stress develops as the unconfined area shears away from the confined area that remains stationary. Consequently, a larger Mohr-circle is obtained and the relationship between normal and shear stress nears one. This process is visually illustrated in Figure 4.8 by means of Mohr circles for identical self-weight (σ_1) stresses.

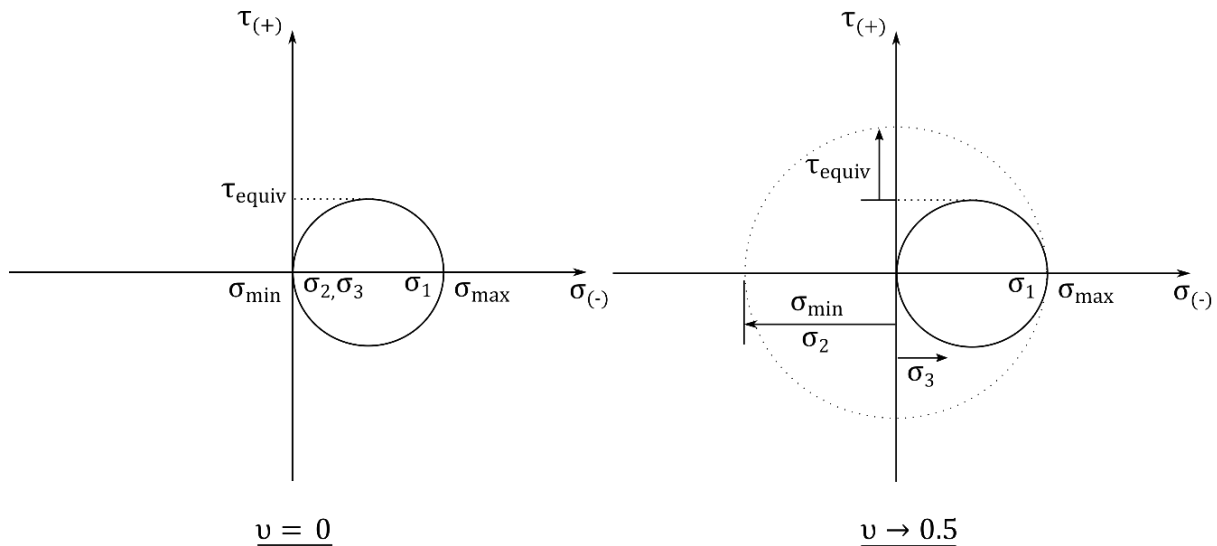


Figure 4.8: Mohr circles that indicate the normal stress state for $\nu = 0$ and $\nu \rightarrow 0.5$ together with accompanying equivalently induced shear stress.

It becomes apparent that an increase in the Poisson's ratio yields an increase in transverse stress for identical loading, thereby expanding the encircling Mohr circle. Consequently, a larger equivalent induced shear stress is obtained for materials that tend to be incompressible, with a maximum normal to shear stress ratio of 1:1. For $\nu = 0$, which is an unlikely scenario for concrete in its plastic state, a 2:1 normal to shear stress ratio is obtained. Equation 4.16 depicts the Poisson-dependent analytical expression for failure in zone 2:

$$(1 - \nu) \cdot \tau_{\text{equiv}} = \frac{\sigma_1}{2}$$

$$H_{\text{max}} = \frac{2 \cdot \tau_{D,i} \cdot (1 - \nu)}{\rho \cdot g} \quad (4.16)$$

Failure zone 3

Zone 3 is depicted in Figure 4.5c and represents the confined area that comprises of a multiaxial state of stress. As mentioned earlier, it is assumed that sufficient friction is present between the print bed surface and the bottom of the filament layer in order to prevent any slip from occurring. The confined area typically remains stationary due to its compressive triaxial stress state. This failure has already been defined in literature by Suiker (2018) for a mechanistic buildability model applicable to 3DPC. Suiker initially proved that the coefficient of lateral stress (K_y) varies between zero and ν for a wall configuration that is unconstrained and fully constrained at its bottom respectively. The author then provides an analytical expression for yield strength, which is based on Mohr-Coulomb theory:

$$\sigma = \frac{2 \cdot c \cdot \cos(\varphi)}{1 - K_y + (1 + K_y) \cdot \sin(\varphi)} \quad (4.17)$$

When assuming that the bottom of the filament layer is fully constrained in the lateral direction (confined, with no slip), the coefficient of lateral stress may be set equal to the Poisson's ratio ($K_y = \nu$) in Equation 4.17. By further assuming for no interparticle friction ($\varphi = 0$), as is consistently done throughout this research, cohesion is set equal to the shear stress ($c = \tau_{\text{equiv}}$) and Equation 4.17 reduces to Equation 4.18:

$$\sigma = \frac{2 \cdot \tau_{\text{equiv}}}{(1 - \nu)} \quad (4.18)$$

Which essentially depicts the Tresca yield criterion based on reaching the maximal shear stress at the bottom of the confined area within the filament layer. By substituting Equation 4.12 and enforcing $\tau_{\text{equiv}} < \tau_{D,i}$, the maximum stable filament layer height whereby plastic yielding will not occur in failure zone 3 is presented by Equation 4.19:

$$\rho \cdot g \cdot H_{\max} = \frac{2 \cdot \tau_{D,i}}{(1 - \nu)}$$

$$H_{\max} = \frac{2 \cdot \tau_{D,i}}{(1 - \nu) \cdot \rho \cdot g} \quad (4.19)$$

Analytical expression of model

The analytical expression for failure in zones 1, 2 and 3 are depicted by Equations 4.15, 4.16 and 4.19 respectively. However, parametric observation of the aforementioned equations demonstrate that Equation 4.16 always governs failure in a filament layer due to the 1:1 to 2:1 relationship between normal and shear stress. Equation 4.15 has a 2:1 relationship between normal and shear stress. Equation 4.19 also possesses a 2:1 relationship between normal and shear stress, with the addition of the Poisson's ratio. The lower bound Poisson's ratio yields a 2:1 normal-shear relationship while the upper bound value yields a 4:1 relationship. Equation 4.16's direct relationship (in the case where $\nu = 0.5$) will therefore always yield the largest shear stress and consequently represents the final analytical expression for filament shape retention. It is postulated that the aspect ratio of a filament layer (height divided by width) does not influence the failure mechanisms as similar stress distribution profiles are obtained for varying aspect ratios.

4.2.4 Confinement check

The model developed in this research is based on the assumption that sufficient friction is present between the print bed surface and the bottom of the filament layer so that no slip occurs. Consequently, confinement develops in the bottom part of the filament layer that increases the material's resistance against plastic yielding. This in turn impedes significant deformations from occurring. A stable filament layer height can be determined and extruded by employing Equation 4.16. However, sufficient friction is to be ensured for the model to be accurate. Large deformations may occur in the absence of adequate friction, which can be determined using Hooke's law. This section derives a simple analytical expression that aims to determine the amount of friction that is required to induce confinement within a filament layer.

Consider a plane strain element of unit thickness as indicated in Figure 4.9a, which represents the cross-section of a filament layer that only accounts for in-plane behaviour. The bottom of the filament layer is fully constrained to replicate the boundary conditions for confinement. Equation 4.20 depicts Hooke's law for vertically induced loading, while

Equation 4.21 depicts the plane strain constitutive formulation for an elastic continuum in order to determine the transverse stress at the filament bottom:

$$\begin{aligned}\sigma_1 &= E \cdot \varepsilon_1 \\ \varepsilon_1 &= \frac{\sigma_1}{E}\end{aligned}\quad (4.20)$$

$$\sigma_2 = \frac{E}{(1 + \nu)(1 - 2\nu)} [\varepsilon_2(1 - \nu) + \varepsilon_1(\nu)] \quad (4.21)$$

Where E is the material Young's modulus and ε_1 and ε_2 the strain in the vertical and horizontal directions respectively. Substituting Equation 4.20 into 4.21 yields Equation 4.22 that depicts the transverse stress as a function of the vertically induced stress:

$$\sigma_2 = \frac{E}{(1 + \nu)(1 - 2\nu)} \left[\varepsilon_2(1 - \nu) + \frac{\sigma_1}{E}(\nu) \right] \quad (4.22)$$

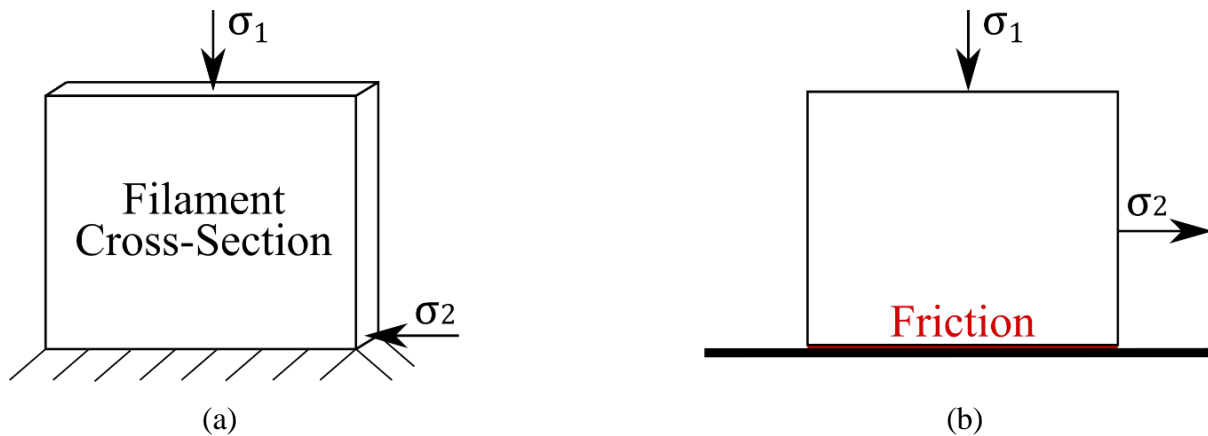


Figure 4.9: a) Plane strain element of unit thickness that represents the cross-section of a fully constrained filament layer and b) a block that rests on a surface with friction.

Now, consider a block that rests on a surface with friction as indicated in Figure 4.9b. In order to move the block, a horizontal tensile stress must overcome the static friction coefficient (μ_s) multiplied by the vertical stress, as depicted by Equation 4.23:

$$\sigma_2 = \mu_s \cdot \sigma_1 \quad (4.23)$$

Thus, the friction coefficient depicts the horizontal stress divided by the vertical stress, which in this case is the self-weight of the filament layer. A comparison can now be made: if the horizontal stress in the filament layer bottom (Equation 4.22) is smaller than the frictional stress (Equation 4.23), then no slip will occur and $\varepsilon_2 = 0$, which yields Equation 4.24:

$$\begin{aligned}\mu_s \cdot \sigma_1 &> \frac{E}{(1 + \nu)(1 - 2\nu)} \left[\frac{\sigma_1}{E} (\nu) \right] \\ \mu_s &> \frac{\nu}{(1 + \nu)(1 - 2\nu)}\end{aligned}\quad (4.24)$$

Equation 4.24 states that for confinement to occur, the friction between the filament layer and print bed surface has to be larger than a certain expression influenced by the material's Poisson's ratio, which intuitively makes sense. If a material does not possess a Poisson's ratio i.e. no lateral deformation occurs under a vertically induced stress, then no horizontal stress will develop in the bottom of the material and consequently no confinement will occur, thus negating any frictional requirement. However, a significant horizontal stress will develop for a perfectly incompressible material ($\nu = 0.5$) as the material seeks to expand laterally under the vertical loading to retain its original volume; thus a larger static friction coefficient is required for confinement.

A problem to this approach is the difficulty in obtaining the static friction coefficient between plastic state concrete and the print bed surface. A pragmatic approach is therefore adopted in order to determine the static friction coefficient for any 3DPC setup. Consider a block that rests on an inclined surface as depicted in Figure 4.10. Assume that the inclination angle (θ) is at the maximum for which the block remains static. It can then be proved from equilibrium that the static coefficient of friction is equal to the tangent function of the inclination angle as follows:

$$\begin{aligned}\sum F: \quad \mu_s \cdot m \cdot g \cdot \cos(\theta) &= m \cdot g \cdot \sin(\theta) \\ \mu_s &= \tan(\theta)\end{aligned}\quad (4.25)$$

The coefficient of static friction can be obtained for any combination of filament and print bed material by following this approach. The print bed with deposited filament layer is to be lifted and the inclination angle whereby the filament layer slides downward determined and used as input parameter for Equation 4.25. Alternatively, Equation 4.26 can be utilized which is obtained by substituting Equation 4.25 into 4.24:

$$\theta > \arctan\left(\frac{\nu}{(1 + \nu)(1 - 2\nu)}\right)\quad (4.26)$$

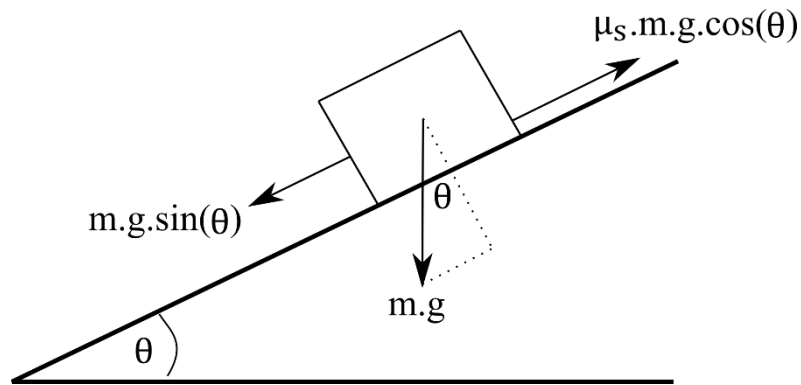


Figure 4.10: Block resting on an inclined surface illustrating the friction and gravitational forces.

Figure 4.11 presents a second (graphical) alternative to determine if confinement occurs. The same approach is followed as previously stated by lifting the print bed surface with filament layer in order to obtain the inclination angle whereby the layer slides downward. Note that a small representative print bed surface material is sufficient for this test. Furthermore, the size and weight of the filament layer is negligible. This angle must then be larger than the angle obtained from Figure 4.11 that correlates with the material's Poisson's ratio indicated on the x-axis in order for confinement to occur.

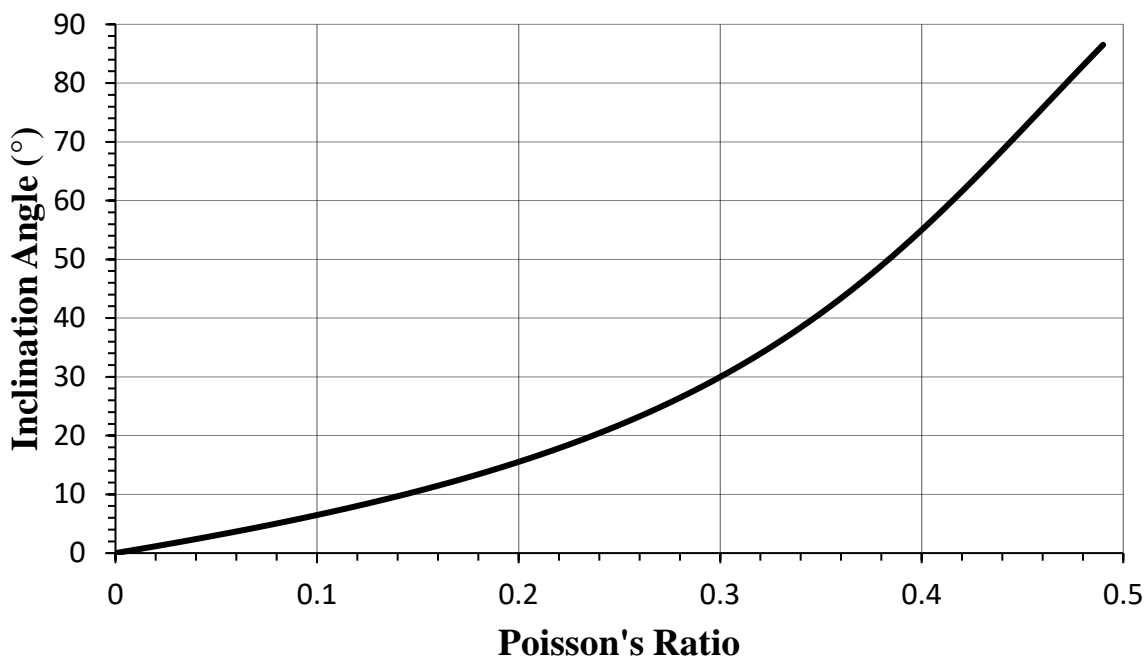


Figure 4.11: Graphical method to determine if confinement occurs for a particular 3DPC setup. Read off the inclination angle that corresponds with the material's Poisson's ratio. This angle must be smaller than the angle obtained for when a filament layer starts to slide downwards if the print bed surface is lifted in order for confinement to occur.

4.3 Experimental verification

4.3.1 Material composition & mixing procedure

The standard 3DPC mix at Stellenbosch University, which is a high-performance (HPC) mix with a water to cement ratio of 0.45, is used for this research and given in Table 4.1. The CEM II 52.5N composite cement contains between 6 and 20 % limestone extender and conforms to SANS 50197-1. Ulula class S fly ash, together with FerroAtlantica silica fume are used as extenders to obtain the required workability properties for 3DPC. The aggregate consists of a continuously graded coarse sand that is locally mined with a maximum particle size of 4.75 mm. Potable tap water is used in conjunction with a new generation superplasticizer, Chryso Fluid Premia 310, which is based on a modified polycarboxylate polymer.

Table 4.1: Standard HPC constituent quantities used for this research.

Constituent	kg
Cement	579
Fly Ash	165
Silica Fume	83
Aggregate	1167
Water	261
Superplasticizer	1.48% by mass of binder

A 50 litre concrete batch is prepared for this research. Initially, each constituent is accurately weighed off and temporarily stored in containers. The dry constituents are then placed into a 120 litre concrete pan mixer in the following order: aggregate, extenders and cement. This dry batch is mechanically mixed for at least three minutes until it is visually observed that the constituents form a homogenous dry mixture. Thereafter, water is poured into the pan mixer at a low rate while mixing. The concrete mixture is further mechanically mixed for one minute after all the water is added. Lastly, the superplasticizer is added to the concrete at a low rate for even distribution of the chemical throughout the concrete mixture. The batch is then further mixed for two minutes after which it is ready for testing.

4.3.2 Material tests & results

The 50 litre 3D printable concrete mixture is prepared, of which 20 litres are used for the rheology test and the remaining 30 litres for the filament extrusion process. Accurate material properties are thus obtained as one concrete batch is used for both the material characterisation and extrusion process. Furthermore, the rheology test is conducted simultaneously with the extrusion process to yield comparable time-dependent structuration properties i.e. the material is sheared at exactly the same starting time. The rheology test protocol presented in Table 4.2 is executed with the use of the Germann ICAR Plus Rheometer (Germann Instruments, n.d.). Only one stress growth test is performed since quasi-static conditions are assumed, hence R_{thix} and A_{thix} are not required. The methodology to determine R_{thix} and A_{thix} is depicted in (Kruger et al., 2019b).

Table 4.2: Rheology test protocol for the determination of the initial static and dynamic yield shear stresses.

Concrete Age After Mixing (min:s)	Test Number	Resting Time Interval	Shear Rate (s^{-1})	Shear Duration (s)	Action	Result
00:00-01:00	-	-	-	-	Transport concrete to rheometer	-
01:00-02:20	1	0 s (Initial)	1	80	Stress growth test	Obtain initial static and dynamic yield shear stress (Figure 4.1)

It is of crucial importance to correspond the rheometer's shear rate to that of the shear rate induced by the pump. In the absence of relevant literature, an approximation of the shear rate is made by corresponding the rotational speed of the rheometer's vane to that of the pump's screw during extrusion. In this research, a pump screw rotational speed of 0.2 rev/s is used that, based on the rheometer's geometry, yields a shear rate of $1 s^{-1}$. Furthermore, it was determined that 80 seconds elapse from placement of concrete to extrusion through the nozzle; thus all stress growth tests were conducted at a shear rate and duration of $1 s^{-1}$ and 80 s respectively. Note that this is only an approximation of the microstructural breakdown induced by pumping, as there currently does not exist any literature that expresses the aforementioned relationship.

The stress growth curve obtained from the rheometer test is depicted in Figure 4.12. Note that only the first 10 seconds of the test is presented out of the total 80-second test duration. It

Chapter 4: Shape Retention Model

is evident that the material is highly thixotropic as there is a significant difference between its static and dynamic yield shear stresses, measured as 6020 and 692 Pa respectively. Additional material properties required for this model are the density and Poisson's ratio. The concrete mix's density is obtained by filling a known volume (1 litre) and thereafter measuring the sample's mass. The density is then calculated by dividing the mass by the volume, which in this research yields 2150 kg/m^3 . The fresh concrete state's Poisson's ratio is chosen as 0.3, following from the experimental results of Wolfs et al. (2018). Suiker (2018) also assumed a Poisson's ratio of 0.3, which in the absence of accurate measurement techniques and limited literature is a justified assumption as an increase in the Poisson's ratio is obtained for increasing saturation levels (Carcione & Cavallini, 2002). The Poisson's ratio for fresh concrete can however be as large as 0.4 (Federal Highway Administration, n.d.). All material parameters are summarised in Table 4.3.

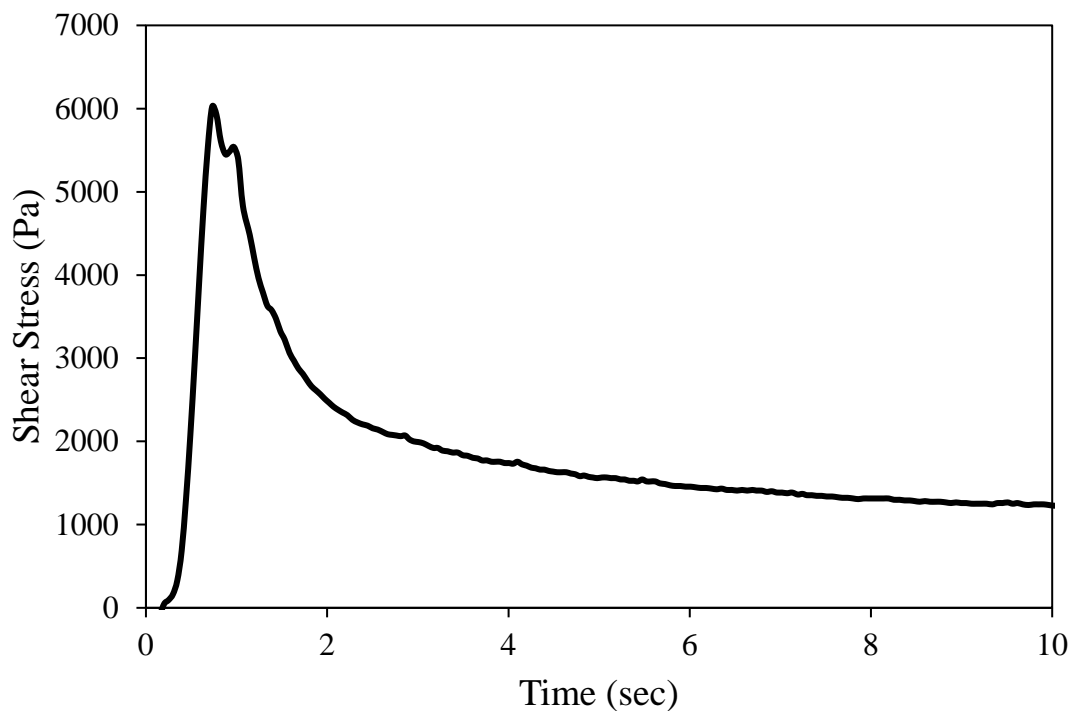


Figure 4.12: Stress growth curve obtained from rheometer testing. Only the first 10 seconds of the total 80-second test duration is shown.

Table 4.3: Summarised material parameters as input for the model.

Material Parameter	Value
$\tau_{D,i}$	692 Pa
ρ	2150 kg/m ³
ν	0.3
$\tau_{S,i}$	6020 Pa

4.3.3 Model prediction

This section demonstrates the use and application of the model developed in Section 4.2, in particular Equations 4.15, 4.16 and 4.19. The material input parameters summarised in Table 4.3 are applied to these equations and the results depicted in Table 4.4. Equation 4.16 predicts the maximum stable filament layer height for this material and extrusion setup as 46 mm. Equation 4.15 predicts that a height larger than 66 mm will initiate plastic flow in zone 1, while Equation 4.19 predicts a layer height larger than 94 mm will initiate plastic flow in zone 3, which is the confined area within the filament layer. It can thus be concluded that the deformed filament failure shape illustrated in Figure 4.7 will realise if a filament layer with height larger than 46 mm is extruded.

Table 4.4: Maximum stable filament layer heights obtained from Equations 4.15, 4.16 and 4.19, which correspond with failure in zones 1, 2 and 3 respectively.

Equation	H_{max} (mm)
4.15	66
4.16	46
4.19	94

4.3.4 Experimental results

A custom-built concrete extruder illustrated in Figure 4.13 is used for this research, as the current SU 3D concrete printer is incapable of extruding large square cross-sectional filament layers. The concrete is fed into the rotating pump screw by pressure from the pneumatic controlled compressor plate. The screw transports the concrete to the nozzle whereafter it is extruded through a 40x40 mm square nozzle. A tapered nozzle is utilised to minimise distortion of flow lines during extrusion that may influence material shearing. It is assumed that material at all positions in the cross-section of a filament are at the same rheo-mechanical state once they are extruded. The particular influence of 3DPC nozzle shape and configuration on shearing are beyond the scope of this research, but recommended for future work (Flitta & Sheppard, 2005). A 40 mm layer height will thus be obtained, which is smaller than the maximum stable filament layer height of 46 mm predicted by Equation 4.16. No plastic flow is therefore expected to occur. The filament is extruded onto a platform consisting of rollers to facilitate movement in the longitudinal (extrusion) direction. This minimises the longitudinal (σ_3) stresses induced by the static nozzle; however, note that no longitudinal stresses are induced in the case of a 3D concrete printer where the nozzle moves and the material is deposited onto a stationary platform. There is insufficient space between the platform and extruder machine to accommodate a lengthy rigid board. Hence, a 170 μm thick polyethylene sheet is placed onto discrete rollers to create a surface for the filament layer. The rollers with diameter 20 mm are spaced at a centre-to-centre distance of 22 mm. The screw rotational speed of 0.2 rev/s yields an extrusion rate of approximately 2 mm/s or volumetric flow rate of 3200 mm^3/s , which is presumed sufficiently small to minimize the longitudinally induced stress.

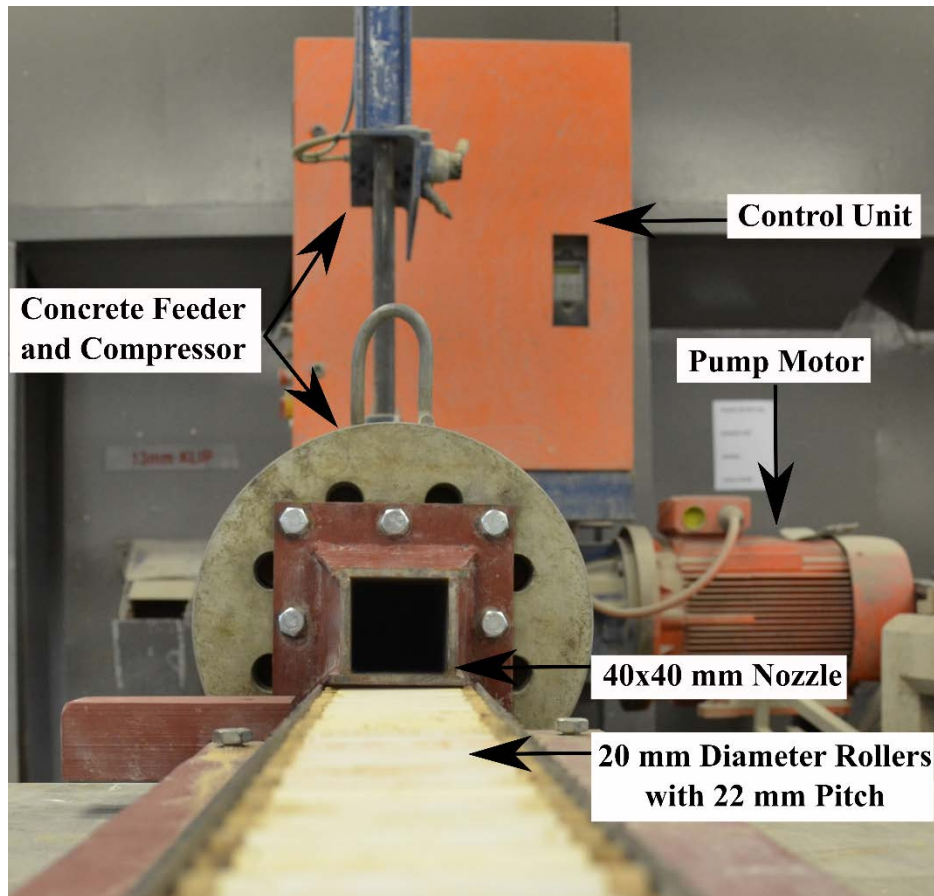


Figure 4.13: Custom-built concrete extruder used in this research indicating the control unit, pump motor, platform equipped with rollers, 40x40 mm square nozzle and the concrete feeder location and compressor.

Figure 4.14 illustrates the extruded filament layer. The extrudate, at a height of 40 mm, did not retain its original shape, with most deformation occurring at the bottom horizontal extremes of the layer. This deformation closely emulates the distorted cross-sectional shape depicted in Figure 4.7, which is coupled to the governing failure in zone 2. This result, however, does not indicate plastic flow of the material. In Figure 4.14a, a clear linear decrease in the filament layer's height is observed starting at a certain distance from the nozzle, which did not experience any significant change in height. This section of extrudate also does not demonstrate the same magnitude of horizontal deformation as the section that experienced a decrease in height, as depicted in Figure 4.14b. The large horizontal bulge observed in Figure 4.14b is due to the increasing longitudinal stress linked to the mass of the extrudate that increases as the length of the extruded filament increases. Consequently, more force is required to extrude the material through the nozzle that induces an increasingly larger longitudinal compressive stress. The section behind the bulge that did not experience significant deformation is ascribed to the

Chapter 4: Shape Retention Model

delay in complete stoppage of the screw's rotational velocity after cutting power to the motor. It is evident that the filament layer height decreases as the absolute extruded distance of the filament increases.

Figure 4.15 depicts this behaviour in more detail. Each picture, numbered to indicate chronological order, depicts the filament cross-section as it passes a roller e.g. picture 1 indicates the filament cross-section that just passed roller 1 and so forth. Notice that the bottom right corner of the filament completely sticks to the plastic sheet and consequently compels the horizontal deformation to occur above that point (refer to Figure 4.7). This horizontal deformation increases with the number of times that particular section of the filament passes a roller. This is due to the plastic sheet not being stiff enough to prevent sagging in between rollers. As a result, an impulse is generated as the filament crosses each roller, reducing its strength. The interparticle forces in failure zone 2, which are under the highest stress due to self-weight (refer to Figure 4.5 and 4.7), are broken due to this additional impact. Consequently, particles settle under gravity, i.e. localised plastic flow occurs, until equilibrium is restored in their new positions due to the re-flocculation thixotropy mechanism (Kruger et al., 2019b). This deformation occurs at each roller and compounds as the extrudate reaches greater absolute lengths. Note that these deformations are indeed permanent and can be regarded as plastic deformations. However, these deformations are limited to the zone where the highest stresses are present and plastic flow of the entire filament does not result. Also, notice that the material does not slip at its bottom where it sticks to the plastic, but rather the horizontal deformation above this point protrudes and rolls over the edge that sticks, yielding a new fixed constraint. This behaviour is evident by following the bottom left corner of the filament in Figure 4.15. This process continues to result in the final deformed shape depicted in Figure 4.14c. The result is significant as it indicates the acute sensitivity of a highly thixotropic material to vibrations, which essentially is equivalent to the cumulative effect that each roller has on the filament (Zaeem et al., 2009). Vibrations should thus be avoided or minimised to yield adequate shape retention after extrusion. This explains the plastic deformations, in particular the decrease in filament height as a function of absolute extruded distance. The filament section that did not experience a decrease in height acts as confirmation that plastic flow did not occur under self-weight for the material that did not cross any roller. The authors therefore conclude that plastic flow did not occur at a 40 mm layer height as predicted by the governing Equation 4.16.

The confinement check test method described in Section 4.2.4 was performed after extruding the filament. The one end of the filament was kept stationary while the other end was lifted until slippage of the filament on the plastic sheet was observed. This occurred at roughly a 42° inclination angle. From Figure 4.11, a material with Poisson's ratio of 0.3 requires an inclination angle of 30° or larger for confinement to occur. Thus, confinement is predicted to occur, which is demonstrated and evident in Figure 4.15. The applicability of the model is therefore justified.

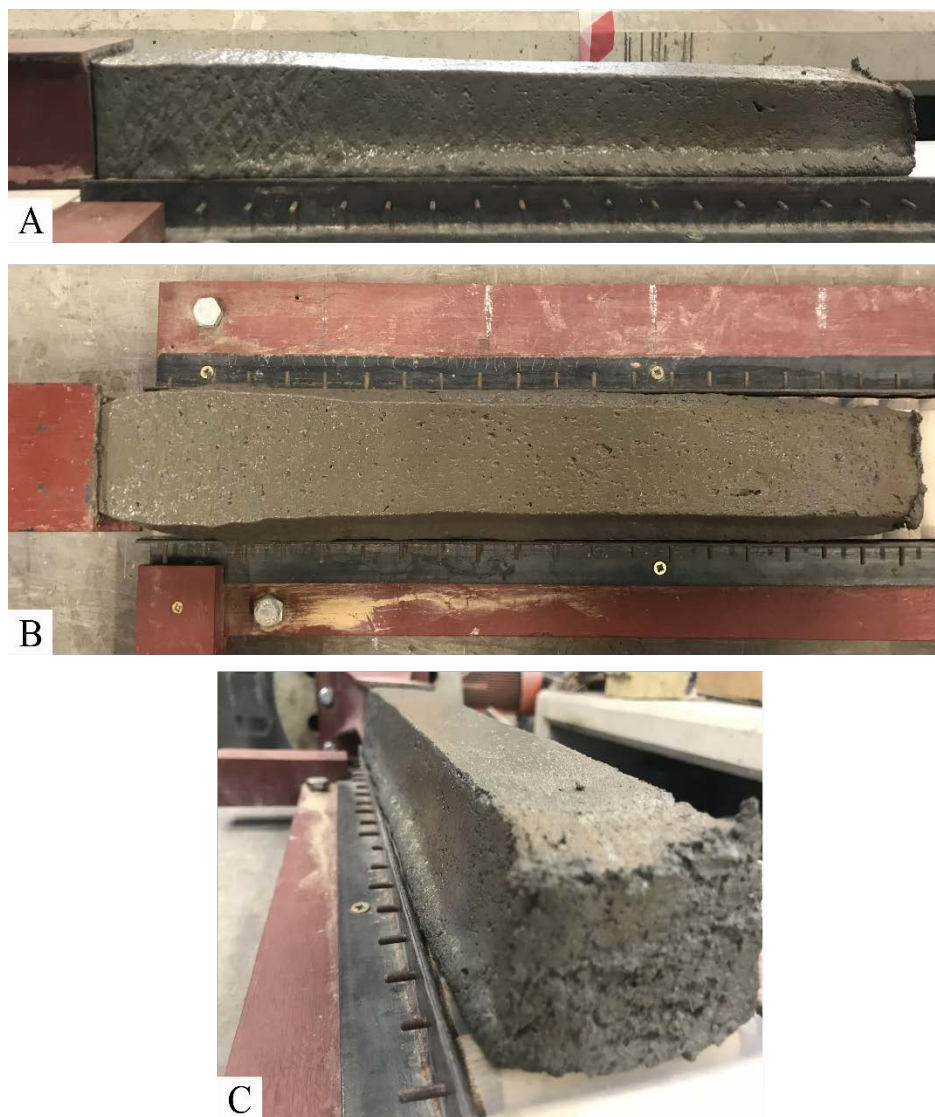


Figure 4.14: Extruded filament layer with dimensions 40x40 mm illustrated by a) side view, b) top view and c) perspective view.

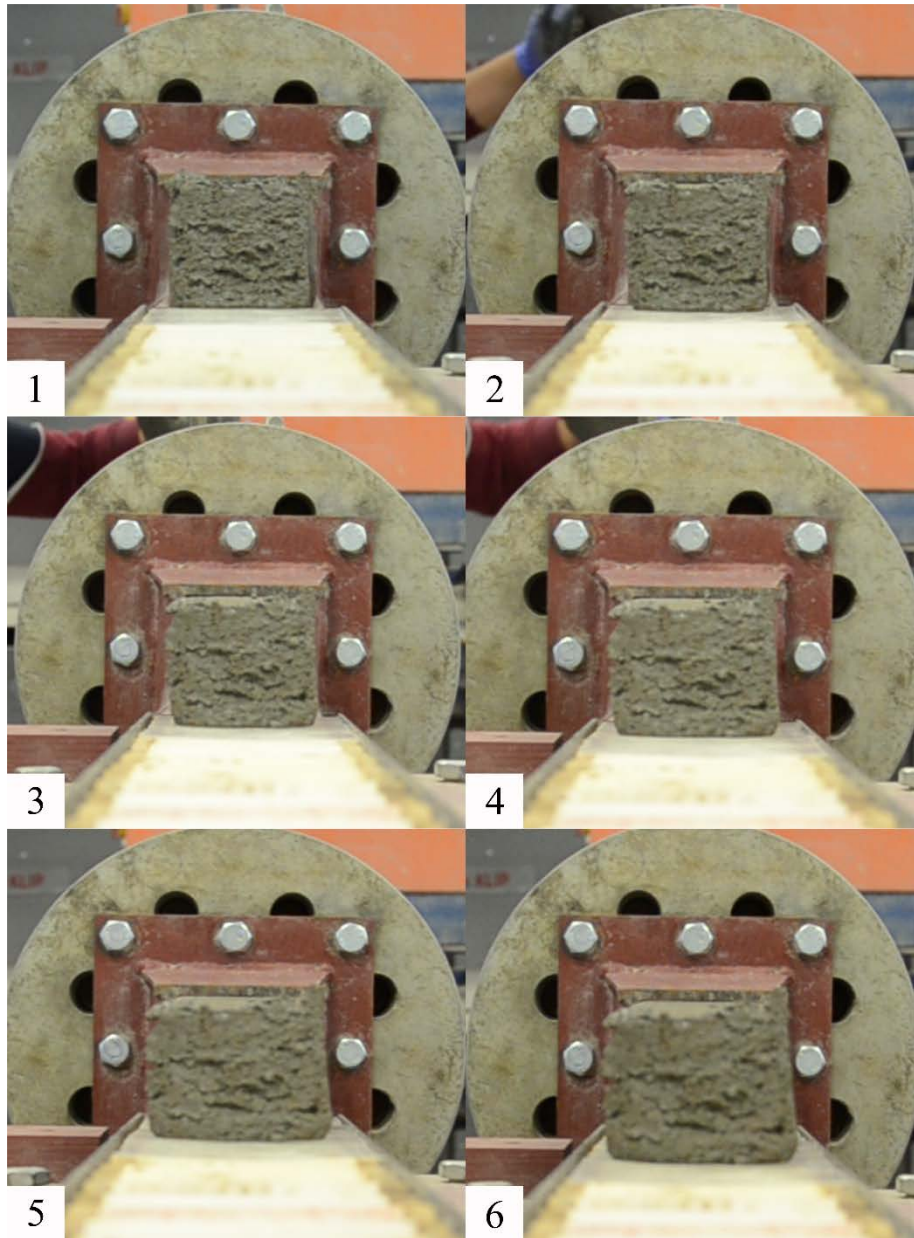


Figure 4.15: Front view of the filament layer as it is being extruded from the nozzle. Each picture, numbered to indicate chronological order, depicts the cross-section of the filament as it crosses a roller.

4.4 Numerical verification

A finite element analysis (FEA) is conducted in order to serve as numerical verification of the model after completion of the experimental verification process. A simplified plane strain section of filament is modelled in Abaqus CAE (Dassault Systèmes, n.d.) and the height at which plastic yielding under self-weight occurs determined. The mechanical properties of the material used for the experimental verification are determined and used as input parameters for

the model. Confinement and the governing failure mode illustrated in Section 4.2 are visually validated in this section.

4.4.1 Material tests & results

The material parameters depicted in Table 4.3, namely the Poisson's ratio and density, are also used as input for the numerical model. The application of the Mohr-Coulomb failure criterion, as described in Section 4.2.3, necessitates the material's cohesion and interparticle friction. Lastly, the elastic response of the material in the form of its Young's modulus is required. Only a brief summary about the determination of these material properties are presented since the focus of this research is mainly on the rheological characterisation component.

The SU 3DPC material's cohesion and interparticle friction are determined via the direct shear test (DST) according to ASTM D3080/D3080M (ASTM Standard D3080/D3080M, 2012), facilitated by the apparatus illustrated in Figure 4.16a. A test rate of 5 mm/min is set for the 19 mm horizontal stroke. Three levels of vertical force are selected to allow a Mohr-Coulomb response evaluation, causing $\sigma_n = 0.25, 3.3$ and 6.5 kPa compressive normal stress respectively. Thereafter, an inverse finite element (FE) analysis is performed with Abaqus to determine the elastic response of the material, due to the unavailability of appropriate testing equipment at SU. The direct shear test is simulated as depicted in Figure 4.16b by assigning all relevant material parameters and then iteratively determining the Young's Modulus. Six-node triangular elements (CPE6M) are used with side lengths of 0.5 mm. The shear box plates are placed 0.5 mm apart and modelled as rigid bodies. The base is constrained against translation, and after application of the self-weight and vertical load, the top plate is displaced horizontally to simulate the shear box action to a full stroke of 19 mm. More detailed information regarding the mechanical characterisation of the SU 3DPC material is available here (Bester et al., 2019).

The results are summarised in Table 4.5. Note that the material is tested immediately after completion of the concrete mixing process. No account is made for the shear history of the material e.g. breakdown of the microstructure due to the pump's screw and transportation via hose for 3DPC. Consequently, these material properties may result in overprediction, as it is not representable of what is actually extruded from the printer's nozzle. In order to address this problem, of which no literature is currently available, the dynamic yield shear stress from the initial rheology test depicted in Figure 4.12 is taken as a fraction of the corresponding static yield shear stress (0.115) and applied to the mechanical test results as an attempt to approximate

Chapter 4: Shape Retention Model

the breakdown induced by the pumping process. The authors acknowledge that this approximation may not be entirely theoretically correct, but in the wake of no literature accepted as a feasible assumption.

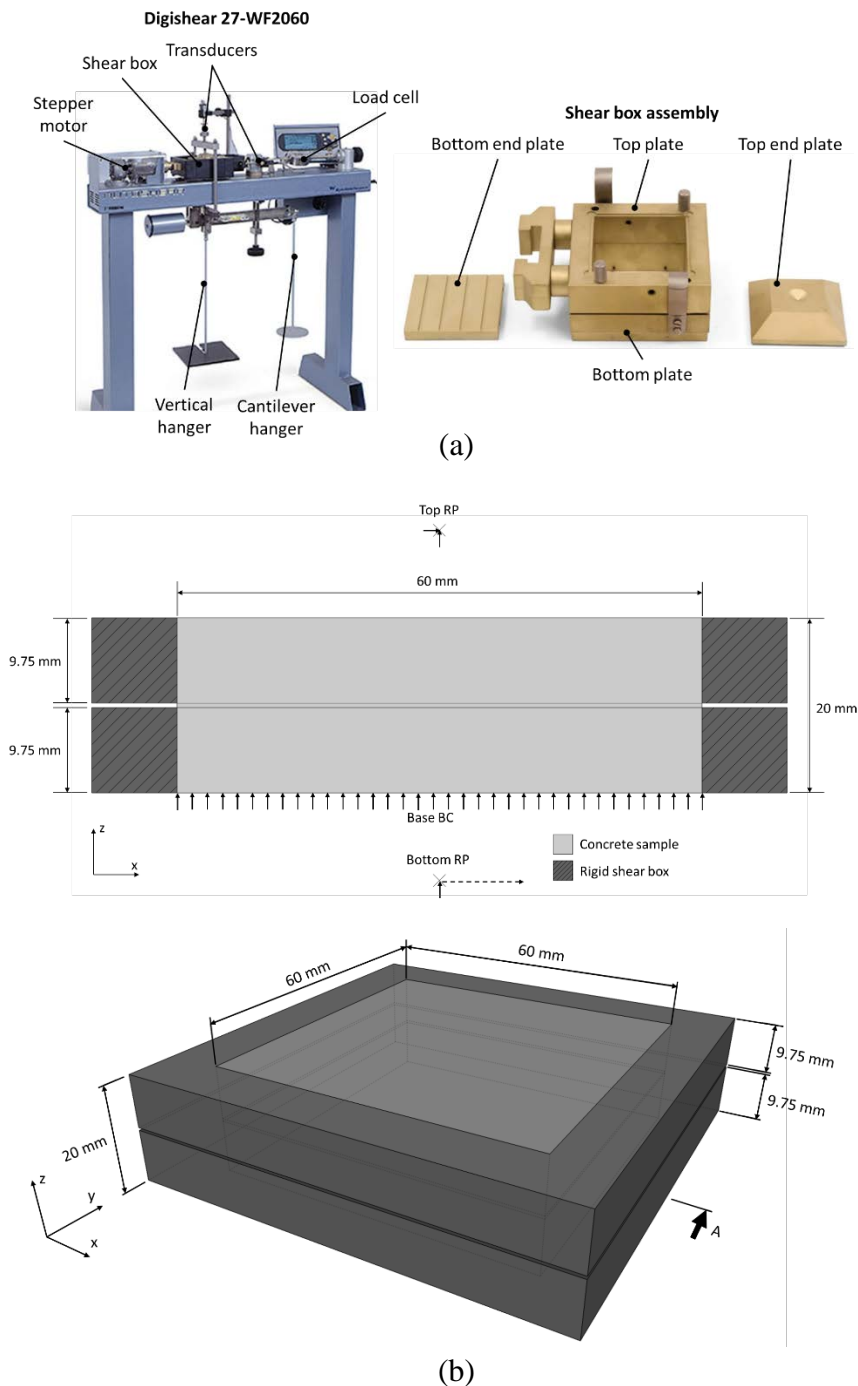


Figure 4.16: Mechanical properties experimental testing indicating a) Digishear 27-WF2060 direct shear test apparatus and b) FE schematisation of the direct shear box test showing (top) the plane stress representation in the FE modelling approach and (bottom) the isometric view of the shear box.

Table 4.5: Summarised material parameters as input for the numerical model. Young's modulus and cohesion adjusted to account for breakdown induced by the pumping process.

	Material Properties from Testing	Material Properties Adjusted for Shearing (11.5%)
Density	2150 kg/m ³	-
Poisson's Ratio	0.3	-
Young's Modulus	107.87 kPa	12.4 kPa
Cohesion	6.01 kPa	0.69 kPa
Interparticle Friction	34.52°	-

4.4.2 Finite element model

A static FE numerical model of the extruded filament is presented by means of a simplified plane strain approach, as also presented in Section 4.2.3. The Mohr-Coulomb failure criterion is employed to correspond with the analytical model developed in Section 4.2. A filament cross-section with unit thickness is considered for the FE model and the material properties summarised in Table 4.5 assigned. The mesh constitutes of 8-node biquadratic plane strain quadrilateral (CPE8) elements with side lengths of 2 mm. The non-linear geometry function is enabled to account for large strains. A gravitational load is applied to induce a self-weight stress in the filament. The bottom of the filament is constrained against translation in the vertical and horizontal directions, which are consistent with the findings in Section 4.3.4 that confinement occurs in this instance. The dilation angle is assumed to be 13° (Wolfs et al., 2018).

4.4.3 Numerical results

Two case studies are presented in this section namely one where interparticle friction is neglected and another where it is included in the analysis. This enables for the comparison with the result obtained by the analytical model (Section 4.3.3) that does not account for interparticle friction. However, the case that accounts for interparticle friction represents the actual shape retention capabilities of the material and depicts the extent to which the analytical model underpredicts the stable filament layer height.

Figure 4.17 illustrates the results of the FEA for the case where interparticle friction is omitted. The filament layer height whereby the onset of plastic yielding transpires was

determined as 42.9 mm, 3.1 mm less than the analytical model's prediction. This height was obtained by parameterisation facilitated by Python scripting of the FEA model. The height at which plastic yielding was initially observed, however small, was chosen as the critical filament layer height due to the low dynamic yield shear stress of the thixotropic material. The material thus provides considerably less resistance against flow after exceeding its static yield shear stress, determined in the previous section as 11.5 % for this study. The flow pattern can be extrapolated from Figure 4.17b that indicates the elastic strains within the critical filament layer, which strongly corresponds with failure zone 2 depicted in Figure 4.5c. Note that the confinement within the filament layer, illustrated in Figure 4.17d, experiences inconsequential deformation that is evident in Figure 4.17b. The FEA model that ignores interparticle friction therefore differs by 6.7 % compared to the analytical model's prediction and depicts profound correspondence to the theory presented in Section 4.2.

Figure 4.18 illustrates the results of the FEA for the case where interparticle friction is included in the analysis. The filament layer height whereby the onset of plastic yielding transpires was determined as 87 mm, which is 41 mm more than the analytical model's prediction. Evidently, the analytical model significantly underpredicts the actual stable filament layer height. The extent of the underprediction is however dependent on the magnitude of the interparticle friction, which in this study is large (34.52°) in comparison with that of other 3D printable concretes (20°) (Wolfs et al., 2018). An advantage of underprediction is the diminution of deformations, which the analytical model does not account for, that improve surface aesthetics of 3D concrete printed elements. An identical plastic flow propagation pattern for the larger aspect ratio is obtained as for the first case where a smaller aspect ratio is obtained, by comparison of Figures 4.18b and 4.17b. This is mainly due to the identical confinement profile obtained for both cases (Figures 4.17d and 4.18d), which confirms the postulation that a filament layer's aspect ratio does not significantly influence the three failure zones.

In summary, the analytical model underpredicted the actual stable filament layer height by 47 % due to simplification of the analytical model by negating the effect of interparticle friction; however, the extent of the underprediction is material-dependent and not universal. The analytical model's prediction is in accord with the numerical result that negates interparticle friction, yielding a 6.7 % difference in stable filament layer height.

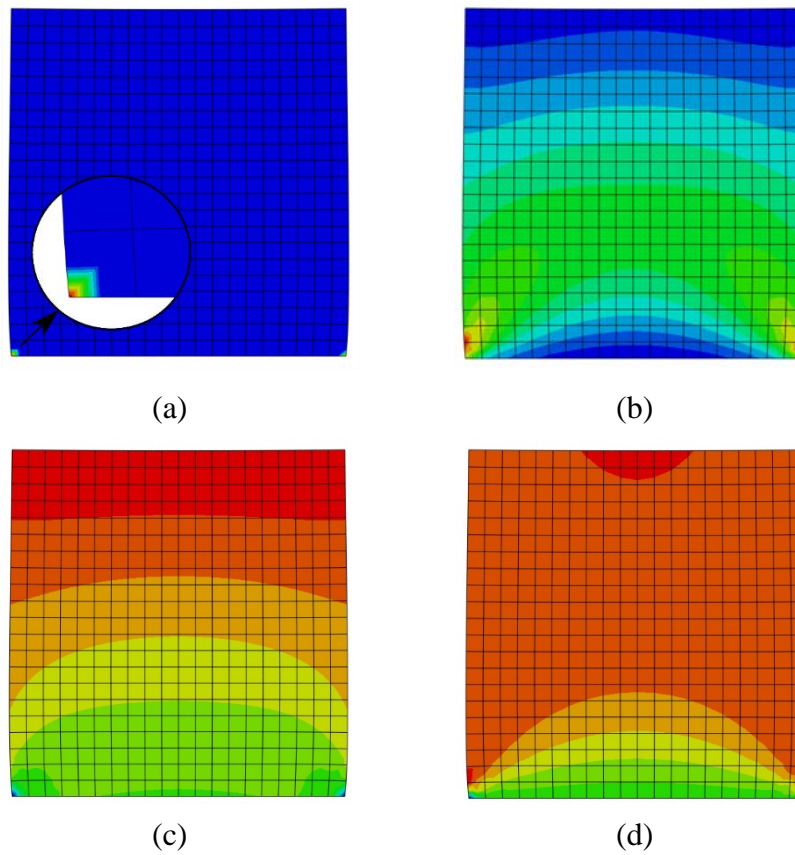


Figure 4.17: FEA of the standard SU 3DPC material with no interparticle friction indicating the a) plastic strains, b) elastic strains, c) vertical stress profile (σ_1) and d) horizontal (confinement) stress profile (σ_2) at the filament height whereby plastic yielding propagates.

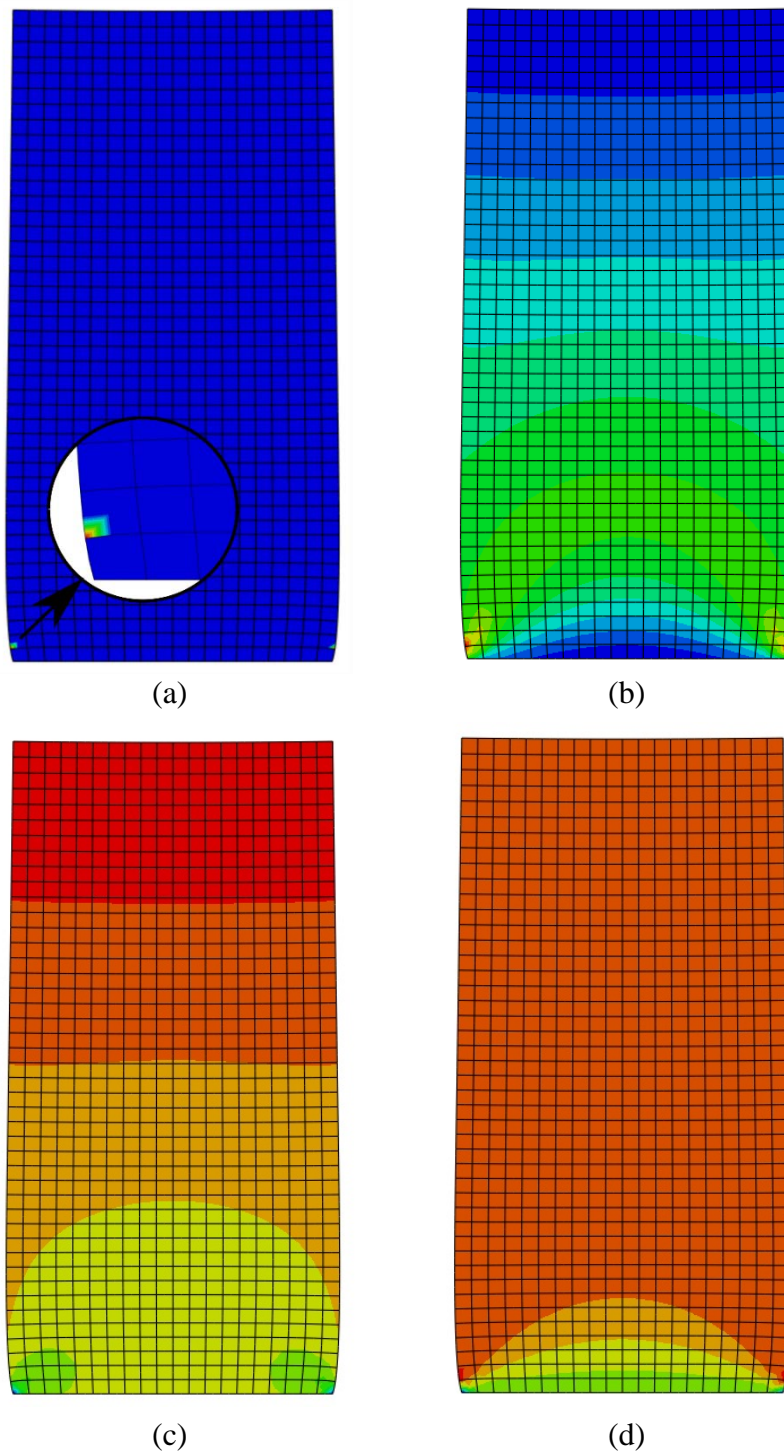


Figure 4.18: FEA of the standard SU 3DPC material with interparticle friction indicating the a) plastic strains, b) elastic strains, c) vertical stress profile (σ_1) and d) horizontal (confinement) stress profile (σ_2) at the filament height whereby plastic yielding propagates.

4.5 Conclusion

A theoretical framework for an analytical filament shape retention model is developed in this research. The model is applicable to digitally fabricated concrete processes that include extrusion, such as 3D printing of concrete. A thixotropy model developed by Kruger et al. (2019b) forms the basis for the model, negating any mechanical characterisation of a material. Relevant failure theory and zones are presented and the respective expressions for each provided. A secondary model is developed to determine whether sufficient friction is present to induce confinement within a filament layer, constituting as prerequisite for the shape retention model.

An experimental verification process is conducted by extruding the 3DPC material at SU through a custom-built extruder. The material is rheologically characterised and the model applied to predict if failure in the form of plastic yielding would occur. Thereafter, a numerical model in the form of a finite element analysis is developed to proffer as numerical verification of the analytical model. Key findings of the study are as follows:

- Equations 4.15, 4.16 and 4.19, gives the final expressions for the analytical shape retention model. As depicted in Section 4.2.3, it is concluded via parametrical observation that Equation 4.16, which describes failure in zone 2 between the laterally unconfined and confined region of the filament, will always govern failure for shape retention. This is verified in Section 4.3.3 that depicts the model predictions for the experimental study.
- The model developed to predict confinement (Section 4.2.4) is applied in the experimental verification process. Based on the material's Poisson's ratio and the simple test developed in Section 4.2.4 (refer to Figure 4.11), it is predicted that confinement will occur as there is no slippage between the filament layer and the extrusion platform. This is verified in the experimental procedure by observation of Figure 4.15.
- The governing expression of the shape retention model, Equation 4.16, predicted a maximum stable filament layer height of 46 mm for the presented material. The experimental procedure verified the applicability of the model where no plastic flow occurred at a filament layer height of 40 mm. Insignificant plastic deformations are however present, which the model does not account for.

Chapter 4: Shape Retention Model

- The analytical shape retention model is conservative, by ignoring interparticle friction for simplicity of model parameter characterisation. A 6.7 % difference in stable filament layer heights are obtained between the analytical and numerical models, for the case where interparticle friction is negated in the numerical analysis, verifying the analytical model accuracy. The numerical analysis that accounts for interparticle friction obtained a stable filament layer height of 87 mm. This is significantly larger than the analytical model's prediction of 46 mm. However, by neglecting the effect of interparticle friction and thus obtaining conservative filament layer heights, deformations are reduced.
- Identical plastic flow and failure propagation patterns were obtained by the numerical analyses compared to that presented in the analytical model's development (Section 4.2). This result is also supported by the experimental extrusion procedure.
- The experimental procedure depicts the acute sensitivity of highly thixotropic materials to vibrations, which should be avoided or minimised to obtain adequate filament shape retention after extrusion.

The authors accounted for shearing-induced breakdown of the microstructure by determining the fraction of the dynamic to static yield shear stress (0.115), and then applied it to the mechanical properties of the material since no shear was induced before testing to replicate typical 3DPC. This approximation yielded accurate numerical results; however, more research is required for confirmation.

Acknowledgements

The authors gratefully acknowledge Mr Seung Cho's assistance with the execution of the experimental testing. The research is funded by The Concrete Institute (TCI) and the Department of Trade and Industry of South Africa under THRIP Research Grant TP14062772324.

Contribution of authors

This work is part of Jacques Kruger's PhD research, executed under the supervision of Professor Gideon van Zijl and Doctor Stephan Zeranka. Mr Kruger conducted all experimental

work, the analysis, interpretation and presentation of data, as well as the writing of the manuscript. Prof. van Zijl and Dr. Zeranka assisted in proofreading of the manuscript and proposed insightful amendments.

4.6 References

- ASTM Standard D3080/D3080M. 2012. *Direct Shear Test of Soils Under Consolidated Drained Conditions*.
- Bester, F., van den Heever, M., Kruger, P.J., Zeranka, S. & van Zijl, G. 2019. Benchmark structures for 3D concrete printing. In International Federation for Structural Concrete *Proceedings of the 16th fib International Symposium*.
- Buswell, R.A., Silva, W.R.L. De, Jones, S.Z. & Dirrenberger, J. 2018. 3D printing using concrete extrusion: A roadmap for research. *Cement and Concrete Research*. 112(October 2017):37–49.
- Carcione, J.M. & Cavallini, F. 2002. Poisson's ratio at high pore pressure. *Geophysical Prospecting*. 50:97–106. [Online], Available: <http://www.lucabaradello.it/carcione/CC02.pdf>.
- Cho, S., Kruger, J., Zeranka, S., van Rooyen, A. & van Zijl, G. 2019. Rheology of 3D printable light weight foam concrete incorporating nano-silica. In Dresden, Germany *Proceedings of the 2nd International RILEM Conference on Rheology and Processing of Construction Materials*.
- Choi, M., Roussel, N., Kim, Y. & Kim, J. 2013. Lubrication layer properties during concrete pumping. *Cement and Concrete Research*. 45:69–78.
- Dassault Systèmes. n.d. *Abaqus unified FEA*. [Online], Available: <https://www.3ds.com/products-services/simulia/products/abaqus/abaquscae/> [2019, April 20].
- Federal Highway Administration. n.d. *Poisson's ratio and temperature gradient adjustments*. Washington. [Online], Available: <https://www.fhwa.dot.gov/publications/research/infrastructure/pavements/pccp/execsumm/valtm12a.pdf>.
-

- Flitta, I. & Sheppard, T. 2005. Material flow during the extrusion of simple and complex cross-sections using FEM. *Materials Science and Technology*. 21:648–656. doi:10.1179/174328405X43045.
- Germann Instruments. n.d. *ICAR Rheometer*. [Online], Available: <http://germann.org/products-by-application/rheology-of-concrete/icar-rheometer> [2018, July 24].
- Kruger, P.J., Zeranka, S. & van Zijl, G.P.A.G. 2019a. 3D concrete printing: A lower bound analytical model for buildability performance quantification. *Automation in Construction*. 106(October 2019):102904.
- Kruger, P.J., Zeranka, S. & van Zijl, G.P.A.G. 2019b. An ab initio approach for thixotropic characterisation of (nanoparticle-infused) 3D printable concrete. *Construction and Building Materials*. 224(2019):372-386.
- Martens, P.A., Mathot, M., Coenders, J.L., Bos, F.P. & Rots, J.G. 2017. Optimising 3D printed concrete structures using topology optimisation. In Hamburg, Germany: International Association for Shell and Spatial Structures *Proceedings of the IASS Annual Symposium*.
- Nerella, V.N., Beigh, M.A.B., Fataei, S. & Mechtcherine, V. 2019. Strain-based approach for measuring structural build-up of cement pastes in the context of digital construction. *Cement and Concrete Research*. 115(August 2018):530–544.
- Paul, S.C., van Zijl, G.P.A.G., Tan, M.J. & Gibson, I. 2017. A Review of 3D Concrete Printing Systems and Materials Properties: Current Status and Future Research Prospects. *Rapid Prototyping Journal*. 24(4):784–798.
- Roussel, N. 2006. A thixotropy model for fresh fluid concretes: Theory, validation and applications. *Cement and Concrete Research*. 36(10):1797–1806.
- Roussel, N. 2012. *Understanding the Rheology of Concrete*. N. Roussel (ed.). Cambridge, UK: Woodhead Publishing Limited.
- Roussel, N. 2018. Rheological requirements for printable concretes. *Cement and Concrete Research*. 112(March):76–85.
- De Schutter, G., Lesage, K., Mechtcherine, V., Nerella, V.N., Habert, G. & Agusti-Juan, I. 2018. Vision of 3D printing with concrete - Technical, economic and environmental potentials. *Cement and Concrete Research*. 112(SI : Digital Concrete 2018):25–36.
-

-
- Secieru, E., Cotardo, D., Mechtcherine, V., Lohaus, L., Schrö, C. & Begemann, C. 2018. Changes in concrete properties during pumping and formation of lubricating material under pressure. *Cement and Concrete Research*. 108(January):129–139.
- Secieru, E., Khodor, J., Schröfl, C. & Mechtcherine, V. 2018b. Formation of lubricating layer and flow type during pumping of cement-based materials. *Construction and Building Materials*. 178:507–517.
- Suiker, A.S.J. 2018. Mechanical performance of wall structures in 3D printing processes: Theory , design tools and experiments. *International Journal of Mechanical Sciences*. 137(January):145–170.
- Vantyghem, G., Steeman, M., Boel, V. & De Corte, W. 2018. Multi-physics topology optimization for 3D-printed structures. In Boston, USA: International Association for Shell and Spatial Structures *Proceedings of the IASS Symposium*. [Online], Available: <http://hdl.handle.net/1854/LU-8583228>.
- Vosahlik, J. 2018. Pumping of Concrete Mixtures: Rheology, Lubrication Layer Properties and Pumping Pressure Assessment. Kansas State University. [Online], Available: <http://hdl.handle.net/2097/39134>.
- Wolfs, R.J.M., Bos, F.P. & Salet, T.A.M. 2018. Early age mechanical behaviour of 3D printed concrete: Numerical modelling and experimental testing. *Cement and Concrete Research*. 106(May 2017):103–116.
- Zaem, M.A., Lapin, S. & Matveev, K. 2009. The effect of vibration on flow rate of non-newtonian fluid. In *Proceedings of the SIAM Conference on “Mathematics for Industry”*. 137–141.

Chapter 5

3D concrete printing: A lower bound analytical model for buildability performance quantification

Jacques Kruger, Stephan Zeranka, Gideon van Zijl

Division for Structural Engineering and Civil Engineering Informatics, Stellenbosch University, 7600, South Africa

Reproduced and reformatted from an article published in the *Automation in Construction Journal*. (DOI: 10.1016/j.autcon.2019.102904)

Abstract

Concrete structures are 3D printed in the plastic state, therefore emphasis should be placed on the rheological characterisation of these materials to ensure that they are appropriate for 3D printing as well as for quality control. In this research, an analytical model based on the novel rheological characterisation of a material is presented as a method for quantifying the buildability performance of a 3D printable concrete/mortar. Structural instability of a freshly printed object e.g. elastic buckling is not accounted for as this model is only based on physical nonlinearity, in particular plastic yielding. The failure mechanism is based on the Mohr-Coulomb failure criterion, and incorporates Tresca and Rankine limit functions, dependent on the degree of confinement. The model is considered a lower bound theorem as stress redistribution occurs in the printed filament layers. The model is verified via an experimental study that yields a conservative error of less than 10 %.

Keywords: 3D concrete printing, buildability, analytical modelling, rheology, mechanics

5.1 Introduction

3D printing of concrete (3DPC) is set to revolutionise the construction industry by yielding unparalleled aesthetics, quality control, cost-effectiveness and reduced construction times. Not only does it enjoy significant attention in the academia (Paul et al., 2017; Li et al., 2018; Perrot et al., 2016; Salet et al., 2018), but also in industry where several companies are embracing this Industry 4.0 technology (Contour Crafting Corporation, 2017; Apis-Cor, n.d.; CyBe Construction, 2018; WinSun, 2017). However, as this technology is based on additive manufacturing i.e. the successive addition of material layers to form an object, more emphasis is required on material rheology which is defined as the branch of physics that describes the deformation and flow of matter. Typically, for conventional concrete casting, the rheology of concrete is assessed via a slump test. However, this simple characterisation provides insufficient information regarding the rheology of the concrete and its appropriateness for 3D printing. A small feasible rheological domain exists for cementitious materials to be 3D printable. Thus, a more detailed rheological characterisation via a rheometer is required for optimum 3D printability. Kruger et al. (2019) proposed a novel approach for thixotropic characterisation of cementitious materials with the use of a rheometer, that specifically appertains to 3DPC.

In addition, material behaviour under loading is of critical importance for 3DPC. It directly influences buildability, defined as a material's ability to retain its shape after several layers have been deposited onto each other. It is important to note that geometrical nonlinearity i.e. elastic buckling can also be a failure mechanism in defining the buildability with a material, and not just physical nonlinearity itself. Several mechanical parameters are required to describe this behaviour. However, these parameters are difficult to obtain for concrete in its plastic state, as it rapidly gains strength and stiffness, especially over the first few hours after mixing. Hence, several tests are required over time to obtain the time dependant mechanical properties in the fresh state. In addition, some tests are not possible to conduct when the concrete's viscosity is too low.

Most models predicting buildability performance of materials for 3DPC are based on the fresh state mechanical properties of the material. Wolfs et al. (2018) developed a numerical model to analyse the mechanical behaviour of concrete in the fresh state for 3DPC purposes. A finite element analysis (FEA) is conducted using the Mohr-Coulomb failure criterion and the results compared to an experimental 3DPC procedure. The model yielded reasonable results, with a 27.5 % over-prediction of the total number of filament layers compared to the

experimental results. Importantly, the correct mode of failure is predicted. Suiker (2018) proposed a mechanistic model that considers both elastic buckling and plastic collapse of a 3DPC straight wall structure in the plastic state. An experimental procedure is conducted and the results compared to that of the model, which under predicted the total number of filament layers by 10 %. Roussel (2018) proposed an analytical model which also accounts for both physical and geometrical nonlinearity. However, as mentioned, all of the aforementioned models are based on the fresh state mechanical properties of materials (except Roussel's model that is partly based on material rheology), which are onerous to quantify experimentally.

In this research, an analytical constitutive model for buildability performance quantification is proposed based on rheological material parameters rather than the mechanical properties of materials. These parameters are obtainable for a material with any viscosity via a rheometer. This approach has the further benefit of providing valuable information regarding the appropriateness of the material for 3D printing, such as the degree of thixotropic behaviour, and can aid in material quality control. In contrast to the models based on mechanical properties, this model only accounts for physical nonlinearity, in particular plastic flow, and does not account for geometrical nonlinearity such as elastic buckling. A simplified approach is adopted to replicate Mohr-Coulomb failure, however, without determining the parameters required for said failure criterion. The ultimate aim for this analytical model is to be a simple and practical design tool to conservatively, yet accurately, determine the number of layers a 3D print can achieve depending on the rheology of the material. An experimental verification process is conducted by performing a 3D print until failure occurs which is then compared to the results obtained via the proposed model.

5.2 Model development

A synopsis of the model that is developed in this section is presented in Figure 5.1. The material resistance to failure is characterised based on a thixotropy model developed by Kruger et al. (2019). The building rate is related to the 3DPC process and determines the normal stress on the critical bottom layer by upper layer depositions. A Mohr-Coulomb plastic failure criterion is presented in Section 5.2.3 and simplified via strength correction factors based on the aspect ratios of filament layers. Section 5.2.4 develops analytical expressions for the model. Finally, limitations of the model are summarised.

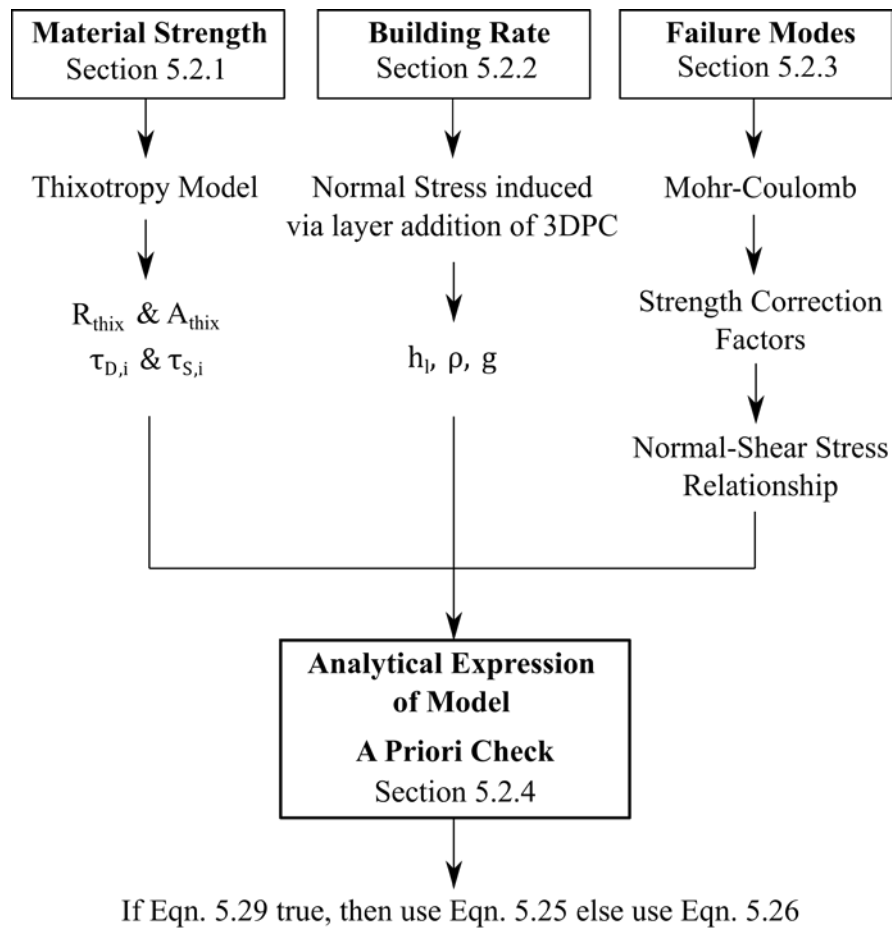


Figure 5.1: Schematic diagram illustrating a synopsis of the model development process in Section 5.2.

5.2.1 Material strength

This model is developed based on a material's shear strength in its plastic state, which can be characterised with a rheometer. The static and dynamic yield shear stresses are distinguished for a thixotropic material, as illustrated in Figure 5.2. Thixotropic material behaviour is ideal for pumping applications, because the inter-particle forces break down and only the dynamic yield stress is required to maintain flow. This results in less strain being placed on the pump as well as a reduced likelihood of segregation. However, a too low dynamic yield stress can also result in segregation of constituents. After shearing of the material stops, i.e. after extrusion through the printer nozzle, the material re-flocculates and rebuilds shear strength. This behaviour increases the load-bearing capacity of concrete in the plastic state (green strength) and improves buildability for 3DPC. More detail regarding thixotropic behaviour and rheology can be found in (Björn et al., 2012).

Chapter 5: Buildability Model

The static yield shear stress is the critical shear value in this model. It is assumed that if the applied load induces a shear stress that exceeds the static yield shear stress, failure will occur. This failure is denoted as *plastic yield*, whereby the material experiences excessive non-linear plastic deformation. For a 3D printed structure, plastic yield of filament layers will result in *plastic collapse* of the structure. Note that the model is also valid for materials that do not have a dynamic yield shear stress (i.e. that are not thixotropic), but only a static yield shear stress, e.g. linear-elastic perfectly plastic behaviour. The curve illustrated in Figure 5.2 is obtained via a material stress growth test executed using a rheometer at a constant shear rate.

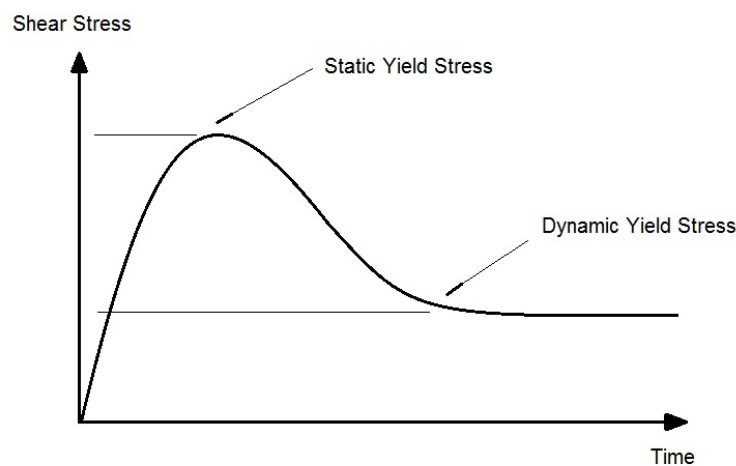


Figure 5.2: Material stress growth test depicting the static and dynamic yield shear stresses of a thixotropic material.

Kruger et al. (2019) proposed a novel approach for thixotropic characterisation of materials. A clear distinction is made between the two mechanisms responsible for thixotropic behaviour, namely re-flocculation and structuration (Roussel, 2006). This is obtained by performing multiple stress growth tests with a rheometer with varying resting time periods between tests. Typically, a test is performed at each of the following resting time periods (seconds): 0, 10, 20, 30, 40, 50, 60, 90, 120, 1200, 2400, 3600. However, these periods should not be assumed as fixed, but recommended intervals to capture thixotropic behaviour in the time frame relevant to 3DPC. For each test conducted, the static and dynamic yield stress is obtained, as illustrated in Figure 5.2.

The re-flocculation rate (R_{thix}) is determined with the yield stresses obtained for the intervals ranging between 0 and 120 seconds (short term). The static yield shear stress of each interval is plotted against its corresponding resting time gap. However, the dynamic yield shear

stress is used for the 0-second time interval. This is to simulate actual printing, whereby, as soon as the material exits the nozzle and shearing halts, the material will rebuild from its dynamic to static yield shear stress. The gradient of this plot is then obtained and represents the rate of re-flocculation (R_{thix}). The structuration rate (A_{thix}) is determined with the yield stresses obtained for the longer intervals, namely 0, 1200, 2400 and 3600 seconds. Similar to the re-flocculation rate, the static yield shear stress of each interval is plotted against its corresponding resting time gap, and the gradient of the plot is determined to yield A_{thix} . Note that in this case no dynamic shear stress value is used.

With these two parameters known, Kruger et al. (2019) proposed a bi-linear model that depicts a material's static yield shear strength evolution over time, and is schematised in Figure 5.3. This curve is used as the basis for the model developed in this research. In summary, it depicts the fresh-state strength of a material in terms of shear capacity as a function of time after deposition, specifically developed for 3DPC.

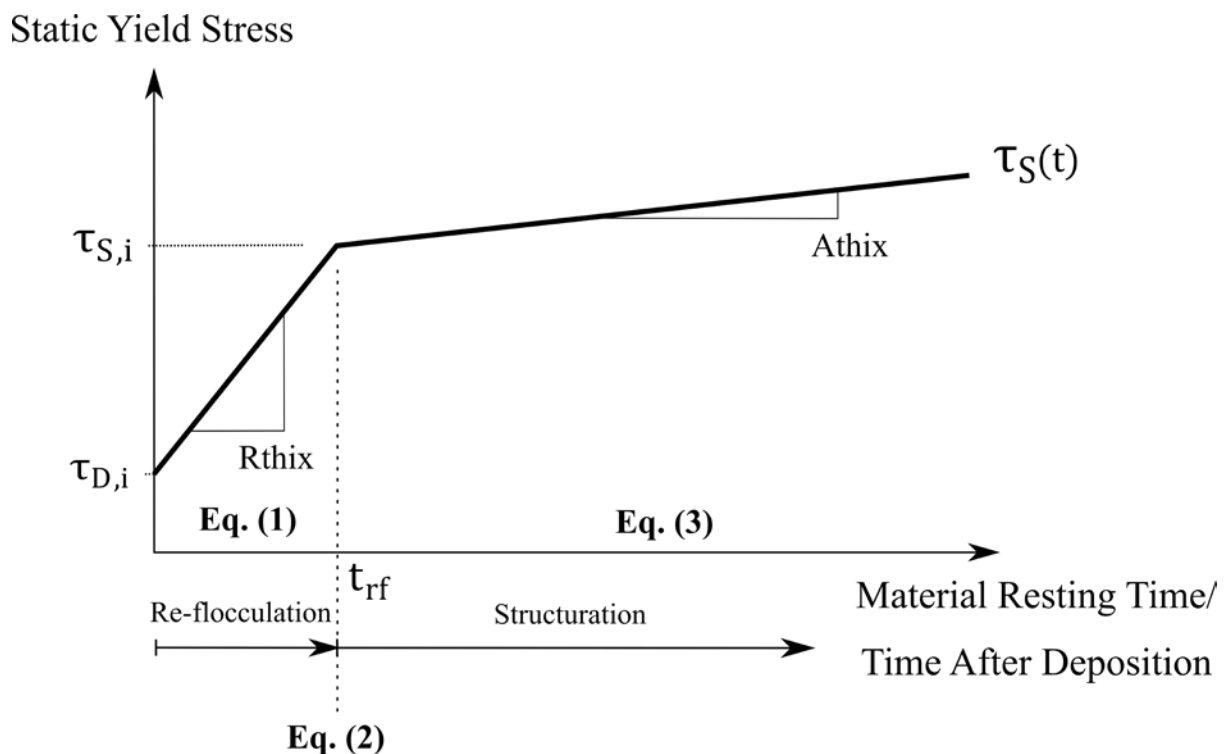


Figure 5.3: Static yield shear stress evolution as a function of resting time illustrated by both the re-flocculation and structuration thixotropy mechanisms. Equation numbers presented for their respective relevant sections.

Chapter 5: Buildability Model

The time-dependant material resistance illustrated in Figure 5.3 can be expressed mathematically as follows:

$$\tau_S(t) = \tau_{D,i} + R_{thix} \cdot t \quad (5.1)$$

$$t_{rf} = \frac{\tau_{S,i} - \tau_{D,i}}{R_{thix}} \quad (5.2)$$

$$\tau_S(t) = \tau_{S,i} + A_{thix} \cdot (t - t_{rf}) \quad (5.3)$$

With the parameters as follows:

$\tau_S(t)$	-	Static or apparent yield shear stress of the material at time t after agitation (Pa)
$\tau_{D,i}$	-	Initial dynamic yield shear stress of the material, measured from first rheological test (Pa)
$\tau_{S,i}$	-	Initial static yield shear stress of the material, measured from first rheological test (Pa)
t_{rf}	-	Time period over which re-flocculation occurs and dominates shear stress increase (s)
R_{thix}	-	Short term re-flocculation rate (Pa/s)
A_{thix}	-	Structuration rate (Pa/s)
t	-	Time since cessation of agitation (s)

Note: prerequisite [$t \leq t_{rf}$] for Equation 5.1.

5.2.2 Building rate

The building rate is defined as the rate at which a structure is 3D printed and depends on print-specific parameters and geometries. For the purpose of keeping the model as simple as possible, we will only consider a constant building rate. However, varying printing speed can be incorporated with relative ease to account for variable building rates. The significance of the building rate is that it depicts the rate of stress increase in the bottom critical layer.

A typical 3D print of an object with uniform geometry and print speed is depicted in Figure 5.4. Since the building rate is assumed to be constant, a constant printing speed and path

length yield a constant time interval per layer. A uniform geometry, referring both to the structure as well as individual filament layers, results in a constant stress increment induced on the bottom critical layer as each filament layer is sequentially deposited. This behaviour is illustrated in Figure 5.4 as a step function. Initially, while the first layer is being printed, no normal stress acts on the layer and hence the stress remains zero for the duration of that specific layer print time. Then, with the start of the next (second) layer, a stress due to the weight of that layer acts on the previous layer and continues for the duration of the layer. This step function will continue for the entire print duration due to the assumed constant building rate.

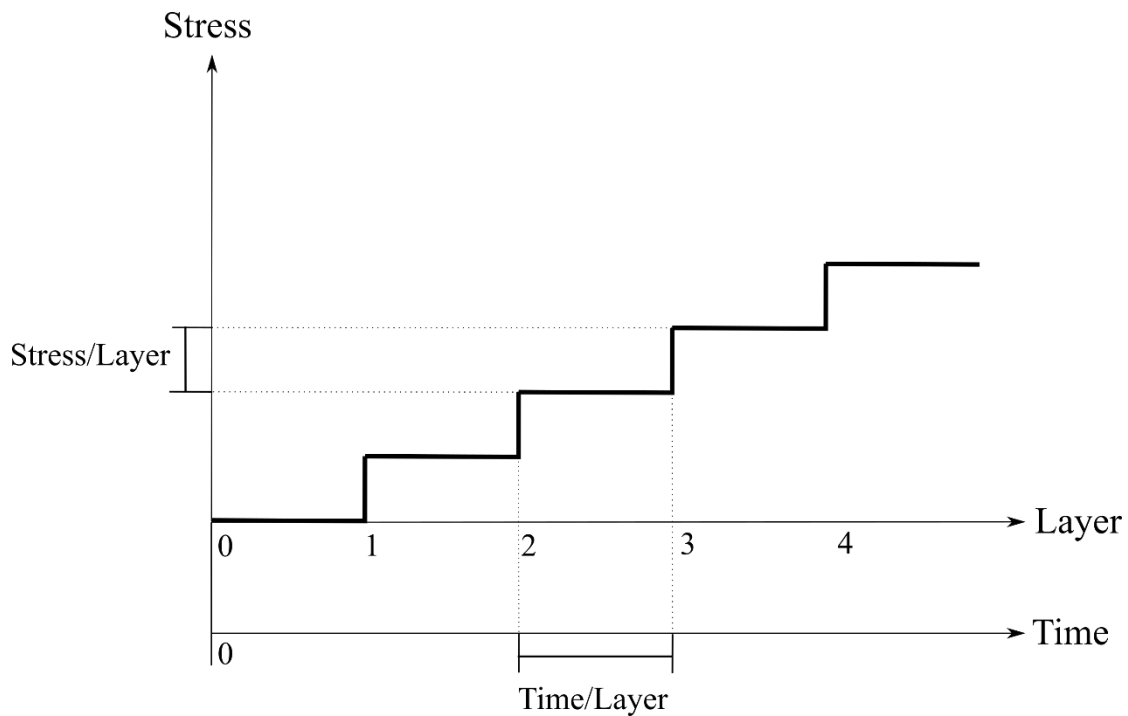


Figure 5.4: Building rate of an object with uniform geometry, defined as a step function.

In order to express the step function mathematically, the time per layer and stress per layer need to be defined in terms of print-specific variables. This is achieved with the help of Figure 5.5, where a cross-section of unit thickness in the longitudinal direction of the printed filament is considered. The expression follows:

$$\text{Normal Stress/Layer} = \frac{F}{A} = \frac{\text{Volume} \cdot g \cdot \rho}{\text{Area}} \quad (5.4)$$

$$= \frac{(h_1 \cdot w_1 \cdot 1) \cdot g \cdot \rho}{(w_1 \cdot 1)} \quad (5.5)$$

$$= h_1 \cdot \rho \cdot g \cdot 10^{-3} \quad (5.6)$$

Chapter 5: Buildability Model

h_1 is defined as the layer height (mm), ρ the material density (kg/m^3) and g the gravitational constant, taken as $9.81 \text{ m}/\text{s}^2$. Equation 5.6 is the normal stress per layer expressed in Pascal.

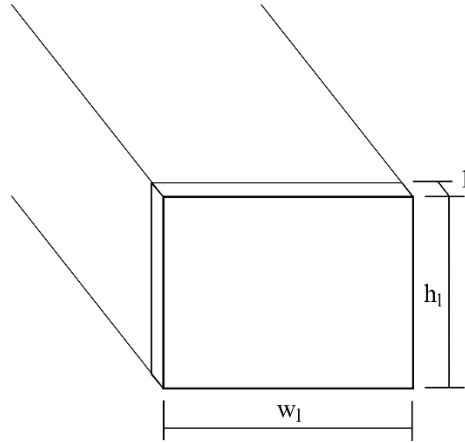


Figure 5.5: Cross-section of unit thickness in the longitudinal direction of a printed filament layer.

The time per layer is expressed by the relation between time, distance and speed:

$$\text{Time/Layer} = \frac{l_p}{v} \quad (5.7)$$

Where l_p is the constant path length of each layer (mm) and v the printing speed (mm/s). Following the characterisation of these two parameters, the step function depicted in Figure 5.4 is mathematically expressed as follows:

$$\sigma(t) = \begin{cases} h_1 \cdot \rho \cdot g \cdot 10^{-3} \cdot (0), & \frac{l_p}{v} \cdot (0) \leq t < \frac{l_p}{v} \cdot (1) \\ h_1 \cdot \rho \cdot g \cdot 10^{-3} \cdot (1), & \frac{l_p}{v} \cdot (1) \leq t < \frac{l_p}{v} \cdot (2) \\ \vdots & \\ h_1 \cdot \rho \cdot g \cdot 10^{-3} \cdot (N_L - 1), & \frac{l_p}{v} \cdot (N_L - 1) \leq t < \frac{l_p}{v} \cdot (N_L) \end{cases} \quad (5.8)$$

The total normal stress acting on the critical layer can thus be expressed as follows:

$$\sigma = \sum_{i=1}^{N_L-1} (h_1 \cdot \rho \cdot g \cdot 10^{-3})_i \quad (5.9)$$

Where N_L refers to the total number of layers as an integer, due to the step function characterisation. However, since it is a tedious process to relate the step function expression in terms of time to the material strength, a continuous normal strength expression is proposed by linearisation:

$$\sigma = \int_0^{N_L} (h_1 \cdot \rho \cdot g \cdot 10^{-3}) dN_L \quad (5.10)$$

$$\sigma(N_L) = h_1 \cdot \rho \cdot g \cdot 10^{-3} \cdot N_L, \quad N_L \in \mathbb{R} \quad (5.11)$$

This linearised function is depicted in Figure 5.6. Equation 5.11 now presents a linear relationship between the stress and time, as N_L is now an element of real numbers. In order to correct for this assumption, final answers obtained using this model (Equations 5.25 and 5.26) must be *rounded up*. This is due to the overestimation of the stress acting on the critical layer by the linearised building rate, which consequently results in an underestimation of the total number of layers obtainable.

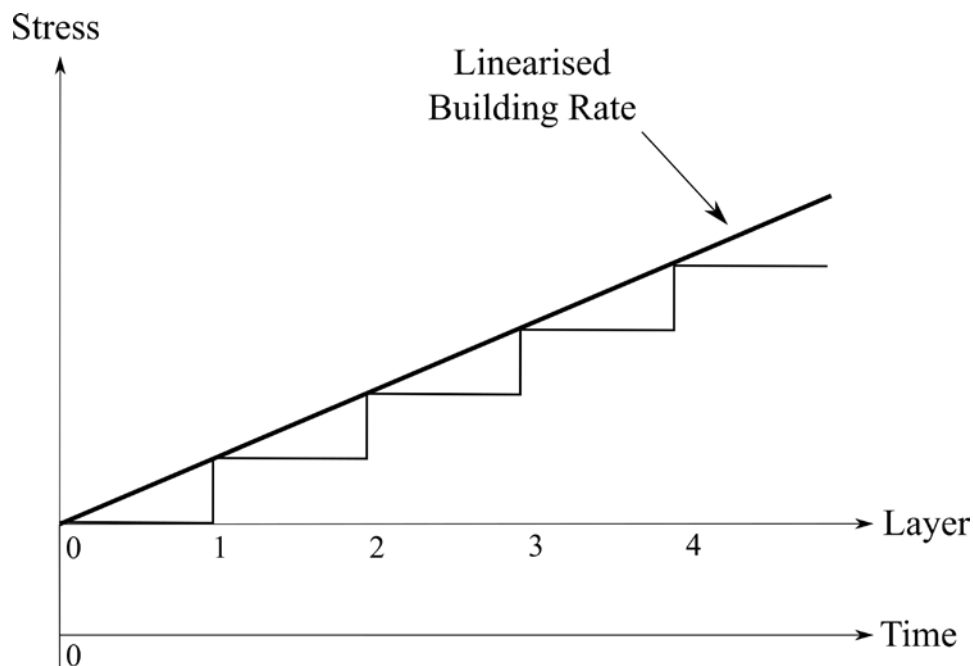


Figure 5.6: A linearised building rate to simplify model development.

5.2.3 Failure modes

The building rate described in Section 5.2.2 is expressed in terms of normal stress. This building rate is compared to the static yield shear stress evolution of a material (refer to Section 5.2.4) to determine failure. Therefore, the building rate needs to be expressed in terms of the equivalent shear stress in order to be comparable. This is achieved with material failure theory that presents a link between normal and shear stresses.

Concrete in its fresh state illustrates similar behaviour to soils. Both possess less capacity in tension than in compression. Furthermore, failure in compression is due to relative movement of particles i.e. shear failure, and not by crushing of the constituents. The pressure-dependent shear stress is described by the Mohr-Coulomb failure criterion, which accounts for both interparticle friction (φ) as well as cohesion (c), and is expressed as follows (Craig, 2004):

$$\tau = c + \sigma \cdot \tan(\varphi) \quad (5.12)$$

Alexandridis and Gardner (1981) found that the shear strength of fresh concrete immediately after mixing is mainly due to interparticle friction. Furthermore, hardening of concrete is mainly due to the development of cohesion from the early hydration products that bind the constituents together, namely ettringite and CH needles. The study concludes that the cohesion of fresh concrete is initially zero and increases with set time. It is postulated that a correlation exists between the rapid re-flocculation rate (R_{thix}) and the interparticle friction angle (φ), however this remains open for significant research. Due to stronger van der Waals interparticle forces, interparticle friction is increased. Therefore, it is theorised that increased thixotropic behaviour yields increasing interparticle friction angles. This in itself could prove significant for 3DPC, since the friction angle is described by a tangent function. Thus, for a friction angle of 45° $f(x) = 1$, and for 55° $f(x) = 1.43$. A mere 10° increase in the friction angle increases the relation between normal and shear stress in the plastic state by 43 %, if the cohesion is assumed to be zero.

Materials with high workability, i.e. highly flowable under self-weight, possess relatively small friction angles. The opposite is also true; however note that an asymptote exists at 90° for the tangent function and is thus theoretically not achievable. Should the friction angle be zero, Equation 5.12 reduces to the maximum shear stress theory, also known as the Tresca failure criterion. If the friction angle approaches 90° , Equation 5.12 is equivalent to the maximum normal stress theory, also known as Rankine's failure criterion. These two failure criteria are the extremes of the Mohr-Coulomb failure criterion, and are essential for this model.

Figure 5.7 clearly illustrates the difference between these failure criteria with the use of infinitesimal elements and Mohr circles. In the case of 3DPC, σ_1 is equivalent to the normal stress induced by subsequent deposited layers. Hence, it is equivalent to the stress depicting the building rate. In Tresca behaviour, the shear failure plane (β) is equal to 45° , which is obtained from the Mohr circle. Consequently, the following normal-shear stress relationship exists if we assume that $\sigma_3 = 0$:

$$\tau = c = \frac{\sigma_1}{2} = \frac{\sigma_{\text{applied}}}{2} \quad (5.13)$$

This simple relationship requires no material properties, which reduces the amount of material tests that need to be conducted. Equation 5.13 will form the basis relationship for the model. Importantly, it should be noted that the ratio of σ_1 to τ_{crit} is normalised as 1 in this case. τ_{crit} is the critical shear stress value where plastic failure will occur and is related to the bilinear time-dependent thixotropy model presented in Section 5.2.1. Note that the thixotropy model takes into account both the interparticle friction and cohesion properties of a material and represents it as a time-dependent value $\tau_{\text{crit}}(t)$.

Mohr-Coulomb presents a shear failure plane between 0 and 45° where in the case of Rankine the failure plane approaches 0° . However, in both these cases a significantly more complex relationship between normal and shear stress can be expressed as follows:

$$\tau(t) = c(t) + \left[\left(\frac{\sigma_1 + \sigma_3}{2} \right) - \left(\frac{\sigma_1 - \sigma_3}{2} \right) \cdot \sin(\varphi(t)) \right] \cdot \tan(\varphi(t)) \quad (5.14)$$

Note that for these two cases it is assumed $\sigma_3 \neq 0$, which is explained further along in this section. More material properties (c , φ) are now required to derive a normal-shear stress relationship, and consequently more material tests need to be conducted. Plane strain conditions are assumed for this model and the associated principle stresses indicated in Figure 5.8.

Chapter 5: Buildability Model

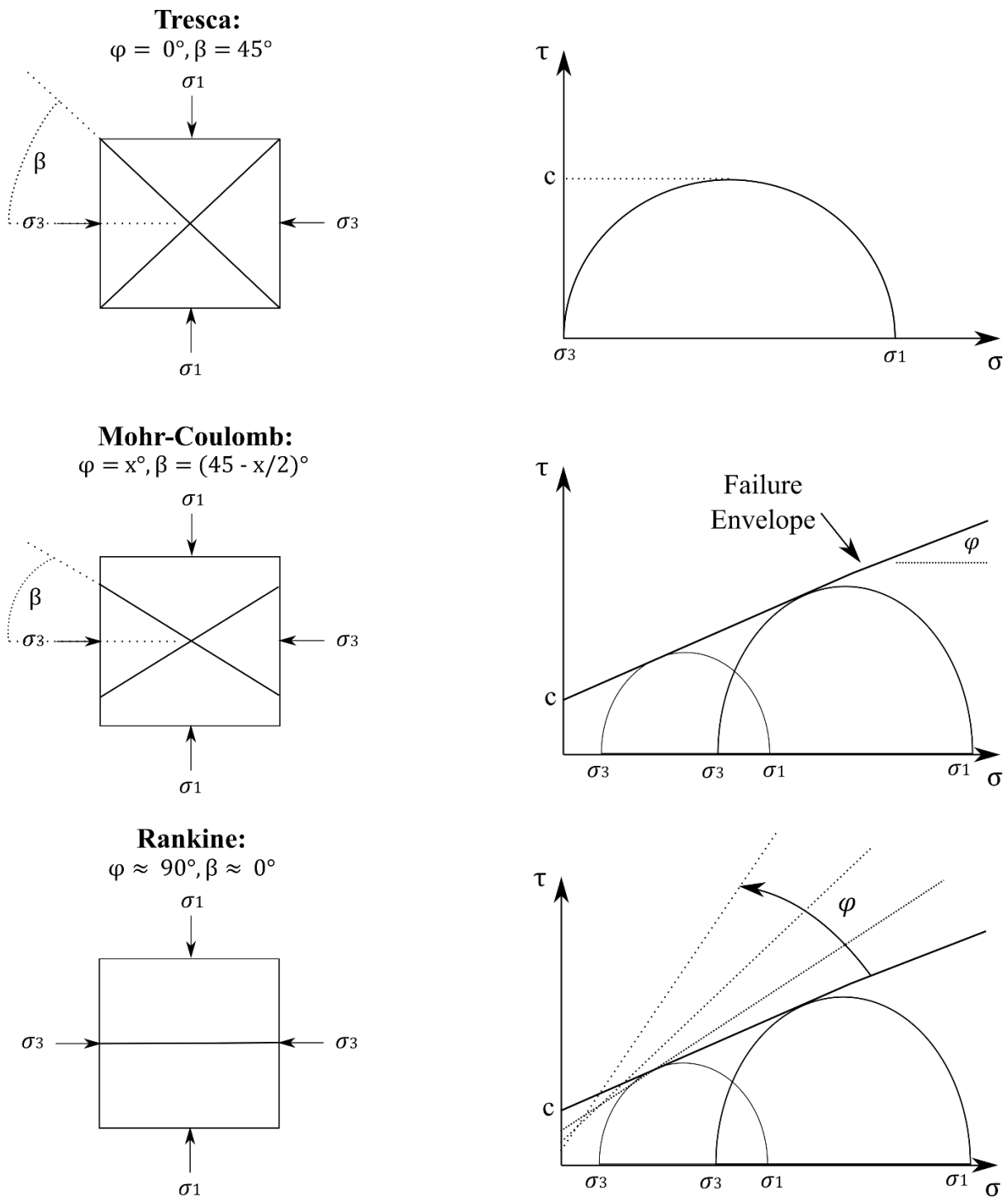


Figure 5.7: Tresca, Mohr-Coulomb and Rankine behaviour illustrated by means of infinitesimal elements and Mohr circles. Parts of figure reproduced from (Saloustrous et al., 2015).

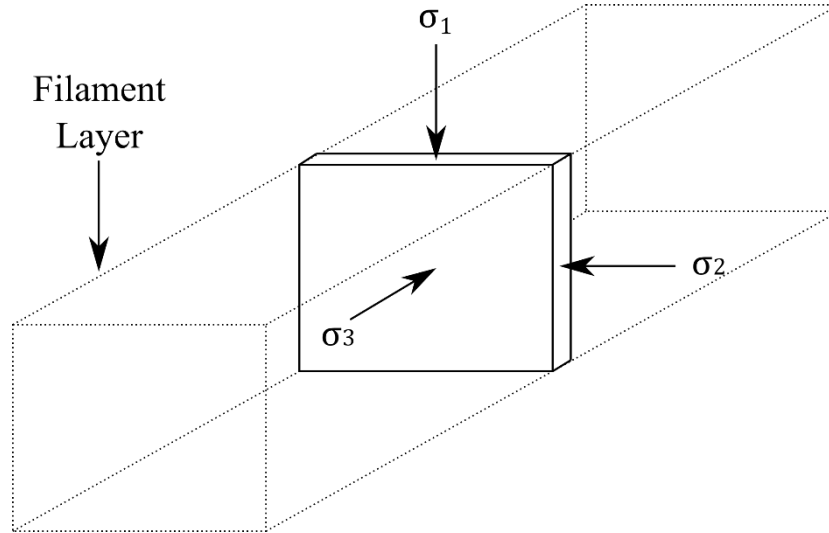


Figure 5.8: Global plane strain element of unit width with its associated principle stress directions.

Plane strain is assumed on the assumption that no deformation can occur in the longitudinal direction of the filament layer ($\epsilon_3 = 0$) due to lateral confinement. Consequently, due to the applied normal stress from subsequent layers (σ_1), the element will experience strain in the transverse direction (ϵ_2), in addition to being compressed in the vertical direction (ϵ_1). However, friction between the print bed surface and filament layer, as well as interlayer friction between successive deposited filament layers, prevents transverse strain. This in turn induces a transverse stress:

$$\sigma_2 = \mu_s(t) \cdot \sigma_1 \quad (5.15)$$

This frictional-restrained stress is depicted as a fraction of the vertically induced stress and depends on the magnitude of the static friction coefficient, μ_s . The first filament layer will always have a higher yield stress than the following layer, as can be interpreted from the thixotropic model in Figure 5.3. As the time between layer deposition increases, so too will the chance of cold joint formation, and consequently increased friction between layers is obtained. However, it is further postulated that a material with a large rapid re-flocculation rate (R_{thix}) and shorter time interval between layer depositions will yield increased interlayer bond strength between filament layers. Since the bottom layer is always stronger and stiffer than the layer on top, the relative transverse deformation of the top to bottom layer may be larger than one under the applied stress. However, due to the strong interlayer bond strength, the relative deformation

will be restrained, and consequently σ_2 grows in magnitude. This statement is open for significant research.

The stress in the longitudinal direction (σ_3) does not equal zero due to the assumption of plane strain conditions and is expressed as follows:

$$\sigma_3 = \nu(t) \cdot (\sigma_1 + \sigma_2) \quad (5.16)$$

$$= \nu(t) \cdot \sigma_1 \cdot (1 + \mu_s(t)) \quad (5.17)$$

Where $\nu(t)$ is the time-dependent Poisson's ratio of the material. Note that σ_3 in Figure 5.7 does not necessarily refer to Equation 5.17, but should be taken as the smallest principle stress of Equation 5.15 and 5.17 ($\sigma_{3, \text{Fig 5.7}} = \min(\sigma_2, \sigma_3)$). This is to allow the determination of the maximum shear stress, which is the radius of the largest Mohr circle representing the material point stresses.

In order to account for Mohr-Coulomb and Rankine behaviour, four additional material properties are required for Equation 5.14: $c(t)$, $\phi(t)$, $\mu_s(t)$ and $\nu(t)$. Furthermore, these additional material tests need to be conducted over a certain time period in order to determine the time-dependent functions. This significantly complicates the buildability model and will become a tedious process to execute. Up until this point, stress states are assumed to be homogeneous throughout the cross-section of the filament layer due to the global plane strain element simplification. However, this is a broad assumption since the stress state on an infinitesimal plane strain element depends on its position globally. In addition, the shape effect of concrete influences the stress state remarkably and is characterised by the aspect ratio of filament layers (h_1/w_1).

This shape effect behaviour is synonymous with the unconfined compression strength (UCS) test. Typical UCS specimens have an aspect ratio of two (length of 200 mm to diameter of 100 mm). In this specimen, no lateral confinement is present and therefore the test only depicts the maximum uniaxial strength of a material in compression. However, that is only assuming global stress state conditions. In actuality, confinement occurs at the contact points between the specimen and testing bed platens due to friction. This induces a multiaxial stress state in certain regions within the specimen as depicted in Figure 5.9 (Chung, 1989). The triangular shaped confinement makes an angle of between 20 and 30° with the direction of the applied load. However, an increase in the measured UCS of the specimens is observed with aspect ratios smaller than two (Lamond & Pielert, 2006; Smith, 2016).

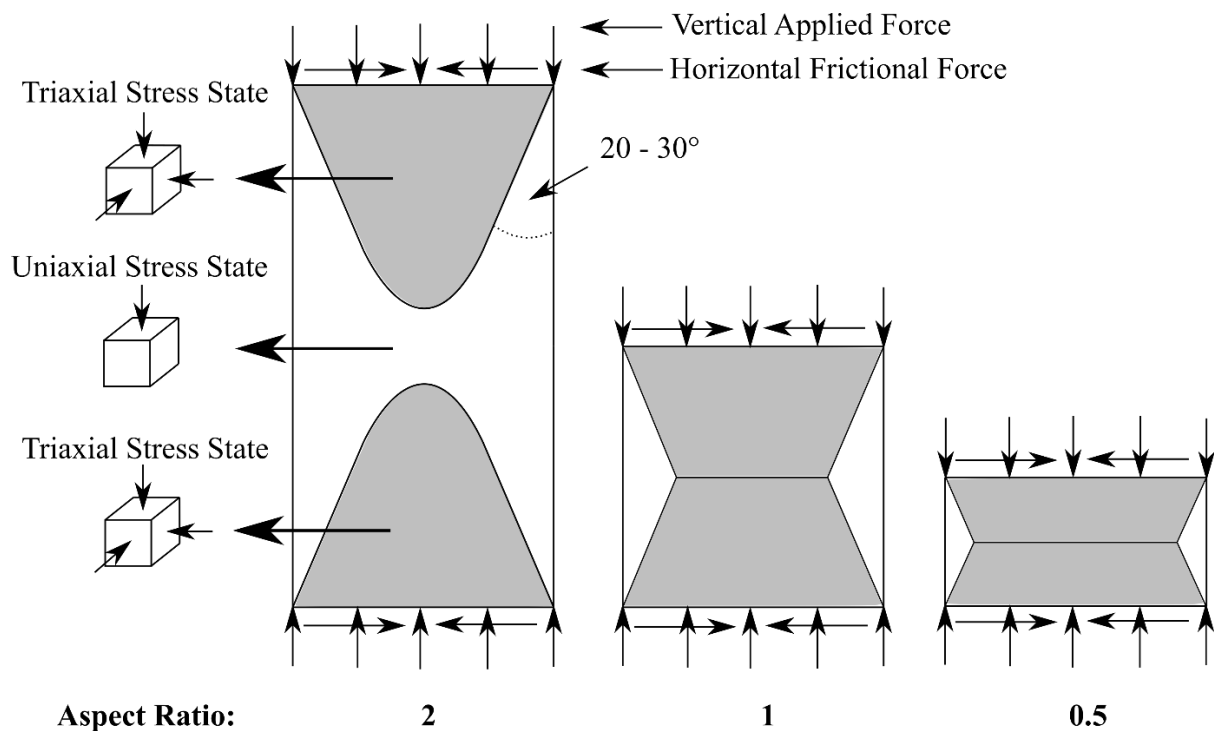


Figure 5.9: Confinement within concrete samples of different aspect ratios together with the respective stress states indicated on infinitesimal elements.

Fresh state concrete specimens for UCS tests with aspect ratios of two typically fail in shear, with a clearly noticeable inclined shear failure plane (Wolfs et al., 2018; Hermens, 2018). In the uniaxial stress state where failure occurs, σ_1 is equal to the applied loading and σ_3 is always equal to zero since there is no confinement in that region. This replicates Tresca failure depicted in Figure 5.7 by means of a Mohr circle, and results in a shear failure plane of roughly 45°. Equation 5.13 therefore depicts the relationship between the applied stress and shear stress for an aspect ratio of two. Thus, Tresca can be regarded as the lower bound failure mechanism as a decrease in the aspect ratio increases confinement and apparent UCS. Consequently, the Tresca failure criterion forms the lower bound failure mechanism of the Mohr-Coulomb failure mechanism that accounts for cohesion and interparticle friction in the uniaxial state of stress region.

It is evident from Figure 5.9 that at lower aspect ratios the uniaxial state of stress diminishes. Consequently, a triaxial state of stress exists due to confinement. In the confined regions, the material experiences an increase in interparticle friction. Cohesion is however determined by

the early age hydration products and is therefore not affected. Recall that the angle of internal friction is depicted by a tangent function. Thus, an increase in the angle of friction due to confinement increases a material's capacity against shear failure, hence the increased apparent UCS at lower aspect ratios. The ratio of confined area to unconfined area increases with a decrease in aspect ratio, which yields increasingly larger UCS. As the aspect ratio decreases, and the average interparticle friction increases in the material, the Mohr-Coulomb failure criterion approaches the Rankine or maximum normal stress failure criterion (upper bound).

This theory can also be applied to 3D printed filament layers, specifically the bottom layer that is considered as the critical layer for this model. The cross-section of a filament layer (Figure 5.8) can be viewed the same as in Figure 5.9. Note that, due to the plane strain assumption, confinement directly affects the transverse stress (σ_2). It does however have an indirect effect on the longitudinal stress (σ_3) as depicted by Equation 5.16. Significant confinement is expected in 3DPC filament layers, as aspect ratios typically do not exceed the value of one. Therefore, σ_3 cannot be assumed to be zero in order to simplify Equation 5.14 and consequently negate the necessity to determine material properties $v(t)$ and $\mu_s(t)$. If it is assumed that there is no friction ($\mu_s(t) = 0$), then from Equation 5.15 $\sigma_2 = 0$, and consequently the lower bound Tresca failure is approached again. However, there will always be some degree of friction present and hence that assumption is also not valid. Therefore, the complete use of Equation 5.14 and the determination of all relevant time-dependent material properties are unavoidable. However, it does not account for confinement effects, whereby the friction angle increases due to the aspect ratio of the filament layer.

A way of addressing this problem is by applying so-called strength correction factors (Murdock & Kesler, 1957; Chung, 1989). These factors account for the confinement effect that becomes prominent at lower aspect ratios. Several codes (EU, ASTM and ACI) account for this effect, however only aspect ratios larger than one are allowed, which is therefore not suitable for 3DPC. Figure 5.10 illustrates strength correction factors for aspect ratios smaller than one (Lamond & Pielert, 2006). It is important to note that these factors are normalised with respect to the strength obtained for an aspect ratio of two. As mentioned, Tresca shear failure (lower bound of Mohr-Coulomb failure) predominantly occurs at aspect ratio of 2 due to the large region that comprises of uniaxial stress. However, it is observed in Figure 5.10 that as the aspect ratio decreases, an almost exponential increase in relative strength is obtained which tends to infinity, implying a vertical asymptote is being approached. Recall that confinement increases a material's friction angle, which is presented by a tangent function

consisting of a vertical asymptote at 90° . It is clear that this asymptote is being approached in Figure 5.10 and presents the upper bound of the Mohr-Coulomb failure, namely Rankine or the maximum normal stress failure theory. A plateau is typically observed between an aspect ratio of 2 and 3, while higher aspect ratio values yield normalised strength correction factors of less than one (Tuncay & Hasancebi, 2009; Chaoyang University of Technology, n.d.). This is mainly due to less lateral stability in such relatively long specimens.

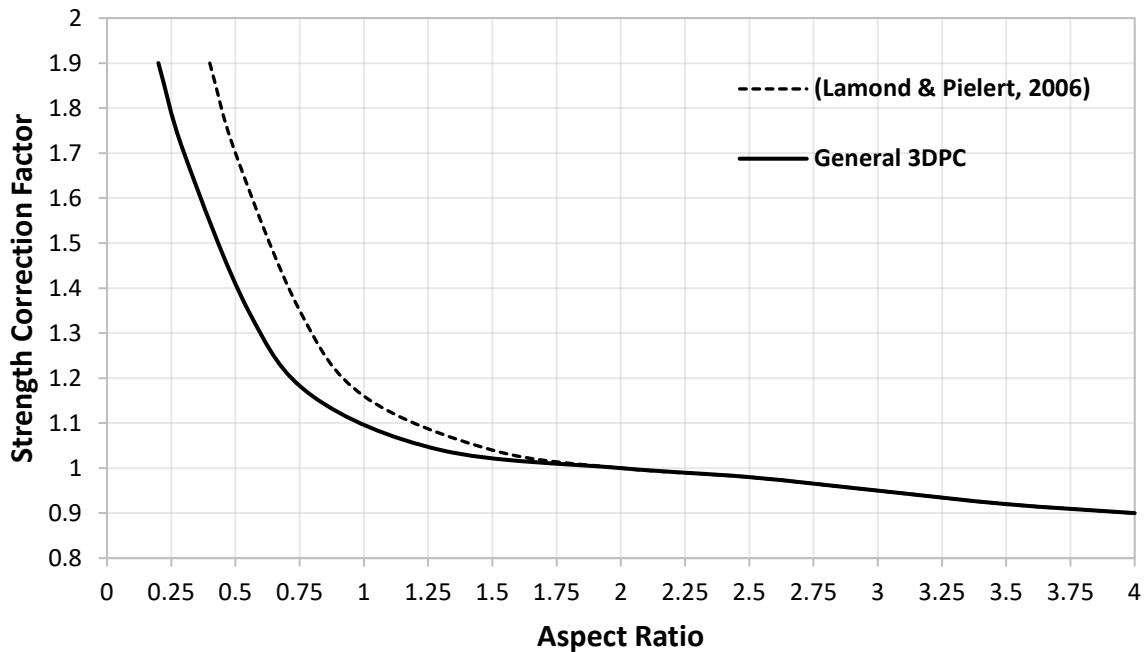


Figure 5.10: Strength correction factors for different aspect ratios.

Effectively what occurs during confinement, is that the friction angle increases and becomes larger than the inherent friction angle of the material itself. This is especially true for aspect ratios smaller than one such as in the case of filament layers for 3DPC, as well as for cementitious materials in the fresh state that typically have a lower friction angle than in the hardened state (Mettler et al., 2016). Therefore, the correction factors account for the friction angle induced by confinement and not due to the inherent interparticle friction of the material. Consequently, the time-dependent friction angle ($\varphi(t)$) of a material is not required for this model.

As mentioned earlier, the ratio between σ_1 and τ_{crit} is one for Tresca failure that is dominant in specimens with aspect ratios of two; mainly in order to correlate with the strength correction factor for an aspect ratio of two. This stress ratio increases as the friction angle increases. By

referring to Figure 5.7, a larger Mohr circle i.e. a larger ratio between σ_1 and σ_3 yields an increasingly larger friction angle. The maximum shear stress is taken as tangent to this Mohr circle. Therefore, it can be interpreted that an increasingly larger friction angle yields an increasingly larger ratio between σ_1 and τ_{crit} . This behaviour is accounted for in the strength correction factors which ultimately depict the σ_1 to τ_{crit} stress ratio for various aspect ratios. Thus, smaller aspect ratios do not increase the strength of a material (τ_{crit} remains constant at a given time interval for a material), but increase the ratio between σ_1 to τ_{crit} . Based on Tresca failure which occurs at aspect ratios of two, and strength correction factors that are normalised at aspect ratios of two, the relationship between the normal and shear stress is:

$$\tau = \frac{\sigma_1}{2 \cdot F_{AR}} \quad (5.18)$$

Where F_{AR} is the strength correction factor that accounts for confinement due to smaller aspect ratios. Tresca failure is obtained if a strength correction factor of one is chosen, whereafter Equation 5.18 correlates with Equation 5.13. This value of one can be assumed in the model if a lower bound solution is desired, effectively implying that no confinement occurs in the filament layers. The strength correction factors obtained by Lamond & Pielert (Figure 5.10) do not accommodate aspect ratios lower than 0.4. However, such small aspect ratios are possible and viable for 3DPC. Therefore, the correction factors were conservatively adjusted to enable for smaller aspect ratios of filament layers, which is denoted as “General 3DPC” in Figure 5.10. The Poisson’s ratio for hardened concrete is typically taken as 0.15, whereas in the fresh state 0.3 is commonly assumed (Wolfs et al., 2018; Suiker, 2018). The correction factors presented by Lamond & Pielert are applicable to hardened concrete; however, 3D printing of concrete is only possible in the fresh state. An increase in Poisson’s ratio (e.g. from 0.15 to 0.3) yields larger lateral stresses under a constant vertically induced stress, effectively increasing the circumference of the Mohr circle that renders a larger equivalently induced shear stress. Failure therefore occurs sooner at larger Poisson’s ratios, which justifies the adjustment of the correction factors in Figure 5.10. These strength correction factors are proposed in the case where a material’s strength correction factors are unknown. However, for more accurate solutions, these factors should be determined for the material in use and normalised with respect to the strength obtained from a specimen with an aspect ratio of two. These factors generally vary depending on various material properties, in particular Poisson’s ratio (ν), Young’s modulus (E) and compressive strength.

5.2.4 Analytical expression of model

Plastic yield of the critical layer occurs when the building rate equals the time-dependent material shear strength. The building rate must be expressed in terms of shear stress, which is achieved by combining Equations 5.18 and 5.11 as follows:

$$\tau(N_L) = \frac{\rho \cdot g \cdot h_1 \cdot 10^{-3} \cdot N_L}{2 \cdot F_{AR}}, \quad N_L \in \mathbb{R} \quad (5.19)$$

Now the building rate is equated to the thixotropy model illustrated in Figure 5.3 in order to determine failure. However, as depicted in Figure 5.11, failure can occur either during re-flocculation (fast building rate) or structuration (slower building rate). Intuitively, it makes sense that a lower building rate will yield a taller structure as the material gains strength over time. Therefore there are two cases, where the material either fails during re-flocculation or structuration, expressed as follows:

$$\frac{\rho \cdot g \cdot h_1 \cdot 10^{-3} \cdot N_L}{2 \cdot F_{AR}} = \tau_{D,i} + R_{thix} \cdot t \quad (5.20)$$

$$\frac{\rho \cdot g \cdot h_1 \cdot 10^{-3} \cdot N_L}{2 \cdot F_{AR}} = \tau_{S,i} + A_{thix} \cdot (t - t_{rf}) \quad (5.21)$$

Equation 5.20 accounts for re-flocculation only and Equation 5.21 for structuration. However, for both equations the time (t) needs to be expressed in terms of the number of layers (N_L). This is achieved by substituting Equation 5.22 into Equations 5.20 and 5.21, which is expressed as follows (refer to Figure 5.6 for linearisation):

$$t = \frac{l_p}{v} \cdot N_L, \quad N_L \in \mathbb{R} \quad (5.22)$$

Substituting Equations 5.2 and 5.22 into Equations 5.20 and 5.21:

$$\frac{\rho \cdot g \cdot h_1 \cdot 10^{-3} \cdot N_L}{2 \cdot F_{AR}} = \tau_{D,i} + R_{thix} \cdot \left(\frac{l_p}{v} \cdot N_L \right) \quad (5.23)$$

$$\frac{\rho \cdot g \cdot h_1 \cdot 10^{-3} \cdot N_L}{2 \cdot F_{AR}} = \tau_{S,i} + A_{thix} \cdot \left(\frac{l_p}{v} \cdot N_L - \frac{\tau_{S,i} - \tau_{D,i}}{R_{thix}} \right) \quad (5.24)$$

The final equations for this model are obtained by simplifying and rewriting the equations above:

$$N_L = - \left[\frac{\tau_{D,i}}{\left(\frac{R_{thix} \cdot l_p}{v} \right) - \left(\frac{\rho \cdot g \cdot h_l}{2 \cdot 10^3 \cdot F_{AR}} \right)} \right] \quad (5.25)$$

$$N_L = - \left[\frac{\tau_{S,i} + \left(\frac{A_{thix} \cdot (\tau_{D,i} - \tau_{S,i})}{R_{thix}} \right)}{\left(\frac{A_{thix} \cdot l_p}{v} \right) - \left(\frac{\rho \cdot g \cdot h_l}{2 \cdot 10^3 \cdot F_{AR}} \right)} \right] \quad (5.26)$$

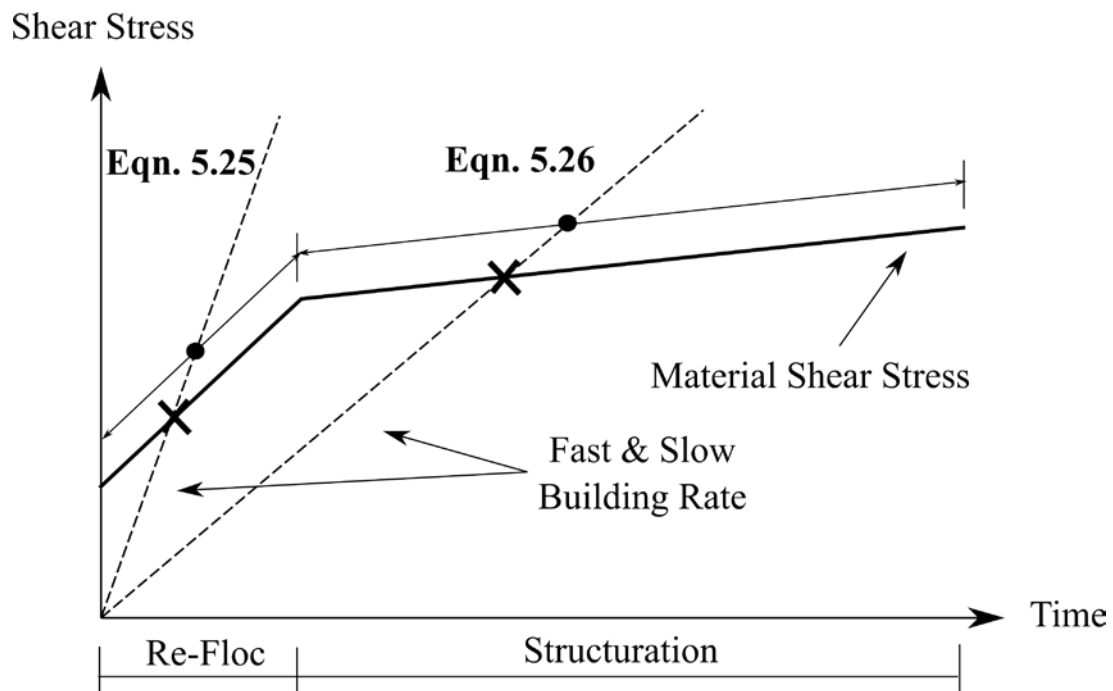


Figure 5.11: Shear stress vs time graph depicting different building rates against material strength, as well as the regions where Equations 5.25 and 5.26 are applicable.

An a priori check is developed to determine whether Equation 5.25 or 5.26 must be used. Initially, the building rate depicted by Equation 5.19 is altered by using Equation 5.22 to eliminate the number of layers (N_L) parameter and is expressed as follows:

$$\tau(t) = \frac{\rho \cdot g \cdot h_l \cdot v \cdot 10^{-3}}{2 \cdot l_p \cdot F_{AR}} \cdot t \quad (5.27)$$

Taking the derivative of Equation 5.27 with respect to time (t) yields the gradient of the building rate. This gradient is compared to a fixed gradient that is determined by the material's strength, as illustrated in Figure 5.12.

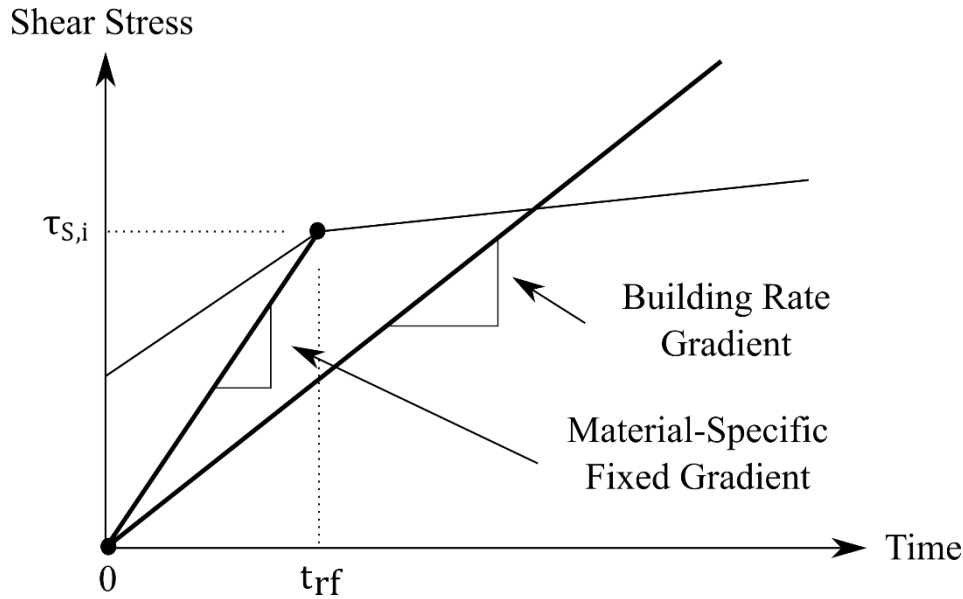


Figure 5.12: Material-specific fixed gradient vs building rate gradient.

The material-specific fixed gradient is determined between the coordinates $(0, 0)$ and $(t_{rf}, \tau_{S,i})$. With the use of Figure 5.12 and Equation 5.2, the gradient is expressed as follows:

$$m_{\text{Mat.}} = \frac{\tau_{S,i} R_{\text{thix}}}{\tau_{S,i} - \tau_{D,i}} \quad (5.28)$$

Therefore, if:

$$\frac{d\tau}{dt} \geq \frac{\tau_{S,i} R_{\text{thix}}}{\tau_{S,i} - \tau_{D,i}} \quad (5.29)$$

then use Equation 5.25, else use Equation 5.26.

5.2.5 Limitations of the model

- This model is based on thixotropic material behaviour, as discussed in Section 5.2.1. Therefore, it does not account for other rheological material behaviour. However, in the case where a material demonstrates no thixotropy i.e. no distinction is noted between the material's static and dynamic yield shear stress (refer to Figure 5.2), then R_{thix} is equal to zero as no re-flocculation occurs. This behaviour is synonymous with elastic perfectly plastic material behaviour. In the case where a material is thixotropic, but the microstructure not broken down due to pumping,

then R_{thix} is also equal to zero as no re-flocculation occurs. All materials will however possess a structuration rate, A_{thix} . In such cases the model is still valid, with the condition that R_{thix} is replaced with A_{thix} and $\tau_{D,i}$ with $\tau_{S,i}$ in Equation 5.25. Equation 5.26 is negated.

- This model is only valid for material failure in the form of plastic yield. Structural failure due to geometry is not considered e.g. elastic buckling in the fresh concrete state. Thin-walled elastic buckling is accounted for by Suiker's model (Suiker, 2018). However, construction of large structural elements via 3DPC e.g. load-bearing walls may typically consist of two thin-walled layers that are joined together in a truss-like manner. This yields a significant increase in resistance against buckling and subsequently material failure at high building rates become more critical.
- The model is a lower bound theorem that yields conservative prediction. It is assumed that if a material's static yield shear stress is exceeded in the critical layer, plastic yield will occur and result in collapse of the printed structure. However, if the entire critical layer uniformly experiences plastic yield, then global subsidence may result instead of collapse. The probability of collapse is greater in the case of differential subsidence. Therefore, this model is synonymous with elastic design of structures, whereby only linear-elastic material behaviour is assumed and structural collapse ensues after the formation of the first plastic hinge. This is obviously not always the case but leads to a conservative prediction that is always equal to or less than the collapse load.

Stress redistribution also occurs in the deposited filament layers, as illustrated in Figure 5.13. The bottom layer will compress and experience horizontal deformation with the addition of each filament layer. This behaviour can be characterised by Hooke's law and Poisson's ratio. Friction may limit the horizontal deformation. Nonetheless, it remains a probable situation. As the layer width increases, so too does the area over which the force is induced and consequently the rate of induced stress in the critical layer becomes non-linear (see Figure 5.13). Furthermore, a smaller filament layer aspect ratio is obtained that increases confinement, depending on the amount of friction present. Therefore, in the case of less friction a non-linear building rate is obtained. Subsequently, more layers are obtained than predicted by the linear building rate of the model. In the case where no horizontal deformation

occurs, when high friction is present, the building rate will be linear. Hence, the linear building rate assumed for this model is lower bound. In the case of no friction, no confinement will occur, and the model may over-predict the number of layers. This is however an unlikely situation. This model is therefore a lower bound theorem as long as sufficient friction is present.

- No provision is made for localised failure in the form of stress gradients that lead to premature plastic yield of the critical layer. This could occur due to many factors including a skew printing surface, global instability of the structure resulting in load eccentricity as well as vertical or horizontal inertia forces induced by the printer nozzle.
- This model, unlike the numerical model developed by Wolfs et al. (2018), does not depict the failure mode of the printed structure. It is assumed that material failure will always instigate global failure. However, elastic buckling could also result in global failure of the structure. Therefore, the model may be less accurate for structures with large aspect ratios (thin-walled), and more accurate for structures with enhanced stability i.e. smaller global aspect ratios.

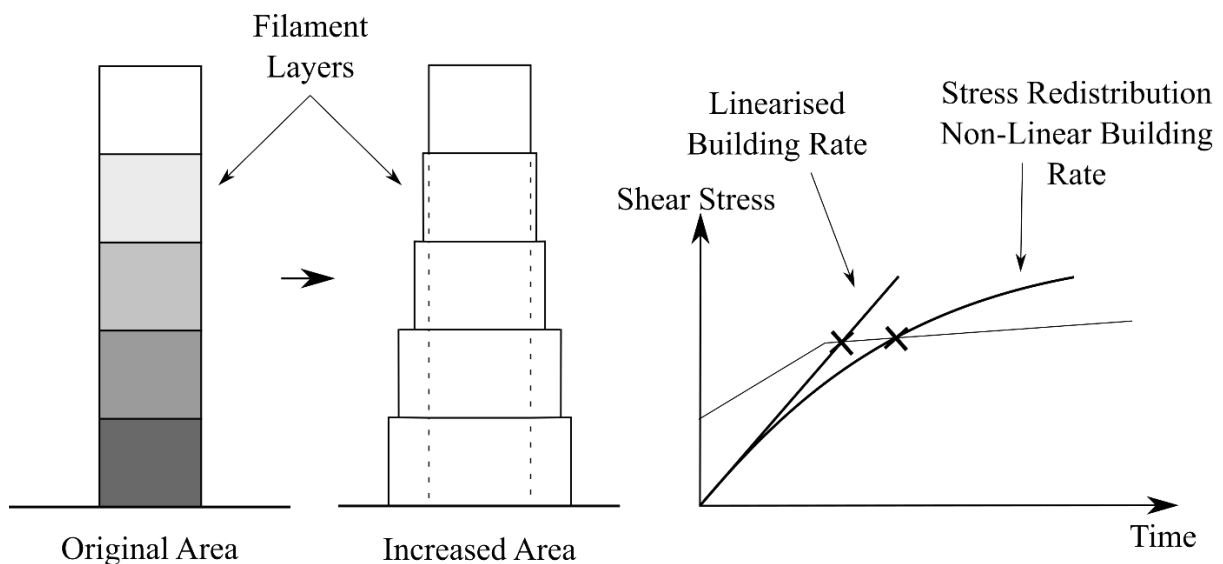


Figure 5.13: Stress redistribution in the critical filament layer that leads to a non-linear building rate and ultimately yields a lower bound model.

5.3 Experimental verification

An experimental verification procedure is conducted and presented in this section. A circular hollow column is 3D printed until failure occurs, of which the number of attained layers is then compared to the number of layers predicted with the model developed in Section 5.2. This also serves as an example for the practical application of the model.

5.3.1 Material composition & preparation process

The standard 3DPC mix at Stellenbosch University, which is a high-performance (HPC) mix with a water to cement ratio of 0.45, is used for this research and presented in Table 5.1. The CEM II 52.5N composite cement consists of between 6 and 20 % limestone extender and conforms to SANS 50197-1. Ulula class S fly ash, together with FerroAtlantica silica fume are used as extenders to obtain the required workability properties for 3DPC. The aggregate consists of a continuously graded coarse sand that is locally mined with a maximum particle size of 4.75 mm. Potable tap water is used in conjunction with a new generation superplasticizer, Chryso Fluid Premia 310, which is based on a modified polycarboxylate polymer.

Table 5.1: Standard HPC constituent quantities used for this research.

Constituent	kg
Cement	579
Fly Ash	165
Silica Fume	83
Aggregate	1167
Water	261
Superplasticizer	1.48% by mass of binder

A 50 litre concrete batch is prepared for this research. Initially, each constituent is accurately weighed off and temporarily stored in containers. The dry constituents are then placed into a 120 litre concrete pan mixer in the following order: aggregate, extenders and cement. This dry batch is mechanically mixed for at least three minutes until it is visually observed that the constituents form a homogenous dry mixture. Thereafter, water is poured into the pan mixer at a low rate while mechanical mixing continuous. The concrete mixture is further mechanically mixed for one minute after all the water is added. Lastly, the

superplasticizer is added to the concrete at a low rate for even distribution of the chemical throughout the concrete mixture. The batch is then further mixed for two minutes after which it is ready for testing.

5.3.2 Input parameters

Print parameters

The print parameters are specific to the geometry of the printed object and the associated manufacturing parameters. In order to verify the model, plastic yielding of the bottom critical layer is required which then results in plastic collapse of the structure. Several factors influence the probability of plastic collapse. The first important factor to consider is the geometry of the printed object, both from a local and global viewpoint. Locally, tilting of consecutively deposited thin-walled filament layers must be prevented. This is achieved by providing lateral support in the form of infill e.g. honeycomb, grid, rectilinear etc. Alternatively, the path length of a straight filament layer must be minimised in relation to lateral support provided by change in direction, such as a 90° bend. Globally, a structure with a similar second moment of area about all axes is required in order to prevent buckling about its weaker axis. For example, a rectangular shaped thin-walled element could experience buckling about its weaker axis before plastic collapse would occur, whereas in a square section resistance against buckling is identical about both axes.

The second important factor to consider is the building rate of the 3D print. If the building rate is too slow, the critical layer attains stiffness and consequently the chance of plastic yield reduces. In contrast, if the building rate is too fast, the layers will deform significantly under the weight of the subsequently deposited layers. A faster building rate therefore leans more towards plastic failure; however, it will result in poor aesthetics (surface finish) of the printed structure. Thus, a relatively fast building rate is envisaged for proper illustration of plastic yield in a 3D printed structure with good aesthetics. The building rate can, other than depicted in Section 5.2.2, be interpreted as the time elapsed between consecutively deposited filament layers, essentially described by Equation 5.7. Therefore, the building rate is primarily influenced by the printing speed and print path length, both which are assumed to be constant for this model. A high printing speed together with a long print path length can yield the same building rate as a slow printing speed together with a short print path length. A slower printing speed is preferred in this research.

Chapter 5: Buildability Model

The geometry that is used for this research is depicted in Figure 5.14. A circular hollow column with diameter 250 mm and height 900 mm is chosen. The circular section ensures for a constant second moment of area about any horizontal axis. Furthermore, it also provides continuous lateral self-support, which minimises the probability of localised tilting of the thin-walled structure. No infill is used as it will increase the time between deposition of subsequent layers, hence decreasing the building rate. Square sections are not considered in order to avoid any stress concentrations that might occur at the corners if over extrusion problems arise. Vase mode, which is the continuous vertical printing of an object i.e. corkscrew-like behaviour, is enabled to further eliminate the probability of stress concentrations. A constant printing speed of 60 mm/s is employed and, together with a print path length of 785 mm, yields one layer every 13.08 seconds. Based on a filament layer height of 10 mm, this translates into one meter vertical height gain every 21 minutes and 48 seconds. Together with a filament layer width of 30 mm, an aspect ratio of 0.33 is obtained that yields a strength correction factor of roughly 1.7 from Figure 5.10. The print parameters required for this model are summarised in Table 5.2.

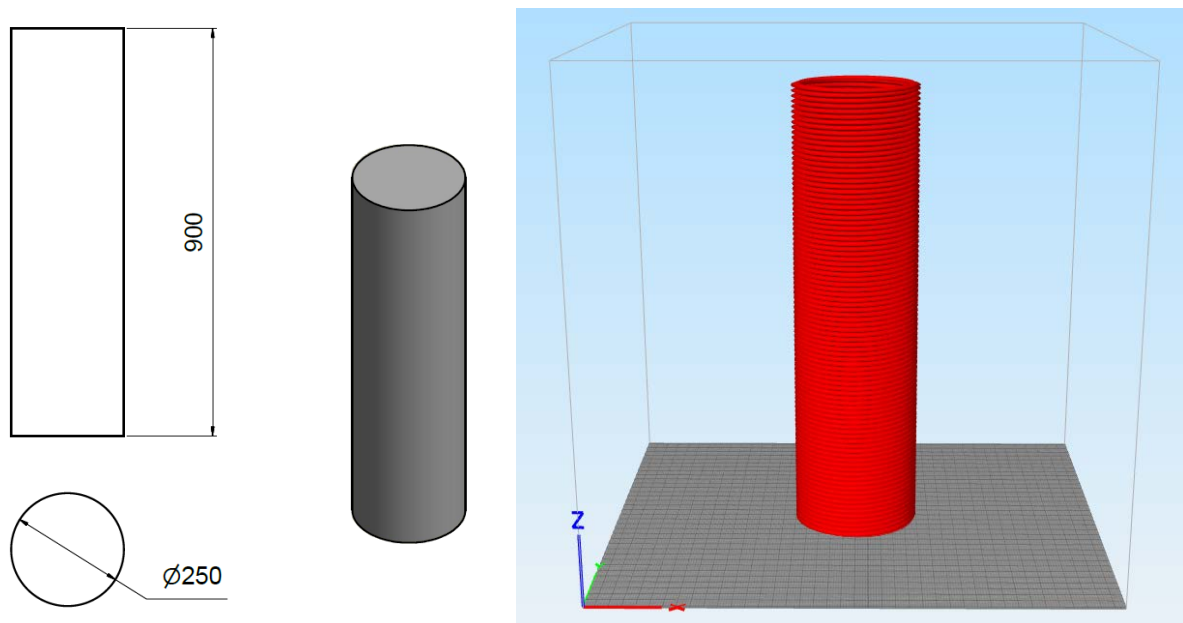


Figure 5.14: AutoCAD Inventor drawing (left) of the object to be 3D printed including dimensions (mm), which is then exported as .stl file format to Simplify3D (right) that slices the object into multiple layers and processes the data for machine interpretation and execution.

Table 5.2: Summarised print parameters as input for the model.

Print Parameter	Value
h_1	10 mm
w_1	30 mm
l_p	785 mm ($2\pi r$)
v	60 mm/s
Aspect Ratio	0.33 (h_1/w_1)
F_{AR}	~ 1.7 (Figure 5.10)

Material parameters

The rheological protocol presented in Figure 5.15 is followed in this research in order to obtain the required material parameters. The 50 litre 3D printable concrete mixture is prepared, of which 20 litres is used for the rheology test and the remaining 30 litres for the 3D print. Thus, accurate material properties are obtained as one batch is used for the 3D print and material characterisation. Furthermore, the rheology test is conducted simultaneously with the 3D print to yield comparable time-dependent structuration properties i.e. the material is sheared at exactly the same starting time. The rheology test is conducted with the Germann ICAR Plus Rheometer (Germann Instruments, n.d.). The procedure followed in order to obtain the required material parameters is explained in more detail in Section 5.2.1 (Kruger et al., 2019).

A shearing rate of 1 s^{-1} is used in this research, which roughly correlates with the shearing induced by the pump's screw, based on number of revolutions per second. A shearing rate that is too high may result in segregation of the constituents and consequently no re-flocculation occurs. In contrast, a shearing rate that is too low may not reflect actual breakdown of thixotropy forces. Nerella et al. (2019) recommends the lowest possible shear rate that yields flow-onset for rheological characterisation by means of a strain-based approach. The shear rate induced by a rheometer is derived from the principle shear rate between two parallel plates, and is calculated as follows:

$$\dot{\gamma} = \frac{\frac{\text{rev}}{\text{s}} \cdot 2\pi \cdot r_i}{(r_o - r_i)} \quad (5.30)$$

where $\frac{\text{rev}}{\text{s}}$ is the rotational speed of the vane, r_i the radius of the vane and r_o the radius of the container. The stress growth curve obtained for the first rheometer test is depicted in

Figure 5.16. From this graph, the initial static and dynamic yield shear stresses are obtained. Table 5.3 depicts all the data points obtained from the rheometer.

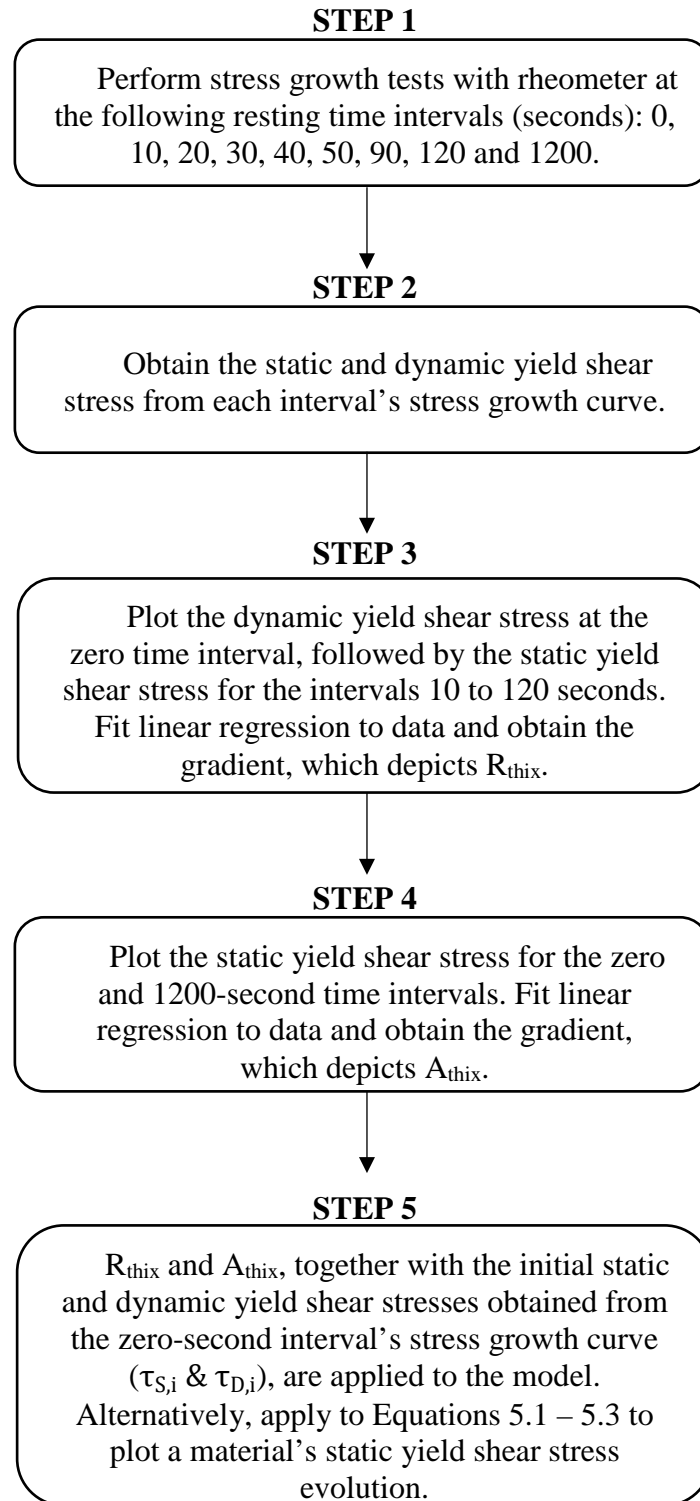


Figure 5.15: Rheological protocol for obtaining the required material parameters as input for the model.

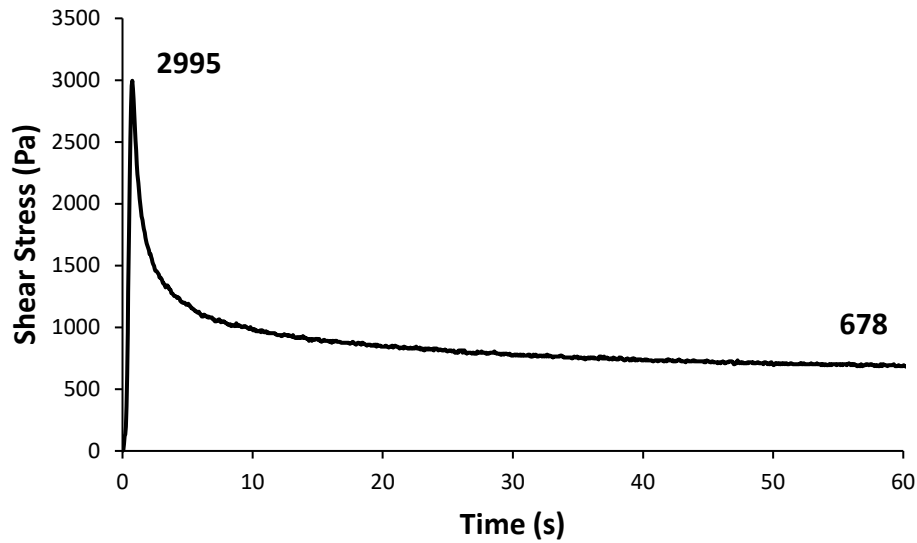


Figure 5.16: Stress growth curve obtained from the initial stress growth rheometer test depicting the static and dynamic yield shear stresses.

Table 5.3: Summary of the data points obtained from the rheometer tests.

	Resting Time Between Tests								
	Initial	10s	20s	30s	40s	50s	90s	120s	20min
Static Yield Shear Stress (Pa)	2995	880	978	1067	1132	1201	1407	1566	4310
Dynamic Yield Shear Stress (Pa)	678	446	466	460	454	452	454	446	535

The data points are plotted against the respective resting times on two different time intervals in order to obtain the re-flocculation and structuration rates (refer to Figure 5.15 and Section 5.2.1), which are illustrated in Figure 5.17 and 5.18 respectively. Linear regression functions are employed to obtain the aforementioned rates. A re-flocculation rate of 6.7 Pa/s and structuration rate of 1.1 Pa/s are obtained. These values are accepted, as the coefficient of determination values for the regression models are high. The last material parameter to obtain is the density. A mould of known volume is filled with concrete and the mass of the sample determined. The density of the fresh concrete is then obtained by dividing the mass of the concrete sample by the volume that it fills. The material parameters required for this model are summarised in Table 5.4.

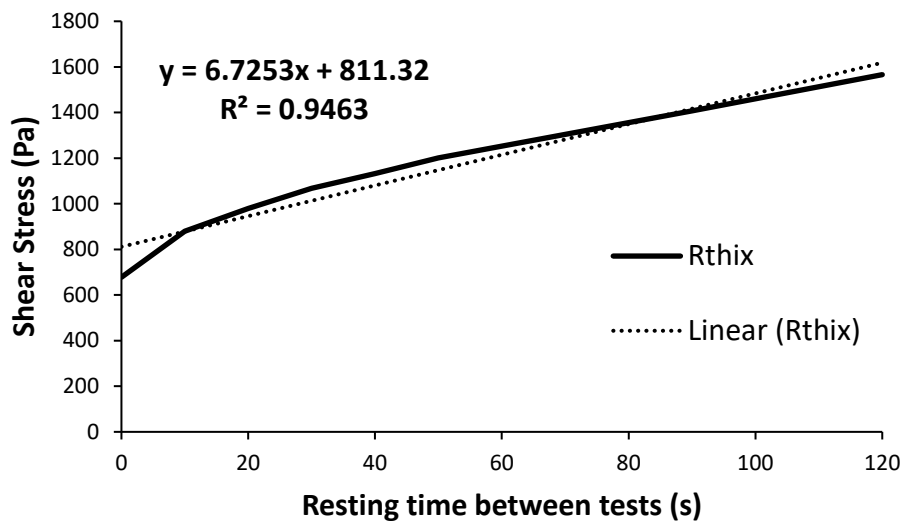


Figure 5.17: Calculation of the re-flocculation (R_{thix}) rate.

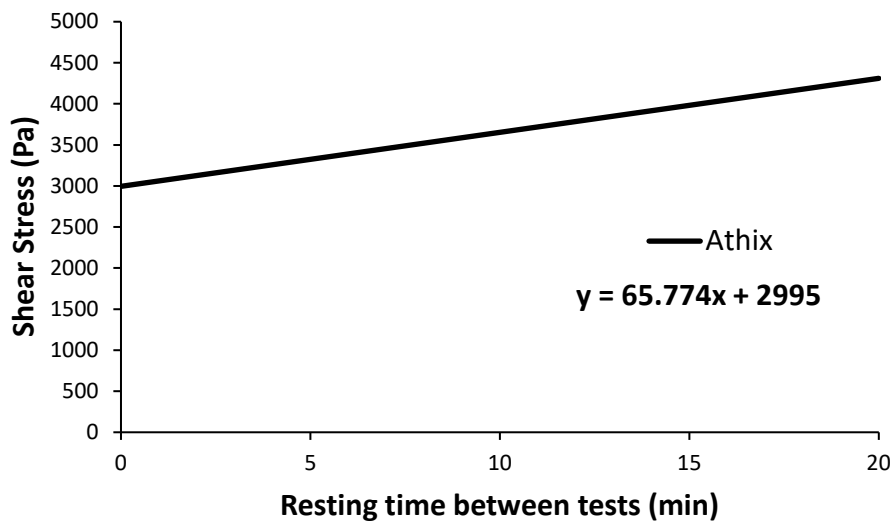


Figure 5.18: Calculation of the structuration (A_{thix}) rate.

Table 5.4: Summarised material parameters as input for the model.

Material Parameter	Value
$\tau_{S,i}$	2995 Pa
$\tau_{D,i}$	678 Pa
R_{thix}	6.7 Pa/s
A_{thix}	1.1 Pa/s
ρ	2150 kg/m ³

5.3.3 Model prediction

This section demonstrates the use and application of the model developed in Section 5.2. Initially, the a priori check is performed (refer to Section 5.2.4) in order to determine which equation to use (either 5.25 or 5.26). Thus, Equations 5.27 to 5.29 are used to achieve this. The input parameters summarised in Tables 5.2 and 5.4 are applied to these equations. The result is summarised in Table 5.5. It is found that the material gradient is larger than the building rate gradient. Consequently, Equation 5.26 is to be used. By substituting the input parameters into Equation 5.26, it is predicted that after 55 layers the structure will collapse due to plastic yield of the bottom layer. This equates to a total height of 550 mm. In contrast, according to Equation 5.25, a total of -27 layers will be obtained, which is impossible. Note that it is not required to calculate Equation 5.25, but is only done here for illustration purposes. This process is also visually illustrated in Figure 5.19. The material strength is depicted by the bi-linear thixotropy model presented in Section 5.2.1 and developed using Equations 5.1 to 5.3. The linear building rate is presented by Equation 5.27. Print failure occurs where this linear building rate crosses the material strength and is depicted by a cross in Figure 5.19. Note that print failure can also be expressed in terms of stress or time by manipulation of the equations presented in this research.

Table 5.5: Summary of the results obtained from the model developed in this research.

Parameter	Equation	Value
$\tau(t)$	5.27	4,74.t
$m_{\text{Mat.}}$	5.28	8.66
$\frac{d\tau}{dt} < m_{\text{Mat.}}$	5.29	4.74 < 8.66
Thus, use Equation 5.26.		
N_L	5.25	-27
N_L	5.26	55
N.B.: Round up number of layers.		

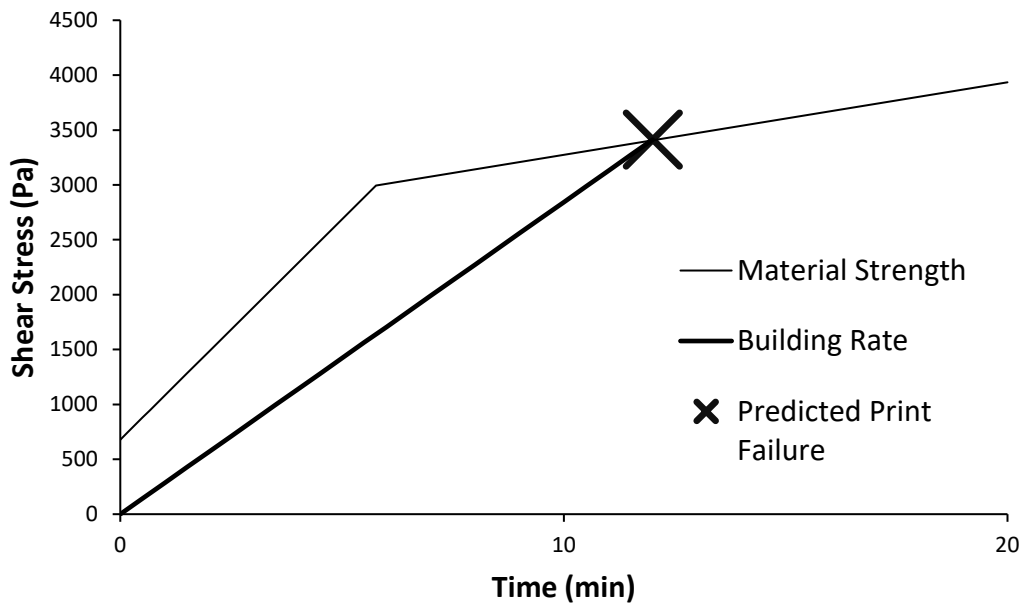


Figure 5.19: Visual representation of the model indicating material strength, building rate of the 3D print and the predicted print failure.

5.3.4 Experimental results

This section reports on the results obtained from the 3D print and compares it to that predicted by the model in Section 5.3.3. The circular hollow column presented in Section 5.3.2 is printed at 60 mm/s until failure occurs. The printing is conducted with the use of Stellenbosch University's 3D concrete printer. Figure 5.20 presents the final shape of the column just before failure occurs. No significant deformation in any form is observed. However, the bottom layers are thinner than the top layers due to the compressive force induced by the subsequently deposited layers. The surface finish of the structure in general is adequate. The total printing time amounted to 13 minutes and 12 seconds, and a total of 60 filament layers are achieved. This is an absolute difference of 5 layers when compared to the prediction of the model. Note that the model predicted 5 layers less than what is actually achieved, confirming that it is indeed a lower bound (conservative) model. The model yielded a conservative relative error of 8.33 %. The results of the experimental verification are summarised in Table 5.6.

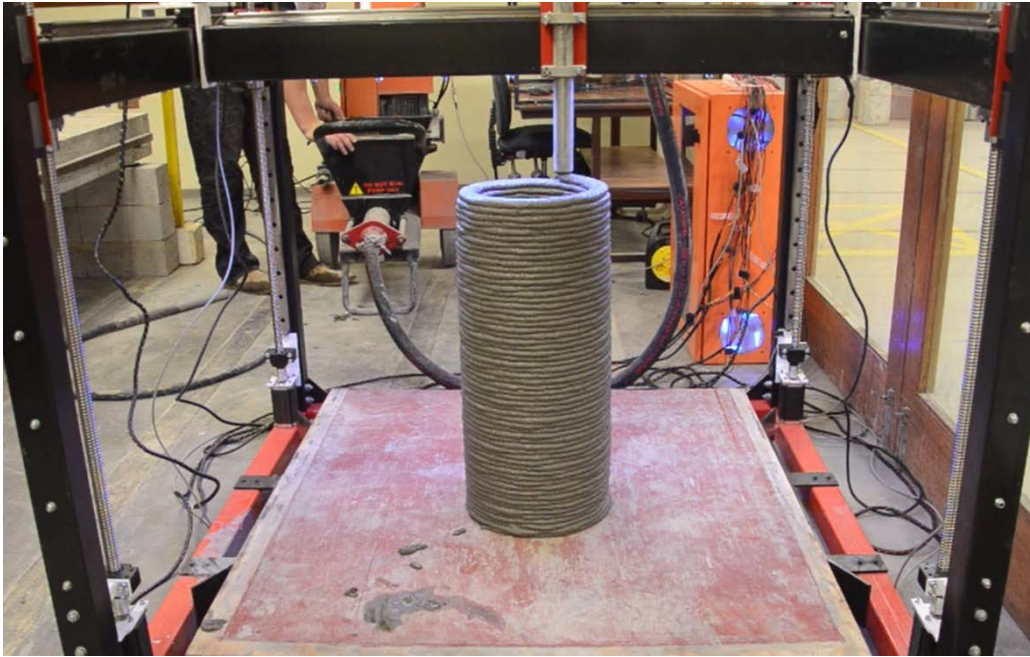


Figure 5.20: Final form of the circular hollow column before failure occurs.

Table 5.6: Summary of the results from the experimental verification.

Filament Layers Predicted	55
Filament Layers Achieved	60
Absolute Difference	5
Conservative Relative Error	8.33 %

The failure progression of the column is indicated in Figure 5.21. It is evident that the bottom layers on the left side of the column experienced plastic yielding. This effect accumulated and resulted in plastic collapse of the structure in less than 1 second. The column collapsed due to the layers experiencing plastic flow and not being able to support the weight of the subsequent layers anymore. Notably, the column remained significantly rigid throughout failure and no indication of global buckling is present. Furthermore, no local tilting of filament layers is observed. Small surface cracks are observed on sections of the layers that yielded, which is a good indication that the material's static yield stress is exceeded. Therefore, since the correct failure mode is obtained, the result of the experimental verification process is accepted.



Figure 5.21: Failure progression of the column clearly indicates plastic yielding of the bottom layers.

5.4 Conclusion

In this research, a lower bound analytical model is developed for buildability performance quantification of 3D printable materials. The model only accounts for plastic yielding of the bottom critical layer and not for buckling in the fresh concrete state. The material strength evolution after extrusion is depicted via a bi-linear thixotropy model, which acts as the basis of the model. Thereafter, a linear building rate is defined that depicts the rate of stress increase due to the accrument of filament layers. The following conclusions are drawn:

-
- Failure of fresh 3D printed elements due to plastic flow induced by the weight of upper layers is captured with reasonable accuracy by a Mohr-Coulomb criterion.
 - Confinement is caused by differences in elastic properties of successive layers, in combination with interlayer and printer bed adhesion. Plastic strength correction is required to account for the triaxial stress state that arises in the 3D printed layer. The strength enhancement is most notable in thin layers of low height to width aspect ratios. This behaviour is accounted for by means of novel strength correction factors.
 - The presented model is a lower bound theorem. Successive layer loading rate linearisation, together with ignorance of stress redistribution in lower layers leads to conservative prediction of the number of printed layers that can be resisted before plasticity-induced collapse occurs. This is validated by collapse after layer 60 was printed in the described validation 3D print, while plastic yield was predicted to occur after 55 layers had been deposited.
 - 3D printing constructability design is possible and accurate with only the rheology characteristics of the re-flocculation rate (R_{thix}), structuration rate (A_{thix}), the initial static and dynamic plastic yield shear stress. Time consuming, elaborate testing of time-dependent mechanical strength, stiffness and Mohr-Coulomb parameters in the fresh state is avoided.

Constructability of non-vertical 3D printed objects in light of resistance to plastic yield in the fresh, unsupported state, is the next step. This may be incorporated by considering eccentricity and contact surface of successive layers, to appropriately account for the stress states in deposited layers. Given the geometrical freedom, a numerical approach may be required. This research facilitates industry adoption of buildability modelling for 3DPC, by significantly expediting the material characterisation process.

Notations

The following parameters are applicable to this model in its complete state:

- A_{thix} is the structuration rate of the material (Pa/s).
 - F_{AR} is the strength correction factor that accounts for confinement (unitless).
 - g is the gravitational constant taken as 9.81 m/s^2 .
 - h_l is the height of a filament layer (mm).
-

- l_p is the constant path length per filament layer (mm).
- N_L is the total number of filament layers (*always rounded up*).
- ρ is the density of the material (kg/m^3).
- R_{thix} is the re-flocculation rate of the material (Pa/s).
- t is the printing time (s).
- $\tau_{D,i}$ is the initial dynamic yield shear stress of the material (Pa).
- $\tau_{S,i}$ is the initial static yield shear stress of the material (Pa).
- v is the constant printing speed (mm/s).
- w_1 is the width of a filament layer (mm).

Acknowledgements

The research is funded by The Concrete Institute (TCI) and the Department of Trade and Industry of South Africa under THRIP Research Grant TP14062772324.

Contribution of authors

This work is part of Jacques Kruger's PhD research, executed under the supervision of Professor Gideon van Zijl and Doctor Stephan Zeranka. Mr Kruger conducted all experimental work, the analysis, interpretation and presentation of data, as well as the writing of the manuscript. Prof. van Zijl and Dr. Zeranka assisted in proofreading of the manuscript and proposed insightful amendments.

5.5 References

- Alexandridis, A. & Gardner, N.J. 1981. Mechanical behaviour of fresh concrete. *Cement and Concrete Research*. 11(3):323–339.
- Apis-Cor. n.d. *Who we are*. [Online], Available: www.apis-cor.com/en/about/who-we-are [2018, July 14].
- Björn, A., de La Monja, P.S., Karlsson, A., Ejlertsson, J. & Svensson, B.H. 2012. *Rheological Characterization, Biogas*. S. Kumar (ed.). InTech.

-
- Chaoyang University of Technology. n.d. *Unconfined Compression Test*. [Online], Available: www.cyut.edu.tw/~jrlai/CE7334/Unconfined.pdf.
- Chung, H. 1989. On Testing of Very Short Concrete Specimens. *Cement, Concrete and Aggregates*. 11(1):40–44.
- Contour Crafting Corporation. 2017. *Introducing Contour Crafting Technology*. [Online], Available: www.contourcrafting.com [2018, July 14].
- Craig, R.F. 2004. *Craig's Soil Mechanics*. 7th ed. London: Spon Press.
- CyBe Construction. 2018. *The first mobile 3D concrete printer*. [Online], Available: www.cybe.eu [2018, July 14].
- Germann Instruments. n.d. *ICAR Rheometer*. [Online], Available: <http://germann.org/products-by-application/rheology-of-concrete/icar-rheometer> [2018, July 24].
- Hermens, L. 2018. Strength development of concrete used for 3D concrete printing. Eindhoven University of Technology. [Online], Available: https://pure.tue.nl/ws/portalfiles/portal/97479239/Hermens_0767411.pdf.
- Kruger, P.J., van den Heever, M., Cho, S., Zeranka, S. & van Zijl, G. 2019. High-performance 3D printable concrete enhanced with nanomaterials. In Rovinj, Croatia: RILEM Publications S.A.R.L. *Proceedings of the International Conference on Sustainable Materials, Systems and Structures: New Generation of Construction Materials*. 533–540.
- Lamond, J.F. & Pielert, J.H. 2006. *Significance of Tests and Properties of Concrete and Concrete-making Materials*. West Conshohocken, Philadelphia: ASTM International.
- Li, Z., Wang, L. & Ma, G. 2018. Method for the Enhancement of Buildability and Bending Resistance of 3D Printable Tailing Mortar. *International Journal of Concrete Structures and Materials*. 12:37.
- Mettler, L.K., Wittel, F.K., Flatt, R.J. & Herrmann, H.J. 2016. Evolution of strength and failure of SCC during early hydration. *Cement and Concrete Research*. 89:288–296.
- Murdock, J.W. & Kesler, C.E. 1957. *Effect of Length to Diameter Ratio of Specimen on the Apparent Compressive Strength of Concrete*. National Ready Mixed Concrete Association. [Online], Available: <https://books.google.hr/books?id=xYmKNwAACAAJ>.
-

- Nerella, V.N., Beigh, M.A.B., Fataei, S. & Mechtcherine, V. 2019. Strain-based approach for measuring structural build-up of cement pastes in the context of digital construction. *Cement and Concrete Research*. 115(August 2018):530–544.
- Paul, S.C., van Zijl, G.P.A.G., Tan, M.J. & Gibson, I. 2017. A Review of 3D Concrete Printing Systems and Materials Properties: Current Status and Future Research Prospects. *Rapid Prototyping Journal*. 24(4):784–798.
- Perrot, A., Rangeard, D. & Pierre, A. 2016. Structural built-up of cement-based materials used for 3D-printing extrusion techniques. *Materials and Structures/Materiaux et Constructions*. 49(4):1213–1220.
- Roussel, N. 2006. A thixotropy model for fresh fluid concretes: Theory, validation and applications. *Cement and Concrete Research*. 36(10):1797–1806.
- Roussel, N. 2018. Rheological requirements for printable concretes. *Cement and Concrete Research*. 112(March):76–85.
- Salet, T.A.M., Ahmed, Z.Y., Bos, F.P. & Laagland, H.L.M. 2018. Design of a 3D printed concrete bridge by testing. *Virtual and Physical Prototyping*. 13(3):222–236.
- Saloustros, S., Pela, L. & Cervera, M. 2015. A crack-tracking technique for localized cohesive-frictional damage. *Engineering Fracture Mechanics*. 150(December 2015):96–114.
- Smith, W.P.Y. 2016. Relating concrete cube, core and cylinder compressive strengths that are cast, cured, prepared and tested in laboratory conditions. University of Cape Town. [Online], Available: https://open.uct.ac.za/bitstream/handle/11427/26895/thesis_ebe_2017_smith_william_peter_younger.pdf?sequence=1&isAllowed=y.
- Suiker, A.S.J. 2018. Mechanical performance of wall structures in 3D printing processes: Theory, design tools and experiments. *International Journal of Mechanical Sciences*. 137(January):145–170.
- Tuncay, E. & Hasancebi, N. 2009. The effect of length to diameter ratio of test specimens on the uniaxial compressive strength of rock. *Bulletin of Engineering Geology and the Environment*. 68(4):491–497.
- WinSun. 2017. *Company profile*. [Online], Available: www.winsun3d.com/En/About/ [2018, July 14].
-

Wolfs, R.J.M., Bos, F.P. & Salet, T.A.M. 2018. Early age mechanical behaviour of 3D printed concrete: Numerical modelling and experimental testing. *Cement and Concrete Research*. 106(May 2017):103–116.

Chapter 6

3D concrete printer parameter optimisation for high rate digital construction avoiding plastic collapse

Jacques Kruger, Seung Cho, Stephan Zeranka, Celeste Viljoen, Gideon van Zijl

Division for Structural Engineering and Civil Engineering Informatics, Department of Civil Engineering, Stellenbosch University, Stellenbosch, 7600, South Africa

Reproduced and reformatted from an article submitted to the *Composites Part B: Engineering Journal*.

Abstract

This research presents the development and application of a constructability design model, which determines the print speed and filament layer height combination that yields the fastest vertical building rate, whilst ensuring for the successful construction of an object. A 3D concrete printed structural wall element is used to validate the model. High variation in material rheological properties lead to an over prediction by the model if mean model parameter values are used. Consequently, a probabilistic design model is developed to reduce the impact of high variation in material properties on the accuracy of the deterministic design model. The first-order reliability method (FORM) is applied and material partial factors derived.

Keywords: automation, analytical modelling, rheological properties, statistical properties/methods, 3D concrete printing

6.1 Introduction

Conventional reinforced concrete elements are designed to satisfy both safety and cost requirements. This is achieved by designing elements to have sufficient strength, while using the least amount of material to accomplish the task. Standardised design guidelines are provided to this end, e.g. the European standards. A reinforced concrete beam design typically consists of a beam assigned with specific outer dimensions and the amount of steel required to resist the imposed load determined. Importantly, all possible material strengths are known prior to the design process and can therefore be specified by the engineer.

An exigency for such design guidelines currently exists to successfully realise 3D concrete printed elements in a safe and cost-effective manner. Failure during concrete printing is common and typically occurs by either plastic yielding or elastic buckling (Wolfs & Suiker, 2019). Several buildability models have been proposed to predict the height that a particular object can obtain before failure (Kruger et al., 2019a; Suiker, 2018; Wolfs et al., 2018; Perrot et al., 2016; Wangler et al., 2016; Panda et al., 2019). However, these models largely function as analysis tools as they do not present the optimum print parameter values to realise an object. Typically, print parameters are chosen (e.g. filament layer dimensions and print speed) and the object's maximum obtainable height predicted according to the material's strength. This could possibly result in a tedious iterative process where the user changes the print parameter values until a realistic or optimised solution is obtained. A solution to this is a constructability design model for 3D concrete printing, i.e. a model that determines the print parameters to successfully construct an object. Similar to conventional reinforced concrete element design, the object's dimensions are to be specified and all feasible print parameter combinations determined that would successfully yield the entire object. This allows for optimisation possibilities, in particular the print parameter combination that successfully yields the entire specified object in the least amount of time. Such design model for 3D concrete printing (3DCP) constructability thus addresses the same requirements as those of conventional reinforced concrete construction, namely safety and cost.

This research addresses the challenge by developing and presenting a rheology-based constructability design model for 3DCP. The model determines the print speed and filament layer height at which the entire specified object geometry can be successfully constructed at the fastest vertical building rate i.e. in the least amount of time. The model only accounts for physical nonlinearity in the form of *plastic yielding* and not geometrical nonlinearity e.g. elastic buckling. Furthermore, the model accounts for plastic yielding of individual filament layers

under self-weight after extrusion by limiting layer heights. A holistic design model is therefore presented that ensures for sufficient buildability as well as surface aesthetics.

An experimental verification procedure follows, where a structural wall element commonly employed in 3DCP applications (Ghaffar et al., 2018; Gosselin et al., 2016) is printed with the optimum print parameters specified by the design model. These walls typically consist of W-type infill to prevent geometrical instability, which is essentially obtained from topological optimisation of a beam (Tsavdaridis et al., 2015). The research concludes by deriving a statistical design model to account for variability in material strength to reduce the deterministic model's probability of failure. Partial material factors are determined and employed for this purpose, which are also commonly adopted by conventional reinforced concrete design norms. Implementation of this constructability design model facilitates commercialisation of 3DCP towards a highly industrialised construction industry.

6.2 Theoretical framework

6.2.1 Background

The constructability design model comprises of three individual analytical models that are particularly relevant to 3DCP (Kruger et al., 2019a,b,c). Firstly, the material characterisation process follows the rheological protocol developed by Kruger et al. (2019b) for thixotropic materials. The research shows that a material's static yield shear stress evolution follows a bi-linear profile after extrusion, as schematically illustrated in Figure 6.1. The model extends Roussel's thixotropy model (Roussel, 2006) by accounting for re-flocculation after agitation (R_{thix}) and structuration (A_{thix}). It is shown from (Kruger et al., 2019b) that a material's shear strength can be expressed as a function of resting time after extrusion with the following equations:

$$\tau_S(t) = \tau_{D,i} + R_{thix} \cdot t \quad \text{for } [t \leq t_{rf}] \quad (6.1)$$

$$t_{rf} = \frac{\tau_{S,i} - \tau_{D,i}}{R_{thix}} \quad (6.2)$$

$$\tau_S(t) = \tau_{S,i} + A_{thix} \cdot (t - t_{rf}) \quad \text{for } [t > t_{rf}] \quad (6.3)$$

Where $\tau_S(t)$ is the static yield shear stress at time (t) after deposition, $\tau_{S,i}$ and $\tau_{D,i}$ the initial static and dynamic yield shear stress and t_{rf} the time period over which re-flocculation occurs as illustrated in Figure 6.1. The advantage of this rheology model over conventional mechanics

is that it quantifies material behaviour in addition to presenting its strength evolution. It further accounts for material shearing induced by pumping (Roussel, 2006) and significantly reduces the time required for complete material characterisation.

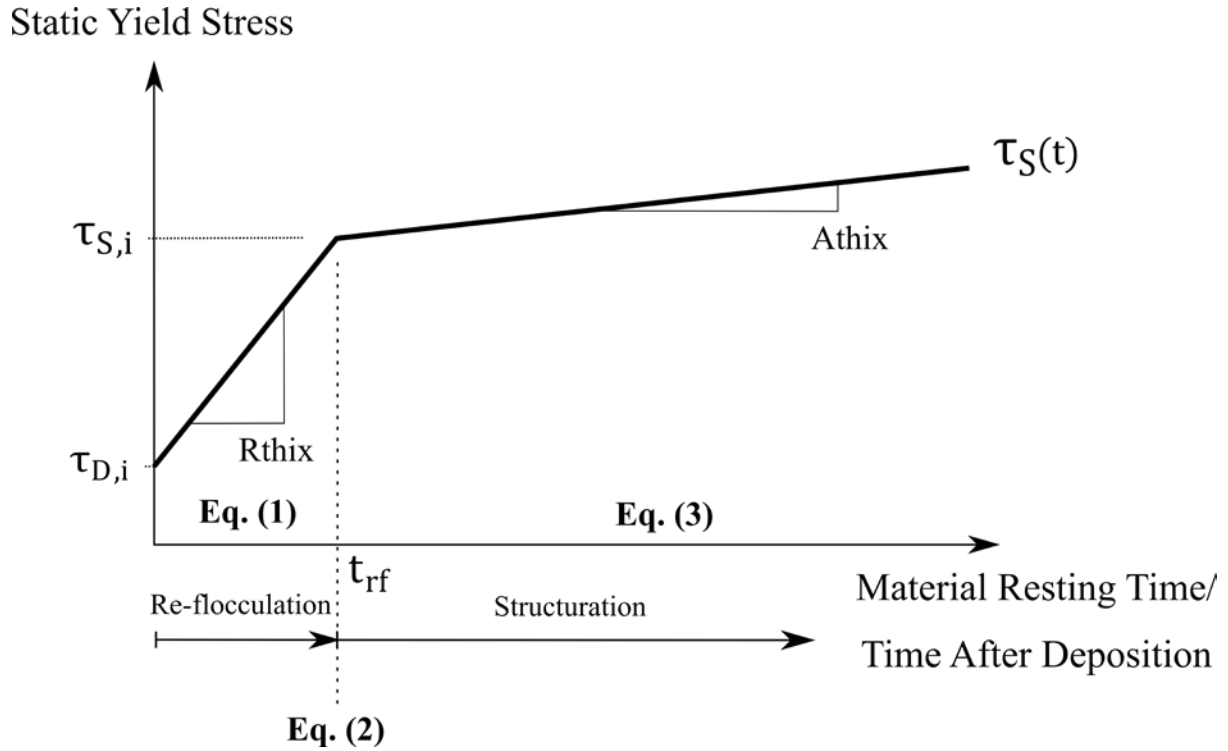


Figure 6.1: Bi-linear thixotropy model of the static yield shear stress evolution as a function of material resting time after extrusion (Kruger et al., 2019b).

Secondly, the filament shape retention model developed by Kruger et al. (2019c) is employed to ensure for adequate surface aesthetics of printed objects. The research essentially develops three analytical expressions that each predict the maximum filament layer height at which no plastic yielding will occur in three different positions within the layer under self-weight and writes as follows:

$$H_{\max} = \frac{2 \cdot \tau_{D,i}}{\rho \cdot g} \quad (6.4)$$

$$H_{\max} = \frac{2 \cdot \tau_{D,i} \cdot (1 - \nu)}{\rho \cdot g} \quad (6.5)$$

$$H_{\max} = \frac{2 \cdot \tau_{D,i}}{(1 - \nu) \cdot \rho \cdot g} \quad (6.6)$$

Chapter 6: Constructability Design

H_{\max} is the maximum filament layer height at which plastic deformations will not occur, ρ is the material density (kg/m^3), g is the gravitational acceleration constant (m/s^2) and ν is the Poisson's ratio. The research then proceeds to show that Equation 6.5 will always govern failure by interpreting Equations 6.4 to 6.6 parametrically. Hence, only Equation 6.5 is employed for the constructability design model. Note that other models have been proposed to this end (Wangler et al., 2016; Panda et al., 2019; Roussel, 2018).

Lastly, failure during 3DCP construction is quantified with the rheo-mechanics buildability model developed by Kruger et al. (2019a). The model is solely based on material rheology characteristics, in particular the bi-linear thixotropy model described earlier. Importantly, the model only accounts for failure in the form of plastic yielding as currently no literature exists on extracting a material's Young's modulus from rheology testing. Thus, failure via elastic buckling is unaccounted for, as it would require additional and extensive material characterisation. The research shows that the following expressions suffice to accurately quantify buildability performance, with Equation 6.7 acting as an a priori check:

$$\text{If } \frac{d}{dt} \left(\frac{\rho \cdot g \cdot h_1 \cdot \nu \cdot 10^{-3}}{2 \cdot l_p \cdot F_{AR}} \cdot t \right) \geq \frac{\tau_{S,i} R_{\text{thix}}}{\tau_{S,i} - \tau_{D,i}} \quad (6.7)$$

$$\text{Then use } N_L = \left[\frac{\tau_{D,i}}{\left(\frac{\rho \cdot g \cdot h_1}{2 \cdot 10^3 \cdot F_{AR}} \right) - \left(\frac{R_{\text{thix}} \cdot l_p}{\nu} \right)} \right] \quad (6.8)$$

$$\text{Else use } N_L = \left[\frac{\tau_{S,i} + \left(\frac{A_{\text{thix}} \cdot (\tau_{D,i} - \tau_{S,i})}{R_{\text{thix}}} \right)}{\left(\frac{\rho \cdot g \cdot h_1}{2 \cdot 10^3 \cdot F_{AR}} \right) - \left(\frac{A_{\text{thix}} \cdot l_p}{\nu} \right)} \right] \quad (6.9)$$

Where ν is the printing speed (mm/s), l_p the print path length per layer (mm), N_L the number of filament layers, h_1 the filament layer height (mm) and F_{AR} a strength correction factor based on the aspect ratio of the layer. The novelty of the model is that it accounts for confinement within filament layers. Confinement increases as a filament layer's height to width aspect ratio decreases, and consequently results in an apparent increase in bearing strength relative to a normalised bearing strength at an aspect ratio of two (Lamond & Pielert, 2006). This behaviour is accounted for via strength correction factors depicted in Figure 6.2. Note that the strength correction factors will differ for each material and therefore require characterisation; however, the factors presented in Figure 6.2 can be employed in most cases to yield accurate model

approximations. The model typically predicts the failure height via plastic yielding within 10 % (Kruger et al., 2019a,d). Other models that have been proposed to quantify buildability performance are depicted in (Wolfs & Suiker, 2019; Suiker, 2018; Wolfs et al., 2018; Perrot et al., 2016; Wangler et al., 2016; Panda et al., 2019; Roussel, 2018; Wolfs et al., 2019; Weng et al., 2018).

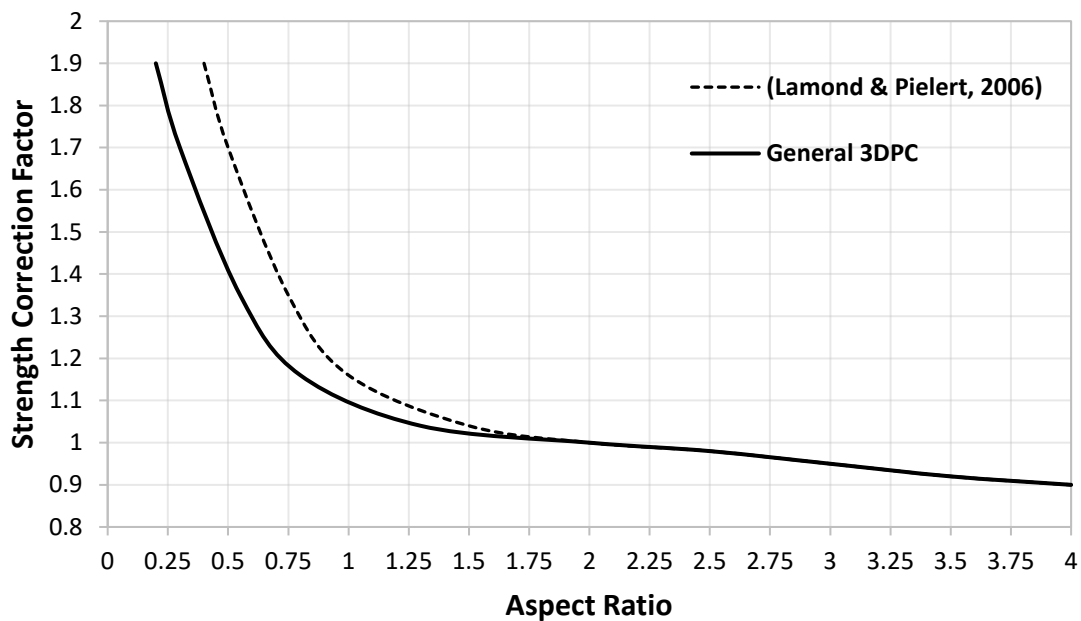


Figure 6.2: Strength correction factors (F_{AR}) for various filament layer aspect ratios (Kruger et al., 2019a).

6.2.2 Constructability design model development

The constructability design model is derived by expanding and manipulating the buildability model, while also incorporating the filament shape retention model. In order to qualify as design, the user must input the object geometry into the model. This geometry is assumed fixed, e.g. the outer dimensions of a 2 m tall structural column as specified by a design engineer. The 3D printable material's strength evolution must be determined before applying the model, preferably obtained from a representative statistical sample. After specifying the geometry and material strength, the model must return the print parameters, i.e. print speed and filament layer height, at which the specified object can be successfully constructed without failure. Note that these are the only remaining variable print parameters if a constant filament layer width is assumed. Various different print parameter combinations are possible to yield an object. For example, printing at 100 mm/s with 10 mm layer height is equivalent in vertical

building rate for constant print path length to 25 mm/s with 40 mm layer height. Although both present identical vertical building rates, they will not reach the same total vertical building height due to the difference in bearing capacity of variable filament layer aspect ratios (see Figure 6.2). Therefore, the model should determine all feasible print parameter combinations that lead towards successful construction of an object. With all the viable combinations known, the optimum print parameter combination that yields the entire object in the least amount of time can be determined.

For this research a constant print path length (l_p) is assumed, which implies that each filament layer possesses identical geometry throughout the print height. Thus, the user specifies l_p together with the design height (H_{design}) that has to be achieved. The predicted height ($H_{\text{predicted}}$) is determined by multiplying either Equation 6.8 or 6.9 (depending on Equation 6.7), which predicts the maximum number of layers achievable, with the filament layer height that was used as input for Equation 6.8 or 6.9. It is assumed that no settlement occurs in each layer so that the entire design height is reached when the specified number of layers have been printed. Therefore:

$$H_{\text{predicted}} \geq H_{\text{design}}^* \quad (6.10)$$

where

$$H_{\text{predicted}} = N_L \cdot h_l^* \quad \text{with} \quad N_L \in \{\text{Equation 6.8, 6.9}\} \quad (6.11)$$

depending on the outcome of Equation 6.7. Note that this does not result in a transcendental equation as all parameters indicated by an asterisk (*) are specified by the user. A closed-form solution is thus obtained. Due to the multiple viable print parameter combinations, numerical computation is recommended to facilitate the iterative solving procedure. A range is specified for both the print speed and filament layer height and the predicted height obtained for each combination probed against the specified design height. In order to allow for numerical computation, a 5th order polynomial equation is fitted to the ‘General 3DPC’ filament aspect ratio curve in Figure 6.2 ($R^2 = 0.999$) as follows:

$$F_{\text{AR,expl}} = -0.0607 \cdot x^5 + 0.5852 \cdot x^4 - 2.1837 \cdot x^3 + 4.0386 \cdot x^2 - 3.8195 \cdot x + 2.535 \quad (6.12)$$

with

$$x = \frac{w_{l,c}^*}{h_l^*} \quad (6.13)$$

where $w_{l,c}^*$ is the chosen filament layer width to be kept constant for the design procedure. Note that this Equation 6.12 is to be used for the case where no strength correction factor data is available on the material from testing, and will therefore only yield approximations. The print speed range is specified by the user based on 3D printer machine limitations or preference:

$$v_{\min} \leq v^* \leq v_{\max} \quad \text{with} \quad v^* \in \{\text{limitations, preference}\} \quad (6.14)$$

The filament layer height range is specified by the user based on 3D printer machine limitations or preference, in addition being limited to the maximum stable filament layer height depicted by Equation 6.5:

$$h_{l,\min} \leq h_l^* \leq h_{l,\max} \quad \text{with} \quad h_l^* \in \{\text{limitations, preference}\} \quad (6.15)$$

where

$$h_{l,\max} \leq H_{\max} \quad \text{from Equation 6.5} \quad (6.16)$$

In essence, $w_{l,c}^*$ and H_{design}^* are chosen and the range for h_l^* and v^* specified. For each combination of h_l^* and v^* , Equations 6.17 to 6.19 are employed, and the result's viability determined by Equation 6.10.

$$\text{If} \quad \frac{d}{dt} \left(\frac{\rho \cdot g \cdot h_l^* \cdot v^* \cdot 10^{-3}}{2 \cdot l_p \cdot F_{AR,expl}} \cdot t \right) \geq \frac{\tau_{S,i} \cdot R_{thix}}{\tau_{S,i} - \tau_{D,i}} \quad (6.17)$$

$$\text{Then use} \quad H_{\text{predicted}} = \left[\frac{h_l^* \cdot \tau_{D,i}}{\left(\frac{\rho \cdot g \cdot h_l^*}{2 \cdot 10^3 \cdot F_{AR,expl}} \right) - \left(\frac{R_{thix} \cdot l_p}{v^*} \right)} \right] \quad (6.18)$$

$$\text{Else use} \quad H_{\text{predicted}} = \left[\frac{h_1^* \cdot \left(\tau_{S,i} + \left(\frac{A_{\text{thix}} \cdot (\tau_{D,i} - \tau_{S,i})}{R_{\text{thix}}} \right) \right)}{\left(\frac{\rho \cdot g \cdot h_1^*}{2 \cdot 10^3 \cdot F_{\text{AR,expl}}} \right) - \left(\frac{A_{\text{thix}} \cdot l_p}{v^*} \right)} \right] \quad (6.19)$$

Additionally, Equation 6.20 can be employed after Equations 6.17 to 6.19 to determine the vertical building rate ($\dot{H}_{\text{predicted}}$) for each viable combination. The fastest vertical building rate yields the lowest total construction time, allowing for construction time optimisation possibilities. Therefore, by employing Equation 6.20, the print parameter combination that successfully yields the entire object in the least amount of time can be obtained. Equation 6.21 approximates the total print duration (t_{print}).

$$\dot{H}_{\text{predicted}} = \frac{h_1^* \cdot v^*}{l_p} \quad (6.20)$$

$$t_{\text{print}} = \frac{H_{\text{design}}^*}{\dot{H}_{\text{predicted}}} \quad (6.21)$$

6.3 Experimental verification

6.3.1 Material composition and mixing procedure

The concrete mix ingredients and proportions used for this research are given in Table 6.1. The concrete is classified as high-performance and has a water to cement ratio of 0.45. A CEM II 52.5N cement that contains between 6 and 20 % limestone extender is employed. DuraPozz Class F fly ash, together with FerroAtlantica Microsilica silica fume, are used as extenders to obtain appropriate concrete rheology for printing. The aggregate is continuously graded and has a maximum particle size of 4.75 mm. Chryso Premia 310 superplasticizer is used as the high-range water-reducing chemical admixture.

Table 6.1: 3DCP mix constituent quantities.

Constituent	Kg
Cement	579
Fly Ash	165
Silica Fume	83
Aggregate	1167
Water	261
Superplasticizer	1.48 % by mass of binder

A 50 litre concrete pan mixer with two blades facilitates the concrete mixing procedure. Initially, each constituent is accurately weighed off and temporarily stored in containers. The dry constituents are then placed into the pan mixer in the following order: aggregate, extenders and cement. This dry batch is mechanically mixed for at least three minutes until it is visually observed that the constituents form a homogenous dry mixture. Thereafter, water is poured into the pan mixer at a low rate while mixing. The concrete mixture is further mechanically mixed for one minute after all the water is added. Lastly, the superplasticizer is added to the concrete at a low rate for even distribution of the chemical throughout the concrete mixture. The batch is then further mixed for two minutes after which it is ready for use.

6.3.2 Material tests and results

The material properties required for input in the design model are determined according to the rheology testing protocol depicted in (Kruger et al., 2019b). The static yield shear stress evolution curve depicted in Figure 6.1 is obtained by performing multiple stress growth tests with a rheometer at varying resting time periods between tests. Typically, a test is performed at each of the following resting time periods (seconds): 0, 10, 20, 30, 40, 50, 60, 90, 120, 1200, 2400, 3600. However, these periods should not be assumed as fixed, but recommended intervals to capture thixotropic behaviour in the time frame relevant to 3DCP. For each test conducted, the static and dynamic yield stress is obtained (Germann Instruments, n.d.). The re-flocculation rate (R_{thix}) is determined with the yield stresses obtained for the intervals ranging between 0 and 120 seconds (short term). The static yield shear stress of each interval is plotted against its corresponding resting time gap. However, the dynamic yield shear stress is used for the 0-second time interval. This is to simulate actual printing, whereby, as soon as the material exits the nozzle and material shearing halts, the material will rebuild from its dynamic to static

yield shear stress. The gradient of this plot is then obtained and represents the rate of re-flocculation (R_{thix}). The structuration rate (A_{thix}) is determined with the yield stresses obtained for the longer intervals, namely 0, 1200, 2400 and 3600 seconds. Similar to the re-flocculation rate, the static yield shear stress of each interval is plotted against its corresponding resting time gap, and the gradient of the plot determined to yield A_{thix} . Note that in this case no dynamic shear stress value is used. $\tau_{S,i}$ and $\tau_{D,i}$ are obtained from the initial (0-second) stress growth rheological test. With these four parameters known, the bi-linear model that depicts a material's static yield shear strength evolution can be determined, and subsequently applied in the constructability design model.

Ideally, one concrete batch must be prepared and utilized for both the printing and rheology testing as to obtain accurate and representative material properties. This is however not possible since the material properties are required to obtain the optimum print parameters from the design model for slicing and printing to commence; hence, the rheological testing and printing cannot be performed simultaneously. For this reason, 5 concrete batches are rheologically characterised prior to printing, in order to account for rheology variation as an effect of concrete batch mixing. Each rheology test requires 20 litres of concrete and is executed with the Germann ICAR Plus Rheometer (Germann Instruments, n.d.). The rheology testing protocol is given in Table 6.2.

Table 6.2: Rheology testing protocol followed for each of the 5 concrete batches in order to obtain the required data for the static yield shear stress evolution curves, as depicted in Figure 6.1.

Concrete Age After Mixing (min:s)	Test Number	Resting Time Interval	Shear Rate (s^{-1})	Shear Duration (s)	Action	Result
00:00-01:00	-	-	-	-	Transport concrete to rheometer	-
01:00-02:00	1	0 s (Initial)	1	60	Stress growth test	Obtain initial static and dynamic yield shear stress for shear stress evolution curve (Figure 6.1)
02:10-03:10	2	10 s	1	60	Stress growth test	Obtain static yield stress, plot against time interval, to determine R_{thix}
03:40-04:40	3	30 s	1	60	Stress growth test	Obtain static yield stress, plot against time interval, to determine R_{thix}
05:40-06:40	4	60 s	1	60	Stress growth test	Obtain static yield stress, plot against time interval, to determine R_{thix}
08:10-09:10	5	90 s	1	60	Stress growth test	Obtain static yield stress, plot against time interval, to determine R_{thix}
11:10-12:10	6	120 s	1	60	Stress growth test	Obtain static yield stress, plot against time interval, to determine R_{thix}
22:10-23:10	7	10 min	1	60	Stress growth test	Obtain static yield stress, plot against time interval, to determine A_{thix}
43:10-44:10	8	20 min	1	60	Stress growth test	Obtain static yield stress, plot against time interval, to determine A_{thix}
74:10-75:10	9	30 min	1	60	Stress growth test	Obtain static yield stress, plot against time interval, to determine A_{thix}

It is of crucial importance to correlate the rheometer's shear rate to that of the shear rate induced by the pump. In the absence of relevant literature, an approximation of the shear rate is made by correlating the rotational speed of the rheometer's vane to that of the pump's screw during printing. However, the print speed is only obtained from the design model after determining the material properties. The pump screw rotational speed is therefore not known before conducting the rheology testing procedure. In this case, a shear rate and duration of $1 s^{-1}$ and 60 seconds respectively are used from previous research that yielded accurate results (Kruger et al., 2019a,b,d). Note that this is only an approximation of the microstructural breakdown induced by pumping, as there currently does not exist any literature that expresses the aforementioned relationship. Recent research does however suggest to use the lowest

possible shear rate that results in flow-onset to obtain the most accurate representation of a material's shear stress (Nerella et al., 2019).

The static yield shear stress evolution curve for each of the 5 concrete batch tests are depicted in Figure 6.3. These curves are constructed by processing the data obtained from the rheology protocol depicted in Table 6.2 and then applying the principles mentioned earlier. The batches named Rheo 1, 3 and 4 present similar rheology characteristics and shear strength evolution. In contrast, Rheo 5 presents significantly higher static yield shear stress and Rheo 2 lower than the other 3 batches. Rheology inconsistency is typically experienced when batch mixing concrete, while continuous mixing pumps generally provide better rheology control methods. For this reason, an average static yield shear stress evolution curve is determined from the 5 concrete batches and used as material input for the design model. Table 6.3 gives the associated rheology parameters for each concrete batch.

Similar variability in measured material properties for 3DCP are observed in literature, with coefficient of variation (CoV) values of up to 22 % in (Wolfs & Suiker, 2019), 20 % in (Wolfs et al., 2019) and 23 % in (Wolfs et al., 2018). Note that these CoV values were derived for concrete obtained from continuous mixing pumps, which typically provide better rheology control measures than batch mixing processes. Therefore, higher CoV values are to be expected for batch mixed concrete. As already manifested in literature (Wolfs et al., 2019), such variability is common for 3DCP setups due to their inherent sensitivity.

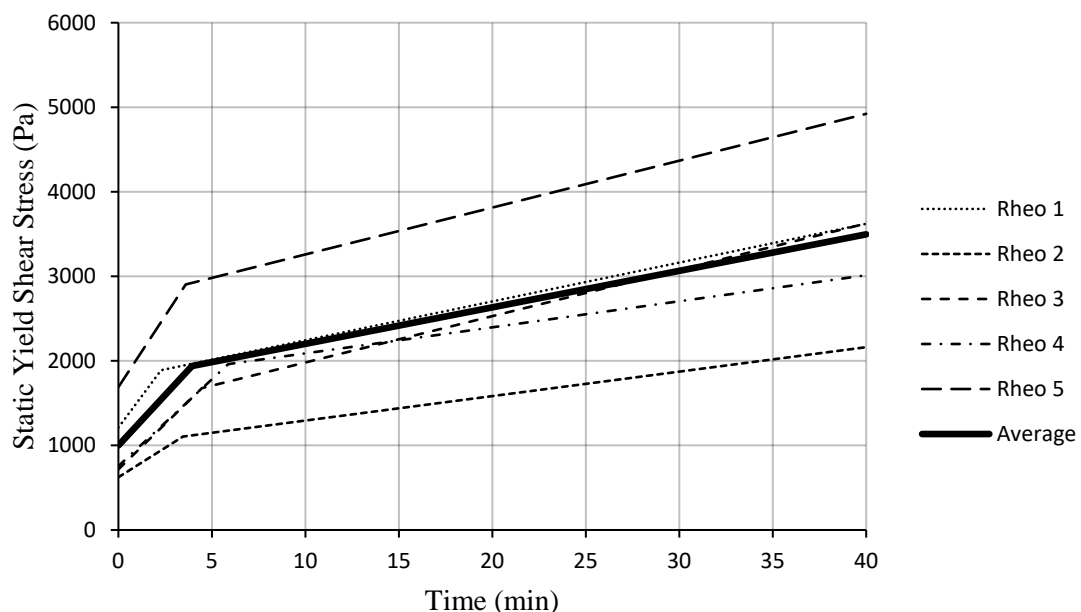


Figure 6.3: Static yield shear stress evolution curves for each concrete batch tested via the rheometer. The average of these curves are used as material input for the design model.

Table 6.3: Rheology parameters associated with each of the static yield shear stress evolution curves depicted in Figure 6.3.

Test Number	Initial Static	Initial Dynamic	R_{thix} (Pa/s)	A_{thix} (Pa/s)
	Yield Shear Stress (Pa)	Yield Shear Stress (Pa)		
Rheo 1	1890	1212	4.95	0.77
Rheo 2	1105	624	2.32	0.48
Rheo 3	1678	717	3.58	0.91
Rheo 4	1962	756	3.42	0.51
Rheo 5	2904	1690	5.62	0.92
Average	1907.8	999.8	3.98	0.72
Std. Dev	650.57	447.78	1.31	0.21
CoV	0.341	0.447	0.329	0.291

Additional material properties required for the model are the density and Poisson's ratio. The concrete mix's density is obtained by filling a known volume (1 litre) and thereafter measuring the sample's mass. The density is then calculated by dividing the mass by the volume, which in this research yields 2150 kg/m³. The fresh concrete state's Poisson's ratio is chosen as 0.3 in the absence of accurate measurement techniques (Wolfs et al., 2018; Suiker, 2018; Federal Highway Administration, n.d.).

6.3.3 Constructability design model application

Model input parameters

Geometrical input is required for the constructability design model, in addition to the material input parameters determined in the previous section. For this research, a 630 x 230 x 500 mm rectangular structural wall element is chosen, as depicted in Figure 6.4. The wall consists of W-type infill that is commonly applied in 3DCP projects (Bos et al., 2016; Begum, 2019). The external dimensions are chosen with no particular structure in mind, but to represent a realistic wall part within the available printer build volume of roughly 1 m³. The infill improves the global stability of the wall by reducing thin-walled behaviour. Essentially, the effective length of the perimeter is reduced and the stiffness of the structure increased by linking both perimeters to one another. This vastly reduces the probability of geometrical nonlinearity, such as elastic buckling which the design model does not account for. The total

Chapter 6: Constructability Design

print path length per layer for this object amounts to 2378 mm and remains constant for each filament layer throughout the entire building height. The filament layer width is chosen as 30 mm.

The feasible print speed range is chosen as 40 to 100 mm/s. The lower bound value is governed by the pump's rotational sensitivity while the upper bound value is simply user preference. The feasible filament layer height range is chosen as 8 to 15 mm. The circular print nozzle has a diameter of 25 mm; therefore, an approximately rectangular filament cross-section is obtained by squeezing of the material. The authors acknowledge that this is not ideal; however, it is currently the only available nozzle type as the 3D concrete printer does not support a 4th rotational degree of freedom. The lower bound value is thus user preference, while the upper bound value is limited by the nozzle size and shape i.e. the extruded filament cross-section becomes increasingly circular as the layer height increases. The maximum stable filament layer height under self-weight is determined as 66.63 mm via Equation 6.5. This is significantly larger than the upper bound value of 15 mm, thereby satisfying Equation 6.16. Table 6.4 summarises the input parameters for this research.

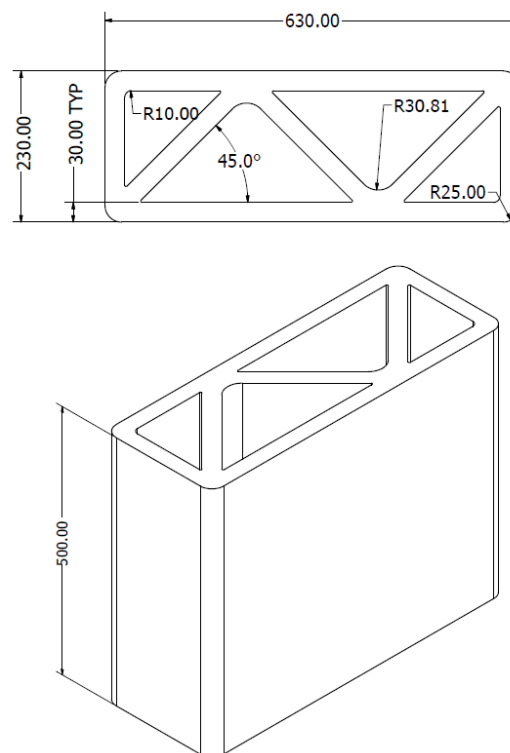


Figure 6.4: A 630 x 230 x 500 mm rectangular structural wall element with W-type infill printed for experimental verification of the constructability design model.

Table 6.4: Summary of the input parameters for the design model.

Material Input Parameters	
$\tau_{S,i}$	1907.8 Pa
$\tau_{D,i}$	999.8 Pa
R_{thix}	3.98 Pa/s
A_{thix}	0.72 Pa/s
ρ	2150 kg/m ³
ν	0.3
Geometrical Input Parameters	
$w_{l,c}^*$	30 mm
l_p	2378 mm
H_{design}^*	500 mm
Feasible Print Parameter Range	
h_l^*	8 – 15 mm
v^*	40 – 100 mm/s

Model output

Figure 6.5 depicts all the feasible print parameter combinations and their corresponding vertical building rates as obtained from the model. No limitations, such as the specified print speed and filament layer height ranges, are yet imparted on these results. Figure 6.5 thus depicts all theoretically plausible print parameter combinations that can successfully yield the entire specified wall element, based only on the material properties. It is evident that higher print speeds are attainable at lower filament layer heights that result in higher stable vertical building rates. This is ascribed to the finer layer resolution that enables the critical layer to develop more strength in conjunction with the increased confinement that yields larger strength correction factors (see Figure 6.2). It is therefore deduced that smaller filament layer heights will generally yield the highest stable vertical building rates.

Figure 6.6 depicts the feasible print parameter combinations and their corresponding vertical building rates after implementing the print speed and filament layer height boundary conditions, as specified in Table 6.4. The fastest vertical building rate is depicted by the highest point in the triangle, which corresponds to a print speed of 87 mm/s at filament layer height of

Chapter 6: Constructability Design

8 mm. This print parameter combination theoretically yields the fastest stable vertical building rate that will thus enable the successful construction of the entire structural wall element in the least amount of time. This print parameter combination is selected and applied for the construction of the wall element. Table 6.5 gives a summary of the optimum design parameters obtained from the model.

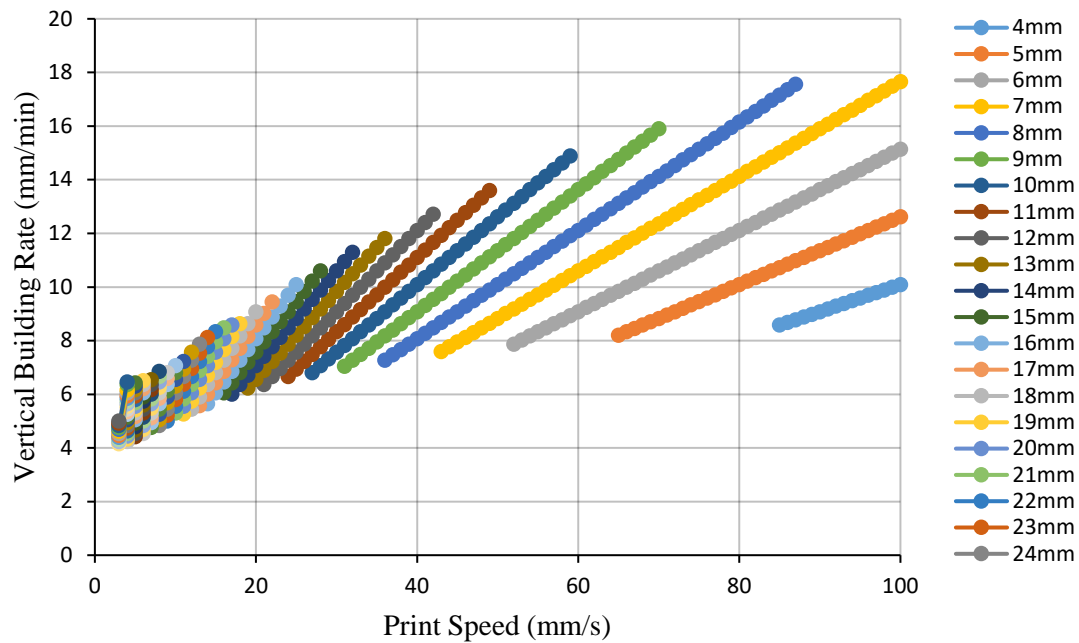


Figure 6.5: Design envelope depicting the entire feasible design parameter domain and corresponding vertical building rate. Filament layer heights are specified in the legend.

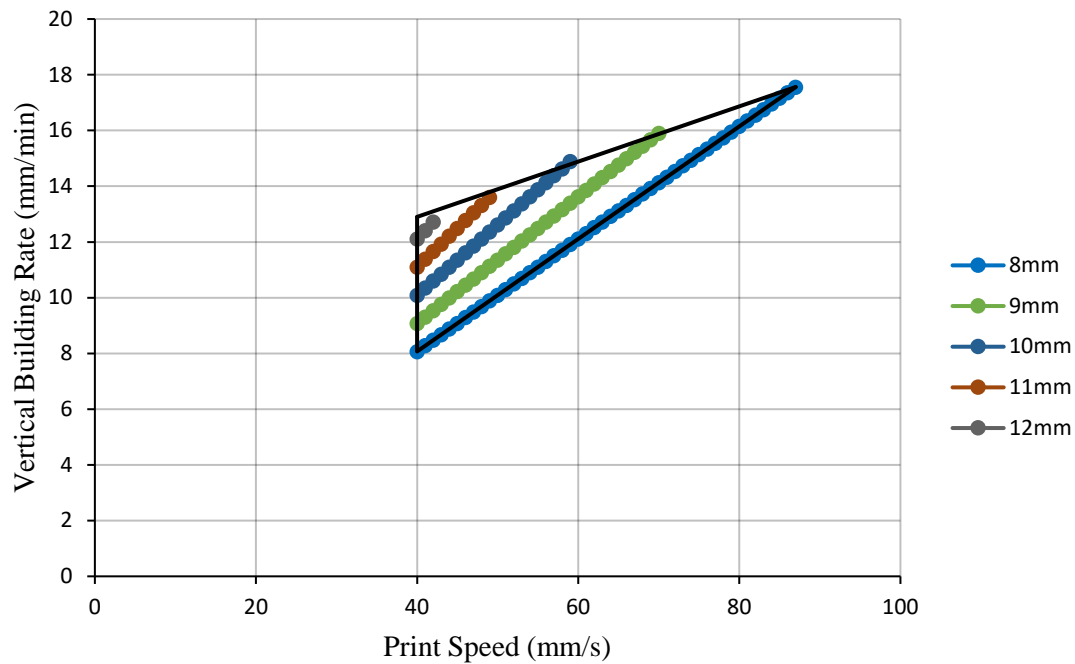


Figure 6.6: Design envelope depicting the feasible design parameter domain and corresponding vertical building rates after implementation of the print speed and filament layer height boundary conditions. Filament layer heights are specified in the legend.

Table 6.5: Summary of the optimum design parameters obtained from the model that are used for the construction of the wall element.

Print Speed (v)	87 mm/s
Filament Layer Height (h_1)	8 mm
Total Print Duration (t_{print})	28.7 min
Vertical Building Rate ($\dot{H}_{\text{predicted}}$)	17.56 mm/min

6.3.4 3D concrete print results

The 3DCP structural wall element indicated in Figure 6.7 is constructed using the optimised design parameters summarised in Table 6.5. A total building height of 360 mm is obtained, which equates to 45 filament layers, in 21 minutes. The wall collapsed shortly after placement of the 45th layer due to plastic yielding of the critical layers on the right-hand side. Figure 6.8 depicts the wall failure initiation and propagation. Failure was near instantaneous, and the presence of surface cracks confirm the failure mode as plastic yielding of the material (Perrot

et al., 2016). The design model therefore over predicted the attainable building height by 28 %, by using the average material properties given in Table 6.3. Note that, if the material properties of concrete batch Rheo 2 (the weakest of the 5 concrete batches given in Table 6.3) are applied to the model, a total vertical building height of 232 mm is predicted. At the other end of the spectrum, if material properties from concrete batch Rheo 5 are applied, a total vertical building height of 960 mm is predicted. Therefore, variation in material rheology properties yields a vertical building height range of 232 to 960 mm, where the obtained height of 360 mm falls within the range. This large deviation in experimentally obtained height from predicted height is not uncommon for 3DCP, where deviations of up to 43 % (Wolfs et al., 2019) and 37 % (Wolfs et al., 2018) were obtained by finite element models that employ the average material properties determined from multiple concrete samples. It is evident that variation in material properties, which must be determined before applying the models, has a consequential influence on the accuracy of the predictions. For this reason, deterministic modelling is insufficient for industry application. While it has been shown that the fundamental model uncertainty or inaccuracy is relatively small (Kruger et al., 2019a,d), material uncertainty is significant. A statistical design model is required to reduce the influence that variation in material properties has on accurate buildability prediction. In addition and to a lesser extent, the following aspects are believed to contribute towards uncertainty and variation in this result:

- As a means of approximating the shear induced by pumping, the rotational speed of the pump's screw is used to obtain a shear rate that is applied for the rheometry testing. In the case of the design model, the optimum print speed (and thus pump speed) is only obtained after several concrete batches' material properties have been determined from rheometry testing and the average thereof applied to the model. It is therefore impossible to correlate the rheometer's vane rotational speed to that of the pump screw's rotational speed, as the pump speed is only obtained after applying the model. The shear strength evolution of a material may therefore be over or under estimated, as the applied shear rate has a significant influence on the measured shear stress (Nerella et al., 2019). More research is required to accurately predict and simulate material microstructural breakdown induced by pumping.
- The average filament layer width was measured as 35 mm during printing. However, due to the cross-section shape of the filament layer, roughly 30 mm of the 35 mm is in contact with subsequent filament layers. More weight is therefore

imparted per filament layer deposition, since 30 mm was applied in the model. Theoretically, failure should occur sooner than predicted.

- Over extrusion of filament occurred at two corners due to slight deceleration of the nozzle at sharp corners, while the extrusion rate remained constant. These positions are at the start and end points of the infill pattern respectively, as can be visually observed in Figure 6.7. More weight is thus imparted on filament layers than what the model accounted for. Failure of the wall did initiate and propagate from the nozzle position indicated in Figure 6.7, which is also one of the two points where over extrusion occurred.

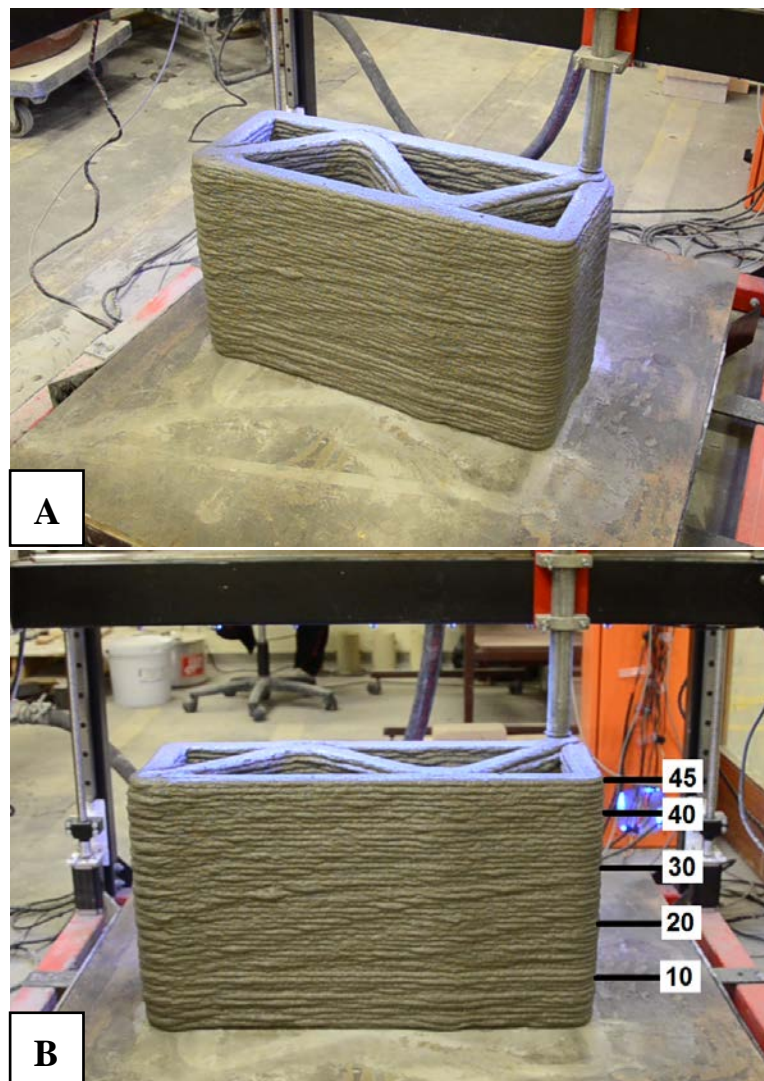


Figure 6.7: a) Isometric view of the printed wall element with W-type infill moments before failure and b) front view of the wall element indicating the position of various filament layers.

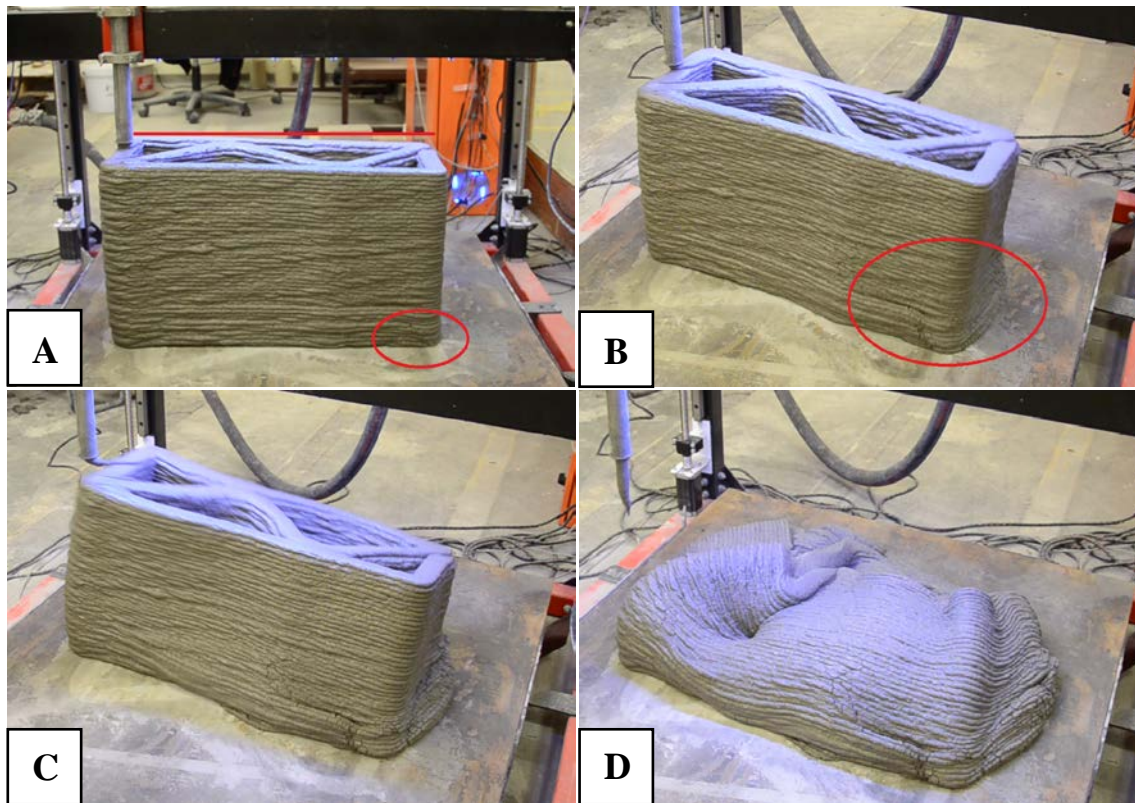


Figure 6.8: Wall failure initiation and propagation indicating a) the development of surface cracks due to plastic yielding in the bottom critical layers, b) flow-onset on the right-hand side of the wall, c) global tumbling of the wall and d) the result of an unsuccessful constructability attempt of a 3DCP structural wall element.

6.4 Proposed statistical design model

Deterministic analytical models are not entirely suitable for industry application. Variation in material parameters, and to lesser degree print or geometrical parameters, contribute towards higher probability of failure, i.e. not achieving predicted building heights. This is evident in this research where large coefficients of variation (CoV) were obtained for the concrete material properties. A probabilistic design model, which incorporates random variables and probability distributions into the model, is developed in this section. Probability distributions are only applied to material parameters and partial factors then derived that reduce the probability of failure to an acceptable extent. This procedure is commonly applied in reinforced concrete design norms to reduce the probability of failure of the deterministic models to an acceptable degree that satisfies both safety and cost requirements. No attempt is made to

account for cost-optimisation in this research, as insufficient 3DCP process data is currently available to this end.

The first-order reliability method (FORM) is employed to determine the reliability of the deterministic design model presented in this research (Manoj, 2016). In addition, the contribution of each variable parameter's sensitivity to the total reliability of the model is determined. Holicky (2009) presents more information on reliability analysis for structural design. The software FreeVaP is utilised to facilitate the FORM analysis (Petschacher, 2019). Initially, the limit state or performance function is based on Equation 6.19 and defined as follows:

$$G(X) = -500 + \left[\frac{8 \cdot \left(\tau_{S,i} + \left(\frac{A_{\text{thix}} \cdot (\tau_{D,i} - \tau_{S,i})}{R_{\text{thix}}} \right) \right)}{\left(\frac{2150.9,81.8}{2 \cdot 10^3 \cdot 1,765} \right) - \left(\frac{A_{\text{thix}} \cdot 2378}{87} \right)} \right] \quad (6.22)$$

The design height of 500 mm used in this research is employed to define the limit state i.e. if the design model (specifically Equation 6.19) predicts larger than 500 mm then a favourable/safe outcome is obtained and vice versa. This is based on the input and output parameters presented in Tables 6.4 and 6.5, which are assumed deterministic. This is mostly the case for additive manufacturing, where parameters such as print speed, layer height and the object geometry can be controlled and specified with almost negligible variation. The material parameters are assigned normal and lognormal distributions, of which their values are presented in Table 6.3, in particular the mean and standard deviation. Note that only material parameter data obtained from 5 concrete batches are used and that larger statistical samples are required for more accurate results.

The results from the FORM analysis are depicted in Table 6.6. The sensitivity factor (α) indicates for both instances that the static yield shear stress and structuration rate impact the reliability of the design model the most. This is due to the relatively long total printing time compared to the total re-flocculation time. By assuming a normal distribution of the material parameters, a 51 % probability of failure is obtained, where failure is defined as the predicted height obtained by Equation 6.19 is less than 500 mm. Assuming lognormal distributions, which are theoretically more representative of actual material parameter variation as values cannot be less than 0, a 61 % probability of failure is obtained. This result clearly demonstrates the exigency for a statistical design model.

Table 6.6: Results obtained from the FORM analysis for both normal and lognormal distributions assigned to the material parameters of the limit state function.

Normal Distribution			Lognormal Distribution		
Parameter	Design Value	Sensitivity Factor (α)	Parameter	Design Value	Sensitivity Factor (α)
$\tau_{S,i}$	1920	-0.853	$\tau_{S,i}$	1954	-0.861
A_{thix}	0.722	-0.497	A_{thix}	0.718	-0.483
$\tau_{D,i}$	1001	-0.130	$\tau_{D,i}$	925.7	-0.122
R_{thix}	3.983	-0.088	R_{thix}	3.815	-0.102
Reliability Index (β)		-0.022	Reliability Index (β)		-0.276
Probability of Failure		0.508	Probability of Failure		0.609

A partial factor is now derived that accounts for variation in material parameters due to the batch mixing process of concrete. A factor is applied to the static yield shear stress as well as the structuration rate. These factors essentially reduce the design model's probability of failure from 61 % to that of a chosen percentage. The dynamic yield shear stress and re-flocculation rate are not considered as their α -values are negligibly small (see Table 6.6). The design probability of failure is chosen as 10 %, assuming laboratory or controlled conditions. Note that this percentage is typically determined by accounting for cost-implications in the event of failure, which is outside the scope of this research due to insufficient data. Further, note that a value larger than 10 % will result in smaller material partial factors and vice versa. The following equation is employed to derive the respective partial factors (Holicky, 2009):

$$\gamma_m = \frac{X_k}{X_d} = \frac{\frac{1}{\sqrt{1+w_x^2}} \cdot e^{\left(u_k \cdot \sqrt{\ln(1+w_x^2)}\right)}}{\frac{1}{\sqrt{1+w_x^2}} \cdot e^{\left(u_p \cdot \sqrt{\ln(1+w_x^2)}\right)}}, \quad p = \Phi(-\alpha \cdot \beta) \quad (6.23)$$

where w_x denotes coefficients of variation of X (see Table 6.3), u_k or u_p the characteristic or p-fractile of the standardised random variable having the same probability distribution as X. Note that in this instance the average material properties are specified as input for the design

model, hence $u_k = 0$ is assumed. Equation 6.23 is only applicable to lognormal distributions, which in this research yielded the worst probability of failure (61 %) for the design model.

The partial factors for the static yield shear stress and structuration rate were determined as 1.376 and 1.171 respectively and conservatively rounded up to 1.4 and 1.2. In addition, a model uncertainty factor that specifically accounts for the variation in shear rate employed for rheometer testing of 1.1 is chosen (refer to Section 6.3.4). EN 1990 (Holicky, 2009; CEN, 2002) specifies that a value between 1.05 and 1.15 can be used in most common cases. This factor is only applicable to the static yield shear stress. Theoretically, the shear rate of the rheometer should only affect the magnitude of the static yield shear stress and not the structuration rate. Therefore, this factor is multiplied only with the partial factor for static yield shear stress to yield a final rounded value of 1.55. The partial factors are summarised in Table 6.7.

Table 6.7: Partial factor values for material parameters in the statistical design model.

Parameter	Value	Description
$\gamma_{M,1}$	1.55	Accounts for $\tau_{S,i}$ variability due to batch mixing process, as well as for variation in $\tau_{S,i}$ due to shear rate applied by rheometer (factor of 1.1)
$\gamma_{M,2}$	1.2	Accounts for A_{thix} variability due to batch mixing process

By applying these partial factors and performing an analysis with Equation 6.19, the total predicted building height reduces to 312 mm, as opposed to 500 mm obtained by the deterministic model. This yields an under prediction of 13.3 % if compared to the experimental results obtained in Section 6.3.4. The impact of the partial factors on the material resistance is visually depicted by the static yield shear stress curves in Figure 6.9. Alternative methods of concrete mixing with better quality control and consistency, e.g. continuous mixing pumps with temperature readings, can yield significantly lower partial factors for material properties than for batch mixing. However, more data is required to determine said partial factors. Note that no partial factors are derived for Equation 6.18 since no experimental data is available. Equation 6.18 is only applicable for exceptionally high vertical building rates and rarely governs failure for 3DCP. The statistical design model for 3DCP is thus proposed as follows, with partial factor values given in Table 6.7:

Chapter 6: Constructability Design

$$\text{If } \frac{d}{dt} \left(\frac{\rho \cdot g \cdot h_1^* \cdot v^* \cdot 10^{-3}}{2 \cdot l_p \cdot F_{AR,expl}} \cdot t \right) \geq \frac{\tau_{S,i} \cdot R_{thix}}{\tau_{S,i} - \tau_{D,i}} \quad (6.24)$$

$$\text{Then use } H_{\text{predicted}} = \left[\frac{h_1^* \cdot \tau_{D,i}}{\left(\frac{\rho \cdot g \cdot h_1^*}{2 \cdot 10^3 \cdot F_{AR,expl}} \right) - \left(\frac{R_{thix} \cdot l_p}{v^*} \right)} \right] \quad (6.25)$$

$$\text{Else use } H_{\text{predicted}} = \left[\frac{h_1^* \cdot \left(\frac{\tau_{S,i}}{\gamma_{M,1}} + \left(\frac{A_{thix} \cdot (\tau_{D,i} - \frac{\tau_{S,i}}{\gamma_{M,1}})}{R_{thix} \cdot \gamma_{M,2}} \right) \right)}{\left(\frac{\rho \cdot g \cdot h_1^*}{2 \cdot 10^3 \cdot F_{AR,expl}} \right) - \left(\frac{A_{thix} \cdot l_p}{v^* \cdot \gamma_{M,2}} \right)} \right] \quad (6.26)$$

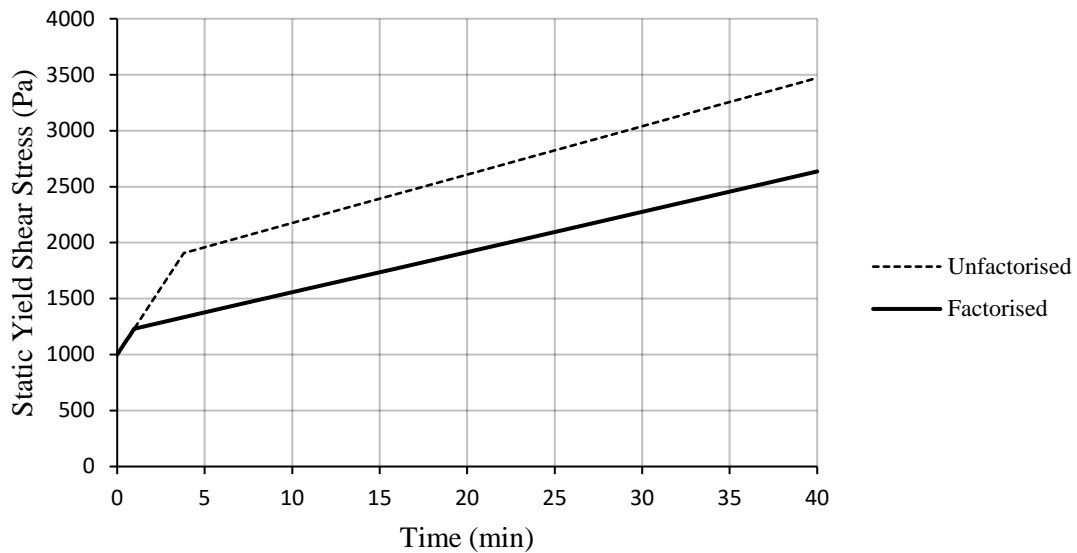


Figure 6.9: Influence of the partial factors given in Table 6.7 as applied on the static yield shear stress curve of the material used for the experimental process.

6.5 Conclusion

A constructability design model is developed that determines the print speed and filament layer height combination that yields the fastest vertical building rate, whilst ensuring for the successful construction of an object. Only physical nonlinearity is accounted for, i.e. plastic yielding of the material. The following conclusions are drawn from the experimental testing:

- High variation in material rheology parameters is obtained due to the concrete batch mixing process. Coefficient of variation values of over 30 % are obtained.
- The working process of the design model can be visually depicted by plotting vertical building rates against print speed for each filament layer height to yield a design envelope. Based on printer limitations, or user preference, the optimum print parameter combination can be determined.
- Only 360 of the total specified 500 mm vertical building height is obtained during experimental testing by employing the print parameter combination obtained from the deterministic design model. This yields an over prediction of 28 %.
- The deterministic design model is not sufficient for industry adoption as it presents a 61 % probability of failure in this research. This is mainly due to the high CoV values of the batch mixed material, as the rheometry testing cannot be conducted simultaneously with the 3D print. Additionally, the rheometer's shear rate cannot be correlated to that induced by pumping.
- A probabilistic design model is developed by employing the first-order reliability method (FORM) and deriving material partial factors to reduce the probability of failure of the design model to 10 %. By analysis, it is determined that if this model was employed for the experimental testing, a 13.3 % under prediction would have been obtained.

The probabilistic design model is a useful tool for the 3D concrete printing industry to allow for time, and indirectly cost, savings. Due to the small statistical sample used to derive the partial factors, plenty opportunity exists for further refinement. Nevertheless, the model serves as a general starting point for 3DCP parameter design and optimisation with low probability of failure. Future research possibilities include the development of a concrete mixing process that significantly reduces variation in material rheology between different batches. Additionally, more research is required to accurately quantify the impact of shear rate on measured material shear stress from rheometry testing.

Notations

The following parameters are applicable to this model in its complete state:

- A_{thix} is the structuration rate of the material (Pa/s).
- $F_{\text{AR,expl}}$ is the explicit analytical expression for the strength correction factors that account for confinement (unitless).
- g is the gravitational acceleration constant taken as 9.81 m/s^2 .
- $\gamma_{\text{M},1}$ material partial factor applicable to $\tau_{\text{S},i}$ (unitless).
- $\gamma_{\text{M},2}$ material partial factor applicable to A_{thix} (unitless).
- h_1^* is the chosen filament layer height (mm).
- $H_{\text{predicted}}$ is the total predicted vertical building height, that can safely be *rounded up* to the nearest multiple of the chosen filament layer height (mm).
- l_p is the constant path length per filament layer (mm).
- ρ is the density of the material (kg/m^3).
- R_{thix} is the re-flocculation rate of the material (Pa/s).
- t is the printing time (s).
- $\tau_{\text{D},i}$ is the initial dynamic yield shear stress of the material (Pa).
- $\tau_{\text{S},i}$ is the initial static yield shear stress of the material (Pa).
- v^* is the chosen constant printing speed (mm/s).
- $w_{1,c}^*$ is the chosen filament layer width to be kept constant for the design procedure (mm).

Acknowledgements

The research is funded by The Concrete Institute (TCI) and the Department of Trade and Industry of South Africa under THRIP Research Grant TP14062772324.

Contribution of authors

This work is part of Jacques Kruger's PhD research, executed under the supervision of Professor Gideon van Zijl and Doctor Stephan Zeranka. Mr Kruger conducted all experimental work, the analysis, interpretation and presentation of data, as well as the writing of the manuscript. Prof. van Zijl and Dr. Zeranka assisted in proofreading of the manuscript and

proposed insightful amendments. Mr Seung Cho assisted with the execution of the experimental work. Professor Celeste Viljoen assisted with the development of the statistical design model.

6.6 References

- Begum, S. 2019. *NTU's 3D-printing robot makes bathrooms nearly twice as fast and cheap*. [Online], Available: www.straitstimes.com/singapore/ntu-team-creates-worlds-first-3d-printed-bathrooms [2019, July 24].
- Bos, F., Wolfs, R., Ahmed, Z. & Salet, T. 2016. Additive manufacturing of concrete in construction: potentials and challenges of 3D concrete printing. *Virtual and Physical Prototyping*. 11(3):209–225.
- CEN. 2002. *EN 1990: Eurocode - Basis of structural design*. [Online], Available: <https://www.phd.eng.br/wp-content/uploads/2015/12/en.1990.2002.pdf>.
- Federal Highway Administration. n.d. *Poisson's ratio and temperature gradient adjustments*. Washington. [Online], Available: <https://www.fhwa.dot.gov/publications/research/infrastructure/pavements/pccp/execsumm/valtm12a.pdf>.
- Germann Instruments. n.d. *ICAR Rheometer*. [Online], Available: <http://germann.org/products-by-application/rheology-of-concrete/icar-rheometer> [2018, July 24].
- Ghaffar, S.H., Corker, J. & Fan, M. 2018. Additive manufacturing technology and its implementation in construction as an eco-innovative solution. *Automation in Construction*. 93(September):1–11.
- Gosselin, C., Duballet, R., Roux, P., Gaudillière, N., Dirrenberger, J. & Morel, P. 2016. Large-scale 3D printing of ultra-high performance concrete - a new processing route for architects and builders. *Materials and Design*. 100:102–109.
- Holicky, M. 2009. *Reliability analysis for structural design*. 1st Editio ed. SUN MeDIA Stellenbosch. [Online], Available: <https://scholar.sun.ac.za/bitstream/handle/10019.1/101856/9781920689346.pdf?sequence=1&isAllowed=y>.
-

- Kruger, J., Zeranka, S. & van Zijl, G. 2019a. 3D concrete printing: A lower bound analytical model for buildability performance quantification. *Automation in Construction*. 106:102904.
- Kruger, J., Zeranka, S. & van Zijl, G. 2019b. An ab initio approach for thixotropy characterisation of (nanoparticle-infused) 3D printable concrete. *Construction and Building Materials*. 224:372-386.
- Kruger, P.J., Zeranka, S. & van Zijl, G.P.A.G. 2019c. A rheology-based quasi-static shape retention model for digitally fabricated concrete.
- Kruger, P.J., Zeranka, S. & van Zijl, G. 2019d. Quantifying constructability performance of 3D concrete printing via rheology-based analytical models. In Dresden, Germany *Proceedings of the 2nd International RILEM Conference on Rheology and Processing of Construction Materials*.
- Lamond, J.F. & Pielert, J.H. 2006. *Significance of Tests and Properties of Concrete and Concrete-making Materials*. West Conshohocken, Philadelphia: ASTM International.
- Manoj, N.R. 2016. First Order Reliability Method: Concepts and Application. Delft University of Technology. [Online], Available: <https://pdfs.semanticscholar.org/9e73/3a66258a41dcd34e1751be66308ec4e4610d.pdf>.
- Nerella, V.N., Beigh, M.A.B., Fataei, S. & Mechtcherine, V. 2019. Strain-based approach for measuring structural build-up of cement pastes in the context of digital construction. *Cement and Concrete Research*. 115(August 2018):530–544.
- Panda, B., Lim, J.H. & Tan, M.J. 2019. Mechanical properties and deformation behaviour of early age concrete in the context of digital construction. *Composites Part B*. 165(December 2018):563–571.
- Perrot, A., Rangeard, D. & Pierre, A. 2016. Structural built-up of cement-based materials used for 3D-printing extrusion techniques. *Materials and Structures/Materiaux et Constructions*. 49(4):1213–1220.
- Petschacher. 2019. *Software & IT*. [Online], Available: <http://www.petschacher.at/en/software-it/> [2019, June 16].
- Roussel, N. 2006. A thixotropy model for fresh fluid concretes: Theory, validation and applications. *Cement and Concrete Research*. 36(10):1797–1806.
-

-
- Roussel, N. 2018. Rheological requirements for printable concretes. *Cement and Concrete Research*. 112(March):76–85.
- Suiker, A.S.J. 2018. Mechanical performance of wall structures in 3D printing processes: Theory, design tools and experiments. *International Journal of Mechanical Sciences*. 137(January):145–170.
- Tsavidaridis, K.D., Kingman, J.J. & Toropov, V. V. 2015. Application of structural topology optimisation to perforated steel beams. *Computers and Structures*. 158(May):108–123.
- Wangler, T., Lloret, E., Reiter, L., Hack, N., Gramazio, F., Kohler, M., Bernhard, M., Dillenburger, B., et al. 2016. Digital Concrete: Opportunities and Challenges. *RILEM Technical Letters*. 1:67–75.
- Weng, Y., Li, M., Tan, M.J. & Qian, S. 2018. Design 3D printing concrete materials via Fuller Thompson theory. *Construction & Building Materials*. 163:600–610.
- Wolfs, R.J.M. & Suiker, A.S.J. 2019. Structural failure during extrusion-based 3D printing processes. *The International Journal of Advanced Manufacturing Technology*.
- Wolfs, R.J.M., Bos, F.P. & Salet, T.A.M. 2018. Early age mechanical behaviour of 3D printed concrete: Numerical modelling and experimental testing. *Cement and Concrete Research*. 106(May 2017):103–116.
- Wolfs, R.J.M., Bos, F.P. & Salet, T.A.M. 2019. Triaxial compression testing on early age concrete for numerical analysis of 3D concrete printing. *Cement and Concrete Composites*. 104(May).

Chapter 7

Conclusions

7.1 Research summary and contributions

This research seeks to develop practicable analytical models based on rheological material properties that collectively contribute towards constructability design for 3DPC. Five main objectives are identified in order to achieve this aim. Chapters 2 to 6 address the objectives in sequential order.

Chapter 2 depicts the development of a 3D concrete printer to enable for the execution of experimental work in subsequent chapters. An industrial-grade, gantry type 3D concrete printer with roughly 1 m³ build volume is designed on AutoCAD and manufactured in the Department of Civil Engineering's workshop. The developmental process of a highly thixotropic 3D printable material is presented, including the application of the Fuller Thompson theory. Hardened mechanical properties indicate that the standard 3DPC material used at Stellenbosch University is classified as a high-performance concrete. The evolution of 3D concrete printing is demonstrated via several 3D prints, from initial skew printing to the latest X-project, which includes fibres in the material as well as surface patterns on printed objects. This chapter proffers as mastering of basic 3DPC technology, from machine and material development to successful implementation and application by practical demonstration of 3D printed objects.

Chapter 3 develops an ab initio approach for thixotropy characterisation of 3D printable concrete. A bi-linear thixotropy model is developed that accounts for re-flocculation (R_{thix}) of particles after agitation, which is a physical process, as well as structuration (A_{thix}) that is a chemical process. The novelty of the model is that it presents the static yield shear stress evolution of a thixotropic material after it has been extruded from the nozzle; thus, shear history i.e. break down of the material's microstructure due to pumping is accounted for. Relevant theory is presented to support the development of the model. The experimental characterisation process is executed solely with the use of a rheometer. The study found that R_{thix} possesses a gradient of up to one order of magnitude larger than A_{thix} , concluding that R_{thix} is a better indicator of thixotropic behaviour suitable for 3DPC than A_{thix} , in particular the transport capability of concrete. The novel application of nano-silica for 3D printable concrete validates the bi-linear model. The improved buildability obtainable by nanoparticle incorporation is

depicted by static yield shear stress evolution curves, which is then confirmed by a 3DPC experimental process where more filament layers were obtained before failure occurred by plastic yielding of the material.

Chapter 4 builds on the thixotropy model by developing a quasi-static filament shape retention model. The model predicts the largest filament layer height whereby no plastic yielding will occur under self-weight, thus preventing excessive deformation after deposition of the filament. This ensures for adequate surface aesthetics of printed objects. The theoretical framework for the model is presented, followed by the development of another model to determine whether sufficient friction is present between a filament layer and the print bed surface. This is a pre-requisite for the shape retention model to be valid. An experimental process is conducted via filament extrusion to verify the model. The model succeeded in predicting the maximum stable filament layer height; however, the acute sensitivity of thixotropic materials to vibrations is demonstrated. Numerical validation via FEA is conducted by means of a simplified plane strain filament layer. A 6.7 % difference in stable filament layer heights is obtained between the analytical and numerical models. The numerical model then further depicts the inherent conservatism of the analytical model, due to it not accounting for interparticle friction. The novelty of the model is that it is simple, practical and based on a single rheological reading, negating extensive material characterisation, whilst yielding conservative filament layer heights to ensure for surface aesthetics of printed objects.

Chapter 5 also builds on the thixotropy model by developing an analytical model for buildability performance quantification. The relevant theoretical framework is presented, and an a priori check given to determine which equation to implement in any scenario. The novelty of the model is firstly that it is solely based on rheological material characterisation, thus negating any fresh state mechanical testing. Secondly, and very importantly, the model accounts for confinement within filament layers due to varying filament height over width aspect ratios. A lower aspect ratio yields an apparent increase in the bearing strength of a filament layer. This is accounted for by simplifying the Mohr-Coulomb failure criterion, and incorporating strength correction factors for various filament layer aspect ratios. An experimental verification process is conducted by printing a circular hollow column until failure occurs. The model predicted failure to occur after the deposition of the 55th filament layer, while actual failure occurred after the deposition of the 60th filament layer, yielding a conservative prediction in vertical building height of 8.33 %.

Chapter 6 presents the culmination of this research whereby a constructability design model is developed for 3DPC. This model is developed by combining all 3 models previously depicted in Chapters 3, 4 and 5. The novelty of this model is that it presents the user with the optimum print parameter combination, i.e. filament layer height and print speed, that successfully yields the entire specified print object in the least amount of time. Therefore, construction time is optimised to indirectly enable for cost savings, ultimately facilitating large-scale industry adoption of 3DPC. A typical 3DPC structural wall element is designed and printed for experimental verification. However, failure occurred before reaching the prescribed design height. Several factors contributed to this result, of which the most prominent is the inconsistency in material rheology obtained by batch mixing of concrete. To account for uncertainty of deterministic models, a statistical design model is developed by performing FORM analyses and developing material partial factors, thereby reducing the probability of failure to 10 %. If the statistical design model was employed for the experimental verification, a 13.3 % under prediction would have been obtained.

In essence, this research presents a novel constructability design model specifically tailored for the 3DPC industry. It is solely based on the rheological characterisation of materials to expedite the material characterisation process, thus avoiding tedious fresh state mechanical characterisation tests. In addition to its time optimisation possibilities, the model presents insight into the behaviour of the material. By interpreting R_{thix} , an idea of the material's thixotropy behaviour, and hence appropriateness for 3DPC, is obtained. Further interpretation of A_{thix} gives insight into the material's buildability performance. The application of this model further guarantees the successful construction of an object to a certain degree, thereby essentially minimising risk. The author of this research hopes that this contribution constitute towards the quotidian tools of the future 3DPC engineer.

7.2 Main research findings

Specific conclusions are given in Chapters 3 to 6. Here, conclusions pertinent to the thesis of rheo-mechanics suitability for modelling 3D concrete printing constructability are drawn.

Chapter 3: Rheology & thixotropy

- The rate of re-building the static yield shear resistance after agitation, is defined in this research as R_{thix} , and shown to be an important buildability parameter for 3D printing. In this research, R_{thix} is a better indicator of appropriate thixotropy behaviour for 3DPC than A_{thix} . For example, the 1 % nano-silica (optimum) mix

has a lower A_{thix} value than the standard mix, which according to current literature, implies that the 1 % nano-silica mix is less thixotropic. However, the 1 % nano-silica mix has a larger R_{thix} value than the standard mix. The 1 % nano-silica mix performed better in the 3DPC test by achieving 5 layers more than the standard mix, mainly due to the contribution of the increased re-flocculation rate. The 1 % nano-silica mix was also visually observed to be the most thixotropic of all mixes.

- An optimum SP dosage exists to obtain highly thixotropic behaviour for HPC's with low w/c ratios. This is particularly evident in the re-flocculation thixotropy mechanism, where a larger R_{thix} value is achieved with an optimum SP dosage. In contrast to fresh state mechanical material characterisation, rheological characterisation efficiently depicts the degree of thixotropy of a material in addition to its strength evolution as a function of time. To capture possible higher initial rates in growth of compressive strength and stiffness for accurate mechanical modelling of the fresh state buildability, would require mechanical tests at small time intervals (seconds, minutes) after agitation, associated with significant experimental effort.
- An optimum amount of nanoparticle addition further increases the re-flocculation thixotropy mechanism. The largest R_{thix} value of 8 Pa/s is achieved in this research with 1 % nano-silica addition. Dosages larger than the optimum (i.e. over-dosage) yield lower R_{thix} values, thus negatively affecting thixotropy behaviour. Rheological characterisation captures this influence, while mechanical testing would require significant and inhibitive testing effort and cost.

Chapter 4: Filament shape retention

- Analytical expressions were developed to determine the maximum filament layer height at which plastic yielding will not occur under self-weight, purely with the use of rheo-mechanics. The governing expression, Equation 4.16, predicted a maximum stable filament layer height of 46 mm for the 3D printable material. The experimental procedure verified the applicability of the model where no plastic yielding occurred at a filament layer height of 40 mm. Insignificant elastic deformations are however present, which the model does not account for.
- The experimental procedure further depicts the acute sensitivity of highly thixotropic materials to vibrations, which should be avoided to obtain adequate filament shape retention after extrusion.

Chapter 5: Buildability

- Failure of fresh 3D printed elements due to plastic flow induced by the weight of upper layers is captured with reasonable accuracy (< 10 %) by a modified Mohr-Coulomb criterion that incorporates strength correction factors to account for varying filament layer aspect ratios.
- Accurately predicting buildability for 3DPC is possible with only the rheology characteristics, namely the re-flocculation rate (R_{thix}), structuration rate (A_{thix}) and the initial static and dynamic yield shear stress. Time consuming, elaborate testing of time-dependent mechanical strength, stiffness and Mohr-Coulomb parameters in the fresh state is avoided.

Chapter 6: Optimised constructability design

- High variation in material rheology parameters is obtained due to the concrete batch mixing process. Coefficient of variation values of over 30 % are obtained. The significant variability is also found for mechanical model parameters, which further motivates the rheo-mechanics approach and limited number of model parameters for which a larger pool of data should be generated for reliable characterisation.
- A deterministic approach using average values for model parameters is not sufficient for industry adoption as it presents a 61 % probability of failure in this research. This is mainly due to the high CoV values of the batch mixed material, as the rheometry testing cannot be conducted simultaneously with the 3D print. Additionally, the rheometer's shear rate cannot be correlated to that induced by pumping.
- A probabilistic design model is developed by employing the first-order reliability method (FORM) and deriving material partial factors to reduce the probability of failure of the design model to 10 %. By analysis, it is determined that if this model was employed for the experimental testing, a 13.3 % under prediction would have been obtained.

7.3 Recommended future research

The constructability design model can be extended by following a systematic approach for future research. Initially, a theoretical framework is required to extract a material's Young's Modulus from rheometer testing. It is important that it must be solely obtained from rheometer testing, as any additional fresh state tests (e.g. mechanical tests for Young's Modulus

determination) will render this model as inefficient for practical application. After successfully achieving this, the buildability model can be extended to include for geometrical nonlinearity in terms of elastic buckling. Furthermore, a non-linear print path length can be specified to account for the construction of non-vertical objects. Additional checks are to be provided for eccentricity and surface contact between successive filament layers, possibly requiring iterative numerical computation. The filament shape retention model can be expanded to either limit the maximum filament layer height by plastic yielding (as the current simplified, conservative model) or elastic deformation with the use of Young's Modulus.

By incorporating the aforementioned improvements, the constructability design model can account for various failure mechanisms for any object geometry, thus acting as a holistic constructability design model based only on rheometer testing. However, deterministic modelling is insufficient for industry application due to large variation in magnitude of certain parameters. It is advised to develop material and load partial factors, based on large and representative statistical samples, for various model applications e.g. under controlled laboratory conditions and on-site construction. The optimum probability of failure can be determined by accounting for cost implications in the event of failed 3D prints, relative to the successful 3D prints. This yields a holistic, statistically safe and cost-optimised constructability design model for the 3DPC industry.

Addendum A – Article Declarations


Declaration by the candidate:

With regard to Chapter 3, the nature and scope of my contribution were as follows:

Nature of contribution	Extent of contribution (%)
Development of theory, conducting experimental work, processing of data, writing of manuscript.	90

The following co-authors have contributed to Chapter 3:

Name	E-mail address	Nature of contribution	Extent of contribution (%)
Dr Stephan Zeranka	szranka@sun.ac.za	Reviewing of manuscript, proposed insightful amendments.	5
Prof Gideon van Zijl	gvanzijl@sun.ac.za	Reviewing of manuscript, proposed insightful amendments.	5


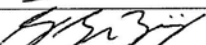
Signature of candidate: 

Date: 01/07/2019

Declaration by co-authors:

The undersigned hereby confirm that

1. the declaration above accurately reflects the nature and extent of the contributions of the candidate and the co-authors to Chapter 3,
2. no other authors contributed to Chapter 3 besides those specified above, and
3. potential conflicts of interest have been revealed to all interested parties and that the necessary arrangements have been made to use the material in Chapter 3 of this dissertation.

Signature	Institutional affiliation	Date
	Stellenbosch University	2019-07-05
	STELLENBOSCH UNIVERSITY	2019-07-01

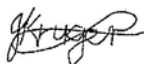
Declaration by the candidate:

With regard to Chapter 4, the nature and scope of my contribution were as follows:

Nature of contribution	Extent of contribution (%)
Development of theory, conducting experimental work, processing of data, writing of manuscript.	90

The following co-authors have contributed to Chapter 4:

Name	E-mail address	Nature of contribution	Extent of contribution (%)
Dr Stephan Zeranka	szranka@sun.ac.za	Reviewing of manuscript, proposed insightful amendments.	5
Prof Gideon van Zijl	gvanzijl@sun.ac.za	Reviewing of manuscript, proposed insightful amendments.	5


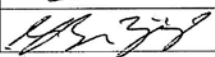
Signature of candidate: 

Date: 01/07/2019

Declaration by co-authors:

The undersigned hereby confirm that

1. the declaration above accurately reflects the nature and extent of the contributions of the candidate and the co-authors to Chapter 4,
2. no other authors contributed to Chapter 4 besides those specified above, and
3. potential conflicts of interest have been revealed to all interested parties and that the necessary arrangements have been made to use the material in Chapter 4 of this dissertation.

Signature	Institutional affiliation	Date
	Stellenbosch University	2019-07-05
	STELLENBOSCH UNIVERSITY	2019-07-01

Addenda


Declaration by the candidate:

With regard to Chapter 5, the nature and scope of my contribution were as follows:

Nature of contribution	Extent of contribution (%)
Development of theory, conducting experimental work, processing of data, writing of manuscript.	90

The following co-authors have contributed to Chapter 5:

Name	E-mail address	Nature of contribution	Extent of contribution (%)
Dr Stephan Zeranka	szranka@sun.ac.za	Reviewing of manuscript, proposed insightful amendments.	5
Prof Gideon van Zijl	gvanzijl@sun.ac.za	Reviewing of manuscript, proposed insightful amendments.	5

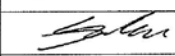

Signature of candidate: 

Date: 01/07/2019

Declaration by co-authors:

The undersigned hereby confirm that

1. the declaration above accurately reflects the nature and extent of the contributions of the candidate and the co-authors to Chapter 5,
2. no other authors contributed to Chapter 5 besides those specified above, and
3. potential conflicts of interest have been revealed to all interested parties and that the necessary arrangements have been made to use the material in Chapter 5 of this dissertation.

Signature	Institutional affiliation	Date
	Stellenbosch University	2019-07-05
	STELLENBOSCH UNIVERSITY	2019-07-01

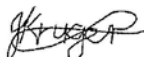
Declaration by the candidate:

With regard to Chapter 6, the nature and scope of my contribution were as follows:

Nature of contribution	Extent of contribution (%)
Development of theory, conducting experimental work, processing of data, writing of manuscript.	80

The following co-authors have contributed to Chapter 6:

Name	E-mail address	Nature of contribution	Extent of contribution (%)
Mr Seung Cho	scho@sun.ac.za	Reviewing of manuscript, assisted with planning and execution of experimental work.	5
Dr Stephan Zeranka	szranka@sun.ac.za	Reviewing of manuscript, proposed insightful amendments.	5
Prof Celeste Viljoen	cbarnardo@sun.ac.za	Assisted with development of statistical model.	5
Prof Gideon van Zijl	gvanzijl@sun.ac.za	Reviewing of manuscript, proposed insightful amendments.	5



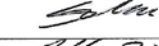
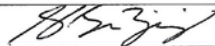
Signature of candidate: 

Date: 01/07/2019

Declaration by co-authors:

The undersigned hereby confirm that

1. the declaration above accurately reflects the nature and extent of the contributions of the candidate and the co-authors to Chapter 6,
2. no other authors contributed to Chapter 6 besides those specified above, and
3. potential conflicts of interest have been revealed to all interested parties and that the necessary arrangements have been made to use the material in Chapter 6 of this dissertation.

Signature	Institutional affiliation	Date
	Stellenbosch University	2019-07-10
	Stellenbosch University	2019-07-10
	Stellenbosch University	2019-07-05
	STELLENBOSCH UNIVERSITY	2019-07-01

Addendum B – Copyright Permission

Elsevier:

Table of Author's Rights

	Preprint version (with a few exceptions- see below *)	Accepted Author Manuscript	Published Journal Articles
Use for classroom teaching by author or author's institution and presentation at a meeting or conference and distributing copies to attendees	Yes	Yes	Yes
Use for internal training by author's company	Yes	Yes	Yes
Distribution to colleagues for their research use	Yes	Yes	Yes
Use in a subsequent compilation of the author's works	Yes	Yes	Yes
Inclusion in a thesis or dissertation	Yes	Yes	Yes
Reuse of portions or extracts from the article in other works	Yes	Yes with full acknowledgement of final article	Yes with full acknowledgement of final article
Preparation of derivative works (other than for commercial purposes)	Yes	Yes with full acknowledgement of final article	Yes with full acknowledgement of final article
Preprint servers	Yes	Yes with the specific written permission of Elsevier	No
Voluntary posting on open web sites operated by author or author's institution for scholarly purposes	Yes (author may later add an appropriate bibliographic citation, indicating subsequent publication by Elsevier and journal title)	Yes, with appropriate bibliographic citation and a link to the article once published	Only with the specific written permission of Elsevier
Mandated deposit or deposit in or posting to subject-oriented or centralized repositories	Yes under specific agreement between Elsevier and the repository	Yes under specific agreement between Elsevier and the repository**	Yes under specific agreement between Elsevier and the repository
Use or posting for commercial gain or to substitute for services provided directly by journal	Only with the specific written permission of Elsevier	Only with the specific written permission of Elsevier	Only with the specific written permission of Elsevier

** Voluntary posting of Accepted Author Manuscripts in the arXiv subject repository is permitted.